STABILITY AND CRUSHING BEHAVIORS OF CYLINDRICAL TUBES WITH A CUTOUT, INCLUDING THE MITIGATION OF THEIR LOCAL INSTABILITY USING SHAPE MEMORY ALLOYS

by

HAIPENG HAN

Submitted
in partial fulfillment of the requirements
for the degree of

Doctor of Philosophy

Major Subject: Civil Engineering

at

Dalhousie University

Halifax, Nova Scotia

September 2006

Your file Votre référence
ISBN: 978-0-494-27640-2
Our file Notre référence
ISBN: 978-0-494-27640-2

DALHOUSIE UNIVERSITY

To comply with the Canadian Privacy Act the National Library of Canada has requested that the following pages be removed from this copy of the thesis:

Preliminary Pages
- Examiners Signature Page
- Dalhousie Library Copyright Agreement

Appendices
- Copyright Releases (if applicable)

For my loving wife, Yan (Ashley),
whose tremendous support, encouragement, patience and understanding
carried out through all the times

TABLE OF CONTENTS

LIST OF FIGURES

LIST OF TABLES

LIST OF SYMBOLS AND ABBREVIATIONS

Latin Alphabet

a	Size of cutout
A_{11}	Axial stiffness
A_f	Austenite finish temperature of shape memory alloy material
A_O	overall area of the section
A_s	austenite start temperature of shape memory alloy material
ABAQUS	Commercial finite element code
ANSYS	Commercial finite element code
ASTM	American society for testing and materials
b	Width of the plate
$[\bar{B}]$	Strain-displacement matrix
$[B_0]$	Matrix for the linear infinitesimal strain
$[B_L]$	Matrix for nonlinear strain components
B_{11}	Bending-extensional coupling stiffness
C	Damping matrix (Chapter 2)
C	Overall circumference of the tubes (Chapter 4)
c	Speed of sound
$[C]$	Constitutive matrix
CTE	Coefficient of thermal expansion
C_N	Net circumference of the tubes
D	Constant for material strain rate behavior
D_1	Plastic energy absorbed by the two stationary axisymmetric plastic hinges
D_{11}	Flexural stiffness
$\overline{D}_{11}$	Effective flexural stiffness
D_2	Plastic energy absorbed by the axisymmetric central hinge
D_3	Plastic energy absorbed in circumferential stretching
D_T	Total energy absorbed during the development of one complete wrinkle
D/t	Diameter over thickness ratio of shells/tubes
DFAILC	Maximum strain for fiber compression
DFAILT	Maximum strain for fiber tension
E	Young's modulus
E_{11}	Elastic modulus in Longitudinal direction
E_{22}	Elastic modulus in transverse direction
$E_a(T)$	Young's modulus of shape memory alloy material
$E_{1m}(T)$	Longitudinal modulus of composite matrix material

$E_{2m}(T)$	Transverse modulus of composite matrix material
EA	Energy absorption
ECTE	Effective coefficient of thermal expansion
F	Nonlinear function of unknown displacement
$\{F\}$	Consistent force vector
$\{f^b\}$	Body force vectors
f_{EXT}	Vectors of the external force
f_{INT}	Vectors of the internal force
f_n	Normal force at the interface
f_s	Shear force at the interface
$\{f^S\}$	Surface force vectors
FBRT	Reduction factor for tensile strength in the fiber direction after matrix failure
FE	Finite element
FRP	Fiber-reinforced plastic
FRPC	Fiber-reinforced polymer composite
G_a	Shear modulus of shape memory alloy actuator
G_{12m}	Shear modulus of host composite material
G_{12}	Shear modulus of shape memory alloy hybrid composite lamina (chapter 7)
G_{12}	In-plane shear modulus (Chapter 5 & 6)
G_{23}	Out-of-plane shear modulus
GB	Global buckling mode
H	Thickness of tube [12]
HPG1	Hybrid of pultruded tube with the glass fiber braiding of 0.3 mm thickness
HPG2	Hybrid of pultruded tube with the glass fiber braiding of 1.0 mm thickness
HPC1	Hybrid of pultruded tube with the carbon fiber braiding of 0.3 mm thickness
HPC2	Hybrid of pultruded tube with the carbon fiber braiding of 1.0 mm thickness
ITS	Impact testing system
J_d	Desired number of iterations for convergence
K	Empirical factor in a function of the geometry of the shells (Section 2.2.2)
K	Gradient of the force/displacement relation (Section 2.2.3)
K_c	Factor relative to the aspect ratio of the shells
K_d	Buckling load reduction factor
K_e	Effective length factor
$[K]$	Stiffness matrix
$[K_T]$	Tangential stiffness matrix
$[K_0]$	Small displacement stiffness matrix

$[K_L]$	Large displacement stiffness matrix
KE	kinetic energy
l	Length of half wrinkle
L	Length of shells/tubes
$L_{\min}$	Smallest element dimension in the mesh
L_0/L	Factor on location of cutout along shells/tubes
LB	Local Buckling
LB-BH	Local buckling followed by buckling capacity hardening
L/D	length/diameter ratio of shells/tubes
LS-DYNA	Commercial finite element code
LY-GB	Local yielding results in global bending and then in global buckling
LY-LB	Local yielding around cutout results in local buckling near the loaded end
M	Mass matrix
M_0	Plastic collapse moment [12]
M_f	Martensite finish temperature
M_s	Martensite start temperature
MAT1	Type one steel material model
MAT2	Type two steel material model
N_1	First buckling load of thin-walled cylindrical shell
N_{cutout}	Peak buckling load of shells with a cutout
N_{cr}	Critical buckling load of thin-walled cylindrical shell
N_{FE}	First buckling load obtained from finite element analysis
NFLF	Normal force at the bond failure
$N_{perfect}$	Peak buckling load of the perfect shell
N_{ref}	Reference buckling load
NSERC	Natural Science and Engineering Research Council of Canada
P	Force
P_I	Peak crushing force
P_{I_A}	Peak crushing force of aluminum tubes
P_{I_S}	Peak crushing force of steel tubes
P_{I_Sref}	Reference peak crushing force for steel tubes
P_m	Mean crushing force
P_only	Pultrusion only
PC	Progressive crushing mode
PC1	The first type of progressive crushing mode (Tables 4.1 and 4.2)
PC2	The second type of progressive crushing mode (Tables 4.1 and 4.2)
PC3	The third type of progressive crushing mode (Tables 4.1 and 4.2)
PC4	The fourth type of progressive crushing mode (Tables 4.1 and 4.2)
q	Constant for material strain rate behaviour
$[Q]$	Plane stress-reduced stiffness matrix

Q-S	Quasi-static
R	Radius of the shells/tubes
R	Scalar residual in arc-length method
R-Square	Coefficient of determination in regression analysis
r_g	Radius of gyration of the tube
S	Surface area of the structure
S_L^+	Longitudinal tensile strength
S_L^-	Longitudinal compressive strength
S_T^+	Transverse tensile strength
S_T^-	Transverse compressive strength
S_{LT}	In-plane shear strength
SCF	Stress concentration factor at the edge of cutout
SEA	Specific energy absorption
SFLF	Shear force at the bond failure
SMA	Shape memory alloy
SME	Shape memory effect
SMAHC	Shape memory alloy hybrid composite
t	Time
t	Thickness of the shells/tubes/plates
T	Temperature
$\{u\}$	Displacement vector
$\dot{u}$	Vectors of generalized velocities
$\ddot{u}$	Vectors of generalized accelerations
u_0	Initial condition of displacement
$\dot{u}_0$	Initial condition of velocities
$\ddot{u}_0$	Initial condition of accelerations
$\{u^{(r)}\}$	The rth eigenvector
V	Volume of the structure
V_0	Impact velocity
x	x-coordinate
y	y-coordinate
YCFAC	Reduction factor for compressive strength in the fiber direction after matrix failure
Z	Coefficient relative to the geometry of the shells
z	z-coordinate

Greek Symbols

$\{\alpha\}$	Vector of coefficient of thermal expansion
α_{1m}	Longitudinal effective coefficient of thermal expansion of composite matrix material

α_{2m}	Transverse effective coefficient of thermal expansion of composite matrix material
α_{1a}	Longitudinal effective coefficient of thermal expansion of shape memory alloy
α_{2a}	Transverse effective coefficient of thermal expansion of shape memory alloy
β	Scaling parameter to ensure the correct scale in arc-length method
Δt	Time step size
Δ_{cr}	Critical displacement corresponding to critical buckling load
$\{\varepsilon\}$	Strain vector
$\dot{\varepsilon}$	Uniaxial plastic strain rate
ε_θ	Mean circumferential strain
$\dot{\varepsilon}_\theta$	Mean circumferential strain rate
γ	Factor that accounts for the difference between theoretical and experimental results
η_1	Structural effectiveness of the section
φ	Ratio of the material volume to the volume enclosed by the section
λ	Loading factor in arc-length method
$\lambda^{(r)}$	The rth eigenvalue
v_a	Volume faction of shape memory alloy material in the shape memory alloy hybrid composite mixture
v_m	Volume faction of host composite material in the SMAHC mixture
v_{21}	Minor Poisson's ratio
$\prod$	Total potential energy
ρ	Material density
$\{\sigma\}$	Stress vector
$\sigma_0^{'}$	Dynamic flow stress
σ_0	Static flow stress
$\sigma_{1a}(T)$	Stress along longitudinal direction of shape memory alloy
$\sigma_{2a}(T)$	Stress along transverse direction of shape memory alloy
$\sigma_{1m}(T)$	Stress along longitudinal direction of composite matrix material
$\sigma_{2m}(T)$	Stress along transverse direction of composite matrix material
σ_{cr}	buckling stress
σ_r	Recovery stress
σ_u	Ultimate strength of the material
σ_u / σ_0	Strain hardening ratio of material
σ_y	Yield strength of the material
υ	Poisson's ratio
$\omega_{\max}$	The highest natural frequency of interest
$\xi_{\max}$	Fraction of critical damping

ACKNOWLEDGMENTS

I would like to express my sincere appreciation and gratitude to my supervisor, Dr. Farid Taheri, professor of Civil and Resource Engineering at Dalhousie University, whose knowledge, experience and guidance have been crucial throughout the course of this study. I could always benefit from the discussions I had with him on various technical issues when I faced a cross-road. Without him, this work would have been impossible. I wish also to express my gratitude to my co-supervisor, Dr. Neil Pegg for his constant support, instructions and insightful discussions. The financial support of NSERC in the form of an operating grant to Drs. Taheri and Pegg in support of this work is gratefully acknowledged.

I also wish to thank Dr. Tasos Georgiades of Department of Mechanical Engineering and Dr. Gordon Fenton of Department of Engineering Mathematics, for their help, advice, time and interest in reviewing this work. Special appreciations are extended to the technicians of the Civil Engineering Department, Mr. Mark Macdonald, Mr. Blair Nickerson and Mr. Brian Leikens, for their valuable assistance in specimen preparation and instrumentation of the tests during the experimental investigation phase of this work. Thanks are also extended to my colleagues, Dr. Zheng Zhang, Brian Yuen, Nader Cheraghi, Khaled Shahin, You Lu and all other fellows in Dr. Taheri's research group, for the helpful technical discussions and pleasant working environment. My special thanks also go to Eric and Marilyn for polishing parts of this thesis.

Last, but not least, I would like to thank my parents, parents-in-law, my two brothers and rest of my family for their support and patience through the course of this study.

ABSTRACT

Cylindrical tubes are commonly used in engineering structures. During their service life, these components are often subjected to axial compressive loading, either statically or dynamically. It is known that the presence of a cutout can lead to substantial stress concentrations in the structure. Nevertheless, there is still a lack of understanding of how a cutout would influence such components' stability and crushing behaviors.

The influence of a cutout on the load-bearing capacity and buckling behavior of aluminum cylindrical shell was studied in the first stage of this thesis. Several parameters that could influence the stability behavior of cylindrical shells, including diameter/thickness (D/t) ratio, length/diameter (L/D) ratio, as well as the cutout's size and location were considered in this study. Through verification of the computational results with an experimental investigation, empirical equations predicting the "buckling load reduction factor" were developed.

The quasi-static and dynamic crushing behaviors and energy absorption capacity of aluminum and steel tubes with a cutout were studied numerically and experimentally. Various L/D ratios of the tubes and different cutout locations along the tubes were considered. A range of impact velocities, from zero up to 20m/s, equivalent to an intermediate speed car crash, were analyzed. Subsequently, the correlation between the material properties, loading speed, cutout location and crushing behavior of the tubes was established. Based on the outcome of this numerical and experimental investigation, a set of empirical equations for predicting the mean crushing force of the tubes having a cutout was developed.

A hybrid of pultruded and braided composite tubes was proposed as a superior effective energy absorber to pultruded tubes. The crushing behavior and energy absorption capacity of this proposed new energy absorber were characterized through numerical and experiment investigations.

A feasibility study was carried out to study the mitigation of local instability in a composite cylindrical shell using shape memory alloy (SMA) materials. The outcome of this preliminary work showed that it is very promising to use SMA in mitigating the local instability of plates/shells. Significant factors influencing the use of SMA in this application were investigated.

Chapter 1 Introduction

1.1 Overview and motivation

Circular cylindrical shells or tubes are commonly used in engineering structures, such as in aircrafts, missiles, silos, pipelines, tanks and automobiles. During their service life, these components are often subjected to axial compressive loading in either a static or dynamic way. In addition these structures often include geometric discontinuities, such as stiffeners and cutouts, which can lead to substantial stress concentrations and influence the buckling capacity as well as crushing behavior of this type of structural components. It is well known that the presence of cutout in a cylindrical shell/tube structure will negatively influence the performance of the structures. People recognize that there is a high stress concentration around the edge of a cutout, and have implemented several practical techniques to mitigate the stress concentration around the cutout. It is also obvious that the presence of a cutout impairs the stability and crushing behavior of these structural components. This, however, has not been identified quantitatively. This is therefore the major motivation of this research.

Under static loading conditions, in addition to other types of structural failures, such as material failure and fatigue, the buckling problem is always the pronounced concern in engineering design. The buckling problem of cylindrical shells has attracted the attention of many researchers for more than a century. The classical buckling equation only applies to thin-walled cylindrical shells made of isotropic elastic materials. For cylindrical shells made of materials with nonlinear behavior, or for moderately thick-walled cylindrical shells, the traditional linear buckling analysis will not yield accurate results. Although a number of closed form solutions exist for cylindrical shells without a cutout, it is very difficult to achieve one for shells with a cutout. In addition to experimental investigation, the nonlinear finite element analysis method could be considered as a viable alternative for determining the buckling collapse load of cylindrical shells with a cutout.

In the first stage of this thesis work, the prebuckling, buckling and postbuckling behavior of the above-mentioned shells will be characterized through nonlinear finite element analysis and experimental investigations. Along with the geometrical aspect ratio of shells, the influences of the cutout size and location on the buckling and postbuckling behavior of the shells, will be investigated.

Under dynamic loading conditions, depending on the speed of the applied axial load, the structural components will be crushed either quasi-statically or dynamically. The term "quasi-static crushing load" refers to the class of compression load that is applied faster than a normal static load but slower than certain limit depending on the type of material. Whereas the term "dynamic crushing load" refers to the class of load which is applied at a speed higher than a certain threshold, and cannot be characterized in a static or quasi-static way due to the strain rate sensitivity of the material. Understanding the crushing behavior of such structural components is very important in design for crashworthiness. For example, the crash performance of a vehicle is directly related to the crushing resistance and energy absorption of its chassis. Consequently, investigation of crashworthiness and crushing behavior of tubular structural components has gained importance for the automobile, oil, gas, and aerospace industries. Investigation into the influence of cutouts on the crushing behavior of tubular structures is very scarce in literature.

Composite materials, due to their high strength-to-weight and stiffness-to weight ratios, have been widely used in industry. The crashworthiness design of composite tubular structures has been found to be more complex than that of their metallic counterparts. The effective design of an energy absorber using composite materials is very important in order to demonstrate the superiority of high strength-to-weight and stiffness-to-weight ratios over conventional metals. Developing of effective energy absorber using composite materials has attracted attention of many researchers in the recent years. Pultrusion and braiding are two widely used cost effective manufacturing process in composite manufacturing industry.

The second stage of the thesis work is projected to numerically and experimentally investigate the influence of a cutout on the crushing behavior and energy absorption capacity of metallic tubes, subject to quasi-static and dynamic impact

loadings. Moreover, in order to produce an economical design for an energy absorber using composite material, a novel structure for a tubular energy absorber using a combination of pultrution and braiding technology is proposed, and numerically and experimentally studied.

Shape memory alloy (SMA) materials are a class of materials that can be returned to their original configuration by heating through the reverse transformation temperature range. In addition, during the reverse phase transformation, the Young's modulus of a SMA can be increased up to 3~6 times of its original state. A pre-strained SMA wire constrained mechanically or elastically, could develop a large tensile recovery force upon the application of heat, due to mechanical end constraints and the intrinsic nature of the shape memory effect (SME). The architecture of shape memory alloy hybrid composite (SMAHC) allows the shape memory alloy to be activated through an inherently elevated temperature in the service environment. Making use of the feature of tailored design in laminate composites, pre-strained SMA wires can be positioned to the required or even optimized location of laminated composite structures, so as to improve the performance of the structures. Research into the structural performance of SMAHC structural components can be very useful in aerospace engineering application. The use of SMA material in active control of composite structures, particularly in the concept of SMAHC, still needs to be consummated.

In the third stage of the thesis work, a preliminary study on mitigating the local instabilities of cylindrical shells having a cutout was carried out. For this preliminary work the mitigation of local instability of a square SMAHC plate with and without cutouts will be investigated. The result of this proposed study can be extended to the application of cylindrical shell structures.

1.2 Organization of this dissertation

The organization of this thesis has been designed to address the work that has been done in the proposed three stages. The thesis has been formatted in a manuscript style. Formatting has been altered from the journal paper to match guidelines of Dalhousie University. The thesis is organized as follows:

The background relative to this thesis work is presented in Chapter Two. In this chapter the general nonlinear finite element procedure for static analysis and the explicit nonlinear finite element method for dynamic analysis are reviewed first. The description and general analysis procedures for the buckling and post buckling problem in a structure are also provided, followed by a review of the buckling of cylindrical shells. A brief introduction on the quasi-static and dynamic crushing of cylindrical tubes is presented. The three available analysis approaches for the crushing events, including the analytical solution scheme, finite element analysis approach and experimental investigation method, are discussed. A literature review on the crushing of composite tubes is carried out and reported in this chapter. In the last section of this chapter, brief introductions on shape memory alloy materials as well as its constitutive behaviors are described. The general application of this class of material is reviewed. The application of active structural control using SMA material is also reviewed. Finally, the concept of SMAHC is introduced.

In Chapter Three a numerical and experimental investigation into the buckling and postbuckling of aluminum cylindrical shells with a cutout were conducted. The influence of the cutout on the buckling and postbuckling behavior of cylindrical shells is characterized. Parametric studies consider the cutout size, cutout location as well as various length/diameter (L/D) ratios of the shells. After calibrating the numerical and experimental results, empirical equations predicting the buckling load deduction factor are developed using linear regression methods. This chapter is a full paper published in the journal of "**Thin-Walled Structures** 44 (2006): 254-270".

The numerical and experimental studies on the crushing behavior of cylindrical tubes with a cutout are reported in Chapter Four. Two types of materials, steel and aluminum, which represent strain rate sensitive and insensitive materials are chosen for this study. Both quasi-static and dynamic loading conditions are considered in this work. In the simulation of dynamic crushing, the crushing speed was up to 20 m/s, which is equivalent to an intermediate level car crash. Likewise, the cutout is located at various locations along the tubes of three different L/D ratios. The influence of cutout on the crushing behaviors and energy absorption efficiency of the tubes are characterized numerically and experimentally. On the basis of the numerical and experimental studies,

empirical equations are also developed using linear and nonlinear regression methods to predict the mean crushing forces of the tubes. This chapter is a full paper submitted to the journal of "**Thin-walled Structures**" and is currently under review.

Chapter Five describes the numerical investigation on the crushing behavior and energy absorption capacity of hybrid pultruded and braided composite tubes. The hybrid of pultrusion and braids was proposed as a new design alternative of energy absorber in this study. Focus is placed on proving that the proposed new energy absorber is superior to the corresponding pultruded tube in terms of energy absorption capacity and crushing mode. This chapter, as a full paper, was accepted for publication in the journal of "**Composite Structures**" in April 2006.

Chapter Six presents the experimental verification of the numerical study in Chapter Five. Quasi-static crushing tests on the pultruded tubes and hybrid tubes were conducted in this study. Very good agreement was observed between experimental and numerical investigations. The content in this chapter was submitted to the journal of "**Mechanics of Advanced Materials and Structures**" in July 2006 and is under review.

In Chapter Seven a preliminary study was conducted to mitigate the local instabilities in a composite cylindrical shell having a cutout subject to axial compression in an elevated temperature environment. As preliminary studies, a four sides simply supported, as well as a two sides simply supported and two sides free SMAHC plate with and without a cutout at its center, were studied. In this SMAHC plate, the mixture layer of composite and shape memory alloy material is located at certain layers of the laminated plate and along certain orientations. The plate was subject to uniform edge pre-compression load and a subsequent thermal load of elevated temperature. With the presence of the SMA material in the plate, under elevated temperature environments, the local instability of the SMAHC plate was mitigated due to the activation of the shape memory effect. The analysis of stress concentrations at the edge of the cutout in the SMAHC plate with a central cutout was also carried out. Experimental work was also conducted to verify the findings from the numerical study. This paper was submitted to the Journal of "**Smart Materials and Structures**" in September 2006 and is currently under review.

Chapter Eight provides the conclusions of work in this thesis and recommendations for future work in this field.

Chapter 2 Background

2.1 Review of the nonlinear finite element methods

If the frequency of applied load to a structure is less than roughly one-third of the structure's lowest natural frequency of vibration, then the problem can be regarded as a static problem; otherwise it is a structural dynamics problem. In a structural dynamics problem, it is usually desirable to get a time-history response of the structure. There are two popular methods in time-history analysis: implicit analysis and explicit analysis. Both of these methods are used in many finite element codes. Presently the finite element method is most widely used in static and dynamic structural analysis, including the buckling and crushing analysis of cylindrical tubes described in this thesis. The primary objective of this section is to review briefly the formulation of the conventional "general purpose" nonlinear finite element method based on continuum mechanics, as well as the explicit finite element method for dynamic analysis.

2.1.1 Nonlinear finite element formulation for static analysis

The finite element formulation is derived from the principle of minimum total potential energy. The total potential energy of a system can be expressed simply as:

$$\Pi = \frac{1}{2}\int_V \{\varepsilon\}^T \{\sigma\}\, dV - \left(\int_V \{u\}^T \{f^b\}\, dV + \int_S \{u\}^T \{f^S\}\, dS \right) \qquad (2\text{-}1)$$

Here Π is the total potential energy, $\{u\}$ is the displacement vector, $\{f^b\}$ and $\{f^S\}$ are body and surface force vectors, V and S are volume and surface area of the structure. The relationship between stresses $\{\sigma\}$ and $\{\varepsilon\}$ strain is of the form:

$$\{\sigma\} = [C]\{\varepsilon\} \qquad (2\text{-}2)$$

where $[C]$ is the constitutive matrix. The condition of equilibrium requires that the first variation of the total potential energy vanish:

$$\delta\Pi = \int_V \{\delta\varepsilon\}^T \{\sigma\} dV - \left(\int_V \{\delta u\}^T \{f^b\} dV + \int_S \{\delta u\}^T \{f^S\} dS \right) = 0 \quad (2\text{-}3)$$

From Zienkiewicz [1], strain can be expressed in matrix notation as

$$\{\varepsilon\} = [\bar{B}]\{u\} = \{[B_0] + [B_L]\}\{u\} \quad (2\text{-}4)$$

where $[B_0]$ is the matrix for the linear infinitesimal strain and matrix $[B_L]$ contains the nonlinear strain components. Using equation (2-4), we can rewrite equation (2-3) as:

$$\delta\Pi = \{\delta u\}^T \left[\int_V [\bar{B}]\{\sigma\} dV - \left(\int_V \{f^b\} dV + \int_S \{f^S\} dS \right) \right] = 0 \quad (2\text{-}5)$$

Therefore

$$\int_V [\bar{B}][C]\{\varepsilon\} dV - \left(\int_V \{f^b\} dV + \int_S \{f^S\} dS \right) = 0 \quad (2\text{-}6)$$

Using the strain-displacement relationship, the further finite element formulation of the system is done by forming a stiffness matrix $[K]$ and consistent force vector $\{F\}$. Finally, the simple form of the finite element discretization of the system for a static analysis can be written as:

$$[K]\{u\} = \{F\} \quad (2\text{-}7)$$

This is ready to be solved using general implicit solution procedure.

2.1.2 Explicit finite element method

The equations of motion of a discretized nonlinear structural system can be written as:

$$M\ddot{u} + C\dot{u} + f_{INT} = f_{EXT} \quad (2\text{-}8)$$

where $\ddot{u}$ and $\dot{u}$ are the vectors of generalized velocities and accelerations, respectively. M and C are the mass and damping matrices, and f_{INT} and f_{EXT} are the vectors of the internal and external forces. The internal forces include the effects of material and geometric nonlinearities. Therefore, the internal force vector has to be updated at each

time step during the time integration of the equations of motion. At the current configuration, the internal forces may be evaluated from

$$f_{INT} = \int_V B^T \sigma dV \tag{2-9}$$

where B is the strain-displacement matrix, V is the current volume, and σ is the vector of Cauchy stresses. For linear problems, the internal forces can be written as

$$f_{INT} = Ku \tag{2-10}$$

where K is the stiffness matrix of the system, and u is the vector of generalized displacements.

The central difference scheme to approximate $\ddot{u}$ and $\dot{u}$ for integrating the equation of motion is given by

$$\ddot{u}_t = \frac{1}{\Delta t^2}\left(u_{t-\Delta t} - 2u_t + u_{t+\Delta t}\right) \tag{2-11}$$

$$\dot{u}_t = \frac{1}{2\Delta t}\left(-u_{t-\Delta t} + u_{t+\Delta t}\right) \tag{2-12}$$

where Δt is an appropriate time step size required for the numerical integration.

The displacement solution for time $t + \Delta t$ is obtained by considering the equation (2-8) at time t.

For the linear system, by substituting equation (2-11) and (2-12) into (2-8), one can obtain:

$$\left(\frac{1}{\Delta t^2}M + \frac{1}{2\Delta t}C\right)u_{t+\Delta t} = f_{EXT\,t} - \left(K - \frac{2}{\Delta t^2}M\right)u_t - \left(\frac{1}{\Delta t^2}M - \frac{1}{2\Delta t}C\right)u_{t-\Delta t} \tag{2-13}$$

The above mentioned integration procedure is called an "explicit" integration scheme because the solution of $u_{t+\Delta t}$ is calculated by using the equilibrium conditions at time t (Equation 2-8). For this reason exactly, such integration scheme does not require decomposition (i.e., factorization) of the effective stiffness matrix K in the step-by-step solution (Equation 2-9) and hence no effective stiffness matrix needs to be decomposed.

Using the "explicit" central difference method, the calculation of $u_{t+\Delta t}$ involves u_t and $u_{t-\Delta t}$. Therefore in order to calculate the solution at the first step (i.e., at time Δt), a special procedure must be used. By applying equation (2-11~2-12) at time $t = 0$ and $t = -\Delta t$, one can have

$$u_{-\Delta t} = u_0 - \Delta t \dot{u}_0 + \frac{\Delta t^2}{2} \ddot{u}_0 \tag{2-14}$$

which is known, given the initial conditions ($u_0, \dot{u}_0, \ddot{u}_0$ at $t = 0$) of the problem.

However, the drawback in the dynamic explicit approach is that it is only conditionally stable. The stability limit for the explicit integration operator is that the maximum time increment must be less than a critical value of the smallest transition time for a dilatational wave to cross any element in the mesh.

The central difference scheme (with no damping) is stable for a time step increment satisfying the following inequality [2]:

$$\Delta t \leq \frac{2}{\omega_{\max}} \tag{2-15}$$

Where $\omega_{\max}$ is the highest natural frequency of the finite element (FE) model. Damping can reduce the stable time step. An upper bound for the stable time step with damping is given by [3]:

$$\Delta t \leq \frac{2}{\omega_{\max}} \left(\sqrt{1 + \xi_{\max}^2} - \xi_{\max} \right) \tag{2-16}$$

Where $\xi_{\max}$ is the fraction of critical damping in the mode with the highest natural frequency.

An approximation to the maximum stable time step is often written as the smallest transient time required for a sound wave to travel through any of the elements in the mesh [2]

$$\Delta t_{cr} = \frac{L_{\min}}{c} \tag{2-17}$$

where $L_{\min}$ is the smallest element dimension in the mesh, and where c is the speed of sound. For an isotropic shell element, the speed of sound can be expressed as [3]:

$$c = \sqrt{\frac{E}{\left(1 - \upsilon^2\right)\rho}} \tag{2-18}$$

where E is the Young's modulus, υ is the Poisson's ratio, and ρ is the material density. For shell elements, the element thickness is not considered in determining the smallest element dimension; the stability limit is based upon the mid-plane dimensions only.

2.2 Buckling and postbuckling of cylindrical shells

Typically, the approach for the instability analysis of structures consists of three steps; (1) analysis of the prebuckling status, (2) determination of the stability boundaries, and (3) tracing of the postbuckling equilibrium path. The first step is to compute the stress and strain distribution in the structure with an initial load just before the instability occurs. This is carried out by a linear stress analysis. The second step is to obtain the buckling load, i.e., to find the critical or bifurcation points on the equilibrium path, often by an eigenvalue analysis which will be discussed in section 2.2.1. The third step of instability analysis is to trace the nonlinear response of the structures, called postbuckling analysis to be discussed in section 2.2.3.

2.2.1 Buckling analysis

The stability criterion can be obtained from the second variation of the total potential energy in a structural system. If the second variation of the total potential energy has a positive value, the system remains stable. On the contrary, if the second variation of the total potential energy is negative then the system is unstable. If one takes the second variation of total potential energy from equation (2-5), one can get

$$\delta^2\Pi = \{\delta u\}^T \left[\int_V \delta\left[\bar{B}\right]^T \{\sigma\} dV + \int_V \left[\bar{B}\right]^T \delta\{\sigma\}^T dV \right] \tag{2-19.1}$$

or

$$\delta^2\Pi = \{\delta u\}^T \left[\int_V \delta\left[\bar{B}\right]^T \{\sigma\} dV + \int_V \left[\bar{B}\right]^T [C]\left[\bar{B}\right]\delta\{u\}^T dV \right] \tag{2-19.2}$$

From Zienkiewicz [1], the first integral of equation (2-19.2) can generally be written as

$$\int_V \delta\left[\bar{B}\right]^T \{\sigma\} dV = \left[K_\sigma\right]\{\delta u\} \tag{2-20}$$

where $\left[K_\sigma\right]$ is the geometric matrix. Substituting equation (2-4) into the second integral of equation (2-19.2) and rearranging, the second variation of the total potential energy can be written as:

$$\delta^2\Pi = \{\delta u\}^T [K_T]\{\delta u\} \tag{2-21}$$

In equation (2-21), the tangential stiffness matrix $[K_T]$ can be written as

$$[K_T] = [K_\sigma] + [K_0] + [K_L] \tag{2-22}$$

$$[K_0] = \int_V [B_0]^T [C][B_0] dV \tag{2-23}$$

$$[K_L] = \int_V \left([B_0]^T [C][B_L] + [B_L]^T [C][B_0] + [B_L]^T [C][B_L]\right) dV \tag{2-24}$$

where $[K_0]$ is the small displacement stiffness matrix and $[K_L]$ is the large displacement stiffness matrix.

A critical point is obtained when the tangent stiffness matrix $[K_T]$ has at least one zero eigenvalue. The stability and equilibrium configuration can be determined by solving the eigenvalue problem at the current equilibrium state:

$$[K_T]\{u^{(r)}\} = \lambda^{(r)}\{u^{(r)}\} \tag{2-25}$$

where $\lambda^{(r)}$ is the rth eigenvalue and $\{u^{(r)}\}$ is the corresponding eigenvector.

Computation of the critical point must be done in two steps. Firstly, the equilibrium configuration associated with a given load level P is computed. Secondly, the eigenvalue of the tangent stiffness matrix at this load level is calculated. Usually, the lowest eigenvalue is of interest in considering the critical buckling load. There are two widely used numerical methods for extracting eigenvalues, namely, the Lanczos method and subspace iteration method. The Lanczos method is generally faster when a large number of eigenvalues is needed for a system with many degrees of freedom. The subspace iteration method is effective for computing a small number of eigenvalues [4].

Based on the assumption that displacements $\{u\}$ are infinitesimal for a small load ΔP, the classical buckling problem based on the linearized simplification can be written as [1]:

$$\left([K_0] + \lambda^{(r)}[K_\sigma(\Delta P)]\right)\{u^{(r)}\} = 0 \tag{2-26}$$

where the large displacement stiffness matrix $[K_L]$ in equation (2-22) is ignored. Note that the application of equation (2-26) should be limited in practical engineering problem. In order to avoid mistakes in calculating the stability point in real engineering

applications, the stability should be investigated using the full tangent stiffness matrix in equation (2-25), or using nonlinear static analysis to trace the buckling and postbuckling of the structural system in the full load path, which will be discussed in section 2.2.3.

2.2.2 Review of the buckling of a cylindrical shell

Buckling of cylindrical shells is characterized by a sudden large deformation resulting from an infinitesimal increase in the applied load thus changing the equilibrium configuration of the shell. The buckling of cylindrical shells has been considered by several researchers [5-7]. The classical equation of critical buckling load for symmetrical buckling of a thin-walled shell made of isotropic material under uniform axial pressure can be expressed by [5]:

$$N_{cr} = \frac{E}{\sqrt{3(1-\nu^2)}}\left(\frac{t^2}{R}\right) \tag{2-27}$$

Owing to initial imperfections, cylindrical shells often buckle into axially nonsymmetrical forms. The critical buckling load for nonsymmetrical buckling under uniform axial compression, as reported by [5], is

$$N_{cr} = K\frac{E}{\sqrt{3(1-\nu^2)}}\left(\frac{t^2}{R}\right) \tag{2-28}$$

where K is an empirical factor and function of the geometry of the shells, expressed by:

$K = 1 - 0.901(1 - e^{-\psi})$, and $\psi = \frac{1}{16}\sqrt{\frac{R}{t}}$

Equations (2-27~2-28) are found to provide satisfactory agreement with the tests results of cylindrical shells having length to radius ratio $(L/R) \leq 5$.

Baker *et al.* [6] reported the buckling load of cylindrical shells having various aspect L/R ratios. They predicted the buckling stress of a simply supported cylindrical shell as:

$$\sigma_{cr} = K_c\frac{\pi^2 E}{12(1-\nu^2)}\left(\frac{t^2}{L^2}\right) \tag{2-29}$$

where K_c is a factor related to the aspect ratio of the shells.

For short cylindrical shells ($\gamma Z \le \pi^2 / 2\sqrt{3}$)

$$K_c = 1 + \frac{12\gamma^2 Z^2}{\pi^4} \tag{2-30}$$

For moderately long cylindrical shells ($\gamma Z \le \pi^2 / 2\sqrt{3}$)

$$K_c = \frac{4\sqrt{3}}{\pi^2}\gamma Z \tag{2-31}$$

For very long cylindrical shells, the buckling equation has to be checked as an Euler column by the equation:

$$\sigma_{cr} = \frac{\pi^2}{2} E(\frac{R^2}{L^2}) \tag{2-32}$$

In equation (2-30 and 2-31), γ is a factor that accounts for the difference between theoretical and experimental results and is a function of the ratio R/t. A chart reporting the values of γ can be found in [6]. Z is the coefficient related to the geometry of the shells, given by:

$$Z = \frac{L^2}{Rt}\sqrt{(1-\nu^2)} \tag{2-33}$$

Considering various shell aspect ratios, Litle [7] also reported the buckling solution of simply supported cylindrical shells (see Figure 2.1). As seen from Figure 2.1, for $0.2 \le L/R \le 40$, the buckling load is almost independent of the shell L/R aspect ratio.

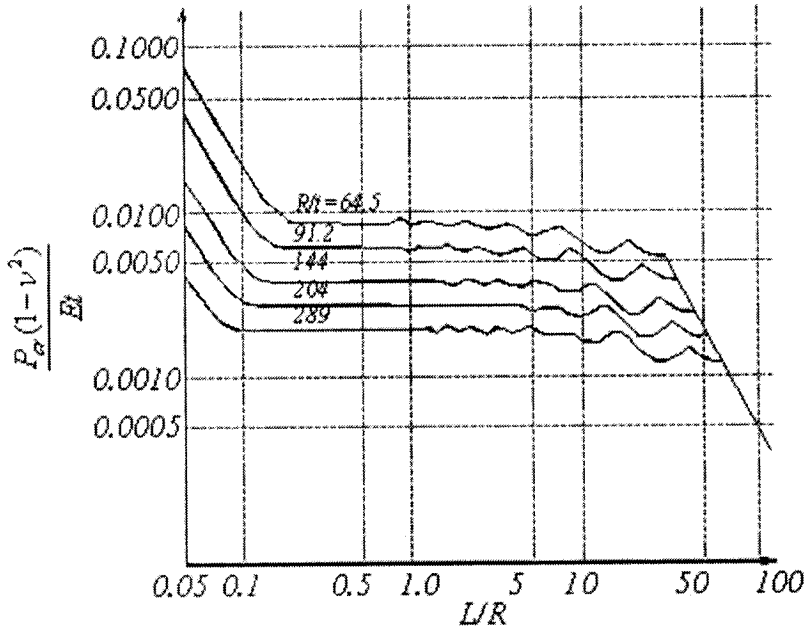

Figure 2-1: Elastic buckling of cylindrical shells under axial compression [3]

2.2.3 Postbuckling analysis

Structures, such as beam, plate or shell, even having an initial geometric imperfection, have the capability to carry loads beyond their buckling limits. In other cases, the structures collapse well below the bifurcation buckling load due to imperfection sensitivity. Or sometimes the bifurcation point does not exist at all (e.g., a non-symmetric laminated composite plate subject to axial compression). In those situations, postbuckling analysis of structures becomes necessary. In the solution for postbuckling problems, generally there are two solution methods, the arc length method and the conventional iterative methods, which include the Newton-Raphson method and the modified Newton-Raphson method.

2.2.3.1 Iterative methods

The Newton-Raphson iterative method is based on a Taylor's series expansion of the nonlinear algebraic equation about the known solution. In finite element implementations, the incremental solution is performed in a step-by-step manner until the full specified loads are applied. In each increment, the above iterative scheme is

performed until convergence is achieved or maximum iterations are reached. The Newton-Raphson method requires evaluation of the tangent stiffness matrix at each iteration, which is computationally expensive. On the other hand, the modified Newton-Raphson method evaluates the tangent stiffness matrix at each load step, thus improving the computational efficiency compared to the Newton-Raphson method. Schematics of the Newton-Raphson method and the modified Newton-Raphson method are shown in Figure 2.2. Although the use of the modified Newton-Raphson method may be more economical in some specific nonlinearity applications, the utilization of this conventional iterative method in general material and geometrical nonlinearities is not always successful, particularly when it is required to provide solution in the neighborhood of a global bifurcation or limit points when the tangent stiffness matrix becomes singular.

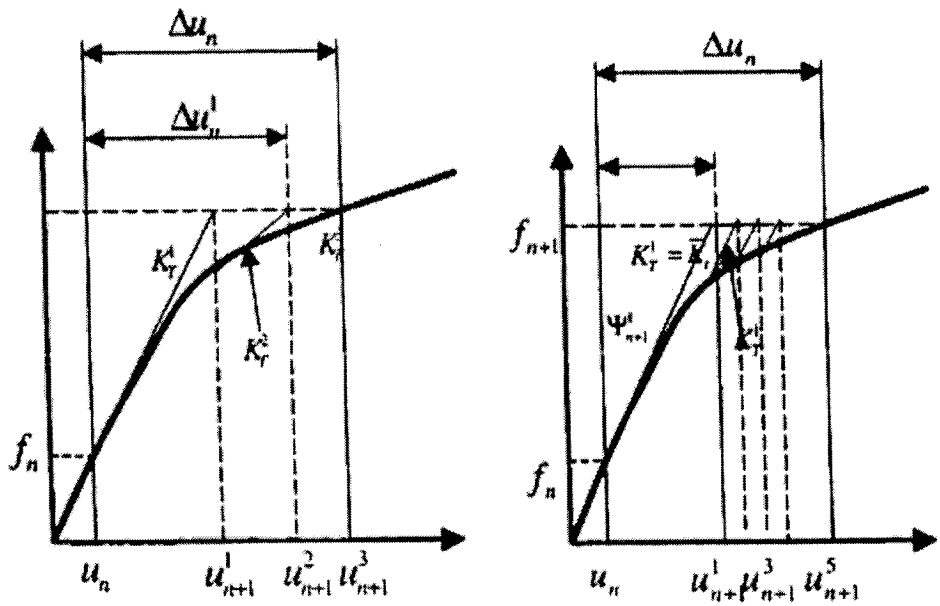

(a) the Conventional Newton-Raphson (b) the Modified Newton-Raphson

Figure 2-2: Schematics of the Newton-Raphson and modified Newton-Raphson methods

2.2.3.2 The Arc Length method

In postbuckling analysis, the conventional solution methods often perform poorly near the singular points, and even cannot cross over the singular points on the path. To overcome this problem, strategies like the arc length continuations need to be employed.

The general goal of the arc length procedure is the control of iteration in the numerical solution of complex nonlinear problems. The main idea of this method is based on the concept of constraining the length of the incremental displacement. The incremental displacement length for each successive iteration is constrained by the length of the previous iteration. Correspondingly, the load is adjusted in order to satisfy the global equilibrium requirement of the system.

The basic feature behind the standard arc-length method is that load level λ is treated as a variable rather than constant during a load increment. The standard equilibrium equation for proportional loading can be written as:

$$F(u) = \lambda P \tag{2-34}$$

where F is a nonlinear function of unknown displacement u, P is the fixed load vector and λ is the loading factor, which controls the applied load (as shown in Figure 2.3).

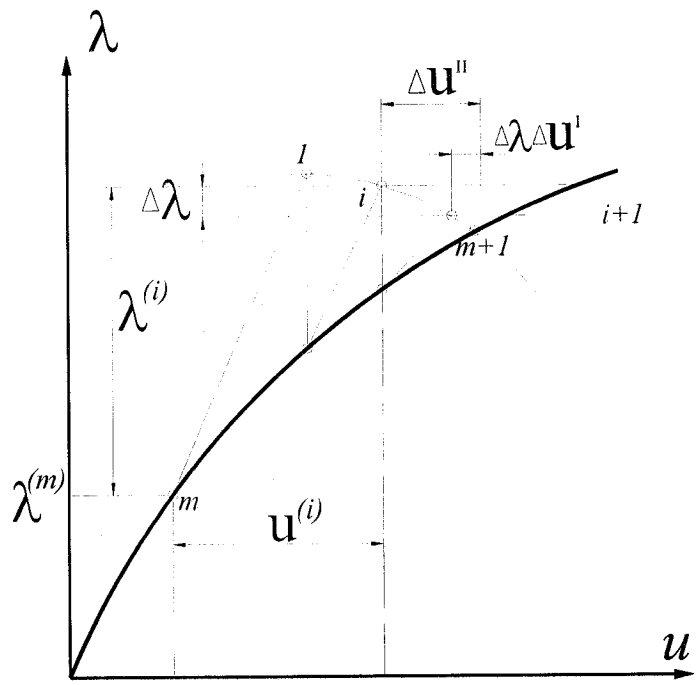

Figure 2-3: the Arc-length incremental scheme

Using the modified Newton-Raphson scheme, one can represent each iteration of the equilibrium relation by the following expression:

$$K^{(i)}\Delta u + F(u^{(i)}) = \lambda P \tag{2-35}$$

where K is the first derivative of F with respect to u (or the gradient of the force/displacement relation), and

$$\Delta u = u^{(i+1)} - u^{(i)} \tag{2-36}$$

Writing λ and u in equation (2-35 and 2-36) in incremental forms

$$\lambda^{(i+1)} = \lambda^{(m)} + \lambda^{(i)} + \Delta\lambda \tag{2-37a}$$

$$u^{(i+1)} = u^{(m)} + u^{(i)} + \Delta u \tag{2-37b}$$

where m represents a point on the load-displacement curve (see Figure 2.2), replacing λ and u in equation (2-35) by equation (2-37a and b) yields:

$$K^{(i)}\Delta u = (\lambda^{(m)} + \lambda^{(i)} + \Delta\lambda)P - F(u^{(i)}) \tag{2-38}$$

the incremental displacement Δu can be written as

$$\Delta u = \Delta\lambda \Delta u^{I} + \Delta u^{II} \tag{2-39}$$

where

$$K^{(i)} \Delta u^{I} = P \tag{2-40a}$$

$$K^{(i)} \Delta u^{II} = (\lambda^{(m)} + \lambda^{(i)})P - F(u^{(i)}) \tag{2-40b}$$

The first term in equation (2-39) is due to a unit load vector multiplied by $\Delta\lambda$ (equation 2-40a) and the second term is due to the unbalanced load (equation 2-40b). In order to find the solution we need another equation to account for the unknown $\Delta\lambda$. For this, a general scalar equation is used to constrain the load and displacement increments. This equation, known as the arc-length equation can be written as:

$$\Delta l^2 = \lambda^{(i)^2} + \beta^2 u^{(i)^T} u^{(i)} \tag{2-41}$$

where β is a scaling parameter (with units of displacement) to ensure the correct scale. Equation (2-41) holds for every sub-step in the iterations. The method is known as "spherical arc-length" when $\beta = 1$, which was originally proposed by Crisfield [8]. However, using this equation results in a quadratic equation. The selections of one of the roots of the equation, which may also have one or two imaginary roots, need additional computational efforts. Forde and Stiemer [9] suggested the method of "explicit iteration on spheres", which gives exactly the same results as those reported by Crisfield, and yet, it does not result in a quadratic equation. They used an iterative procedure to derive $\Delta\lambda$ as:

$$\Delta\lambda = \frac{R^{(i)} - u^{(i)^T} \Delta u^{II}}{\lambda^{(i)} + u^{(i)^T} \Delta u^{I}} \tag{2-42}$$

where R is a scalar residual. Using equation (2-40) and equation (2-42), one can obtain Δu. The solution is updated on equations (2-37) and (2-38) until the specified convergence is reached. The procedure continues up to the desired load. At the beginning of each load step, an initial load increment $\lambda^{(1)}$ should be chosen to ensure the efficiency of the algorithm. Using a large load step may cause slow or no convergence, whereas a small load step may reduce efficiency of the method. Moreover, using an automatic load increment strategy mostly depends on the nature of the problem, and therefore, makes it difficult to specify an exact formula for the load increments. Ramm [10] suggested the following formula for the automatic load increment:

$$\lambda^{(1)} = \bar{\lambda}^{(1)} \sqrt{\frac{J_d}{J_{m-1}}} \tag{2-43}$$

where J_d is the desired number of iterations for convergence, typically between 3 and 5, J_{m-1} is the actual number of iterations required for the $m-1^{th}$ load step and $\bar{\lambda}^{(1)}$ is the load increment for the $m-1^{th}$ load step. Further details of this solution scheme are given in Ref. [8].

2.3 Crushing of cylindrical tubes

2.3.1 General Introduction

For crushing of metallic cylindrical shells, the current design criteria requires that under an axial compressive loading, a box component of a specific geometry undergoes an axial crushing response as opposed to the other axial collapse modes, such as the elastic column buckling and bending. To prevent elastic column instability, the critical length can be determined from the Euler buckling formula [11]:

$$L \leq \frac{\pi r_g}{K_e} \sqrt{\frac{E}{\sigma_y}} \tag{2-44}$$

where L is the length of the undeformed tube, r_g is the radius of gyration of the tube, K_e is the effective length factor, E is the modulus of elasticity and σ_y is the yield strength of the material. To prevent the paneling collapse of square box columns of mild and high strength steels, so that a steel square box component has the ability to undergo axial crush-folding response, the wall thickness of the section has to satisfy the following condition [11]:

$$\frac{t}{b} \geq 0.48 \sqrt{\frac{(1-\nu^2)\sigma_y}{E}} \tag{2-45}$$

where t is the wall thickness, b is the width of the ''buckling'' plate and ν is the Poisson's ratio of the material.

Before delving into an extensive investigation into the crushing performance of tubular structural components subjected to axial compression loading, it is particularly necessary to distinguish the difference between the two phenomena, crash and crush.

A crash occurs when a moving object with relatively high speed collides with a rigid body. For example, a moving car with velocity of 30~75mph collides with a concrete wall. The crash event happens in a time-duration of the order of a few milliseconds. The term 'structural crashworthiness' is used to describe an investigation into the impact performance of a structure when it collides with another object. The primary goal in crashworthiness is to minimize the relative velocity between the occupants and the interior fixtures during the crash event and to prevent intrusion of different components in the structure. Another objective of the study into the crashworthiness of a system is to calculate the forces during a collision, which are used to assess the damage to the structures and survivability of its occupants. These goals are achieved by management of crash energy absorption. In many reports such as [12], the 'crash' is also called 'dynamic crushing'.

The crushing of structural components occurs at a relatively low speed, which means the structural components are compressed in a static or quasi-static manner. Normally, if the frequency of the applied load is less than one third of the lowest natural frequency of the structures, the problem is regarded as a static or quasi-static problem [2]. For example, the laboratory experiment to identify the crushing behavior is performed by crushing the car slowly, at about 0.02 mph in 10-30s duration using a device to push a thick steel plate onto the car roof, and measuring the load-deformation relation [13]. Investigation into the crushing behavior of structural components, including energy absorption capability and crushing force, is very important for crashworthiness design. Figure 2.4 shows the static axial crushing behavior of a thin-walled mild steel circular tube, including the load versus axial crushing distance curve and photographic record on the development of wrinkles during the axial crushing.

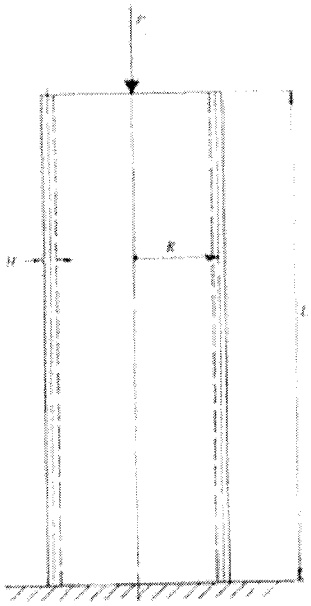

(a)

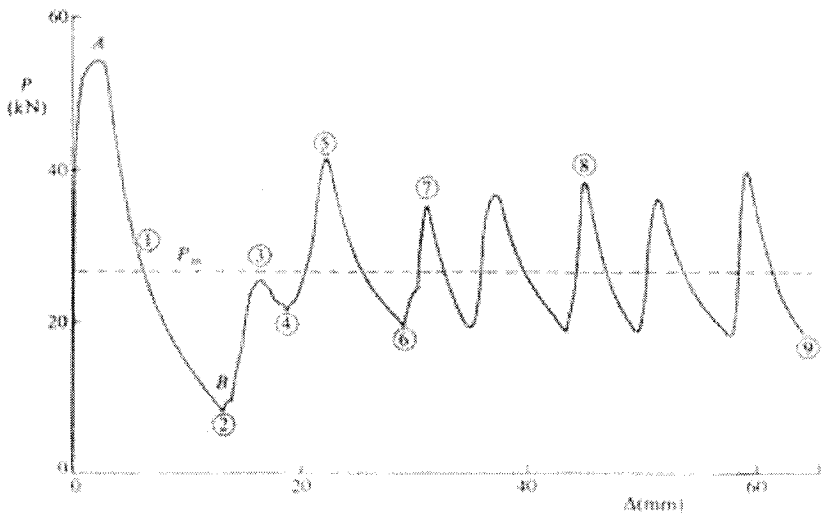

(b)

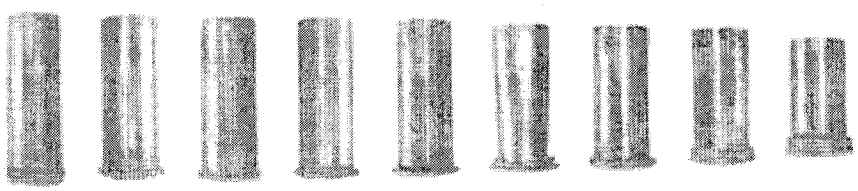

(c)

Figure 2-4: Thin-walled mild steel cylindrical tube subjected to a quasi-static axial crushing force P [12]

The difference between crash and crushing lies mainly on the difference of the loading speed. In most reports, e.g. [12], the two events are called dynamic crushing and static crushing. The two important factors that govern the need for different analysis methods for the two events include inertia effect and strain rate sensitivity. Inertia is an acceleration-based effect, which has to be considered in intermediate to high velocity impact event.

The strain rate is rate of change in strain with units of $(\text{sec})^{-1}$. Strain rate sensitivity, or viscoplasticity, is a material effect and is independent of the structural geometry. Many different constitutive equations for strain-rate-sensitive behavior of materials have been reported in the literature [12]. The constitutive equation of Cowper and Symonds [12] provides a reasonable estimate of the strain rate sensitive behavior of most materials, and is expressed by:

$$\dot{\varepsilon} = D\left(\frac{\sigma_0^{'}}{\sigma_0} - 1\right)^q, \quad \sigma_0^{'} \geq \sigma_0 \tag{2-46a}$$

or

$$\sigma_0^{'} = \sigma_0\left(1 + \left(\frac{\dot{\varepsilon}}{D}\right)^{\frac{1}{q}}\right) \tag{2-46b}$$

where $\sigma_0^{'}$ is the dynamic flow stress at a uniaxial plastic strain rate $\dot{\varepsilon}$, σ_0 is the associated static flow stress and D and q are constants determined experimentally for a given material, respectively.

The static crushing analysis is a quasi-static event, in which the influence of the inertia force is negligible and the material strain rate sensitivity is often ignored. For the dynamic crushing of a circular tube, the analysis procedure has to be chosen properly, dependent on the velocity of axial impact load and material type. For example, the axial impact of circular aluminum tube at low velocity (up to 10m/s) is usually taken as quasi-static event, and the inertia effect is usually ignored; the influence of material strain rate sensitivity can be ignored as well. For a dynamic crushing with higher velocity (from 10m/s and higher for circular metal tube), both the inertia force effect and material strain rate sensitivity should be included in the analysis procedure.

A dynamic crush with loading speed of up to 40m/s (144 km/h) is high enough to warrant a dynamic analysis in a normal car crash. However, in aerospace structures, the load speed involved in a crushing can be much higher (several hundred m/s). In such very high-speed events, the dynamic buckling (both elastic and plastic) problem may arise. The purpose of dynamic buckling analysis is to estimate the threshold velocity that structures could tolerate without excessive permanent deflections or damage. The dynamic buckling problem is out of the scope of this thesis work. In this thesis work, investigation into quasi-static and dynamic crushing involving the loading speed of up to 20m/s, which is comparable to the intermediate level car crash, will be carried out. Based on the above information, there will be only two terms, called "quasi-static crushing" and "dynamic crushing", being considered in the later chapters of this thesis. The three schemes for crushing analysis are briefly reviewed in the following sections.

2.3.2 Analytical solution scheme

2.3.2.1 Quasi-static crushing

For the quasi-static crush analysis of a thin-wall cylindrical shell, Alexander [12] developed an approximate theoretical model. The basic assumption in his analysis is that the tube is made from a rigid, perfectly plastic material and the mode of collapse is in the axisymmetric deformation pattern illustrated in Figure 2.5.

For design purpose, the fluctuation in the load-displacement diagram (shown in Figure 2.4) is often ignored and a mean crushing force (P_m) is used.

The total external work done by a constant axial force P_m during the formation of one wrinkle is $P_m \times 2l$.

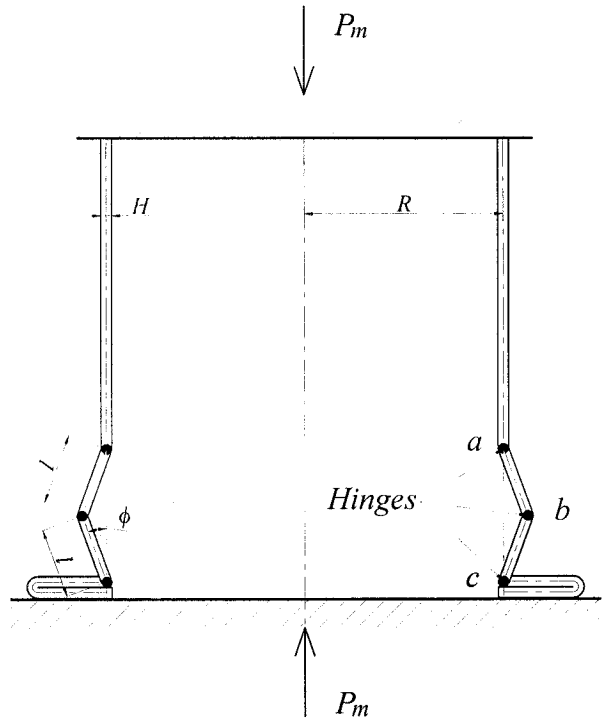

Figure 2-5: Idealized axisymmetric or concertina crushing mode for an axially compressed cylindrical shell [12]

The total plastic energy absorbed by the two stationary axisymmetric plastic hinges at a and c in Figure 2.5 during the formation of one wrinkle is

$$D_1 = 2 \times 2\pi R M_0 \times \pi / 2 \tag{2-47}$$

where the plastic collapse moment M_0 for the cross section (per unit circumference length) is calculated by:

$$M_0 = (2\sigma_0 / \sqrt{3}) H^2 / 4 \tag{2-48}$$

where σ_0 is the yield stress of the material.

During the formation of one complete winkle the radial position of the axisymmetric plastic hinge b increases from R to $R + l$. The energy absorbed by the axisymmetric central hinge b in Figure 2.5 is given by the following equation:

$$D_2 = 4\pi M_0 (R \times \pi / 2 + l) \tag{2-49}$$

During the formation of the wrinkle the axisymmetric portion *ab* and *bc* are stretched circumferentially. Based upon a mean engineering strain increment, the energy absorbed in circumferential stretching is given by the following equation:

$$D_3 = 2\sigma_0 l^2 H\pi \tag{2-50}$$

The total energy absorbed during the development of one complete wrinkle in a thin-walled tube is:

$$D_T = D_1 + D_2 + D_3 \tag{2-51}$$

From the principle of energy conservation, the total external work equals to the total absorbed energy, thus

$$P_m \times 2l = D_1 + D_2 + D_3 \tag{2-52}$$

Substituting equations (2-46~2-49) into equation (2-52) and minimizing the axial crushing force by $dP_m / dl = 0$ gives:

$$l = \sqrt{\frac{\pi RH}{\sqrt{3}}} \tag{2-53}$$

Substitution of equations (2-47, 49, 50 and 53) into equation (2-52) gives the mean crushing forces

$$\frac{P_m}{M_0} = 29.31\sqrt{\frac{R}{H}} + 2\pi \tag{2-54}$$

Equation (2-54) was obtained using the collapse mechanism in Figure 2.5, which assume that the convolution, or wrinkles, forms on the outward face of the tube. Alexander [12] also calculated the theoretical analysis and found that the mean crushing force for a tube with convolutions forming inward instead of outward is:

$$\frac{P_m}{M_0} = 29.31\sqrt{\frac{R}{H}} - 2\pi \tag{2-55}$$

Alexander assumed that the average of equation (2-54) and equation (2-55) provides a more accurate estimation of the actual mean crushing force. Thus, substituting equation (2-47) into the averaged crushing force produces:

$$P_m = 2(\pi H)^{\frac{3}{2}} R^{\frac{1}{2}} \sigma_0 3^{-\frac{1}{4}} \tag{2-56}$$

2.3.2.2 Dynamic crushing analysis (low to intermediate velocity impact)

For the dynamic crushing involving a low velocity impact, which can be considered as a quasi-static event, the inertia effect can be neglected. However the influence of material strain rate sensitivity must be retained for many materials. Thus, the yield stress in equation (2-56) has to be modified when considering the low velocity impact dynamic crushing. Jones [12] replaced the yield stress (σ_0) in equation (2-56) with the dynamic flow stress (σ_0' in equation 2-46) and obtained:

$$P_m = 2(\pi H)^{\frac{3}{2}} R^{\frac{1}{2}} \sigma_0 \left[1+\left(\frac{\dot{\varepsilon}}{D}\right)^{1/q}\right] 3^{-\frac{1}{4}} \tag{2-57}$$

The strain rate in equation (2-57) is taken as a constant, although it varies spatially and temporally during an impact event. According to Alexander's model shown in Figure 2.5, the mean circumferential strain in a completely flattened buckle of a circular tube is

$$\varepsilon_\theta \cong l/2R \tag{2-58}$$

so that the mean circumferential strain rate is

$$\dot{\varepsilon}_\theta \cong \varepsilon_\theta / T \tag{2-59}$$

The time required to form the first winkle, or convolution, is

$$T = 2l/V_0 \tag{2-60}$$

where V_0 is the impact velocity at the free end of the shell.

Therefore the average strain rate is

$$\dot{\varepsilon}_\theta \cong \varepsilon_\theta / T = V_0 / 4R \tag{2-61}$$

Substituting equation (2-61) into equation (2-57) yields the mean crushing force under dynamic crushing with low velocity impact as

$$P_m = 2(\pi H)^{\frac{3}{2}} R^{\frac{1}{2}} \sigma_0 \left[1+\left(\frac{V_0}{4RD}\right)^{1/q}\right] 3^{-\frac{1}{4}} \tag{2-62}$$

As $D \to \infty$ for a strain rate insensitive material, the equation (2-62) reduces to equation (2-56) as expected.

2.3.2.3 Dynamic crushing analysis (high velocity impact)

For the dynamic crushing of a cylindrical shell involving high velocity impact, both strain rate sensitivity of material, and the inertia effects need to be taken into consideration. For cylindrical shells, the inertia effect also includes the influence of lateral inertia, which favors the development of lateral displacement fields with high mode numbers [14]. Several researchers [15-16] have been investigating the dynamic behaviors of cylindrical shells subjected to high-speed axial impact. Most researchers assumed that the dominant solution was axisymmetric and uniform, and dynamic plastic buckling stemmed from the temporal growth of small axisymmetric initial imperfections in the cylindrical shell. Jones summarized the previous research and reported an analytical solution using the perturbation method. Written in a dimensionless form, the governing equation in his work was:

$$\ddot{u} + S_0\{\beta^2\dot{u}'''' + 2\alpha^2\beta^2\dot{u}'' + 48\alpha^2(1+u_i)\dot{u}\} + \gamma S_0(3u'''' - 2\alpha^2 u'') + 36S_0(u'' + u_i'') = 0 \tag{2-63}$$

where

$u_i = \frac{w^i}{R}$, $u = \frac{w}{R}$, $\xi = \frac{x}{l}$, $\tau = \frac{V_0 t}{L}$, $\alpha = \frac{L}{R}$, $\beta = \frac{H}{R}$, $\gamma = \frac{\beta^2 E_h}{\sigma^0}$, $S_0 = \frac{\sigma^0}{36\rho V_0^2}$, $\dot{u} = \frac{\partial u}{\partial \tau}$ and

$u' = \frac{\partial u}{\partial \xi}$

Jones assumed the perturbed behavior of the cylindrical shell as:

$$u(\xi,\tau) = \sum_{n=1}^{\infty} u_n(\tau)\sin(n\pi\xi) \tag{2-64}$$

and the initial imperfections were represented by:

$$u_i(\xi) = \sum_{n=1}^{\infty} a_n \sin(n\pi\xi) \tag{2-65}$$

He then solved the displacement and velocity amplification at various mode numbers analytically. The detailed procedure on the analytical solution of the dynamic crushing of cylindrical tubes subject to high velocity impact can be found in ref. [12].

2.3.3 Finite element simulation schemes

Diverse numerical studies have been reported on the simulation of crushing of metallic or composite tubes using commercial finite element software. The metallic cylindrical shells can be easily modeled by 3-D shell element, but attention should be paid to the selection of the material model. Depending on the speed of the crushing event, a proper material model should be employed. Moreover, the plastic behavior of material should be properly modeled. In commercial explicit finite element method software, several techniques are available to build up and connect a multi-layered model for composite structures. For example, a shell element is usually used because it allows the definition of composite lay-ups with failure and material degradation of each individual ply. In another approach, each individual lamina can be modeled with shell or solid elements and connected together using tied contacts or multi-point constraints. However, due to the complexity of failure modes in composite materials, an appropriate model has to be constructed to simulate the possible failure modes. The following sections discuss the approaches in finite element analysis of quasi-static and dynamic crushing events.

2.3.3.1 FE analysis of quasi-static crushing

There are two different schemes for conducting quasi-static crushing analysis. One is the implicit solution scheme and the other one, frequently used, is the explicit solution scheme.

2.3.3.1.1 Implicit solution scheme

A static implicit approach can analyze a quasi-static crushing process using the nonlinear Newton-Raphson or the Riks methods, which is a reliable and rigorous scheme in considering the equilibrium at each step of the deformation. The detail of the Newton-Raphson and the arc-length methods has been addressed in a previous section. However, the unconditionally stable implicit method will encounter some difficulties when a complicated three-dimensional problem is considered. One of the likely situations is that as the reduction of the time increment continues, a nearly singular tangent stiffness matrix is often encountered, thus resulting in poor convergence rates or in convergence to physically unrealistic solutions.

2.3.3.1.2 Explicit solution scheme

The explicit solution scheme has been widely used in the simulation of quasi-static crushing events. As stated, the major demerit of the explicit procedure is that the stable time increments are typically very small compared to the real time of the quasi-static crushing processes. However, the analysis can be accelerated in the following ways; Firstly, the speed of the process can be increased, for instance, by increasing the loading rate in a quasi-static crushing operation, which is called the time scaling technique. Secondly, the stable time increment can be increased by artificially increasing the mass density of the material, which is called mass scaling. In any case, it is more significant to determine how much a process can be accelerated and still be kept quasi-static, that is, to have no noticeable inertia effects or dynamic effects in the solution.

One general means of evaluating whether or not an explicit simulation is producing an appropriate quasi-static solution relies on studying the various energies of the structural model. The two most important energies are the internal energy and the kinetic energy. For an elastically deformed structure, the internal energy is the strain energy.

The following ad hoc rules were used to determine if a quasi-static solution could be achieved:

1. The kinetic energy of the deformed structure shall not exceed a small fraction (about 5%) of its internal energy throughout most of time period of the explicit analysis.
2. The ratio of the kinetic energy to the internal energy shall be less than 0.1% at the steady state.
3. The time rate of change of the internal energy shall be negligible at the steady state.
4. The maximum out-of-plane deformation shall reach a constant value at the steady state.

As long as the dynamic effects are insignificant, the proper quasi-static solution should be obtained. More information about mass scaling techniques in explicit analysis of quasi-static crushing events can be found in [17].

2.3.3.2 FE analysis of dynamic crushing

For dynamic crush analysis, a normal procedure of explicit finite element analysis would be the best choice, because the explicit codes are designed for events with very fast speed and very short duration. The general introduction of explicit analysis scheme has been presented in a previous part in this chapter.

2.3.4 Experimental investigation scheme

Another frequently used investigation scheme in crushing analysis is by experimental test. Most of the quasi-static crushing tests [18-28] were carried out on a hydraulic loading device. The test speeds were in the range of 1~60mm/min. For low-speed dynamic crushing (up to 10m/s), the tests were performed using a drop hammer [20, 25, 27, 29]. For high-speed crush (20 m/s and higher), the tests were conducted using a gas gun [22, 29-31].

In both the quasi-static and dynamic tests the crushing force versus crushing displacement curves, the peak and mean crushing forces are of interest. The area under the load versus displacement curve is used to determine the energy absorption capacity. Several crashworthiness parameters, such as specified energy absorption (SEA), load ratio (the ratio of the first peak load to the average crush load [27] and stroke efficiency (the ratio of the volume of the energy-absorbing part to the total volume of a device) [32] are also important parameters to be considered during the test.

2.3.5 Review on crushing of composite tubes

The crushing mode of composite cylindrical shells is controlled by the mechanical properties of the matrix, fiber orientation of the laminate and the tensile stiffness and failure strain of fibers oriented in a circumferential direction. The various global crushing modes that composites are able to exhibit can be divided into three modes as identified by Farley and Jones [33], shown Figure 2.6.

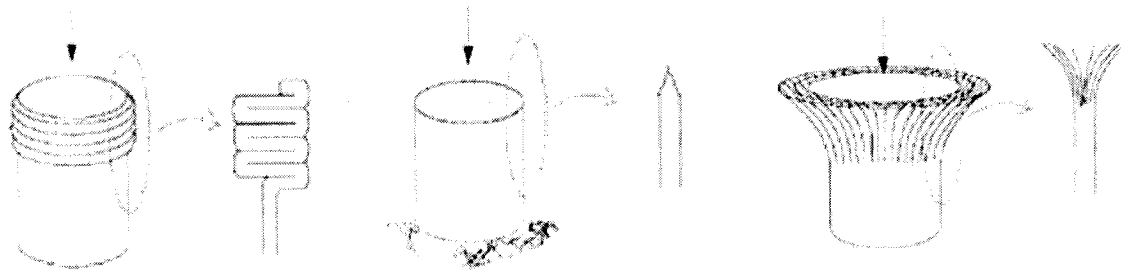

(a) Local buckling (b) Transverse shear (c) Laminar bending

Figure 2-6: Crushing mode of composite tubes [33]

Laminates containing ductile fibers, such as Kevlar, generally fail in local buckling modes comparable with those of metals, shown in Figure 2.6a. The transverse shearing crushing mode is characterized by a wedge-shaped laminate cross section, with one or more multiple short interlaminar and longitudinal cracks which form partial lamina bundles, as illustrated in Figure 2.6b. The laminar bending crushing mode is characterized by very long interlaminar, intralaminar and parallel-to-fiber cracks, but the laminar bundle does not fracture, as shown in Figure 2.6c. The transverse shearing and laminar bending crushing modes are exhibited exclusively by brittle fiber-reinforced composites and these two modes can be regarded as a catastrophic failure. But both ductile and brittle fiber-reinforced composites can exhibit the local buckling crushing mode. It is also worth mentioning that thin-wall tubes can fail due to the column instability and thick-wall tubes can fail in a circumferential tension failure mode. It is difficult to initiate a progressive crushing mode for very thin and very thick-wall tubes. Catastrophic failure of a tube, as a mechanism for absorbing energy in a crash, usually occurs at load levels that are much higher than that of a comparably designed structure crushed in a progressive manner. Therefore, these catastrophic failure modes are normally not of interest in practical design.

Transverse shearing mode is generally insensitive to strain rate. For laminar bending crushing and local buckling modes, energy absorption capability can be influenced by changing the crushing speed.

Chiu and Lu [21] experimentally investigated the static crushing behavior of a 3-D braided composite square tube. Both Kevlar and carbon fiber were used in the tube specimen. Typical failure modes exhibited during crushing included compressive shear failure, bending fracture, local buckling of the axial fibers, shear and tensile failure of the braiders, matrix crushing, interface debonding and open mode crack propagation. The carbon tube showed higher specific energy absorption capability than the Kevlar tubes. However, the Kevlar tubes demonstrated better post-crush structural integrity than the carbon tubes.

Mamalis *et al.* [22] investigated the static and dynamic crushing of square, circular and frusta composite sections. They found that crushing speed did not have significant effect on the specific energy absorption (SEA) of thin-wall circular and square sections. The crushing mechanism of tubular specimens with large thickness at higher crushing speed differed from the static case.

Hamada *et al.* [24] studied the energy absorption capability of carbon fiber/PEEK tubes of $[\pm\theta]$ lamina sequence and found that the $[\pm 15^0]$ composite tube displayed the highest SEA.

Schultz and Hyer [27] investigated the static and dynamic energy-absorption capacity of filament wound graphite-epoxy tubes. They found that changing the fiber orientation schemes did not have much effect on the SEA capacity, nor on the crushing modes, but the presence of 0^0 fibers led to higher load ratios (ratio of the peak load to the final average load) for the tubes. The specimens tested dynamically had lower SEAs and higher load ratios than similar specimens that were tested statically.

Velmurugan *et al.* [34] investigated the effect of stitching on the crush behavior of fiber reinforced plastic cylindrical shells. It was observed that stitching could improve the delamination strength, and reduce the in-plane crack growth rate, which in turn increases the crushing behavior of the shells.

2.4 Shape memory alloy (SMA) and its applications

Shape memory alloy materials have the unique ability to memorize a shape (extension, bending, and twisting) at one temperature and recover that shape at a different

temperature via phase transformation. Increasing attention has been devoted to this material since 1962 when Nitinol was developed [35]. A SMA is able to recover its original configuration after it has been deformed by heating the alloy above its characteristic transition temperature. This unique property of martensitic SMA is often referred to as shape memory effect (SME). A pre-strained SMA wire constrained mechanically or elastically, develops a large tensile recovery force upon heat application due to mechanical end constraints and the SME.

The thermomechanical behavior of SMA material depends on the phase (austenite or martensite) that the material resides in, its temperature and the stresses in the material. When SMA material is heated, a phase change takes place. The phase transformation may be affected by temperature and/or stress. The phase transformation from martensite to austenite is called the reverse transformation ($M \rightarrow A$), and the transformation from austenite to martensite is called the forward transformation ($A \rightarrow M$). There are two characteristic temperatures associated with the reverse transformation and two more associated with the forward transformation. The temperatures associated with reverse transformation are the austenite start temperature A_s, indicating the start of the phase change, and the austenite finish temperature A_f, marking the completion of the phase change. Similarly, the temperatures associated with the forward transformation are the martensite start temperature M_s, signifying the start of martensite formation, and the martensite finish temperature M_f, marking the completion of martensite formation. At temperatures between M_s and M_f, and temperatures between A_s and A_f, the material resides in a mixed phase of both austenite and martensite. The recoverable strain resulting from this phase transformation can reach as much as 8%. Note that in many constitutive models, the material is characterized by the volume fraction of martensite ξ, the volume of martensite divided by the total volume of martensite and austenite. Figure 2.7 illustrates the typical one-cycle phase transformation of SMA material with the changes in temperature. It is seen that there is a hysteresis associated with martensitic transformations. An important characteristic of SMA wires is that during the reverse transformation there is an increase in the Young's modulus. The modulus of the wire in the austenite phase can range from 3–6 times the modulus of the wire in the martensite

phase. The ability of SMA materials to recover large plastic deformations originates from the reversible phase transformation characteristic.

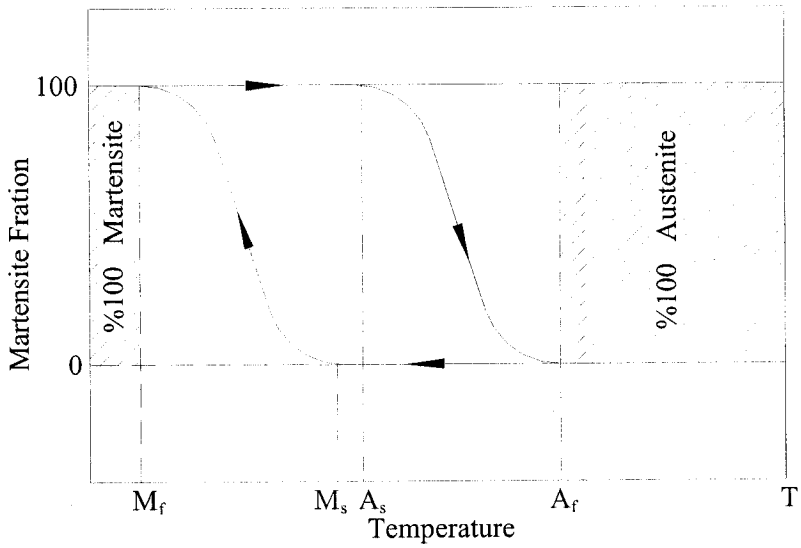

Figure 2-7: Schematic of transformation and reverse transformation of SMA

2.4.1 Constitutive model

A reliable constitutive relation is needed to predict this recovery force in SMA wire actuators. However, the stress-strain relationship of SMA is not as simple as for common materials. The constitutive models relating the stress and strain of common materials cannot be applied to SMA. Various approaches have been taken by researchers thus far to develop constitutive models: macroscopic, microscopic, and mixed. In the macroscopic approach, the constitutive model describes the material behavior based on experimental data. For the microscopic approach, the constitutive model attempts to predict and describe the material behavior based on fundamental physical concepts, such as the micro structure of the crystal lattice. The mixed approach uses both microscopic and macroscopic concepts for better modeling [36]. The various models proposed by many researchers can be classified into five different types of models: internal variable models, ferroelectric models, plasticity models, hysteresis models, and non-isothermal models.

The internal variable model is derived from the concept of the Helmholtz free energy, which can be derived from thermodynamic principles. Many researches [37-41] have contributed to complete this model and made it easier to use by choosing different functions of the martensite transformation fraction. Tanaka [37] proposed an exponential function of stress and temperature according to transformation kinetics. Liang and Rogers [38] proposed a cosine function of martensite fraction. Brinson [39] developed another cosine model based on Liang and Rogers's model. Liang and Rogers's as well as Brinson's models make the internal variable model easier to be used in the computations of the stress-strain relations and the super-elastic effects of SMA. Boyd and Lagoudas [40] proposed a one-dimensional model based on Tanaka's exponential model. In this model, the tensile stress was replaced with von Mises stress, considering the inelastic process. Later on Bo and Lagoudas [41] generalized the model by assuming some parameters as a function of the martensite fraction and unified the models proposed by Tanaka [37], Liang and Rogers [38], and Boyd and Lagoudas [40].

Ferroelectric models are good for studying the transformation process in the SMA material, but are difficult to use in engineering applications. Plasticity models can be used in elastic and inelastic processes although they are usually used in smooth transition processes. Hysteresis models work well in inelastic processes, although they are more phenomenological than physical. Non-isothermal models are especially suitable for adiabatic process, such as high loading rates. An intensive review on the constitutive models of SMA can be found in ref. [36].

Overall, the above-mentioned constitutive models have been successfully used in many research works. Although these models are very comprehensive in capturing the complex behavior of SMA materials, they are difficult to implement in commercial structural analysis codes and are difficult to use in practice. An effective coefficient of thermal expansion (ECTE) model of SMA material has been recently developed by Turner [42] (discussed in Chapter Eight of this thesis.) The ECTE model greatly simplifies advanced structural analysis of SMA materials.

2.4.2 Structural control using shape memory alloys

SMAs have been investigated for a variety of applications since their discovery. Early applications of SMA included self-erecting structures, thermally actuated devices, and energy-conversion systems [43]. Other potential applications including damping or energy absorbing devices, thermally actuated couplings and fasteners, and biomedical devices were briefly described by Buehler and Wiley [44]. Later, more detailed descriptions of specific devices such as pipe couplings, thermostats, a robot hand, and various biomedical systems were reported in [45, 46]. These unique properties allow SMA to be used in the application of active structural control, such as in shape control, vibration control and buckling control of structures. The super-elastic effect also makes SMA very useful in many applications, such as SMA springs. SMA has also been used in hybrid composites in a variety of applications.

Four plausible and distinct configurations have been used in active control of structures using SMA materials; embedding SMA in composite structures, surface bonding the SMA wire to the host structures, connecting externally to the structure, and inserting in composite structures via sleeves. For example, Han *et al.* [47] directly embedded coiled SMA wires in an epoxy column to enhance its buckling capacity. In that experimental study, a plastic column was constructed with fixed-free boundary conditions. When the coiled SMA wires were heated, the SMA would exert an axial push force due to the SME and the constraints provided by the column. An appreciable increase in capacity was obtained by the use of the SMA spring. Xu [48] performed a numerical and experimental investigation on the shape control of composite beams with surface bounded SMA wires. It was found that by activating the SMA wires using electric current, the shape of the beam could be changed to the desired shape. Baz and Tampe [49] was first to investigate the feasibility of using SMA actuators for active buckling control of flexible structures. They used an external SMA helical spring to enhance the buckling characteristics of a long slender beam. The spring was connected to a pneumatic powered cylinder that in turn would apply tensile loading to an elastic member. The net effect was therefore a reduction of the compressive loading on the slender member and prevention of the out-of-plane deformation. Thompson and Loughlan [50] performed an experimental investigation on the post-buckling behavior of

laminated SMA-composite plates that were fabricated by the insertion of an SMA wire through the sleeves located within the neutral plain of the composite plates. The buckling control was achieved by alleviation of the post-buckled deflection.

2.4.3 Concept of shape memory alloy hybrid composite

An entire new field of applications was created when Rogers and Robertshaw [51] introduced the idea of embedding SMA actuators in a composite laminate. A structure of this type has been termed a shape memory allot hybrid composite (SMAHC). A representative volume element from an individual SMAHC lamina, with principal material direction 1 and 2, and the SMA actuator embedded in the 1-direction, is shown schematically in Figure 2.8. The composite matrix in Figure 2-8 is actually composed of both fiber and matrix (i.e., ordinary fiber-reinforced laminated composite material).

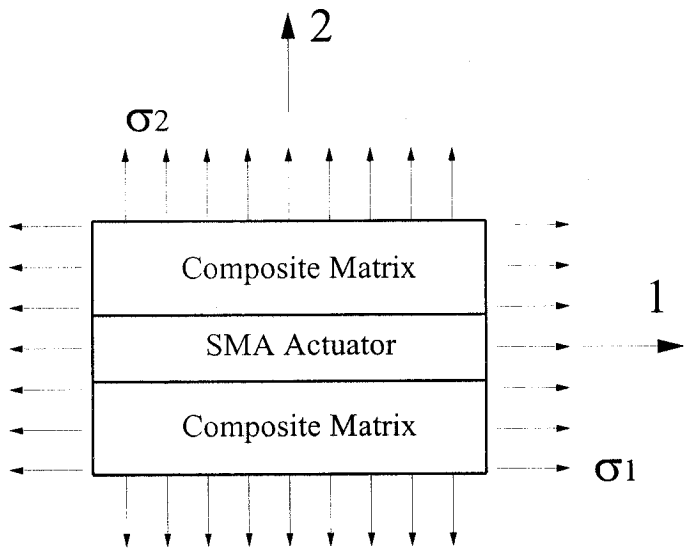

Figure 2-8: Representative volume element for a SMAHC lamina

As we know, the thermo-elastic constitutive relation in principal material coordinates for a thin orthotropic lamina under conditions of plane stress can be expressed in the following form:

$$\begin{Bmatrix}\sigma_1\\ \sigma_2\\ \tau_{12}\end{Bmatrix}=\begin{bmatrix}Q_{11} & Q_{12} & 0\\ Q_{12} & Q_{22} & 0\\ 0 & 0 & Q_{66}\end{bmatrix}\left(\begin{Bmatrix}\varepsilon_1\\ \varepsilon_2\\ \gamma_{12}\end{Bmatrix}-\int_{T_0}^{T}\begin{Bmatrix}\alpha_1(\tau)\\ \alpha_2(\tau)\\ 0\end{Bmatrix}d\tau\right) \tag{2-66}$$

where $[Q]$ is the plane stress-reduced stiffness matrix, $\{\varepsilon\}$ is the total strain vector, and $\{\alpha\}$ is the vector of coefficient of thermal expansion. The function of SMA material in the SMAHC is applied in two aspects. Firstly the participation of shape memory alloy material changes the stiffness of the composite structural system, in term of change in reduced stiffness matrix $[Q]$. The second one, which is the most important one, is that the SME activated at an elevated thermal environment contributes to a big change in the thermal induced stress components. Such changes could be favorable or adverse to the original composite structural system. The tailored design of composite structures allows the flexibility of using such mechanism so as to take advantage of the positive aspect of SME. The constitutive modeling of SMAHC plate based on the of ECTE model of SMA material will be provided in Chapter Eight of this thesis.

2.5 Reference in this chapter

[1] Zienkiewicz O.C., *The Finite Element Method*, third edition, McGraw-Hill, London, 1977.

[2] Cook R.D., Malkus D.S., Plesha M.E. and Witt R., *Concepts and Applications of Finite Element Analysis*, John Wiley & Sons Inc, 2001.

[3] *LS-DYNA V.970 Keyword User's Manual*, LSTC, Livermore, CA, USA, 1997.

[4] *ANSYS User's Manual*, ANSYS Inc., Canonsburg, PA, USA, 2003.

[5] Ugural A.C., *Stresses in plate and shells*, McGraw-Hill Book Company, 1981.

[6] Baker E.H., Kovalevsky L. and Rish F.L., *Structural analysis of shells*, McGraw-Hill Book Company, 1972.

[7] Litle W.A., *Reliability of shell buckling predictions*, The MIT Press, Cambridge, Massachusetts, 1964.

[8] Crisfield M.A. (1981), A fast incremental/iterative solution procedure that handle "snap through", *Computer Structures* 13: 55-62.

[9] Forde B.W.R. and Stiemer S.F. (1987), Improved arc length orthogonality methods for nonlinear finite element analysis, *Computer and Structures* 27: 625-630.

[10] Ramm E., Strategies for tracing the nonlinear response near limit points, in *Nonlinear Finite Element Analysis in Structural Mechanics*, Springer-Verlag, Berlin Germany 63-69, 1981.

[11] Bleich F., *Buckling Strength of Metal Structures*. McGraw-Hill Book Company, Inc., New York, NY. 1952.

[12] Jones N., *Structural Impact*, Cambridge University Press, 1997.

[13] Bathe K.J., Walczak J, Guillermin O, Bouzinov PA and Chen HY (1999), Advances in crush analysis, *Computers and Structures* 72: 31-47.

[14] Murasea K. and Wada H. (2004), Numerical study on the transition of plastic buckling modes for circular tubes subjected to an axial impact load, *International Journal of Impact Engineering* 30: 1131-1146.

[15] Florence A.L. and Goodier J.N. (1968), Dynamic plastic buckling of cylindrical shells in sustained axial compressive flow, Transactions of the ASME, *Journal of Applied Mechanics* 35 (1): 80-86.

[16] Lindberg H.E. and Florence A.L., *Dynamic pulse buckling*, Martinus Nijhoff Publishing, 1987.

[17] Olovsson L., Simonsson K. and Unosson M. (2005), Selective mass scaling for explicit finite element analyses, International *Journal for Numerical Methods in Engineering* 63:1436-1445.

[18] El-Hage H.H. (2004), A numerical study on the quasi-static axial crush characteristics of square aluminum and aluminum-composite hybrid tubes, *PhD thesis*, Department of Mechanical Engineering, University of Windsor.

[19] Guillowa S.R., Lu G. and Grzebietab R.H. (2001), Quasi-static axial compression of thin-walled circular aluminum tubes, *International Journal of Mechanical Sciences* 43: 2103-2123.

[20] Yamashita M., Gotoh M. and Sawairi Y. (2003), Axial crush of hollow cylindrical structures with various polygonal cross-sections Numerical simulation and experiment, *Journal of Materials Processing Technology* 140: 59-64.

[21] Chiu C.H. and Lu C.K. (1997), Crushing characteristics of 3-D braided composite square tubes, *Journal of Composite Materials* 31 (22): 2309-2327.

[22] Mamalis A.G., Yuan Y.B. and Viegelahn G.L. (1992), Collapse of thin wall composite sections subjected to high speed axial loading, *International Journal of vehicle Design* 13(5/6): 564-579.

[23] Gupta N.K., Velmurucan R. and Gupta S.K. (1997), An analysis of axial crushing of composite tubes, *Journal of Composite Materials* 31(13): 1262-1286.

[24] Hamada H., Ramakrishna S. and Sato H. (1996), Effect of fiber orientation on the energy absorption capability of carbon fiber/PEEK composite tubes, *Journal of Composite Materials* 30 (8): 947-963.

[25] Schneider F. and Jones N. (2004), Impact of thin-wall high strength steel structural section, *Proceedings of the Institution of Mechanical Engineers 218 (D): Journal of Automobile Engineering*, 131-158.

[26] Shin K.C., Lee J.J., Kim K.H., Song M.C. and Huh J.S. (2002), Axial crush and bending collapse of an aluminum/GFRP hybrid square tube and its energy absorption capability, *Composite Structures* 57: 279-287.

[27] Schultz M.R. and Hyer M.W. (2001), Static and Dynamic Energy-Absorption Capacity of Graphite-Epoxy Tubular Specimens, *Mechanics of Composite Materials and Structures* 8: 231-247.

[28] Dipaolo B.P., Monteiro P.J.M. and Gronsky R. (2004), Quasi-static axial crush response of a thin-wall, stainless steel box component, *International Journal of Solids and Structures* 41: 3707-3733.

[29] Zhao H. and Abdennadher S. (2004), On the strength enhancement under impact loading of square tubes made from rate insensitive metals, *International Journal of Solids and Structures* 41: 6677-6697.

[30] Wang B. and Lu G. (2002), Mushrooming of circular tubes under dynamic axial loading, *Thin-Walled Structures* 40: 167-182.

[31] Bouchet J., Jacquelin E. and Hamelin P. (2000), Static and dynamic behavior of combined composite aluminum tube for automotive applications, *Composites Science and Technology* 60: 1891-1900.

[32] Mahdi E., Hamouda A.M.S. and Sahari B.B. (2002), Axial and lateral crushing of the laminate wound laminated composite curved compound system, *Advanced Composite Materials* 11 (2): 171-192.

[33] Farley G.L. and Jones R.M. (1992), Crushing characteristics of continuous fiber reinforced composite tubes, *Journal of Composite Materials* 26 (1): 37-50.

[34] Velmurugan R., Gupta N.K., Solaimurugan S. and Elayaperumal A. (2004), The effect of stitching on FRP cylindrical shells under axial compression, *International Journal of Impact Engineering* 30: 923-938.

[35] Buehler W.J. and Wiley R.C. (1965), Nickle-based alloys, *US Patent* 3,174,851.

[36] Jia H. (1998), Impact Damage Resistance of Shape Memory Alloy Hybrid Composite Structures, *PhD thesis*, Virginia Polytechnic Institute and State University.

[37] Tanaka K. (1986), A thermomechanical sketch of shape memory effect: one-dimensional tensile behavior, *Res. Mechanica* 18: 251-263.

[38] Liang C. and Rogers C.A. (1990), One-dimensional thermomechanical constitutive relations for shape memory materials, *Journal of Intelligent Material Systems and Structures* 1: 207-234.

[39] Brinson L.C. (1993), One-dimensional constitutive behavior of shape memory alloys: thermomechanical derivation with non-constant material functions and redefined martensite internal variable, *Journal of Intelligent Material Systems and Structures* 4: 229-242.

[40] Boyd J.G. and Lagoudas D.C. (1994), A constitutive model for simultaneous transformation and reorientation in memory materials, *Mechanics of Phase Transformations and Shape Memory Alloys*, AMD-89/PVP-292: 159-172 ASME.

[41] Bo Z. and Lagoudas D.C. (1994), Comparison of different thermomechanical models for shape memory alloys, *Adaptive Structures and Composite Materials: Analysis and Application*, AD-45/MD-54: 9-19 ASME.

[42] Turner T.L. (2000), A New Thermoelastic Model for Analysis of Shape Memory Alloy Hybrid Composites, *Journal of Intelligent Material Systems and Structures* 11: 382-394.

[43] Buehler W.J. and Wiley R.C. (1962), TiNi-Ductile Intermetallic Compound, *Transactions of the American Society of Metals* 55: 269-276.

[44] Wayman C.M. and Shimizu K. (1972), The Shape Memory ("Marmem") Effect in Alloys, *Metal Science Journal* 6: 175-183.

[45] Wayman C.M. (1980), Some Applications of Shape-Memory Alloys, *Journal of Metals* June: 129-137.

[46] Otsuka K. and Shimizu K. (1986), Pseudo-elasticity and Shape Memory Effects in Alloys, *International Metals Reviews* 31 (3): 93-114.

[47] Han H.P., Ang K.K., Wang Q. and Taheri F. (2006), Buckling enhancement of epoxy columns using embedded shape memory alloy spring actuators. *Journal of Composite Structures* 72 (2): 200-211.

[48] Xu Z.J. (2002), Shape control of beam structures using shape memory alloy wire actuators, *M.Eng. thesis*, National University of Singapore.

[49] Baz A. and Tampe L. (1989), Active control of buckling of flexible beams, in *Proceeding of ASME: Design Technical Conference*, Montreal, Canada, 211-218.

[50] Thompson S.P. and Loughlan J. (1995), The active buckling control of some composite column strips using piezoceramic actuators, *Composite Structures* 32 (1-4): 59-67.

[51] Rogers C.A. and Robertshaw H.H. (1988), Shape Memory Alloy Reinforced Composites, *Engineering Science Preprints* 25, Society of Engineering Science, Inc., ESP25.8027.

Chapter 3 Numerical and Experimental Investigations of the Response of Aluminum Cylinders with a Cutout Subject to Axial Compression

Haipeng Han[a], Jinquan Cheng[a], Farid Taheri,[a] and Neil Pegg[b]
[a]Department of Civil Engineering, Dalhousie University, 1360 Barrington Street, Halifax, NS B3J 2Z1
[b]Defense Research and Development Canada , Dartmouth, NS B2Y 3Z7

Thin-Walled Structures 44 (2006): 254-270

3.1 Abstract

Understanding how a cutout influences the load bearing capacity and buckling behavior of a cylindrical shell is critical in the design of structural components used in automobiles, aircrafts, and marine applications. Numerical simulation and analysis of moderately thick and thin unstiffened aluminum cylindrical shells (D/t=45, 450 and L/D=2, 5, 10), having a square cutout, subjected to axial compression were systematically carried out in this paper. The investigation examined the influence of the cutout size, cutout location, and the shell aspect ratio (L/D) on the prebuckling, buckling, and postbuckling responses of the cylindrical shells.

An experimental investigation on the moderately thick-walled shells was also carried out. A good correlation was observed between the results obtained from the finite element simulation and the experiments. Furthermore, empirical equations, in the form of a "buckling load reduction factor" were developed using the least square regression method. These simple equations could be used to predict the buckling capacities of several specific types of cylindrical shells with a cutout.

Keywords: Cylindrical shell structures, Cutout, Buckling, Finite element analysis

3.2. Introduction

Circular cylindrical shells are commonly used in engineering structures such as aircraft, missiles, silos, pipelines, tanks, automobiles, and some submarine structures. During their service life, these components are often subjected to axial compressive loading. In addition, these structures often have geometric discontinuities, such as stiffeners and cutouts; which can lead to substantial stress concentrations and subsequently influence the stability of the structures. As a result, the buckling problem of cylindrical shells has attracted the attention of researchers for more than a century. Early works focused on determining linearly elastic bifurcation buckling loads. It was quickly realized however that these would only provide an upper bound to the experimentally observed buckling loads. Several experimental investigations [1, 2] have proved that the buckling capacity of thin cylindrical shells are often much lower than that predicted by the classical theory [3]. Sophisticated experimental studies have been conducted with precise measurements of the geometrical imperfection of such shells in an attempt to correlate the experimentally obtained buckling load with that predicted by the classical theory. Unfortunately, the success rate has been very low thus far.

The classical theory can be used to predict the linearly elastic bifurcation buckling capacity of thin cylindrical shells subject to uniform axial pressure by using the following equation:

$$N_{cr} = \frac{E}{\sqrt{3(1-\nu^2)}}\left(\frac{t^2}{R}\right) \tag{3.1}$$

where E is the Young's modulus, ν is the Poisson's ratio, t is the wall thickness, and R is the radius of the shell. Equation (3.1) is found to provide satisfactory agreement with the test results of thin cylindrical shells having $L/R \leq 5$ without a cutout [4], giving an upper bound to experimental data. Equation (3.1) applies to the cylindrical shell that is fixed at its bottom end, free at top end and subject to pure compression along its longitudinal direction. For moderately thick cylindrical shells (R/t<50), Equation (3.1) always over-estimates the capacity, as the shell may yield or collapse before the load reaches the predicted elastic buckling value. It is also noted that Equation (3.1) applies only to shells of isotropic elastic materials. Available numerical and experimental studies

on the buckling of imperfect composite shells (e.g., [5]) have shown that the linear buckling (eigenvalue) analysis provides a lower bound to the experimentally determined buckling capacity. Based on the above information, one can appreciate the importance of conducting a nonlinear analysis or an experimental investigation to accurately predict the buckling behavior of shell structures. Considering the expense associated with experimental investigations, the nonlinear finite element analysis method could be considered as a viable alternative for determining the buckling collapse load.

Only a few researchers have considered the effect of cutouts on the buckling behavior of cylindrical shells. In 1998, Jullien *et al.* [2] experimentally and numerically investigated the effect of openings on the buckling of thin cylindrical shells subject to axial compression. They conducted a parametric investigation on the shape and dimensions of cutouts. The effects of the location and the number of cutouts were also studied. The geometric parameters of their shells were D/t=565 and L/D=1. The finite element code used in their study was CASTEM 2000, developed by the French Atomic Energy Commission. For perfect cylindrical shells, their experimental buckling load was about 47% of the analytically determined load from the classical theory (i.e., Equation 3.1). At the same time, Yeh *et al.* [6] analytically and experimentally studied the bending and buckling of moderately thick-walled cylindrical shells with cutouts. The dimensions of their shells were D/t=50 and L/D=7.9. It was found that the limiting buckling moment would be higher if the cutout was on the tension side rather than on the compression side. They also performed parametric studies on the influences of shape, size, and location of a cutout on the buckling capacity. Hilburger *et al.* [7] analyzed the buckling behavior of thin composite cylindrical shells with cutouts. The geometric parameters of shells in his study were D/t=390 and L/D=1.0. They studied three different sizes of cutouts with dimensions of 12.7mm, 25.4mm, and 38.1mm. The STAGS finite element code, which uses a standard arc-length projection method, was employed in their work. It was observed that nonlinear analysis results were more accurate than those from the traditional linear bifurcation analysis. Similar to the above, Tafreshi [8] also numerically studied the buckling and postbuckling response of composite cylindrical shells subjected to internal pressure and axial compression loads using ABAQUS. He studied the

influences of size and orientation of cutouts and found that an increase of internal pressure resulted in an increase in buckling capacity.

To the best of the authors' knowledge, most available literature has only reported the buckling behavior of short ($L \leq D$) and very thin walled (D/t>300) cylindrical shells with cutouts. Only a few works have investigated the influence of cutouts on the intermediate- length or slender cylindrical shells. Moreover, there are only a few studies that have considered the buckling behavior of moderately thick shells without cutouts. Linear analytical or numerical methods do not produce good predictions for failure of thin-walled or moderately thick-walled cylindrical shells with a cutout. Therefore, either a nonlinear FE analysis or an experimental investigation must be considered.

In this paper a series of nonlinear finite element analyses were conducted to examine the influence of cutouts on thin and moderately thick cylindrical shells. Experiments were also conducted to verify the results in moderately thick-walled shells, and very good correlation between experiments and numerical simulations was observed. The prebuckling, buckling, and postbuckling behaviors of these shells were characterized. Parametric studies examining the influence of the shell aspect ratio (L/D), cutout size, and cutout location on the shell response were also carried out. Empirical equations were also developed based on the results, using the least square regression method, which can be used to determine the buckling capacities of the shells.

3.3 Numerical Analysis using the Finite Element Method

3.3.1 Shell geometry and properties

The general geometry of the shells analyzed in this study is defined in Figure 3.1. The shells have various lengths, a 40mm diameter and wall thickness (t) of 0.889mm and 0.0889mm, which give the diameter/thickness ratios of 45 and 450, and are considered to be moderately thick and thin shells, respectively. The shells have square cutouts of 5.3mm × 5.3mm, 7.5mm × 7.5mm, 10.6mm × 10.6mm and 15.0mm × 15.0mm. The distance between the centre of the cutout to the bottom end of the shell is denoted as L_0. To alleviate the stress concentration around the cutout, corner chamfers of 0.25, 0.5, 1.0, and 1.5mm radius were introduced, respectively, for the above square cutouts.

The shells are typically laboratory-scale cylindrical shells and are made of 6061-T6 aluminum alloys with the sheet rolling direction in the circumferential direction. The engineering stress-strain curves were determined using six dog-bone tensile specimens machined from the walls of the extruded pipe according to ASTM B557. Based on the experimental results, a multi-linear isotropic hardening constitutive model was used to represent the uniaxial stress-strain behavior of the aluminum, which uses the von-Mises flow rule as yield criteria, as shown in Figure 3.2. A multi-linear isotropic hardening constitutive model was used to represent uniaxial stress-strain behavior of the aluminum, as shown in Figure 3.2. The Young's modulus and Poisson's ratio of the material were assumed to be 68.948 GPa and 0.33, respectively.

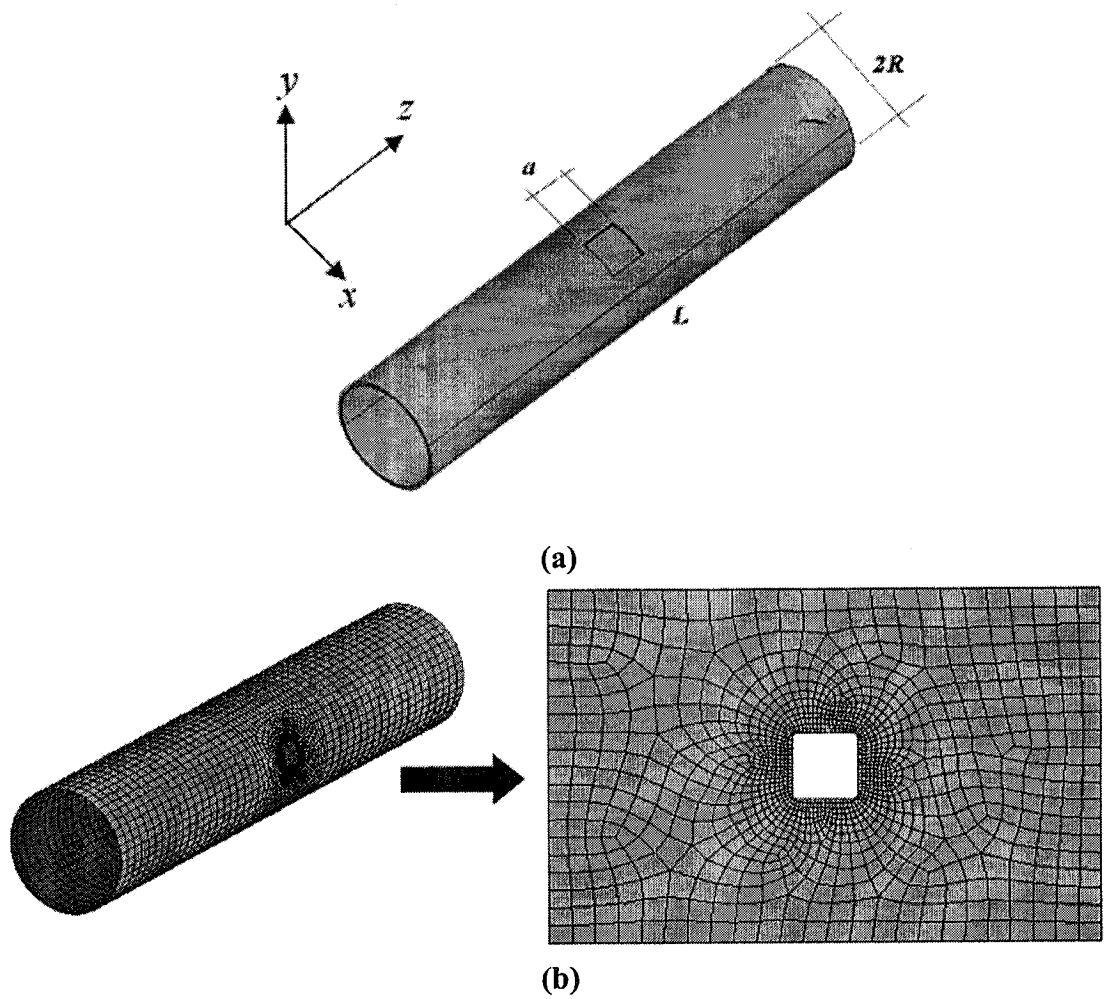

Figure 3-1: Geometry and FE model of the cylindrical shell with a cutout

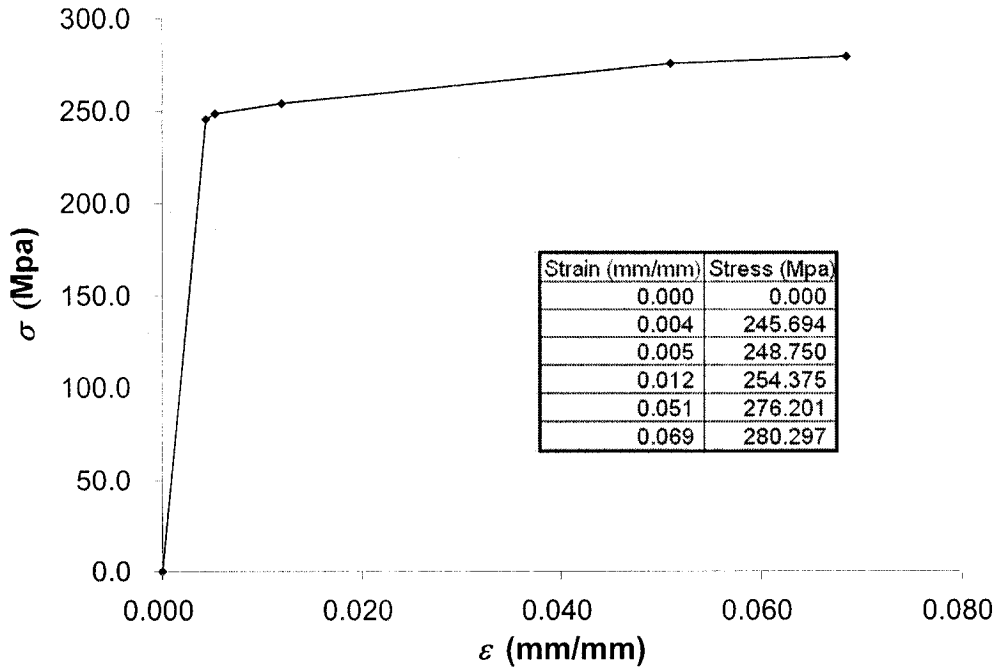

(a)

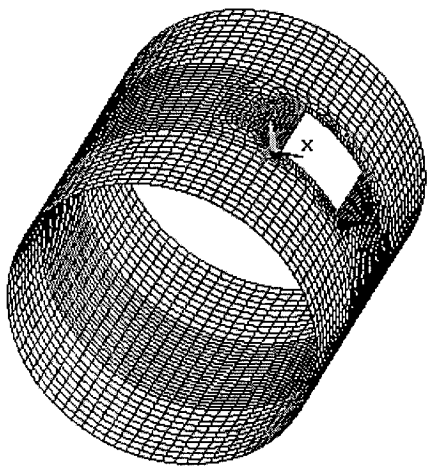

(b)

Figure 3-2: (a) The bilinear material model, and (b) the FEM mesh used for verification

The numerical simulations were carried out using the general commercial finite element program ANSYS [9]. The Shell-181 element of ANSYS was used to model the shells. This element is extremely suitable for analyzing thin to moderately thick shell structures. The element is a 4-node element with six degrees of freedom at each node and is well-suited for large strain nonlinear applications. Both full and reduced

integration schemes are supported. Shell-181 uses a penalty method to relate the independent rotational degrees of freedom about the normal (to the shell surface) with the in-plane components of displacements.

The FE model consists of the complete cylindrical shell, as there is no geometrical axisymmetry due to the presence of the geometric imperfection (cutout).

3.3.2 Mesh convergence study

Starting with a 12×10 finite element mesh, using the linear buckling analysis, a convergence study was conducted for a perfect thin cylindrical shell (L=2D, D/t=450). The results from each refinement of the mesh are compared with that from the classical buckling equation (N_{cr}) and are summarized in Table 3.1.

Table 3-1: Mesh convergence study of cylindrical shells

Mesh size (circumferential x axial)	**1st buckling load** N_1 ***(N/mm)***	$(\frac{N_1 - N_{cr}}{N_{cr}}$ **X100) % error**
12x10	23.78	43
24x20	18.168	9
24x40	17.017	2
48x20	17.938	8
48x40	16.874	1

Accepting an error margin of 1% for the linear numerical buckling load, a mesh consisting of 48×40 (element size=2.5mm $\times$ 2mm) in the circumferential and axial directions, respectively, was considered in the remaining numerical analyses. As mentioned above, the chamfer corner radii of 0.25, 0.5, 1.0, and 1.5mm were used to reduce the stress concentration for the cutouts. The analyses showed that a typical element size of 0.5mm could be used to model the area around the cutout. This mesh was validated against the results in Reference 2, as will be outlined in the following verification section. The cylindrical shell of L=2D with a cutout was modeled with 4251 elements connected with 5336 nodes.

3.3.3 Boundary conditions

A uniform line pressure loading was applied to the nodes at the top end of the cylindrical shells. With reference to the coordinate system shown in Figure 3.1, the loaded end was kept flat and circular by applying a coupling equation so that the Z-component of the displacement was uniform at each load step. The top edge was also restricted in translational *x*- and *y*- directions, whereas the bottom end was fixed by setting the translational DOF in x-, y- and z- directions to be zero.

3.3.4 Analysis procedure

In each case using the thin cylindrical shells, a linear buckling analysis was conducted, in which the Block Lanczos [9] method was used to obtain a rough estimation of the buckling capacity of each shell. As pointed out by several researchers in this area, a linear buckling analysis is not sufficient to evaluate the buckling performance of a moderately thick cylindrical shell, and would pose great limitations on determining the stability response of cylindrical shells with a cutout. This is because the response would generally involve geometric nonlinearity. Therefore a series of nonlinear analyses were conducted using the arc-length method for performing the postbuckling analysis. The arc-length method performs well in snap-through type problems, in which the equilibrium path of load-displacement is smooth and does not branch. The numerical analyses revealed that numerically tracing the buckling behavior beyond the peak load would be a difficult task if only geometric nonlinearity is considered, because of the rapid growth of displacement and the possible mode change, especially in the thin cylindrical shells (D/t=450 in the present study). For the moderately thick cylindrical shells (D/t=45 in the present study), local or global buckling usually occurs after the net section yields. Therefore, material nonlinearity has to be included for an accurate simulation, allowing the load-end shortening curve to be traced well into the postbuckling region. For thin shells, the numerical results obtained by considering geometric nonlinearity were basically identical to those obtained by considering both geometric and material nonlinearities. Therefore, it was decided to consider both geometric and material nonlinearities to characterize the shells.

3.3.5 Verification of the model

In order to confirm the integrity of the numerical analyses using ANSYS, a series of nonlinear analyses were conducted. Typical mesh with element sizes of 2.5mm×2mm was used to model the cylindrical shells with and without a cutout as shown in Figure 3.2, as well as the cylindrical shell investigated in Reference 2. The results from the present ANSYS models were compared with those from the experimental and numerical investigations reported in Reference 2. The comparison of the results reported in Table 3.2 indicates that the nonlinear ANSYS analyses could adequately simulate the response.

Table 3-2: Verifications of the buckling load of cylindrical shells with and without a cutout

	Buckling load (kN)	
Without cutout	Present (linear analysis)	23.69
	Present (nonlinear analysis)	22.21
	The classical buckling equation	23.29
	Ref[2] numerical (linear analysis)	25.06
With 25.92mmX25.92mm square cutout	Present (linear analysis)	4.28
	Present (nonlinear analysis)	7.94
	Ref[2] numerical (linear analysis)	4.5
	Ref[2] numerical (nonlinear analysis)	7.96
	Ref[2] experimental	7.82

3.4. Numerical Results and Discussions

The results for the thin and moderately thick aluminum cylindrical shells with a square cutout are presented in this section. For the moderately thick cylindrical shells, the results are generated from the nonlinear analysis involving both geometric and material nonlinearity. For the thin cylindrical shells, the results are obtained from linear buckling analyses and nonlinear buckling analyses, including both geometric and material nonlinearity.

3.4.1 Reference shell

For moderately thick cylindrical shells, the classical linear buckling equation (Equation 3.1) is not admissible since the shell itself may yield and collapse before reaching the buckling capacity, rendering the results from a linear finite element buckling

analysis invalid. In the present study, the "reference buckling load" of the shell was defined to be: $N_{ref} = \sigma_Y t = 276N/mm^2 \times 0.889mm = 245.36N/mm$, which is essentially the yield load, where σ_Y is the yield strength of the material and t is the thickness of the moderately thick-walled shell. In the load-deflection analyses, all loadings are normalized with respect to the "reference buckling load", and the corresponding end shortenings are normalized with respect to the length of the shells. For thin cylindrical shells, all loads are normalized with respect to the buckling load of $N_{cr} = 16.6639N/mm$, obtained from the classical linear buckling equation (Equation 3.1); the corresponding end shortenings are normalized to the critical displacement given by the relation $\Delta_{cr} = \frac{N_{cr}L}{Et}$ [7]. With consideration of the variable parameters (namely: shells' length, and size and location of the cutout), a total of 50 cases were numerically investigated. Three different shell lengths were analyzed, representing short, intermediate-length, and long/slender cylindrical shells. For the slender and intermediate-length cylindrical shells, results were generated for the shells having different cutout locations. As mentioned in Section 3.3.3, the boundary conditions are symmetric with reference to the mid-height of shells. Therefore, when the cutout is located along half of the shell length, due to the presence of symmetry, it would reflect the influence of the cutout's location along the entire length of the shells. The designation and analysis details of each model are summarized in Tables 3.3 and 3.4.

3.4.2 Moderately thick shells

3.4.2.1 Load vs. deformation and stress state relationship

Figure 3.3 shows a typical load-end shortening response of the intermediate length (L=5D), moderately thick (D/t=45) shell with a centrally located cutout. The isometric and plane views of the deformed cylindrical shell are considered; and the corresponding von Mises stress contours at certain loading stages are also examined. After the end-shortening curve reaches its first peak value, the axial load begins to drop dramatically. It is observed that significant deformations occur near the cutout region soon after the

peak load is reached. This peak load is considered to be the threshold for initiation of global bending of the shell. As the load drops to a certain level, the regions near both ends buckle with a significant radial deformation. It is seen that the radial displacement near the cutout becomes very large, comparable to the radius of the shell, thus signifying a global buckling and collapse. It should be mentioned that the cylindrical shell global buckling is quite similar to the Euler column buckling. However, the shell's local buckling comes in conjunction with significant deformations occurring only at some local portion of the shell, without the global collapse of the shell. It is observed that the wall of the shell near the corner of the cutout yields first when the load reaches its peak level, after which the yielded region (shaded area in Figure 3.3) rapidly expands around the cutout after the peak load level. The expanding yielded regions lead to the failure of the shell wall around the cutout and in turn to the global bending and rapid collapse of the shell. It is also observed that the regions near both ends of the shell yield and the yield region expands with the increase of end shortening.

Figure 3.4 shows typical behavior of the intermediate length (L=5D), moderately thick (D/t=45) shell with a cutout located near its loaded end. As can be seen from the load-end shortening curve, the load increases linearly to its first peak value, at which stage only a very small deformation occurs, but the shell walls around and opposite to the cutout region begin to yield (see shaded region in Figure 3.4, stage A). With the increase of further end shortening, the yielded regions then keep expanding and finally connect to one another. The yielded region (stage C in Figure 3.4), is however limited only to the region near and below the loaded end. Even though significant deformations occur above the cutout, the portion of the shell beneath the cutout appears to remain intact.

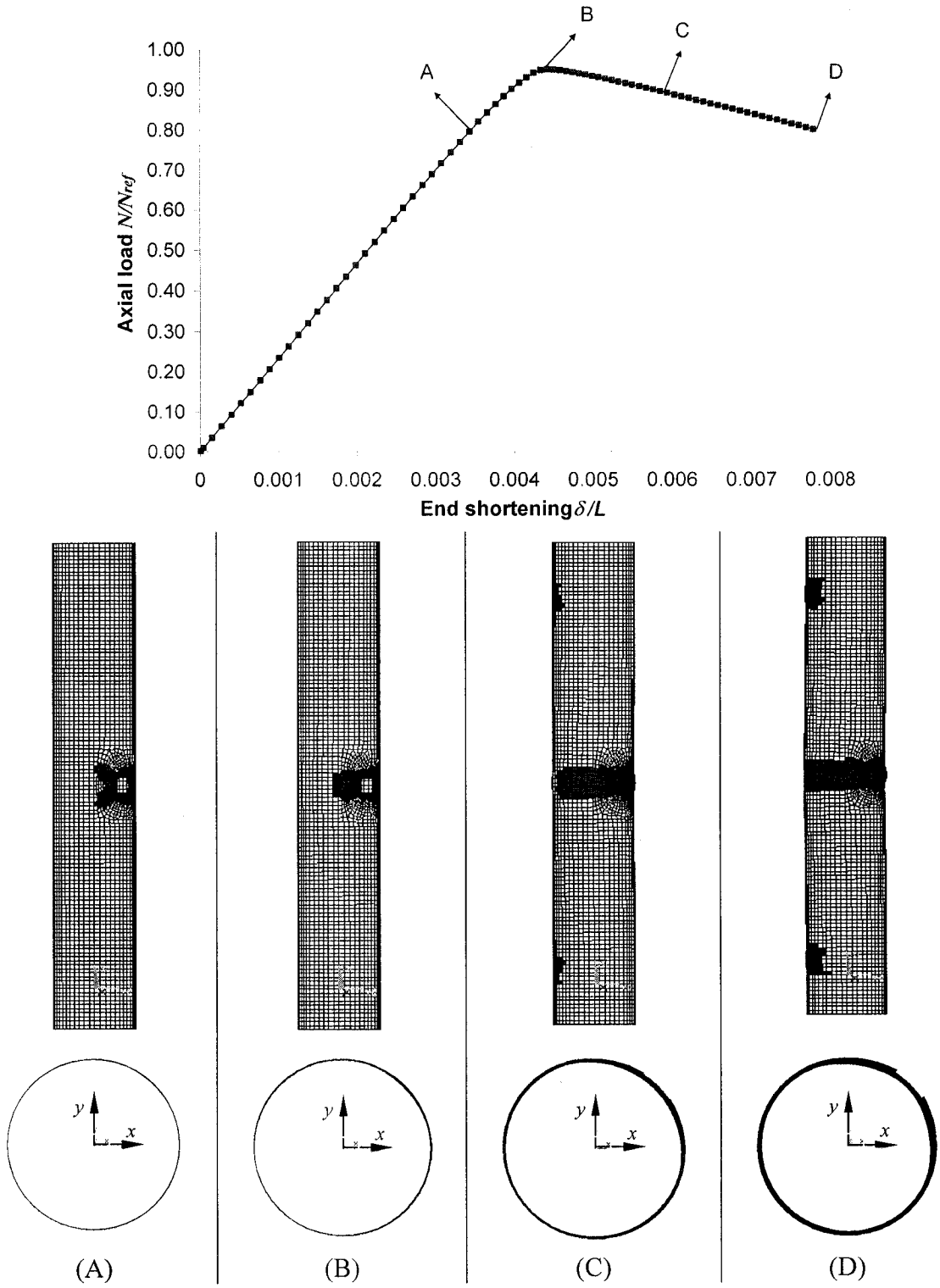

Figure 3-3: Plots of load vs. end shortening, the shell deformations, as well as the von Mises stress state at various loading stages of the moderately thick (D/t=45), intermediate length (L=5D) cylindrical shell with a 7.5mmx7.5mm cutout at its mid-height

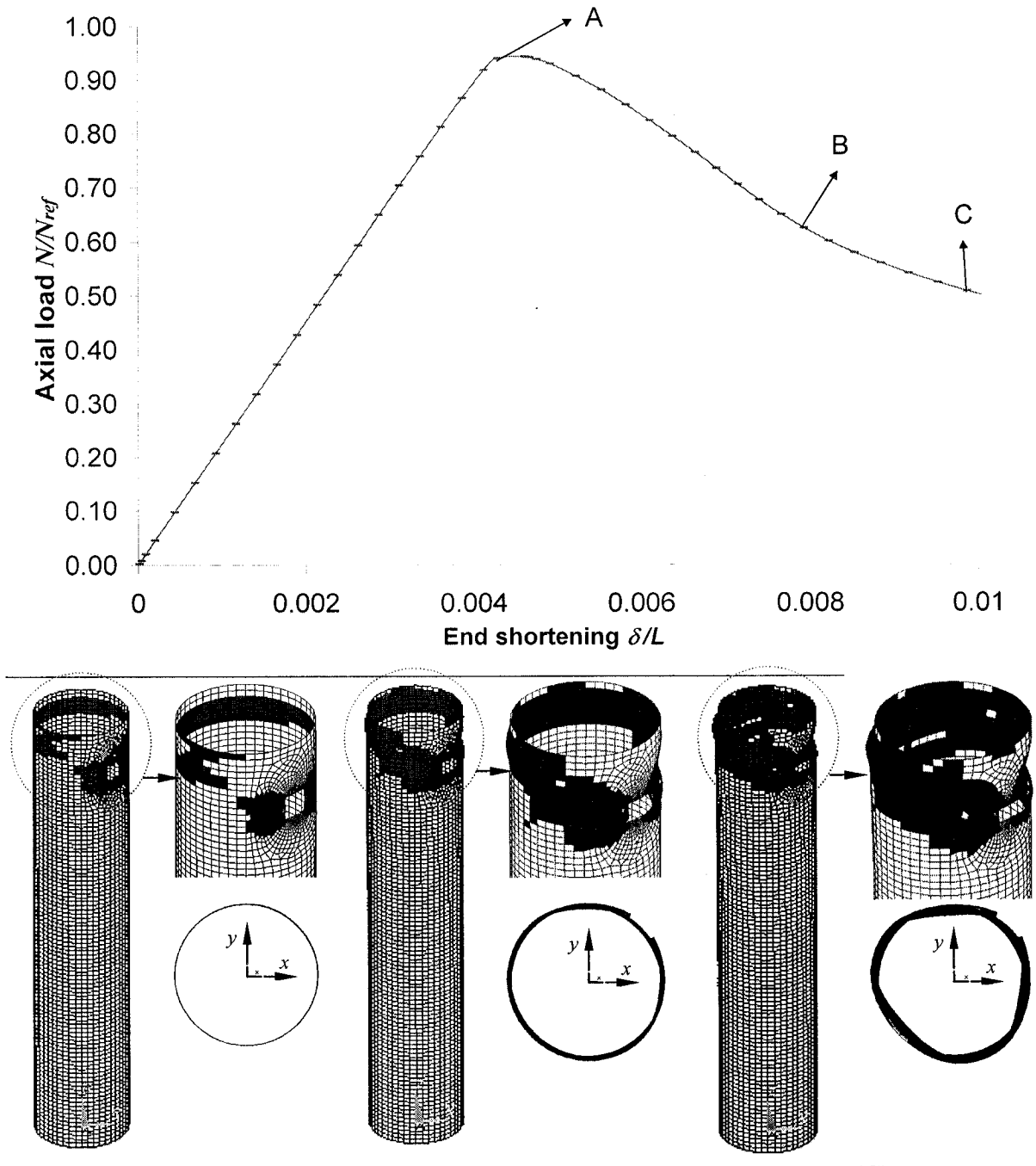

Figure 3-4: Plots of load vs. end shortening, the shell deformations, as well as the von Mises stress state at various loading stages of the moderately thick (D/t=45), intermediate length (L=5D) cylindrical shell with a 7.5mmx7.5mm cutout near its loaded end

Table 3-3: Summary of the case studies for moderately thick-walled shells

Moderately thick-walled shells, D=40mm, t=0.889mm, D/t=45					
Model designation	**Shell length** (mm)	**cutout size** (mmxmm)	**Location of cutout** (*L0/L*)	**Normalized first peak load** (*N/Nref*)	**Buckling type**
T1_10D_5_50L	400	5.3x5.3	0.50	0.9741	LY-GB
T1_10D_5_65L	400	5.3x5.3	0.65	0.9782	LY-GB
T1_10D_5_75L	400	5.3x5.3	0.75	0.9870	LY-GB
T1_10D_5_85L	400	5.3x5.3	0.85	0.9945	LY-LB
T1_10D_5_95L	400	5.3x5.3	0.95	0.9863	LY-LB
T1_10D_7_50L	400	7.5x7.5	0.50	0.9252	LY-GB
T1_10D_7_65L	400	7.5x7.5	0.65	0.9333	LY-GB
T1_10D_7_75L	400	7.5x7.5	0.75	0.9415	LY-GB
T1_10D_7_85L	400	7.5x7.5	0.85	0.9537	LY-LB
T1_10D_7_95L	400	7.5x7.5	0.95	0.9659	LY-LB
T1_10D_10_50L	400	10.6x10.6	0.50	0.8640	LY-GB
T1_10D_10_65L	400	10.6x10.6	0.65	0.8640	LY-GB
T1_10D_10_75L	400	10.6x10.6	0.75	0.8803	LY-GB
T1_10D_10_85L	400	10.6x10.6	0.85	0.9007	LY-LB
T1_10D_10_95L	400	10.6x10.6	0.95	0.9211	LY-LB
T1_10D_15_50L	400	15.0x15.0	0.50	0.7772	LY-GB
T1_10D_15_65L	400	15.0x15.0	0.65	0.7866	LY-GB
T1_10D_15_75L	400	15.0x15.0	0.75	0.8111	LY-GB
T1_10D_15_85L	400	15.0x15.0	0.85	0.8477	LY-LB
T1_10D_15_95L	400	15.0x15.0	0.95	0.8722	LY-LB
T1_5D_15_50L	200	15.0x15.0	0.50	0.8396	LY-GB
T1_5D_15_60L	200	15.0x15.0	0.60	0.8396	LY-GB
T1_5D_15_70L	200	15.0x15.0	0.70	0.8465	LY-GB
T1_5D_15_80L	200	15.0x15.0	0.80	0.8543	LY-LB
T1_5D_15_90L	200	15.0x15.0	0.90	0.8396	LY-LB
T1_5D_5_50L	200	5.3x5.3	0.50	0.9950	LY-GB
T1_5D_7_50L	200	7.5x7.5	0.50	0.9510	LY-GB
T1_5D_10_50L	200	10.6x10.6	0.50	0.8970	LY-GB
T1_2D_5_50L	80	5.3x5.3	0.50	1.0150	LY-GB
T1_2D_7_50L	80	7.5x7.5	0.50	0.9750	LY-GB
T1_2D_10_50L	80	10.6x10.6	0.50	0.9300	LY-GB
T1_2D_15_50L	80	15.0x15.0	0.50	0.8760	LY-GB

Note: LY-GB: *Local yielding results in global bending and then in global buckling*

LY-LB: *Local yielding around cutout results in local buckling near the loaded end*

Table 3-4: Summary of the case studies for thin-walled shells

Thin-walled shells, D=40mm, t=0.0889mm, D/t=450					
Model designation	Shell length (mm)	cutout size (mmxmm)	Location of cutout (*L0/L*)	Normalized first peak load (*N/Ncr*)	Buckling type
T2_10D_7_50L	400	7.5x7.5	0.50	0.235	LB
T2_10D_7_65L	400	7.5x7.5	0.65	0.239	LB
T2_10D_7_75L	400	7.5x7.5	0.75	0.272	LB
T2_10D_7_85L	400	7.5x7.5	0.85	0.267	LB-BH
T2_10D_7_95L	400	7.5x7.5	0.95	0.321	LB-BH
T2_10D_5_50L	400	5.3x5.3	0.50	0.278	LB
T2_10D_10_50L	400	10.6x10.6	0.50	0.215	LB
T2_10D_15_50L	400	15.0x15.0	0.50	0.195	LB
T2_10D_5_95L	400	5.3x5.3	0.95	0.351	LB-BH
T2_10D_10_95L	400	10.6x10.6	0.95	0.307	LB-BH
T2_10D_15_95L	400	15.0x15.0	0.95	0.285	LB-BH
T2_5D_5_50L	200	5.3x5.3	0.50	0.29	LB-BH
T2_5D_7_50L	200	7.5x7.5	0.50	0.257	LB-BH
T2_5D_10_50L	200	10.6x10.6	0.50	0.243	LB-BH
T2_5D_15_50L	200	15.0x15.0	0.50	0.245	LB-BH
T2_2D_5_50L	80	5.3x5.3	0.50	0.344	LB-BH
T2_2D_7_50L	80	7.5x7.5	0.50	0.353	LB-BH
T2_2D_10_50L	80	10.6x10.6	0.50	0.367	LB-BH
T2_2D_15_50L	80	15.0x15.0	0.50	0.373	LB-BH

Note: **LB** - Local Buckling
LB-BH – Local buckling followed by buckling capacity hardening

3.4.2.2 Influence of cutout size and length/radius ratio

In a moderately thick cylindrical shell with a cutout located at its mid- height, a variation in the size of the cutout can significantly influence the shell's load bearing capacity. This behavior holds true for all shells of various lengths, because the global buckling is prompted by the yielding of the net section around the cutout. As expected, a large cutout results in a lower bearing capacity. To fully understand the effect of cutouts on the behavior of the shell, the shell is compressed well into its postbuckling region. In this case, the end shortening curve follows up to the first completed wrinkle of the perfect shell, as shown in Figure 3.5. This figure illustrates the load–end shortening response of

the cylindrical shells of various lengths with various size cutouts located at their mid-height. It can be seen that the presence of a cutout has less effect on the peak load bearing capacity of the short shells. For instance, a 5.3mmx5.3mm cutout leads to a 2.5% drop in the peak load for the short shell but results in 20.4% and 21.4% decreases for the intermediate-length and the slender cylindrical shells, respectively. Figure 3.5 also shows that after the peak load, the load bearing capacity of a shell with a central cutout would decrease monotonically with the increase in the end shortening. It is also observed that the longer the shell, the more sensitive it is to changes in the cutout size. For example, the load bearing capacity decreases by approximately 14%, 16%, and 20% for short, intermediate-length, and long cylindrical shells, respectively when changing the cutout size from 5.3mm to 15.0mm. Furthermore, for short cylindrical shells, the presence of a cutout at its center height can interestingly increase the load-bearing capacity of the shells when the end shortening varies between 0.05L and 0.13L, as shown in Figure 3.5(a). This phenomenon occurs perhaps because the short shells with a cutout are more efficient in redistributing the load than the shells without a cutout, when they are compressed up to the end shortening of between 0.05L and 0.13L. In contrast, in the intermediate-length and long cylindrical shells, the presence of a cutout at mid-height would completely reduce the shell's load-bearing capacity, with the increase in end shortening, as shown in Figure 3.5 (b and c).

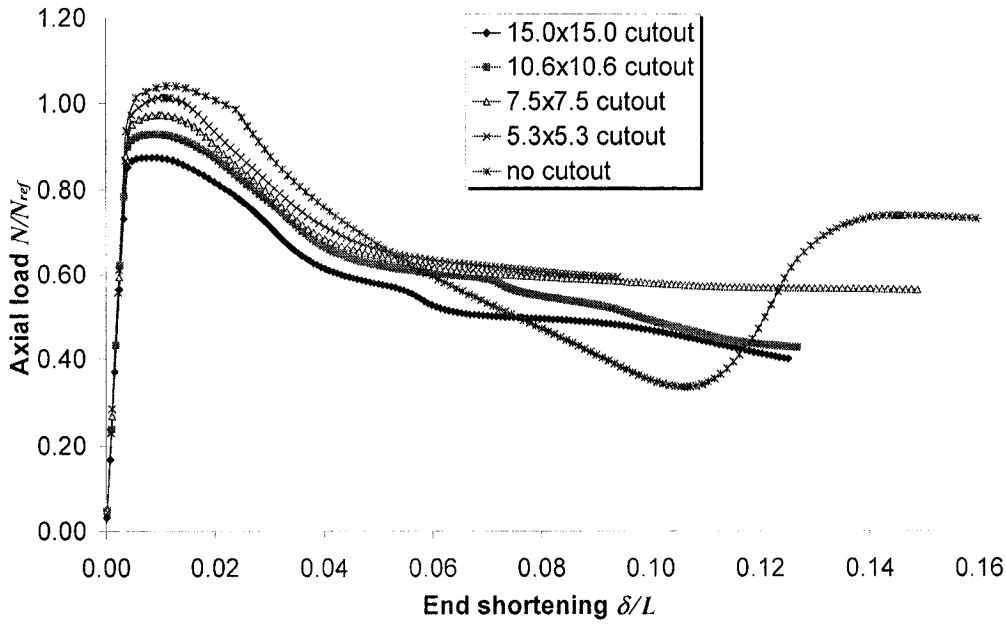

(a)

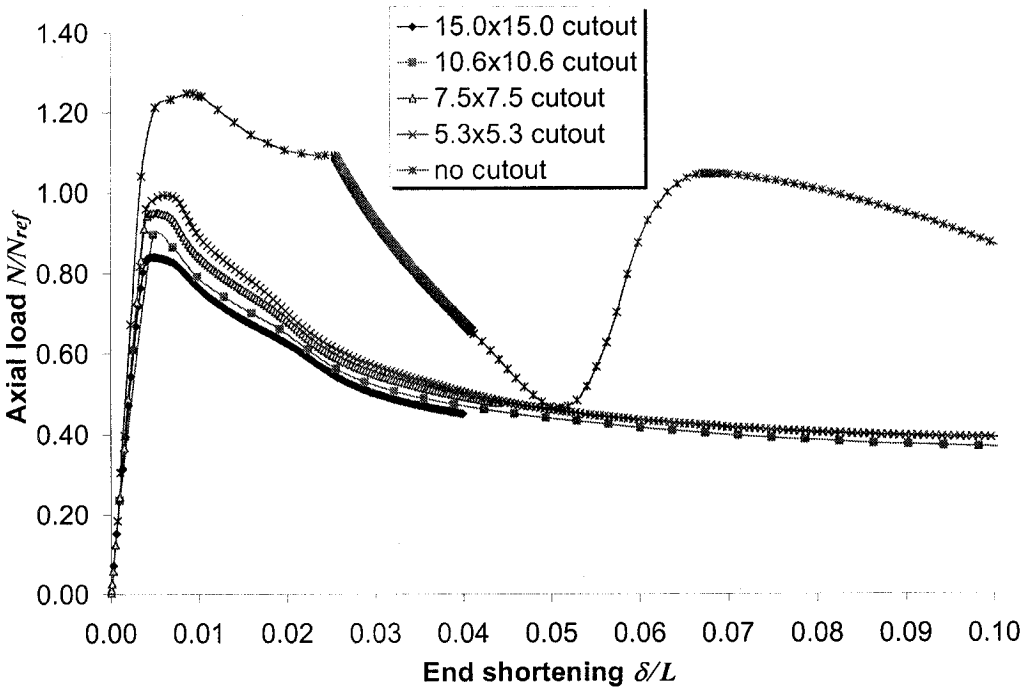

(b)

--- (c) to be continued on next page

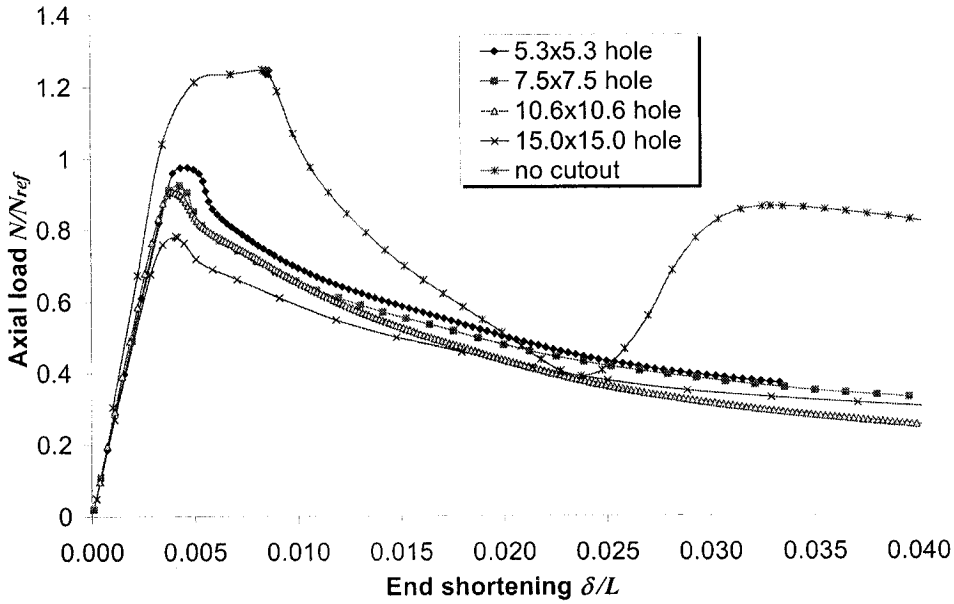

(c)

Figure 3-5: Load-end shortening behavior of the moderately thick (D/t=45) cylindrical shells of various lengths with and without a cutout at mid-height (a) Short shells (L=2D), (b) Intermediate-length shells (L=5D) and (c) Long shells (L=10D)

3.4.2.3 Influence of the location of the cutout

The results in this study indicate that the presence of a cutout at different locations in the shell can influence its buckling capacity in a different manner. To examine the effect of cutout locations, the numerical simulations considered end shortening of up to 2.5% of the shell length for the long shells. The load-end shortening behaviors of the long cylindrical shells with a cutout (four different sizes and various locations along the height of the shells) are plotted in Figure 3.6 and summarized in Figure 3.7. It can be seen from these curves that the first peak load is basically below the normalized value of 1. As mentioned earlier, this reference buckling load is a function of the yield strength of the material. The first peak load can also be considered the buckling capacity, which in turn causes the net section around the cutout region to yield. The curves in Figure 3.6 also indicate that the axial stiffness (the initial slope of the load-end shortening curve) of the cylindrical shells is almost identical before the load reaches its first peak point,

regardless of the cutout size. In fact, the axial stiffness of these shells prior to buckling is equal to the axial stiffness of the net section of the cutout region.

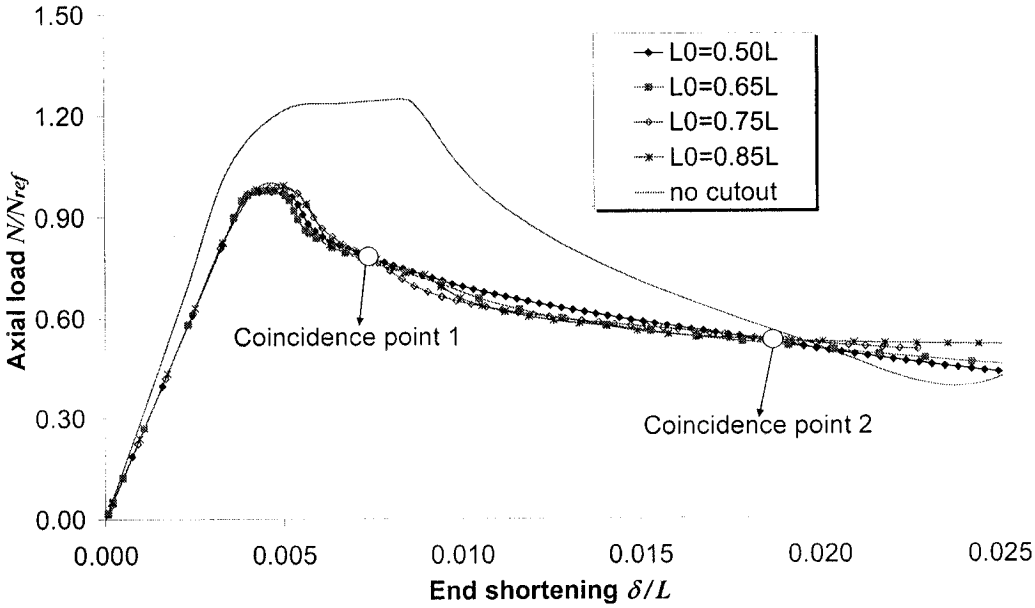

(a) 5.3mmx5.3mm cutout

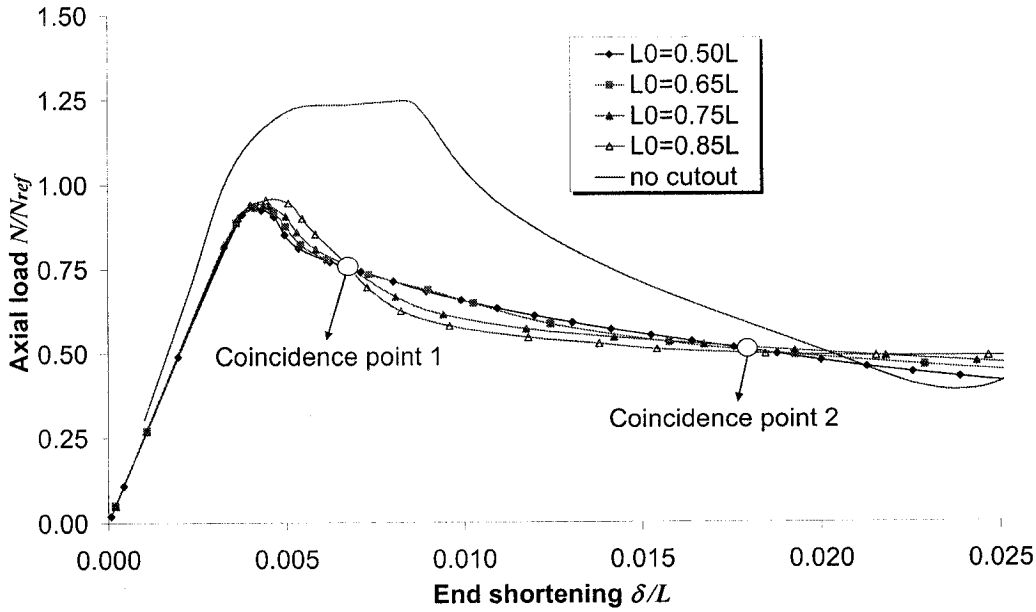

(b) 7.5mmx7.5mm cutout

---(c) and (d) continued on next page

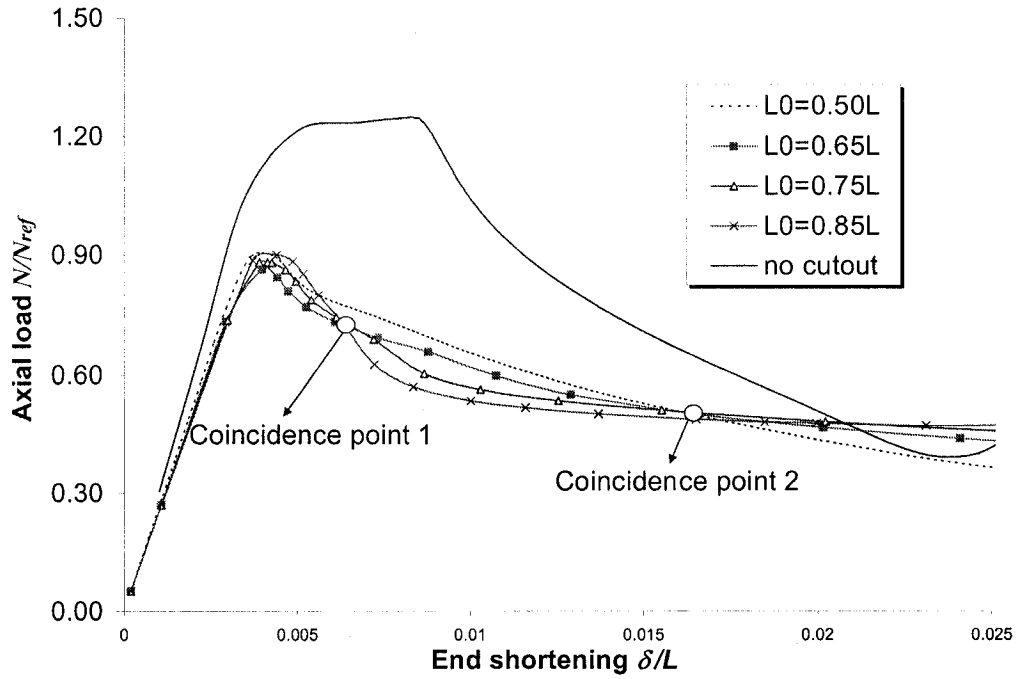

(c) 10.6mmx10.6mm cutout

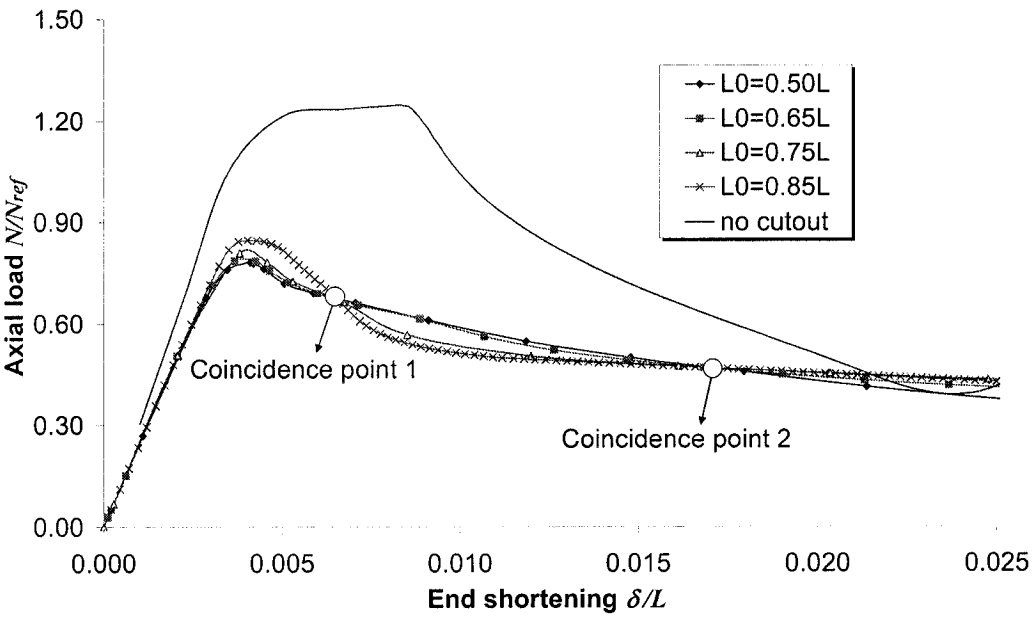

(d) 15.0mmx15.0mm cutout

Figure 3-6: Load-end shortening behavior of the long (L=10D), moderately thick (D/t=45) cylindrical shells with (a) a 5.3mmx5.3mm, (b) a 7.5mmx7.5mm, (c) a 10.6mmx10.6mm and (d) a 15.0mmx15.0mm cutout positioned at various locations

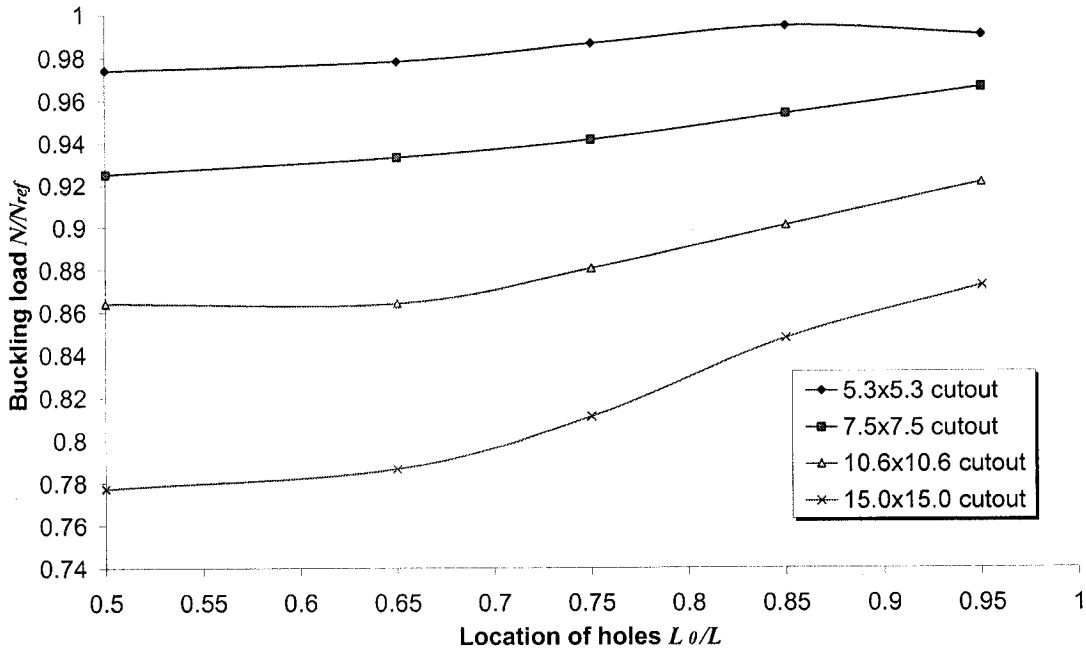

Figure 3-7: Summary of the buckling capacity of the long (L=10D), moderately thick (D/t=45) shells with a different size cutout situated at various locations

To summarize all the results, the buckling phenomena can be characterized as: the net section yielding around the cutout leads to global bending, which in turn leads to global instability; or, the net section yielding around the cutout leads to local buckling around the cutout. The first phenomenon occurs if the cutout is located near the mid-height of the shell ($0.25L \le L_0 \le 0.75L$), whereas the second phenomenon only takes place if the cutout is located near the loaded end ($0..05L \le L_0 \le 0.25L$ or $0.50L \le L_0 \le 0.95L$).

Figure 3.6 illustrates that when the end shortening is about 0.007L and 0.018L, the load bearing capacity of the cylindrical shells with a cutout at various locations along their length coincide with each other. Before the first coincidence of the buckling load, the cylindrical shells with the cutout located near their mid-height have a lower load bearing capacity than those with the cutout located much closer to the loaded end. In fact, this is a common scenario before and at the first peak load. Between the first and

second coincidence points (see Figure 3.6), the load bearing capacity of the cylindrical shell with a cutout located at its mid-height is the highest, while the capacity is the lowest with the cutout located nearest to the loaded end. It can be seen that the response of the shells switches after reaching the second coincidence point in Figure 3.6. The reason behind this phenomenon is because of the resulting load redistribution. A high level of load redistribution results in a high load bearing capacity and vice versa.

It is observed from Figure 3.7 that for cylindrical shells with a small size cutout, the buckling capacity increases almost linearly as a function of the cutout's location. For shells with a larger size cutout, the shell buckling capacity decreases more rapidly when the size of the cutout located near the end region increases. From the above analysis it is clear that the influence of the location of the cutout depends strongly on the size of the cutout; the smaller the size, the lesser the effect, and vice versa.

3.4.2.4 Experimental verification

Experimental tests using an INSTRON universal testing machine were conducted to verify some of the cases investigated in the numerical simulations. Tests were carried out on the intermediate length and long cylindrical shells with cutouts at various locations. The specimens were constrained by steel sleeve fixtures inserted at both ends, which mimics the fixed-fixed boundary condition used in the finite element simulations (see Figure 3.8). Three specimens were tested for each case and almost identical results were obtained compared to those obtained from the numerical simulations. Figures 3.8 to 3.10 show the comparisons of results from experimental tests and finite element simulations for three different cases (corresponding to the models identified as: T1_5D_7_50L, T1_5D_7_80L, and T1_10D_7_95L, respectively), tabulated in Table 3.3. The results are correlated by comparing the peak buckling load, the load-end shortening response, as well as the deformation behaviors at certain loading stages. Very good correlations are observed.

It can be seen that for the moderately thick cylindrical shell with a cutout located at its mid-height, any variation in cutout size could significantly influence the load bearing capacity of the shell. This behavior holds for all shells of various lengths, because the

global buckling is prompted by yielding of the net section around the cutout. As expected, a larger cutout results in a lower bearing capacity.

3.4.3 Thin cylindrical shells

For thin cylindrical shells, both linear and nonlinear buckling analyses are conducted. The nonlinear buckling analysis involves either geometric nonlinearity only, or both geometric and material nonlinearities. As stated by Litle [10], the load-end deformation behavior of a thin cylindrical shell is sensitive to the ratio of shell length to shell radius. For very short cylinders ($L/R \leq 0.1$) the behavior observed is analogous to the Euler buckling of a strip element. For very long cylinders ($L/R \geq 50$) the tube also acts as an Euler column. For intermediate lengths ($0.1 \leq L/R \leq 50$), the behavior tends toward symmetrical rippling of the side walls, and the critical buckling load can be calculated by the classical equation (Equation 3.1). For the sake of comparison, the buckling analysis of the reference (perfect) cylindrical shells was carried out first, which included the short, intermediate-length and long/slender shells. As can be seen from the results tabulated in Table 3.6, both linear and nonlinear buckling analyses provide very close results to those obtained from the classical equation. The linear buckling results ($1.02\,N_{cr}$ ~$1.03\,N_{cr}$) are slightly above the exact value, while the nonlinear analysis results of ($0.952\,N_{cr}$ ~$0.968\,N_{cr}$) are slightly below.

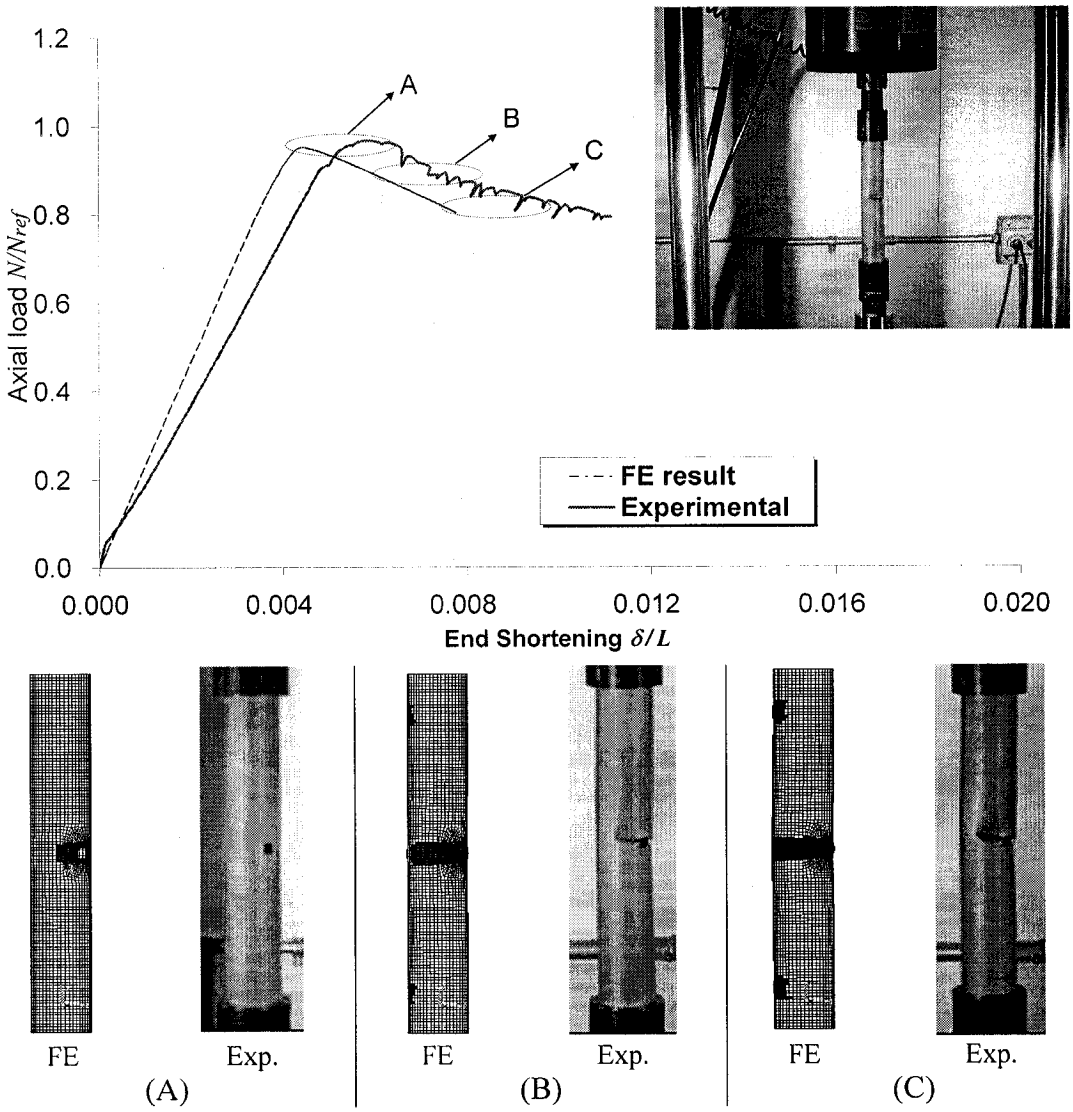

Figure 3-8: Comparison of the experimental and numerical results for the intermediate length (L=5D), moderately thick (D/t=45) cylindrical shells with mid-height cutouts

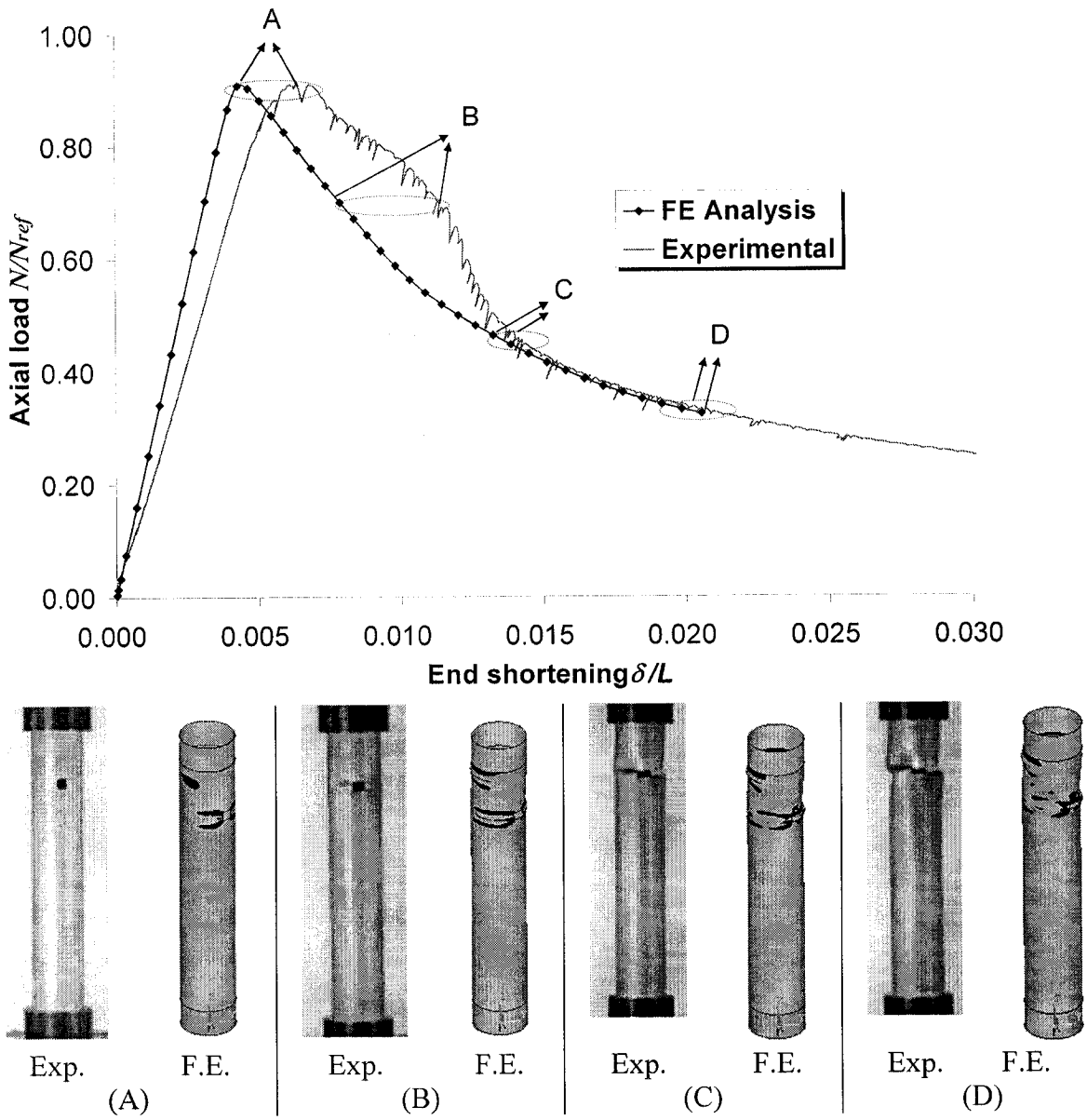

Figure 3-9: Comparison of the experimental and numerical results for the intermediate length (L=5D), moderately thick (D/t=45) cylindrical shells with a cutout near its loaded end ($L_0 = 0.80L$)

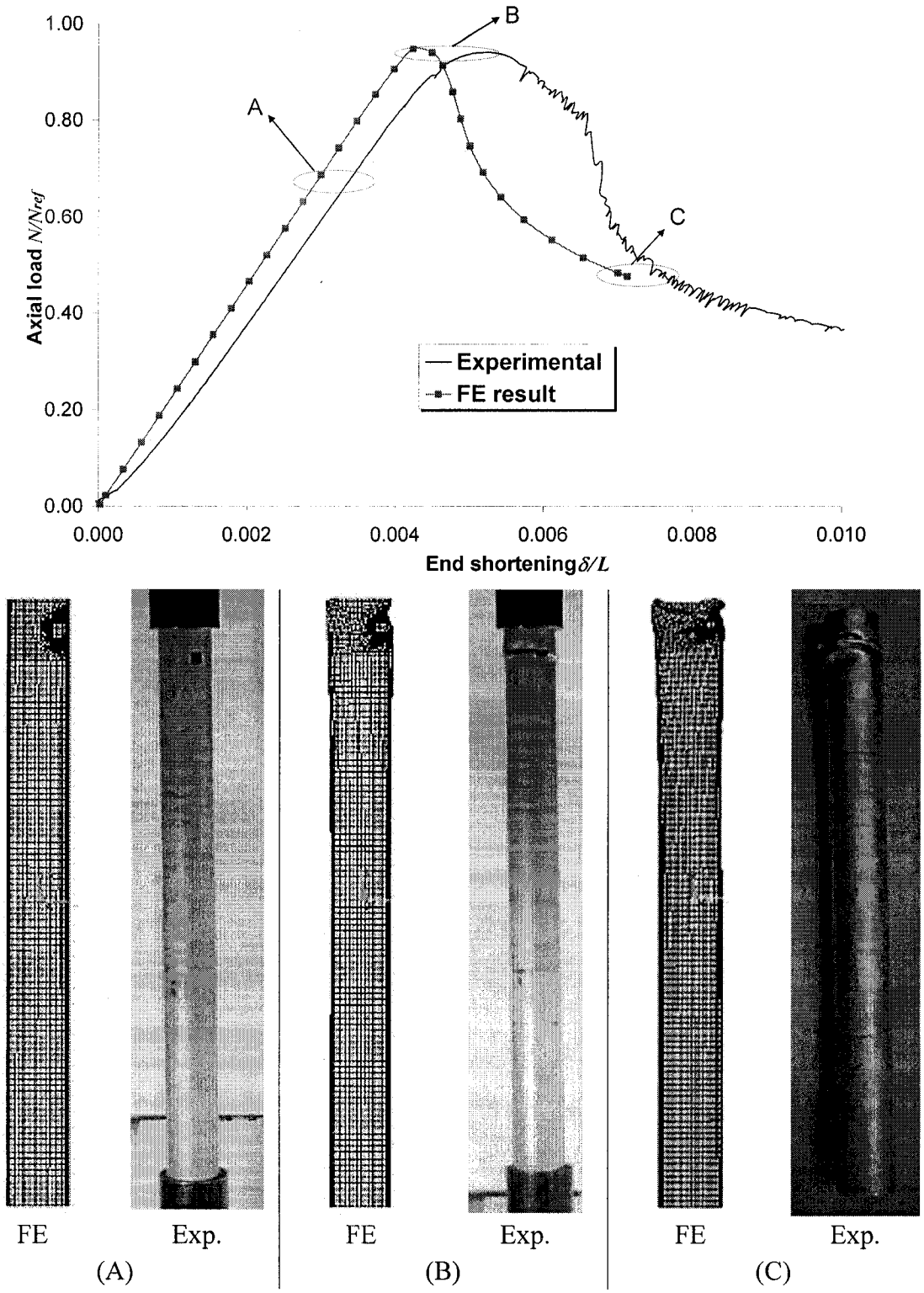

Figure 3-10: Comparison of the experimental and numerical results for the long (L=10D), moderately thick (D/t=45) cylindrical shells with a cutout near its loaded end ($L_0 = 0.95L$)

Table 3-5: The computed buckling loads for thin (D/t=450) cylindrical shells with a 7.5mmx7.5mm cutout located at mid-height

length	L=2D		L=5D		L=10D	
	N_{FE} (N/mm)	$\frac{N_{FE}}{N_{cr}}$	N_{FE} (N/mm)	$\frac{N_{FE}}{N_{cr}}$	N_{FE} (N/mm)	$\frac{N_{FE}}{N_{cr}}$
Linear buckling analysis	2.650	0.159	2.363	0.142	2.297	0.138
Nonlinear analysis (geometric nonlinearity only)	5.870	0.352	5.110	0.307	3.910	0.235
Nonlinear analysis (both geometric and material nonlinearity)	5.890	0.353	5.110	0.307	3.910	0.235

Similar analyses were conducted for the thin cylindrical shells with a 7.5mmx7.5mm central cutout. As listed in Table 3.5, the linear buckling results ($0.138N_{cr}$~$0.159N_{cr}$) are well below the nonlinear buckling results ($0.235N_{cr}$ ~$0.353N_{cr}$). It is found that the results obtained from nonlinear analyses considering only geometric nonlinearity, and those considering both geometric and material nonlinearities, provide almost identical results. It is also observed that the presence of a cutout could significantly reduce the buckling capacity. Several researchers (e.g. [5]) found that there was a very good correlation between the experimental results and those obtained from nonlinear finite element analysis. In the present paper, the nonlinear analysis (including both geometrical and material nonlinearities) is used for verification. Figures 3.11 and 3.12 illustrate the typical load-end shortening response of thin cylindrical shells with a cutout at two different locations. The isometric views of the deformed shells at different load stages are also shown in the figures. The contour plots of the von Mises stress at various load stages reveal that net section yielding did not occur prior to reaching the peak load level, and that buckling occurred only locally, near the cutout. Our investigation on thin cylindrical shells indicates that the buckling mode for all the thin cylindrical shells with a cutout would be in the form of localized buckling. Moreover, as will be discussed later, for the various cases studied here, the local buckling was accompanied with the so-called "buckling capacity hardening" phenomenon.

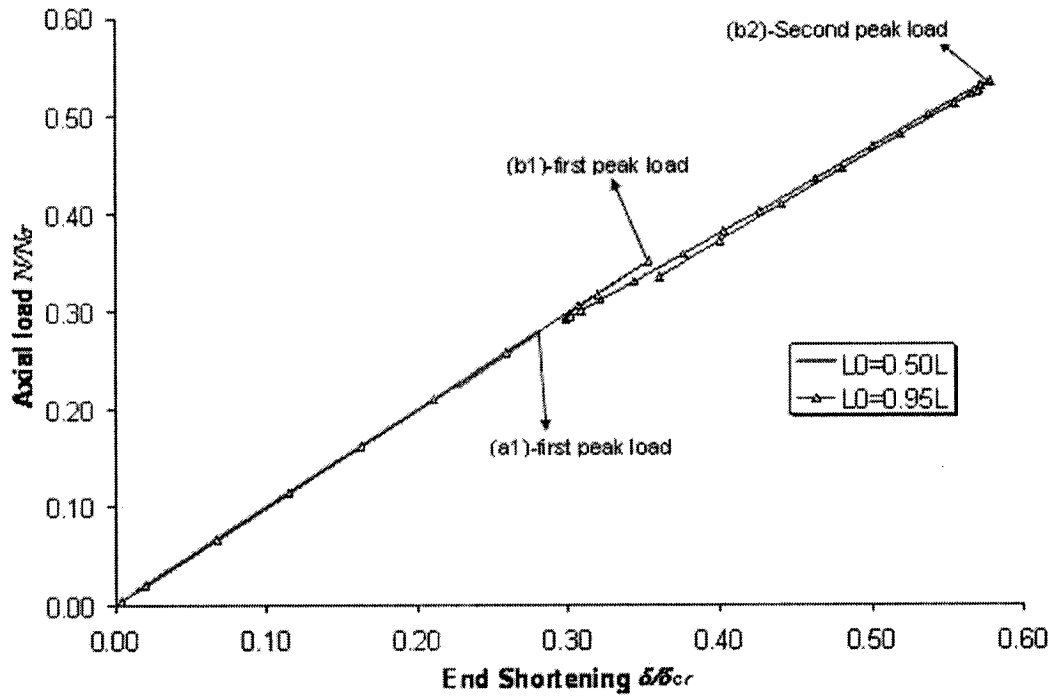

(a) Load-end shortening behavior

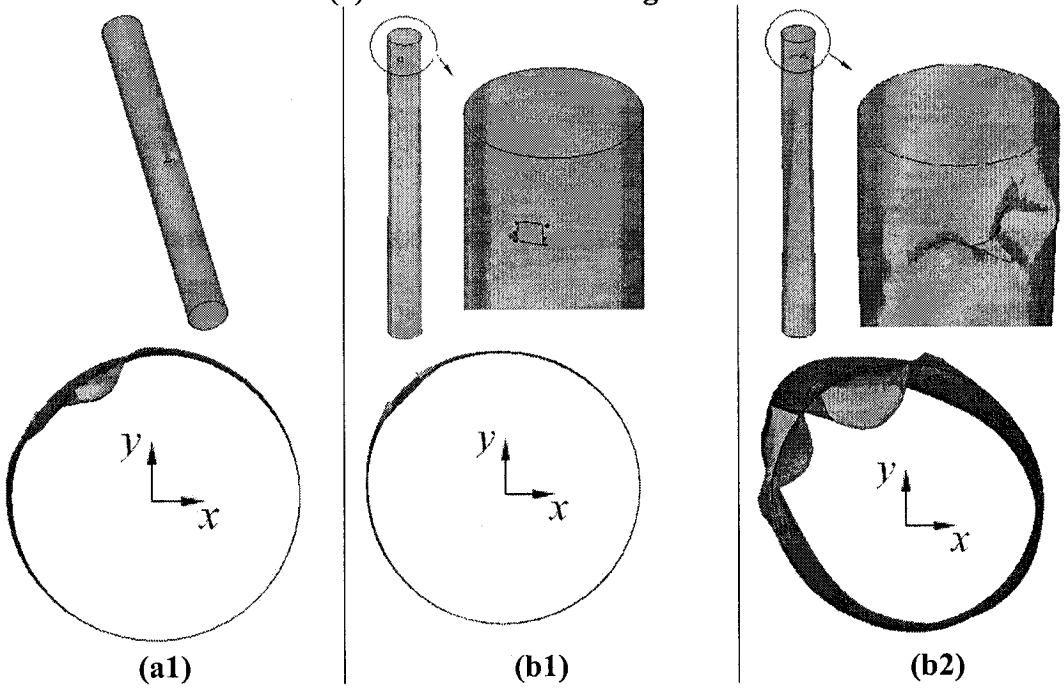

(a1) **(b1)** **(b2)**

(b) Isometric and plan view at each load stage

Figure 3-11: Load-end shortening behavior of the thin (D/t=450), long (L=10D) cylindrical shells with a 5.3mmx5.3mm cutout located at the mid-height and near the loaded end

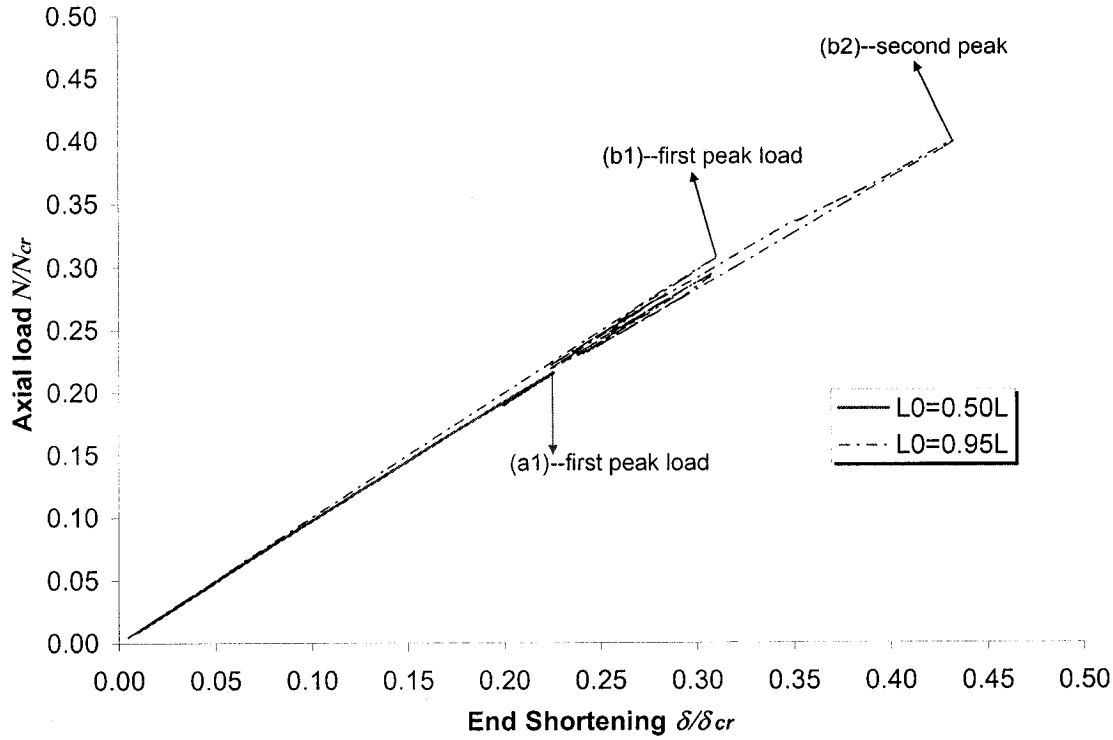

(a) Load-end shortening behavior

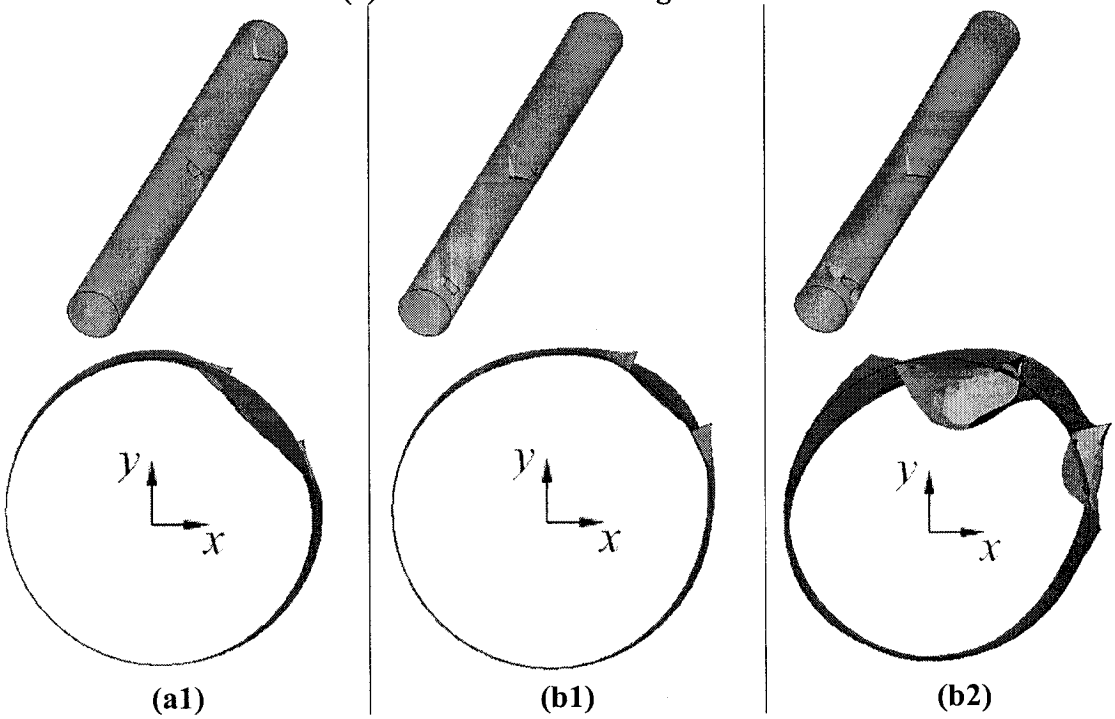

(a1) **(b1)** **(b2)**

(b) Isometric and plan view at each load stage

Figure 3-12: Load-end shortening behavior of the thin (D/t=450), long (L=10D) cylindrical shells with a 10.6mmx10.6mm cutout located at the mid-height and near the loaded end

Table 3-6: The computed buckling loads[b] for thin (D/t=450) cylindrical shells with a cutout of various sizes located at mid-height

L=2D - Short cylindrical shells					
Cutout size (mmxmm)	**no cutout**	**5.3x5.3**	**7.5x7.5**	**10.6x10.6**	**15.0x15.0**
Linear buckling analysis	1.03	0.222	0.159	0.129	0.117
1st peak in nonlinear buckling analysis [a]	0.952	0.344	0.353	0.367	0.373
2nd peak in nonlinear buckling analysis [a]	N/A	0.665	0.600	0.374	0.412
2nd peak load/1st peak load	N/A	1.930	1.701	1.018	1.106
L=5D – intermediate-length cylindrical shell					
Cutout size (mmxmm)	**no cutout**	**5.3x5.3**	**7.5x7.5**	**10.6x10.6**	**15.0x15.0**
Linear buckling analysis	1.03	0.210	0.142	0.103	0.081
1st peak in nonlinear buckling analysis [a]	0.957	0.290	0.257	0.243	0.245
2nd peak in nonlinear buckling analysis [a]	N/A	0.600	0.443	0.377	0.334
2nd peak load/1st peak load	N/A	2.066	1.725	1.553	1.365
L=10D – Long/slender cylindrical shell					
Cutout size (mmxmm)	**no cutout**	**5.3x5.3**	**7.5x7.5**	**10.6x10.6**	**15.0x15.0**
Linear buckling analysis	1.02	0.208	0.138	0.096	0.071
1st peak in nonlinear buckling analysis [a]	0.968	0.278	0.234	0.215	0.195
2nd peak in nonlinear buckling analysis [a]	N/A	N/A	N/A	N/A	N/A

**Note:*

a. The nonlinear analysis involved both geometrical and material nonlinearities (the bilinear material model).

b. All buckling loads are normalized with respect to the critical buckling load calculated based on the classical buckling equation [Equation 3.1].

3.4.3.1 Effect of the cutout size and L/D ratio

Figures 3.13 illustrates the load-end shortening behaviors of the thin cylindrical shells (for L=2D, L=5D, and L=10D) with cutouts of various sizes located at the mid-height of the shells. The first peak load of these cases is summarized in Table 3.6. It can be seen that for the long cylindrical shells (L=10D), a larger cutout results in a lower buckling load, regardless of the location of the cutout along the shell height. From Figure 3.14 it can be seen that when the cutout is located near the loaded end, the same trend holds. However, this did not hold for the shorter cylindrical shells. Results tabulated in Table 3.6 also indicate that for the intermediate-length cylindrical shells (L=5D), a

10.6mmx10.6mm cutout and a 15.0mmx15.0mm cutout would produce an almost identical impact on the buckling capacity (i.e. $0.243\,N_{cr}$ compared to $0.245\,N_{cr}$). It is also noted that a 15.0mmx15.0mm cutout in the short shell (L=2D) generates a smaller reduction effect (also referred as the knock-down factor) than a 10.6mmx10.6mm cutout. Considering the influence of a cutout of the same size on shells with different lengths, one can see a more negative effect on the long cylindrical shells than on the shorter ones. For example, a 5.3mmx5.3mm cutout results in a buckling load of $0.278\,N_{cr}$ for the long cylindrical shells, while the same cutout results in $0.290\,N_{cr}$ and $0.344\,N_{cr}$ for the intermediate-length and short shells, respectively. The load-end shortening behavior of the thin cylindrical shells with a 5.3mmx5.3mm cutout at their mid-height is shown in Figure 3.15. For the shorter shells with a central cutout, the load bearing capacity can achieve a second peak level, after going through a sharp valley, as shown in Figures 3.13(a-b). This second peak load is correlated to a higher buckling mode. The ratio of the second peak load to the first peak load is higher for the smaller size cutout. Furthermore, for the same size cutout, the ratio of the second peak value to the first is higher for the intermediate-length shells compared to the short ones, as shown in Table 3.6. However, this phenomenon basically does not hold for the long shells when the cutout is located at their mid-height.

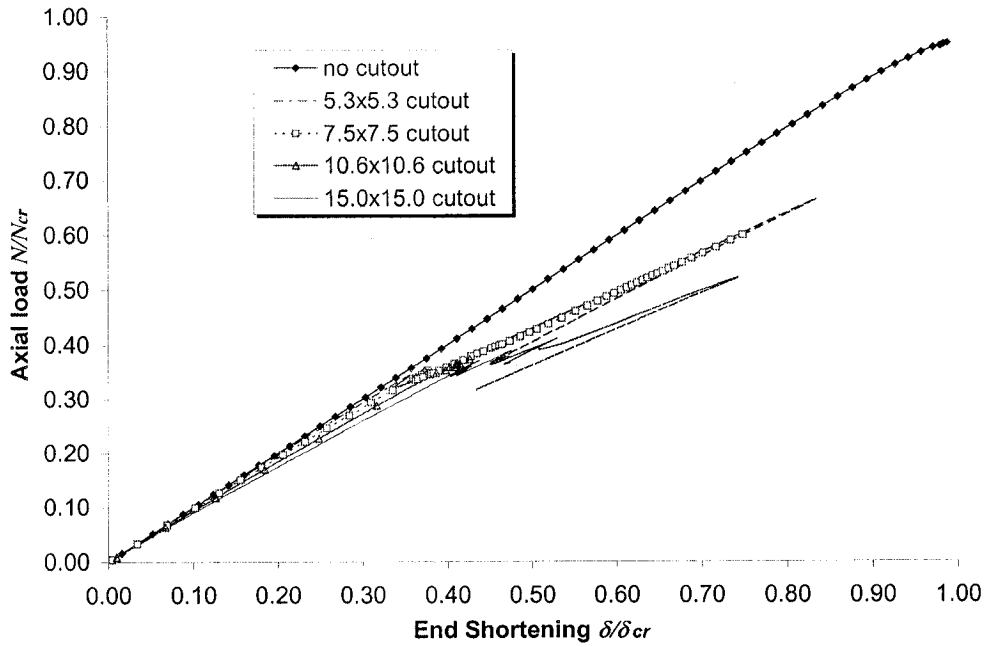

(a) short (L=2D)

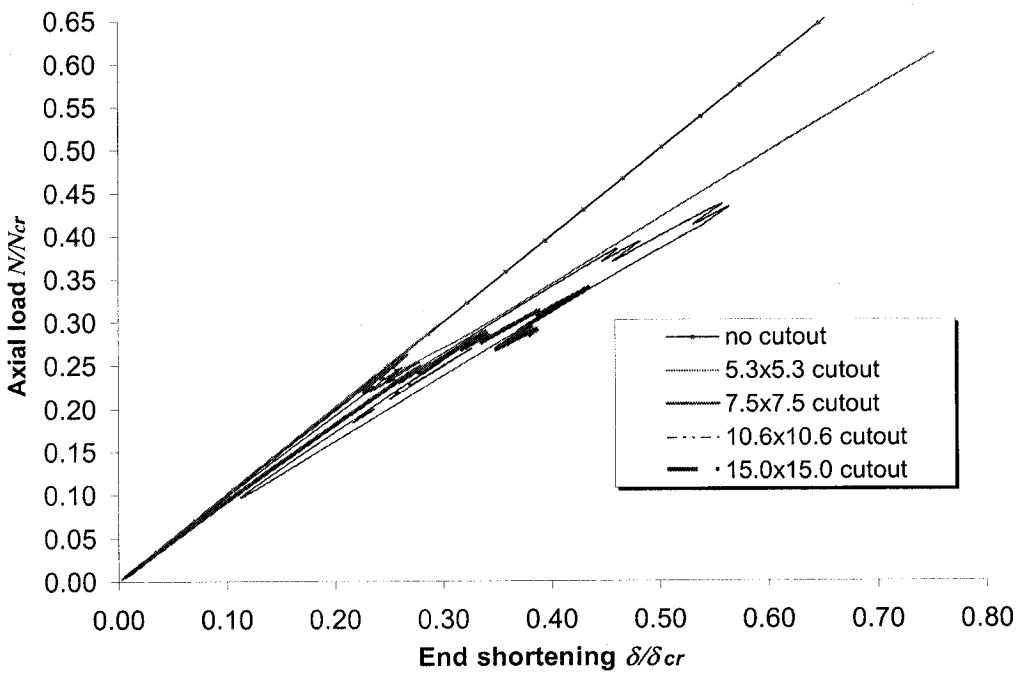

(b) intermediate-length (L=5D)

---(c) to be continued on next page

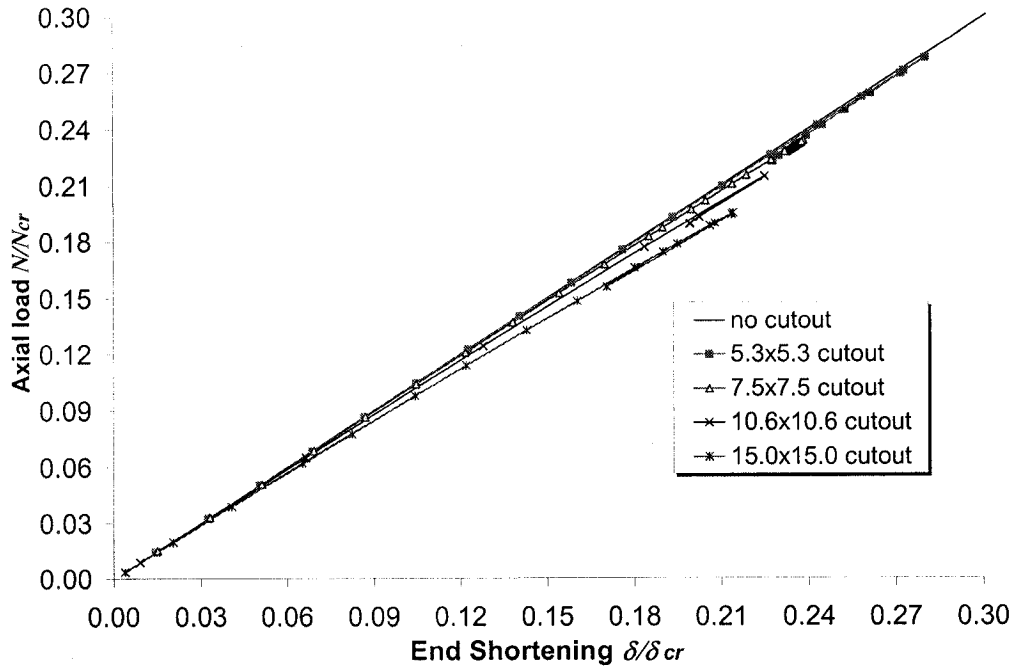

(c) long (L=10D)

Figure 3-13: Load-end shortening behavior of thin (D/t=450), (a) short (L=2D) (b) intermediate-length (L=5D) and (c) long (L=10D) cylindrical shells with cutout of various sizes located at their mid-height

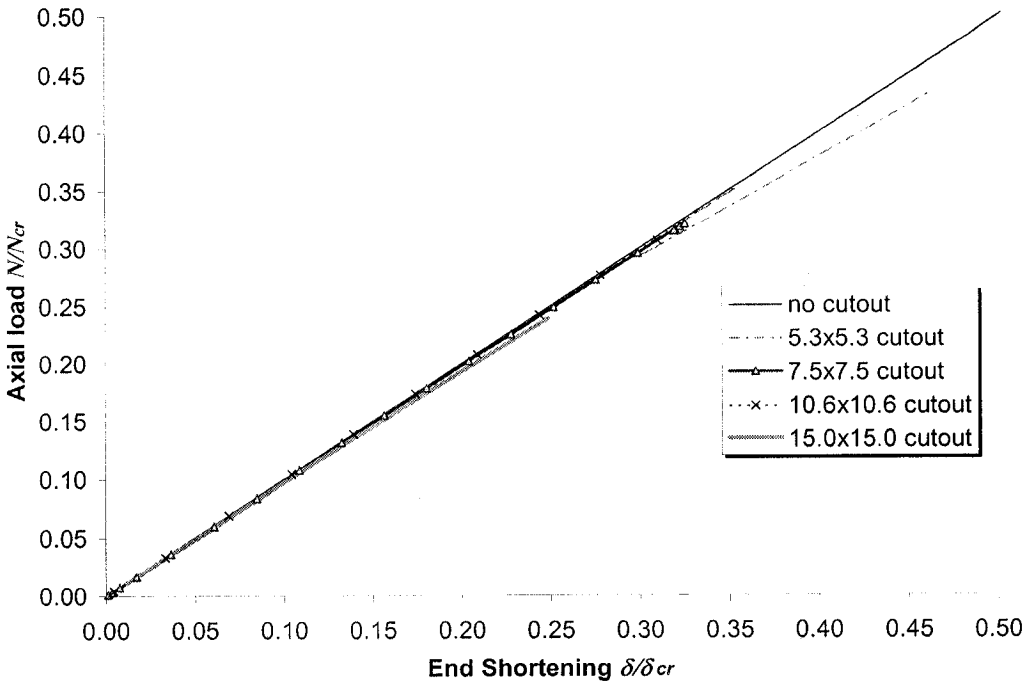

Figure 3-14: Load-end shortening behavior of thin (D/t=450), long (L=10D) cylindrical shells with various sizes cutouts located near loaded end

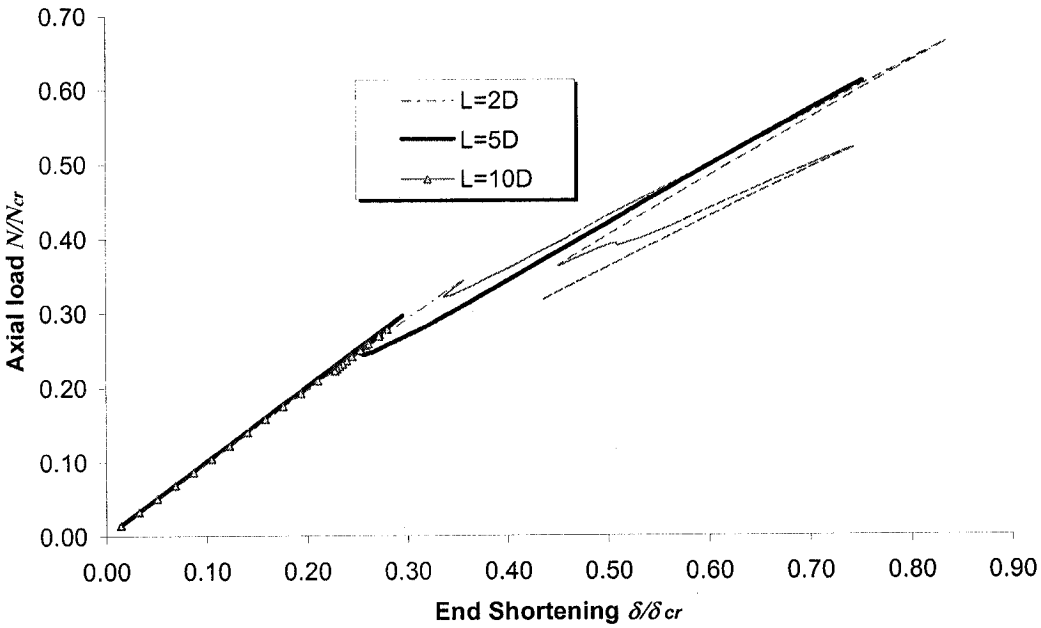

Figure 3-15: Load-end shortening behavior of thin (D/t=450) cylindrical shells of various lengths with a 5.3mmx5.3mm cutout at their mid-height

One can conclude from the above observations that it would be more economical to choose intermediate-length shells (say, 5D), if a cutout is to be present. The cylindrical shells considered in this study exhibited similar first peak buckling strength to that of the short cylindrical shells, as well as a similar highest ratio of the second peak to the first peak load. It was also observed that the longer the cylindrical shells, the more unlikely it would be to see a transition from the lower local buckling mode to the higher local buckling mode.

3.4.3.2 Effect of location of cutout

As seen in the analyses of the moderately thick cylindrical shells, it was observed that the cutout location along the shell's height had a significant influence on the buckling capacity. A study similar to the one mentioned above was conducted for the thin (D/t=450) and long (L=10D) cylindrical shells. For each cutout type, the results were generated when the cutout was located at mid-height, as well as near the loaded end of the shells. For the $7.5mm \times 7.5mm$ cutout, the results are obtained for the cutout located along five different locations along the shell's height.

Table 3.7 summarizes the buckling capacities of the thin (D/t=450), long (L=10D) cylindrical shells having cutouts of various sizes positioned at two different locations (i.e. at mid-height ($L_0 = 0.50L$), and near the loaded end ($L_0 = 0.95L$)). When the cutout is located at mid-height, the cylindrical shell's buckling capacity is almost equivalent to the load level at which the first local buckling occurs. When the cutout is located near the loaded end, a transition from the first local buckling mode to a higher local buckling mode would take place, which could significantly increase the shells' buckling capacity. It is observed that changing the location of the cutout from 0.50L to 0.95L increased the first peak load by 26.3% and 46.2% for cutouts with sizes ranging from 5.3mmx5.3mm to 15.0mmx15.0mm, respectively. Considering the final buckling capacity of the shells with a cutout, it is perceived that by changing the cutout location, one would see an increase in the buckling capacity of the shells by 79.5% - 92.1%, depending on the cutout size.

Table 3-7: The computed buckling loads[b] for thin (D/t=450), long (L=10D) cylindrical shells having a cutout of various sizes located at two different locations along their height

Cutout is at center height ($L_0 = 0.50L$)					
Cutout size (mmxmm)	**no cutout**	**5.3x5.3**	**7.5x7.5**	**10.6x10.6**	**15.0x15.0**
Linear buckling analysis	1.020	0.208	0.138	0.096	0.071
(***A1***)-1st peak in nonlinear buckling analysis [a]	0.968	0.278	0.234	0.215	0.195
(***A2***)-2nd peak in nonlinear buckling analysis [a]	N/A	N/A	N/A	N/A	N/A
Cutout is near the loaded end ($L_0 = 0.95L$)					
Cutout size (mmxmm)	**no cutout**	**5.3x5.3**	**7.5x7.5**	**10.6x10.6**	**15.0x15.0**
Linear buckling analysis	1.020	0.224	0.161	0.129	0.103
(***B1***)-1st peak in nonlinear buckling analysis [a]	0.968	0.351	0.321	0.307	0.285
(***B2***)-2nd peak in nonlinear buckling analysis [a]	N/A	0.534	0.467	0.400	0.350
2nd peak load/1st peak load (***B2/B1***)	N/A	1.522	1.455	1.302	1.228
Ratio of 1st peak load (***B1/A1***)	N/A	1.263	1.372	1.428	1.462
Ratio of 2nd peak load (***B2/A1***)	N/A	1.921	1.996	1.859	1.795

**Note:*

1. The nonlinear analysis involved both geometrical and material nonlinearities (the bilinear material model).

2. All buckling loads are normalized with respect to the critical buckling load obtained from the classical buckling equation [Equation 3.1]

Figure 3.11 shows the load–end shortening behavior of the long thin cylindrical shells (L=10D) with a 5.3mmx5.3mm cutout located at 2 different locations. Figure 3.12 presents similar results for a 10.6mmx10.6mm cutout. It can be observed that when the cutout is located at mid-height, the overall buckling load is below the limit of $0.30\,N_{cr}$. However, when the cutout is located near the loaded end, the final buckling load would increase to $0.55\,N_{cr}$ in those shells with a 5.3mmX5.3mm cutout, and to $0.40\,N_{cr}$ for those with a 10.6mmX10.6mm cutout. Table 3.8 tabulates the buckling load of the long (L=10D), thin (D/t=450) cylindrical shells with a 7.5mmx7.5mm cutout situated at five different locations. It is observed that the buckling capacity increases correspondingly as the cutout moves from mid-height toward the loaded end.

Table 3-8: The computed buckling loads for long (L=10D), thin (D/t=450) cylindrical shells with a 7.5mmx7.5mm cutout at various locations along their height

Location of cutout (L_0/L)	**Linear buckling analysis**		**Nonlinear analysis** (geometrical nonlinearity only)		**Nonlinear analysis** (both geometrical and material nonlinearities)	
	N_{FE} (N/mm)	$\frac{N_{FE}}{N_{cr}}$	N_{FE} (N/mm)	$\frac{N_{FE}}{N_{cr}}$	N_{FE} (N/mm)	$\frac{N_{FE}}{N_{cr}}$
no cutout	16.997	1.02	16.131	0.968	16.131	0.968
0.5	2.297	0.138	3.910	0.235	3.910	0.235
0.65	2.311	0.139	4.000	0.240	3.990	0.239
0.75	2.340	0.140	4.610	0.277	4.530	0.272
0.85	2.403	0.144	4.750	0.285	4.450	0.267
0.95	2.679	0.161	5.270	0.316	5.350	0.321

3.5 Empirical Equations

As discussed, a systematic numerical and experimental study was carried out to investigate the influence of square cutouts on the buckling capacity of aluminum cylindrical shells with various L/D and D/t. The influence of the size and location of a cutout along the length of the shells was also investigated. It is therefore desirable to be able to determine the buckling load reduction factor for such structural components, knowing the material and geometric parameters of the shells.

The results indicated that in general, for the moderately thick shells with a cutout, the transition from a global buckling to a local buckling mode would occur when the cutout is located near the loaded end ($L_0 = 0.9 \sim 0.95L$). Therefore one could define the buckling load reduction factor K_d, as the ratio of the peak buckling load (N_{cutout}) of shells of the moderately thick and thin walls, with a cutout, to the peak buckling load of the perfect shell ($N_{perfect}$) as:

$$K_d = \frac{N_{cutout}}{N_{perfect}} \tag{3.2}$$

The factors are developed using the least-square regression method. Five empirical equations (Equations 3.4 to 3.8) were developed for various shell geometries, following the form:

$$K_d(\alpha,\beta,\gamma) = A + B\alpha + C\beta + D\gamma + E\alpha^2 + F\beta^2 + G\gamma^2 + H\alpha^3 + I\beta^3 + J\gamma^3 + K\alpha\beta + L\alpha\gamma + M\beta\gamma + N\alpha^2\beta + O\alpha\beta^2 + P\beta^2\gamma + Q\beta\gamma^2 \quad (3.3)$$

In the above relation, $\alpha = L/D$, $\beta = a/D$ and $\gamma = L_0/L$, in which L, D, a and L_0 signify the shell's length and diameter, and cutout's size and location, respectively.

The exact form of the resulting equations is summarized in Table 3.9. In summary, Equation (3.4) represents the reduction factor applicable to the moderately thick shells with a cutout at mid-height. Equation (3.5) is the reduction factor for the long, moderately thick shells with a cutout at various locations. Equations (3.6) and (3.7) predict the first and second buckling loads of the thin shells with cutouts located at mid-height, respectively. Finally, Equation (3.8) can be used to predict the buckling capacity of long, thin-walled shells with cutouts situated at various locations. The R^2 values tabulated in Table 3-9 indicate that these equations fit the numerical results very well.

Table 3-9: The empirical equations for predicting the buckling load reduction factors of cylindrical shells

Equation No.	Parameters		Empirical Equations	R^2 value
Eq.-3.4	α	β	$K_d(\alpha,\beta) = 1.24 - 0.102\alpha - 0.720\beta + 0.00677\alpha^2 - 0.0147\alpha\beta + 0.485\beta^2$	98.9%
Eq.-3.5	β	γ	$K_d(\beta,\gamma) = 1.12 - 0.60\beta - 1.14\gamma - 0.26\beta^2 + 1.56\gamma^2 + 0.90\beta^3 - 0.631\gamma^3$	98.6%
Eq.-3.6	α	β	$K_d(\alpha,\beta) = 0.472 - 0.0454\alpha - 0.281\beta + 0.00349\alpha^2 - 0.0498\alpha\beta + 0.833\beta^2$	99.3%
Eq.-3.7	α	β	$K_d(\alpha,\beta) = 1.27 - 0.0363\alpha - 4.71\beta - 0.046\alpha\beta + 6.55\beta^2$	97.8%
Eq.-3.8	β	γ	$K_d(\beta,\gamma) = 0.360 - 1.48\beta + 0.064\gamma + 2.07\beta^2 + 0.914\beta\gamma - 1.45\beta^2\gamma$	96.9%

3.6. Concluding Remarks

A systematic numerical investigation was carried out to examine the influence of square cutouts of various sizes on the nonlinear response of moderately thick and thin aluminum cylindrical shells subjected to axial compression. To that end, shells with various L/D and D/t ratios were considered. The influence of the size and location of cutouts along the length of the shells was also investigated. In addition, an experimental investigation was conducted to examine the behaviour of the moderately thick-walled shells. Very good correlation was observed between the results of the experimental and numerical simulations. The numerical simulations provided valuable insight into the behaviour of the shells, and enabled us to produce empirical equations that could be used to assess the buckling capacity of the shells with square cutouts.

It was observed that the location and size of the cutout could significantly influence the buckling capacity and performance of the shells. The presence of a cutout in the moderately thick-walled shell induced global bending, leading to the collapse of the shells when the cutout was located near the mid-height of the shell, whereas when the cutout was located near the loaded end, local buckling occurred. The numerical results of the moderately thick shells indicated that a cutout located near the loaded end could effectively absorb energy, and redistribute the load more efficiently. Another important finding is that the effective length of the shell could be reduced when the cutout is located near the loaded end due to stress redistribution near the cutout, thereby enhancing the buckling capacity of the shell.

The numerical analyses of the thin shells indicated that the presence of a cutout could significantly reduce the buckling capacity of the shells. For thin shells with a cutout, the linear buckling analyses produced results well below those obtained from the nonlinear analyses. It is worth noting that a transition from lower local buckling modes to higher modes could occur when the cutout was located at mid-height in the short cylinders, and near the loaded end in the long cylinders. Therefore, the performance of such cylindrical shells could be optimized by properly situating the cutout along the length of the shells. Using cutouts as an energy absorbing mechanism could be very useful in the design of cylindrical shells provided that the extent of deformation is acceptable from a serviceability point of view.

3.7 Acknowledgements

The financial support of the Natural Sciences and Engineering Council of Canada (NSERC) in the form of Discovery Grants to the third and fourth authors in support of this work is gratefully acknowledged

3.8 References

1. Arbocz J. and Hol J.M.A.M., (1991). Collapse of axially compressed cylindrical shells with random imperfections, *AIAA Journal,* 29: 2247-2256.

2. Jullien J.F. and Limam A. (1998). Effect of openings on the buckling of cylindrical shells subjected to axial compression, *Thin-Walled Structures*, 31: 187-202.

3. Timoshenko S.P. and Gere J.M., 1961. *Theory of elastic stability* (2nd Edition), McGraw-Hill, New York.

4. Ugural AC, *Stresses in plates and shells*, McGraw-Hill Book Company, 1981

5. Chryssanthopoulos M.K., Elghazouli A.Y. and Esong I.E., (2000). Validation of FE models for buckling analysis of woven GFRP shells, *Composite structures*, 49:355-367

6. Yeh M.K., Lin M.C. and Wu W.T., (1999). Bending buckling of an elastoplastic cylindrical shell with a cutout, *Engineering Structures*, 21: 996–1005.

7. Hilburger M.W., Vicki O.B. and Michael P.N., (2001). Buckling behavior of compression-loaded quasi-isotropic curved panels with a circular cutout, *International Journal of Solids and Structures* 38: 1495-1522.

8. Tafreshi A., (2002). Buckling and postbuckling analysis of composite cylindrical shells with cutout subjected to internal pressure and axial compression load, *International Journal of Pressure Vessels and Piping*, 79: 351-359

9. ANSYS user's manual, 2003. ANSYS Inc. USA

10. Litle W.A., (1964). *Reliability of shell buckling predictions*, The MIT Press, Cambridge, Massachusetts.

Chapter 4 Quasi-static and Dynamic Crushing Behavior of Aluminum and Steel Tubes with a Cutout

Haipeng Han[a], Farid Taheri[a*] and Neil Pegg[b]

[a]Department of Civil Engineering, Dalhousie University, 1360 Barrington Street, Halifax, NS B3J 2Z1
[b]Defense Research and Development Canada , Dartmouth, NS B2Y 3Z7

Submitted to the Journal of "**Thin-Walled Structures**" in May 2006

4.1 Abstract

Tubular members are commonly used as an energy absorber in engineering structures and many such members have a cutout. In this study, the crushing behaviors of tubes with a cutout are characterized and the effects of a cutout on the energy absorption capabilities of these tubes are quantified. Systematic parametric studies were carried out to study the effect of material properties, including yield and ultimate strength of material, strain rate effect, location of cutout, tube length and impact speed on the crushing behaviors and energy absorption capacity of aluminum and steel tubes. First, a numerical model was constructed with a commercial explicit finite element code. It will be first shown that the numerical simulation can produce sufficiently accurate results in an economic manner. Subsequently, the crushing behavior of aluminum and steel tubes with a cutout was experimentally characterized and their energy absorption capacity was evaluated in terms of mean crushing force, peak crushing force and specific energy absorption (SEA). Tubes of various lengths with a cutout located at different locations, subject to both quasi-static and dynamic impact loadings were considered. For steel tubes, the numerical simulation investigated the influence of the strain rate effect and variation in strain hardening ratio of the material. Empirical equations describing the mean and peak crushing forces of aluminum and steel tubes with a cutout were developed

* To whom correspondence should be addressed, email: farid.taheri@dal.ca, Phone:1-902- 494-3935; fax: 1-902-484-6635

using linear and nonlinear regression methods applied to the results obtained from the numerical and experimental studies.

Keywords: Energy Absorption, Tubes, Cutout, Finite Element, Strain Rate, Empirical Equation

4.2 Introduction

An energy absorber is a system that converts, totally or partially, an applied kinetic energy into another form of energy. Energy dissipated in the form of plastic deformation in metallic energy absorbers is irreversible. Generally, the objective of an energy absorber is to dissipate the energy that is applied to the structure, so that the contents or occupants of the structure are protected. An intensive review on the types and behaviors of collapsible impact energy absorbers can be found in reference [1].

Tubular sections are commonly used in engineering structures, such as in fuselages and landing gears in aircrafts, in pipelines and oil/gas risers in offshore oil fields, and in the chassis of automobiles. These structures commonly include some geometric discontinuities, such as attachments of stiffeners and cutouts. Impact events are generated by many means, such as traffic accidents, natural collisions, and earthquakes. Therefore, understanding the crushing behaviors of tubular structures has been the subject of several scholarly works [2-8].

It was shown in previous studies that perfect tubes can be crushed in several modes, such as the concertina (axisymmetric) mode and the diamond (unaxisymmetric) collapse mode. Research has also been done to study the crushing behaviors of tubes made of materials with and without strain hardening and strain rate effects. Previous work has investigated energy absorbers with the shapes of tubes, frusta, multi-cornered columns, struts, sandwich plates, honeycomb cells and other shapes including single-hat and double-hat thin-walled sections [2-12].

It was found that among various cross sections, circular tubes provide the best energy absorption capacity under axial compression [2]. For the quasi-static crushing of circular tubes, Alexander [3] constructed a theoretical model and concluded that the mean crushing force of a circular tube can be evaluated as:

$$P_m = 2(\pi t)^{3/2} R^{1/2} \sigma_0 3^{-1/4} \tag{4.1}$$

where t and R are the thickness and radius of the tube and σ_0 is the yield strength of the material. Magee and Thornton [4] developed an empirical equation to predict the mean crushing force P_m for a general hollow section member based on a large number of axial crushing experiments of different cross section, represented by:

$$P_m = \eta_1 \sigma_u \varphi A_O \tag{4.2}$$

where η_1 is called the structural effectiveness of the section, φ is the ratio of the material volume to the volume enclosed by the section, σ_u is the ultimate strength of the material and A_O is the overall area of the section defined by its outer circumference. For a hollow cylindrical section of radius R and wall thickness t, $\eta_1 = 2\varphi^{0.7}$ and $\varphi = 2t/R$, and equation (4.2) becomes

$$P_m = 4\pi R t \sigma_u \left(\frac{2t}{R}\right)^{0.7} \tag{4.3}$$

Equation (4.3) can be used to accurately predict the mean crushing force in the case of quasi-static crushing of metallic circular-sectioned tubes.

In dynamic crushing involving an intermediate velocity impact, the influence of material strain rate sensitivity must be considered for most materials. Jones [13] replaced the yield strength (σ_0) in equation (4.1) with the dynamic flow stress σ_0' (Eqn. 4)

$$\sigma_0' = \sigma_0 \left(1 + \left(\frac{\dot{\varepsilon}}{D}\right)^{\frac{1}{q}}\right) \tag{4.4}$$

and concluded that the mean crushing force of the tubes subject to dynamic crushing can be expressed as:

$$P_m = 2(\pi t)^{\frac{3}{2}} R^{\frac{1}{2}} \sigma_0 \left[1 + \left(\frac{V_0}{4RD}\right)^{1/q}\right] 3^{-\frac{1}{4}} \tag{4.5}$$

In equations (4.4-4.5) $\dot{\varepsilon}$ is the uniaxial plastic strain rate, t and R are the thickness and radius of the tube, D and q are constants for a particular material and V_0 is the velocity of impact loading.

The forms and amplitudes of geometric imperfections and their effects on the crushing behavior have been widely studied for tubular structures. However, the tubes with a cutout have received minimal attention. Kormi *et al.* [14] numerically investigated the crushing behavior of steel cylindrical shells with a large cutout. Three different loading conditions, including axial compressive load, axial torsion load and bending moment, were considered in their study. The static nonlinear approach, including the linear isotropic work hardening characteristics of the material, was adopted in their work. The geometry of the shell was $D \times t \times L = 150mm \times 1mm \times 610mm$. The size of the opening was about $200mm \times 100mm$. The deformation under each load case was characterized. Sahu [15-16] investigated the dynamic stability of curved isotropic and composite panels having a cutout subject to periodic loading. From his studies, it was concluded that the instability behavior of laminated curved panels with geometric discontinuity was greatly influenced by the size of the cutout, geometry of the panel, ply lay-up orientation and boundary conditions. To the best of the authors' knowledge, there has been no systematic study on the crushing behavior and energy absorption capacity of tubes with a cutout. In such scenarios understanding the effect of a cutout located along various locations on the tubes of different lengths, is very valuable for the design of an energy absorber of this type.

In this study, the response of tubes of various length/radius ratios with a cutout situated at different locations along the length is investigated numerically and experimentally. The behaviors of the tubes are characterized and effects of the cutout on the energy absorption capabilities of tubes are quantified. The general procedure of numerical analysis using LS-DYNA is first introduced. Then an experimental program is developed to experimentally characterize and verify several of the cases considered in the numerical studies. It will be shown that the results from the numerical study are sufficiently accurate in comparison to the corresponding experimental verifications. Empirical equations describing the mean crushing force and the peak crushing initiation force of the tubes with and without a cutout are developed using linear and nonlinear regression methods applied to the results obtained from the parametric numerical study.

4.3 Numerical analysis using the finite element method

The aluminum and steel tubes selected are typical laboratory-scale sizes, with a 40 mm outside diameter and wall thickness (t) of 0.889 mm, as shown in Figure 4.1. A square cutout of 7.5 mm×7.5 mm was created at various locations along the length of the tubes. The distance between the centres of the cutout to the bottom end of the tube is denoted as L_0. The variation of L_0 ($=0.50L-0.95L$) was considered. To alleviate the excessive stress concentration around the cutout, corner chamfers of 0.5 mm radius were introduced around the cutout. As stated in [17], only a few works have investigated the influence of a cutout on the intermediate-length or slender cylindrical shells when subjected to either static or dynamic axial compression loading. In this paper, short (L=2D=80 mm), intermediate-length (L=5D=200 mm) and long (L=10D=400 mm) tubes with and without a cutout, subject to both quasi-static and dynamic axial impact loading conditions are investigated.

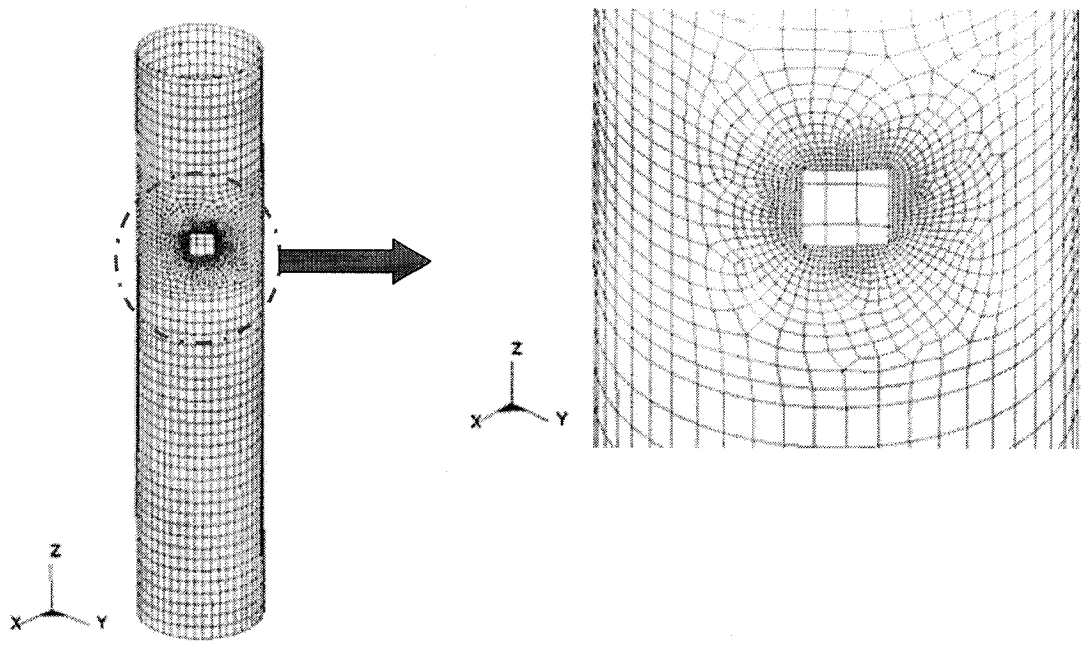

Figure 4-1: FEM model of the aluminum and steel tubes

The commercially available code, LS-DYNA, was used for the numerical simulation. Material model 24 of LS-DYNA (MAT_PIECEWIRE-LINEAR-PLASTICITY) [18], was selected to model both the aluminum and steel tubes. The material models are schematically shown in Figure 4.2. The aluminum tubes are made of

6061-T6 aluminum alloys with the sheet rolling direction in the circumferential direction. The engineering stress-strain curves were determined using six dog-bone tensile specimens machined from the walls of the extruded tubes according to the ASTM B557 standard. Based on the experimental results, a multi-linear isotropic hardening constitutive model was constructed to represent the uniaxial stress-strain behavior of the aluminum material, using the von-Mises flow rule as the yield criterion. Two types of material models, namely MAT1 and MAT2, were chosen to represent the steel in the numerical simulation. These models represent two types of strain hardening ratios, which is defined as the ratio of ultimate strength to the yield strength of the steel materials. MAT1 and MAT2 have the same value of yield strength ($\sigma_0 = 275$MPa). However, MAT1 is high-strength low-alloyed steel, with relatively high strain hardening ratio ($\sigma_u / \sigma_0 = 1.65$), while MAT2 is mild steel, with relatively low strain hardening ratio ($\sigma_u / \sigma_0 = 1.32$). Aluminum has been found to be less strain rate sensitive [13], therefore, the strain rate effect is not considered for the aluminum tube. For both MAT1 and MAT2, the parameters that describe the strain rate effect of the material in equation (4.4) are taken as $D = 40.4$ and $q = 5$ [13].

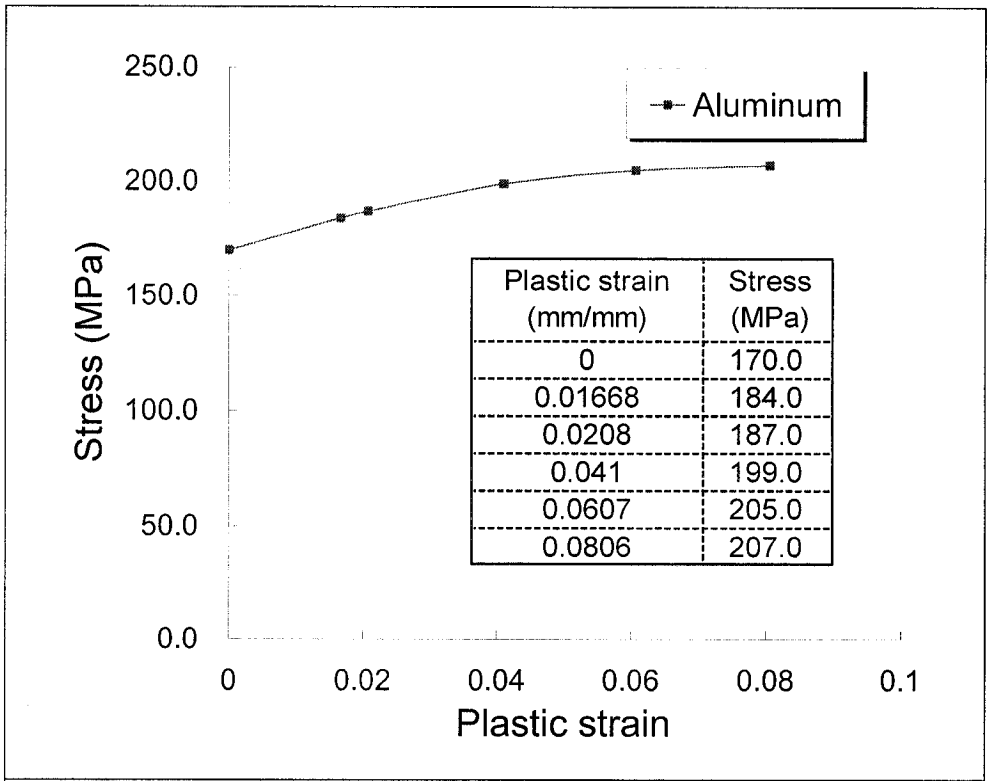

Plastic strain (mm/mm)	Stress (MPa)
0	170.0
0.01668	184.0
0.0208	187.0
0.041	199.0
0.0607	205.0
0.0806	207.0

(a) Aluminum

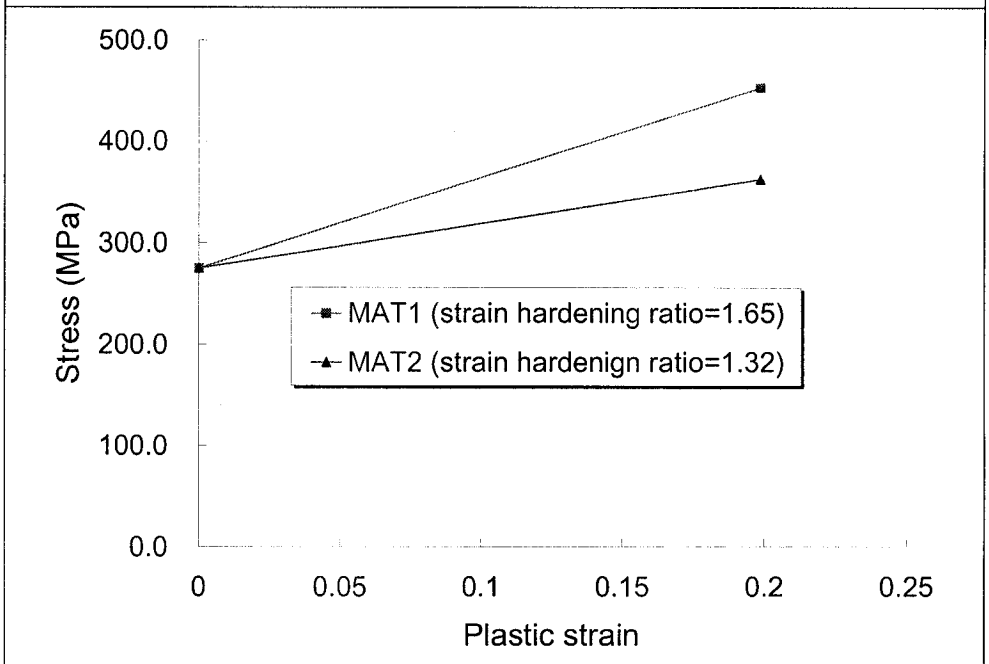

(b) Steel

Figure 4-2: Material models of the aluminum and steel tubes

Belyschko-Tsay quadrilateral shell elements [18] were used to model the wall of both aluminum and steel tubes. The meshed shell elements were located at the mid-plane of the tube's wall.

In the modeling of quasi-static crushing, the bottom end of the tube was assumed to be built-in and was constrained in all degrees of freedom. The upper end was free and subject to compression by the rigid loading plate. The loading plate was modeled as a rigid wall and its mass was assumed to be 100 Kg. In the simulation of a quasi-static crushing event, the mass of both loading plate and tube can be scaled up to a certain limit for the purpose of computational saving, while still maintaining the quasi-static condition [19, 20]. In this study, the density of the loading plate and tube were all scaled-up by a factor of 1000. It was shown that the ratio of total kinetic energy (KE) to the total internal energy was less than 5% over the crushing process, thus maintaining the quasi-static condition. The loading plate was displaced using *BOUNDARY_ PRESCRIBED_MOTION_RIGID at a constant loading rate of 100 mm/sec. Two types of contact algorithms were used to simulate the boundary conditions of quasi-static crushing. The first one was to simulate the interface between the loading plate and the upper end of the tube using the *CONTACT_CONSTRAINT _NODES_TO_SURFACE command of LS-DYNA. The interface force between the loading plate and the tube was used to obtain the force-displacement responses. The other was to prevent the tube from drifting on the bottom end; this was done by employing the *RIGIDWALL_ GEOMETRIC_FLAT command in LS-DYNA, by which a flat rigid surface was defined beneath the tube. In this way the tube would always stay on the top of this flat surface, even if the tube started folding at the bottom end.

For simulation of the dynamic axial crushing, the same boundary conditions were applied to the bottom end of the tubes and the upper end was set free in all degree of freedom. The tube was impacted by the loading plate with certain downward velocity. The initial velocity of the loading plate was introduced by the *INITIAL_VELOCITY_RIGID_BODY command. In both quasi-static and dynamic crushing simulations, a self-contact algorithm, invoked by the *CONTACT_ AUTOMATIC_SINGLE_SURFACE command was used to prevent interpenetration during the folding of the tubes.

4.4 Experimental program

Test specimens were cut from commercially available aluminum tubes of intermediate-length (L=5D). A square cutout of 7.5 mm×7.5 mm was carefully drilled and machine-finished along three different locations on the tubes, at locations L_0 =0.50L, 0.75L and 0.95L.

4.4.1 Quasi-static crushing test

These tests were conducted using a MTS loading frame controlled by Instron 8500 electronics to study some of the cases investigated in the numerical simulations. The crushing speed was 10 mm/min in the test. The specimens were constrained by a steel sleeve fixture at their bottom end while the top end was set free and subject to compression by the rigid loading plate, mimicing the fixed-free boundary condition used in the numerical simulations. The crushing force versus crushing displacement response was recorded. Three identical specimens were tested for each case, and the average of the data was used for comparison purpose.

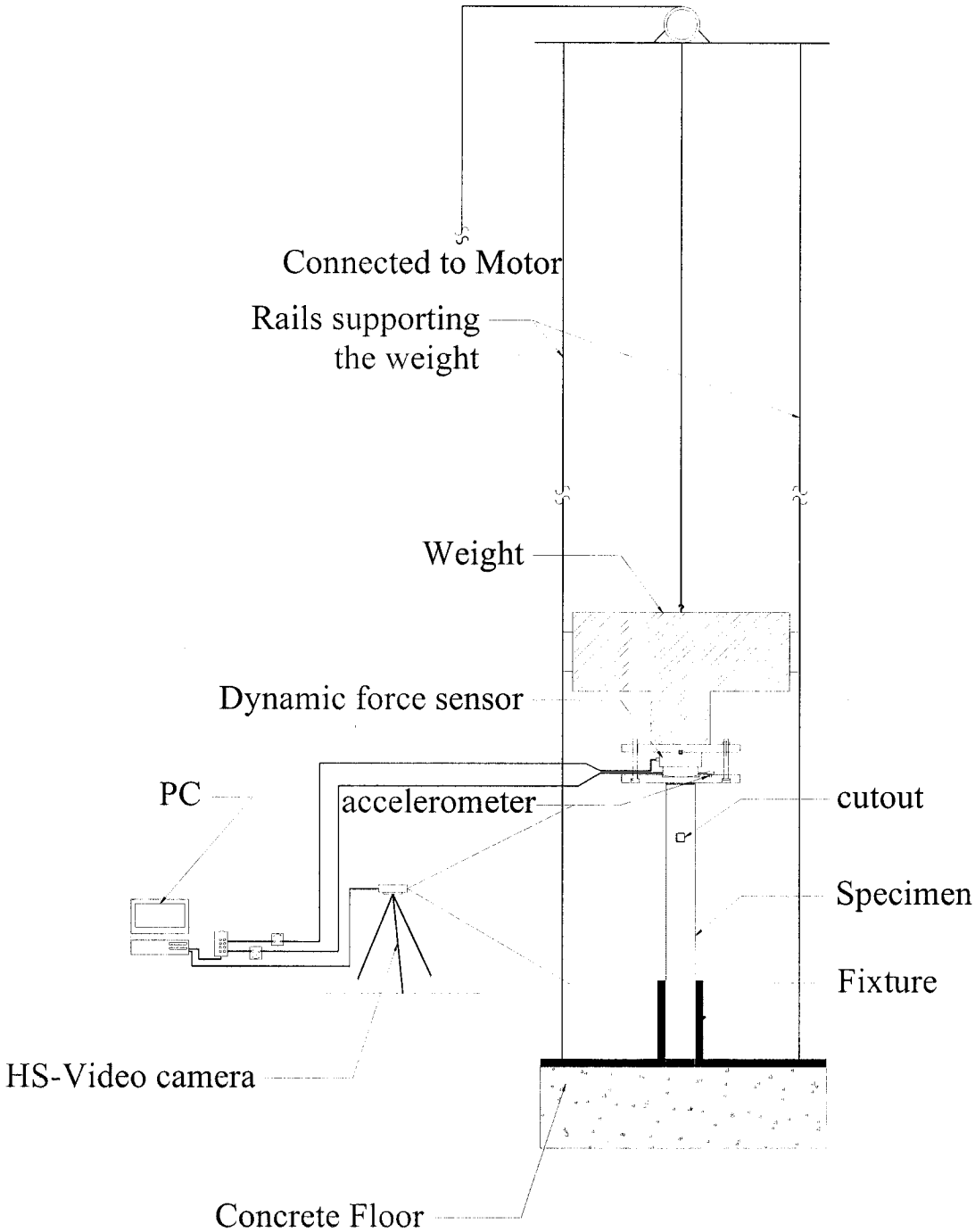

Figure 4-3: Schematic impact testing system

4.4.2 Impact load testing

The impact testing system (ITS) was fabricated in our research laboratory, as shown in Figure 4.3. The drop tower testing machine controlled by a motor is about 3.25 meters high, which results in a maximum impact velocity of 8.0m/s. A dynamic force sensor (Model 200C50, 50000 lb capacity, PSB Piezotronics Inc. Depew, NY) was used to catch the instantaneous compression force. Three quartz shear model ICP accelerometers (Model 353B15) were mounted on the top of the loading plate to measure the acceleration during the impact event. The signals from the force sensor and accelerometers were directed through an ICP signal conditioner, and were then collected by an 8 channel, 12 bit, 200ks/s data acquisition card (NI PCI-6023E, E-series multifunctional) connected to the computer. A high speed video camera (Photron USA Inc., San Diego, CA) connected to the built-in data acquisition card of the same computer was also used to record the crushing event of the tubes. The maximum frame rate of the high speed camera was 10000 Frame/sec. The Motion Tool software (Photron USA Inc., San Diego, CA) associated with the high speed video camera, was used to synchronize the real time image with the corresponding signal from the force sensor and accelerometers. By tracking the motion of the loading plate via the recorded images, the crushing distance versus time history could be constructed. This was synchronized with the force versus time history recorded by the dynamic force sensor. Thus, the load-crushing displacement curve could be obtained.

4.5 Results and discussions

The numerical simulations of the crushing event were carried out for tubes with and without a cutout. Tubes of three different length/diameter ratios (L/D=2, 5 and 10), thereafter called 2D, 5D and 10D tubes, were analyzed. The 7.5 mm×7.5 mm cutout was located at mid-height ($L_0 = 0.50L$) of the 2D tubes. A cutout of the same size was located at three different locations for the 5D tubes ($L_0 = 0.50$L, 0.70L and 0.90L) and the 10D tubes ($L_0 = 0.50$L, 0.75L and 0.95L). Therefore, the cutout was essentially located at the upper half of the tubes. Both quasi-static and dynamic crushing with various impact

velocities were carried out for each tube. The velocity of impact varied between 6 m/s~20 m/s. In each case, the crushing force versus crushing displacement response and the crushed profile information were used to identify the crushing mode. The absorbed energy, peak crushing force, mean crushing force within certain crushing displacement and the specific energy absorption (SEA) were used to evaluate the energy absorption capability of the tubes.

The experimental program was carried out to verify a set of selected cases in the numerical studies. The cases studied in the experimental program included the 5D aluminum tubes with and without a cutout. The tests included quasi-static and dynamic tests. Due to the height limitation of the drop tower and capacity of the impact testing system (ITS), the maximum capacity of the dropping mass and velocity were at 60 kg and 8 m/s, respectively. Therefore all of the tubes are impacted by a drop mass of 60 kg and velocity of 7 m/s, so that the total energy input to the system was $E = \frac{1}{2}mv^2 = 1470J$. It was noted that rebound impacts would occur after the first impacting stroke; nonetheless, in all tests, only the information corresponding to the first crushing stroke was of interest. Although the high speed video camera and sensors recorded the entire event including the multiple impacts after the first impulse, the analyses were carried out only with reference to the first crushing stroke.

Figures 4.4~4.9 illustrates the crushing force versus displacement responses of tubes that have been simulated. Tables 4.1 and 4.2 tabulate the summary of the crushing response and energy absorption capacity of the aluminum and steel tubes, respectively, with and without a cutout obtained through the numerical analyses. The results in Tables 4.1 and 4.2 indicate that the crushing modes of all simulated tubes could be classified into two categories; that is, a global buckling (GB) mode or a progressive crushing (PC) mode. In the PC category, depending on the variation of tube length and location of the cutout, the mode could be further classified into 4 sub- modes, namely PC1, PC2, PC3 and PC4. The descriptions of these crushing modes are listed at the end of each table. Section 4.5.1 provides the detail of the experimental results and comparisons with the corresponding numerical simulations. Section 4.5.2 and 4.5.3 presents the results and

discussions on numerical crushing simulation of the aluminum and steel tubes with a cutout.

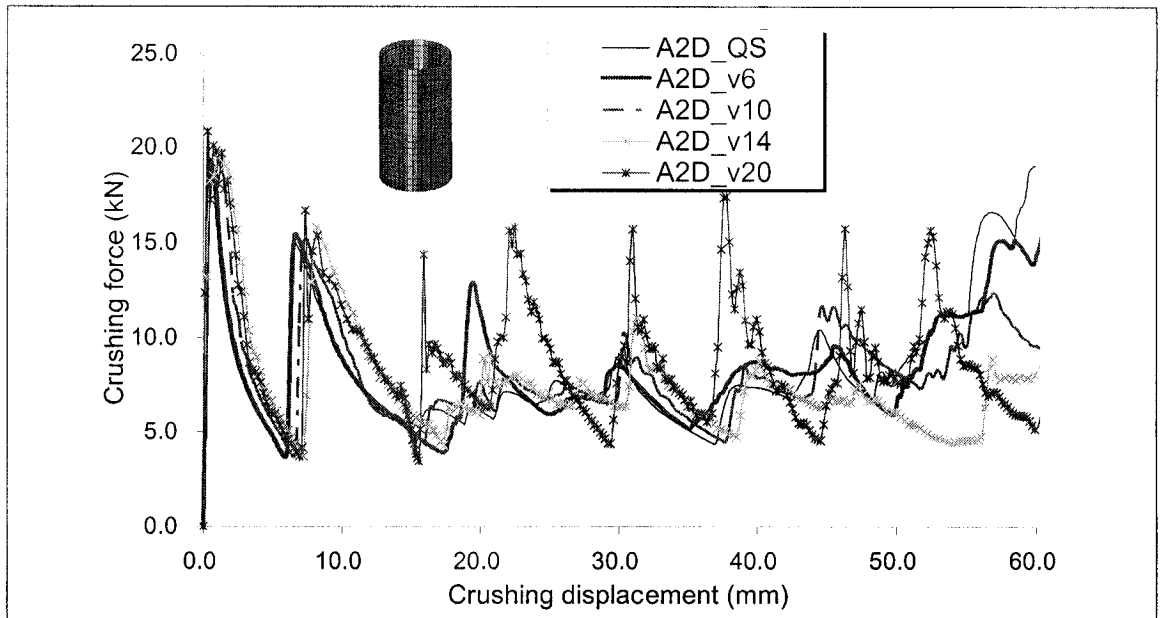

(a) 2D aluminum tube without cutout

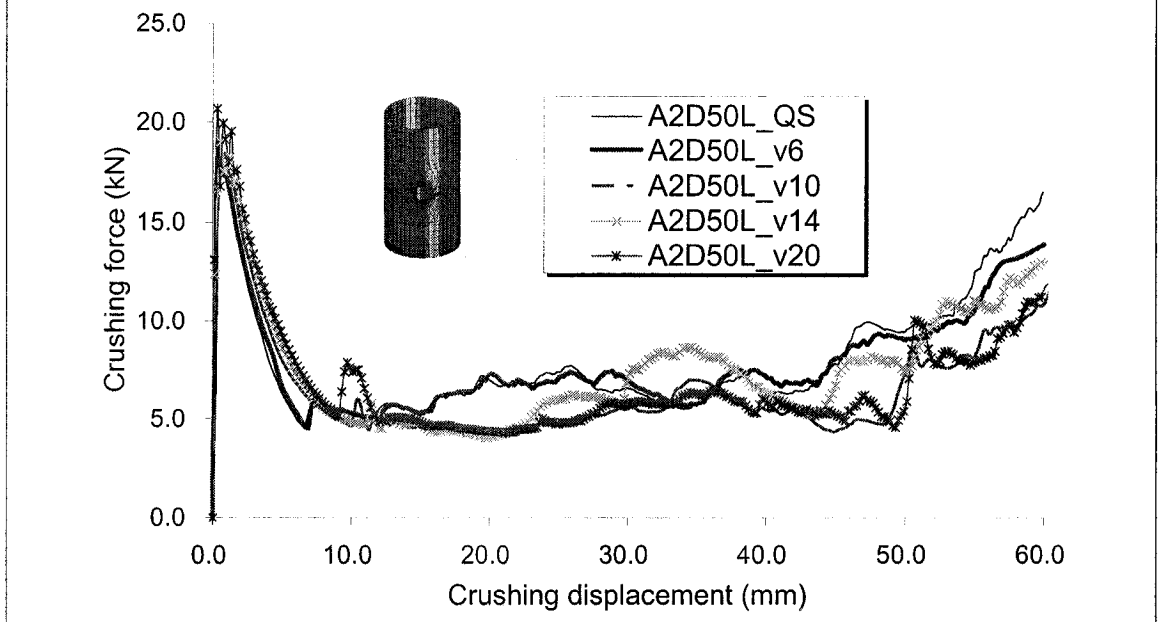

(b) 2D aluminum tube with cutout at mid-height

Figure 4-4: Crushing force versus crushing displacement response of the 2D aluminum tubes with and without a cutout subject to quasi-static and dynamic crushing

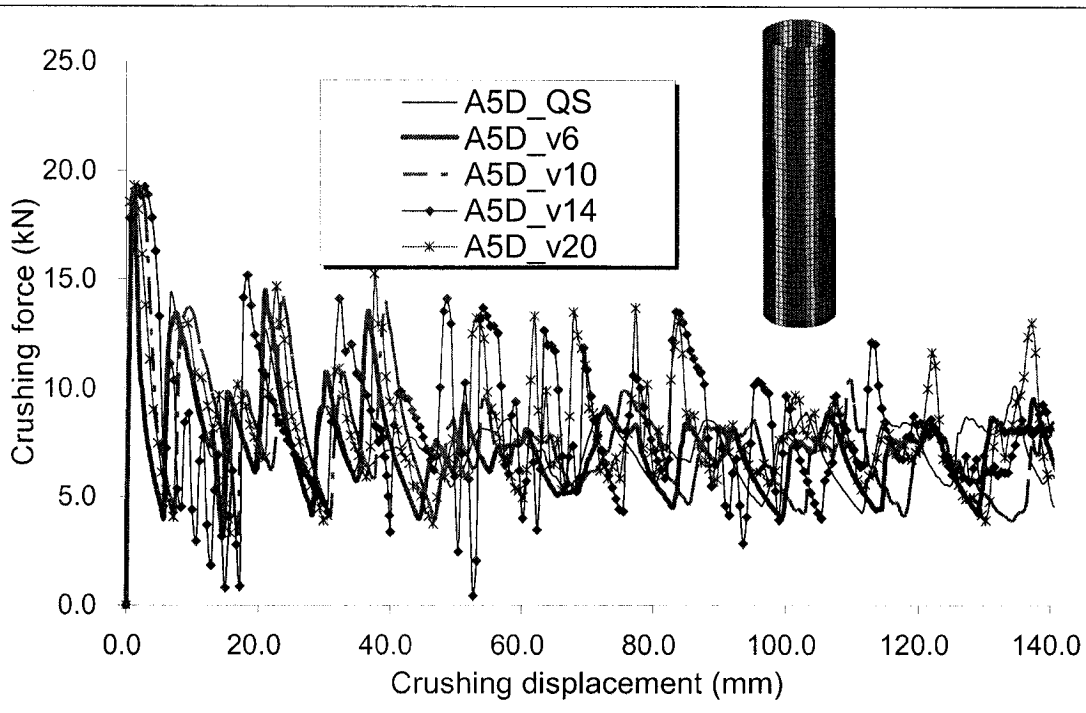

(a) 5D aluminum tube without cutout

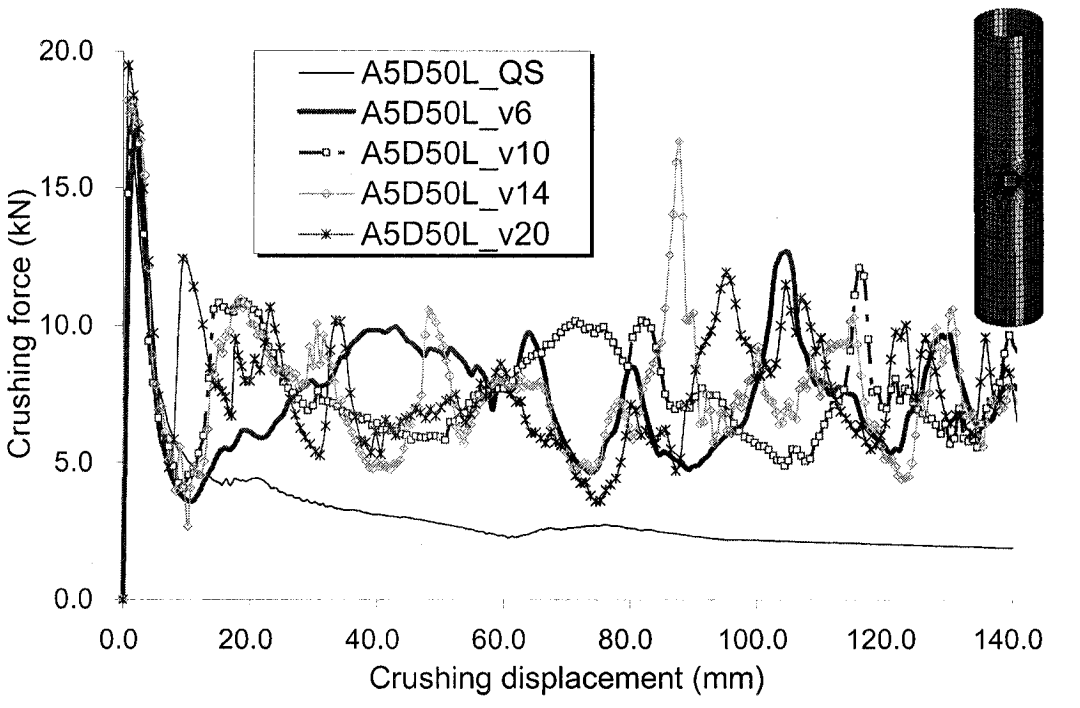

(b) 5D aluminum tube with a cutout at 50% height

(c) and (d) on next page

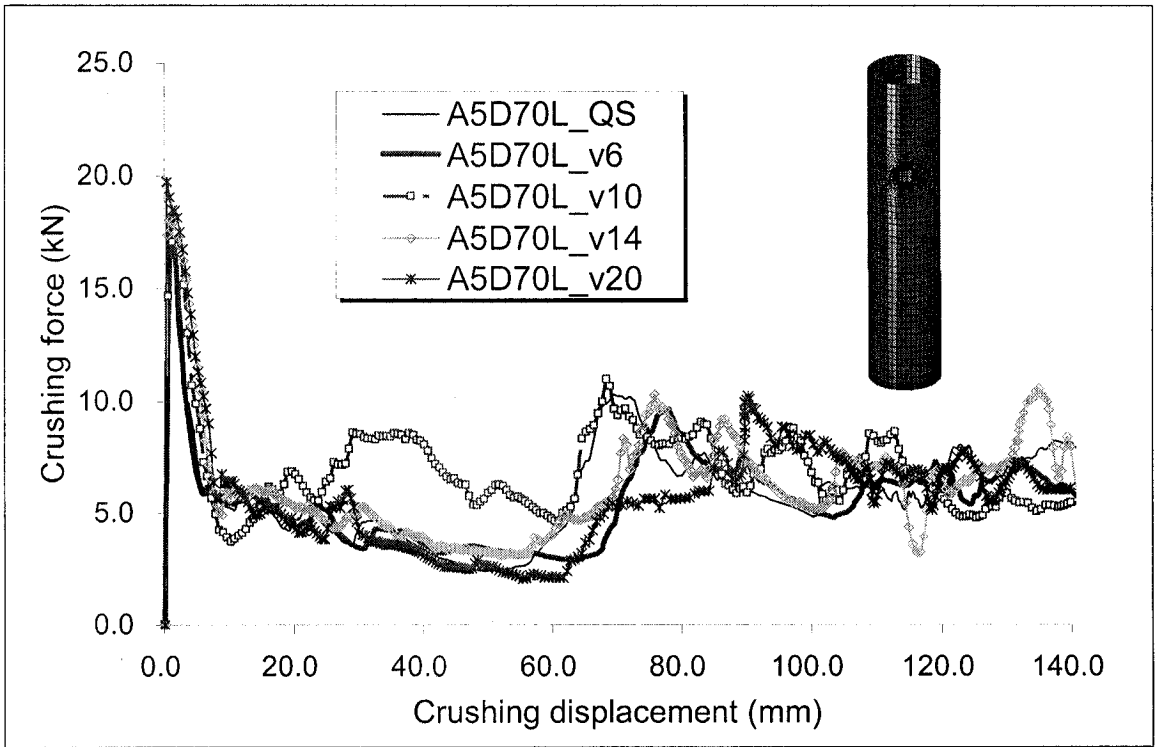

(c) 5D aluminum tube without cutout at 70% height

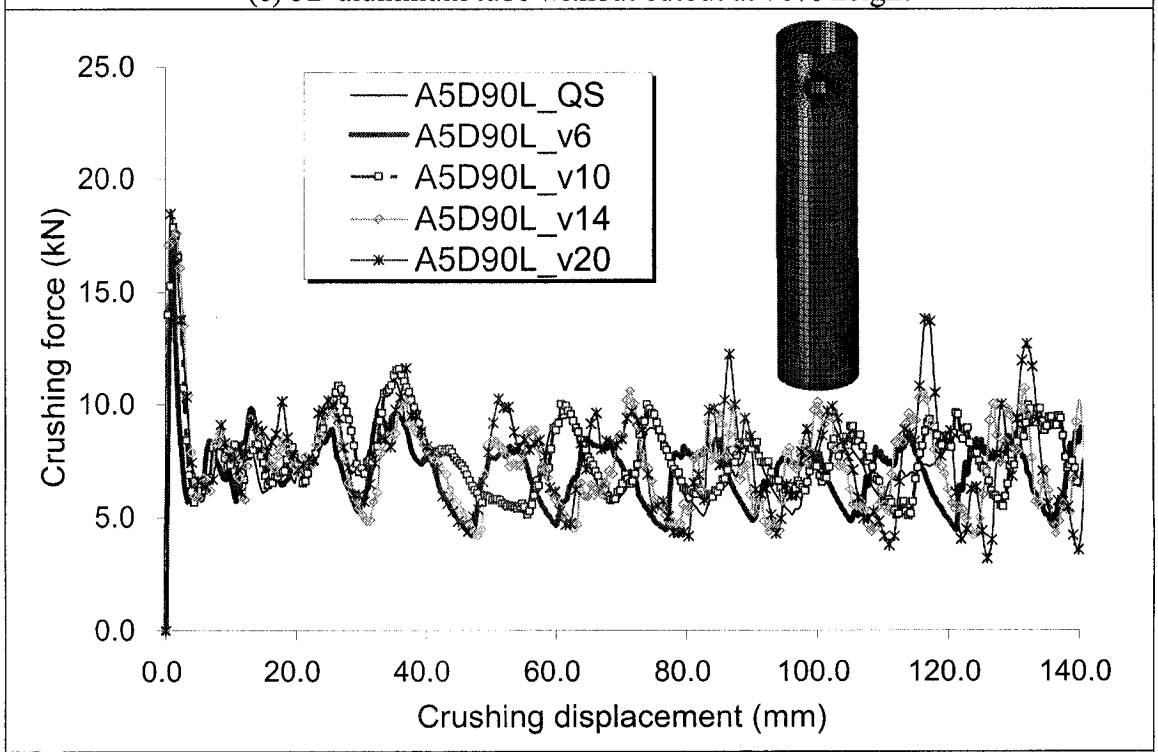

(d) 5D aluminum tube with a cutout at 90% height

Figure 4-5: Crushing response of the 5D aluminum tubes with and without a cutout subject to quasi-static and dynamic crushing

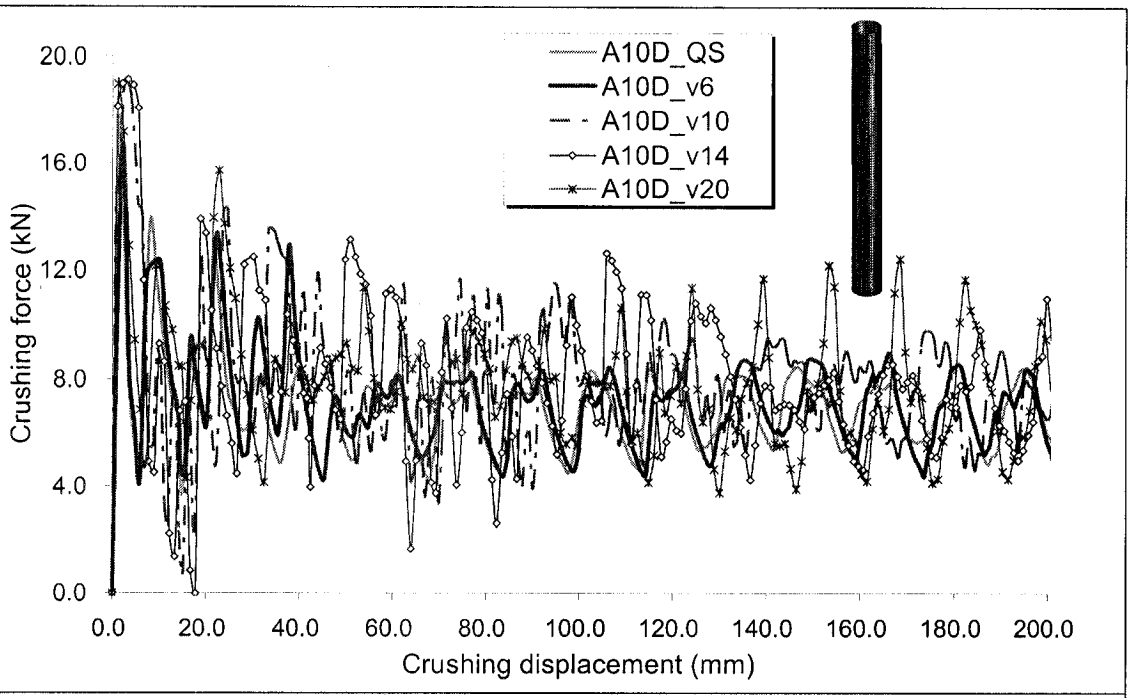

(a) 10D aluminum tube without cutout

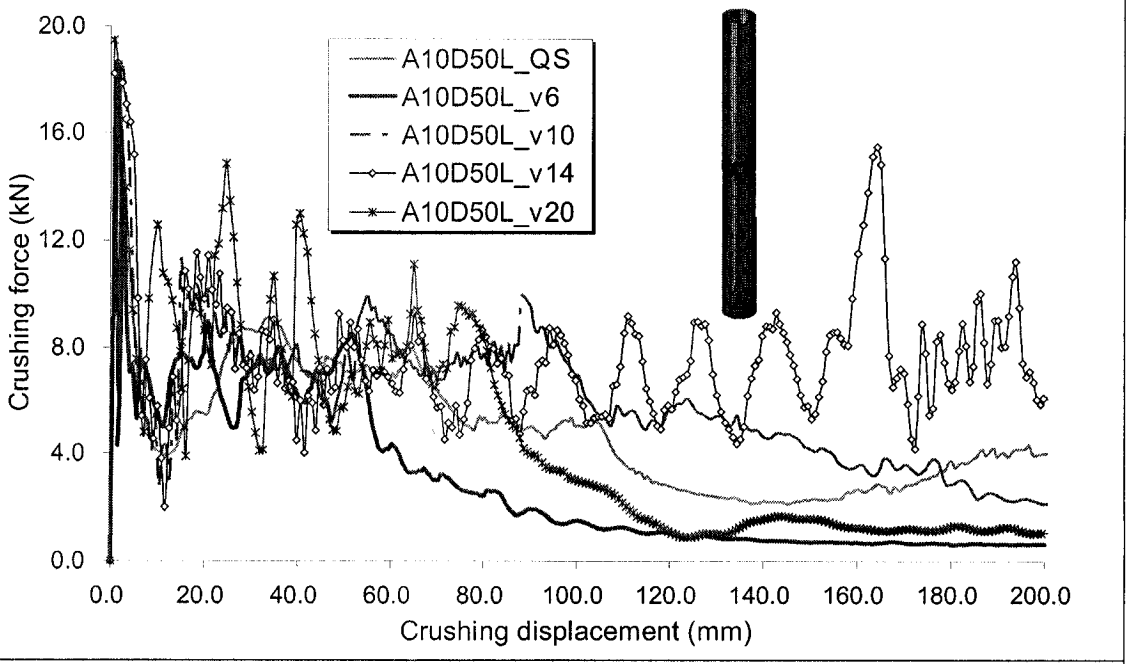

(b) 10D aluminum tube with a cutout at 50% height

(c) and (d) on next page

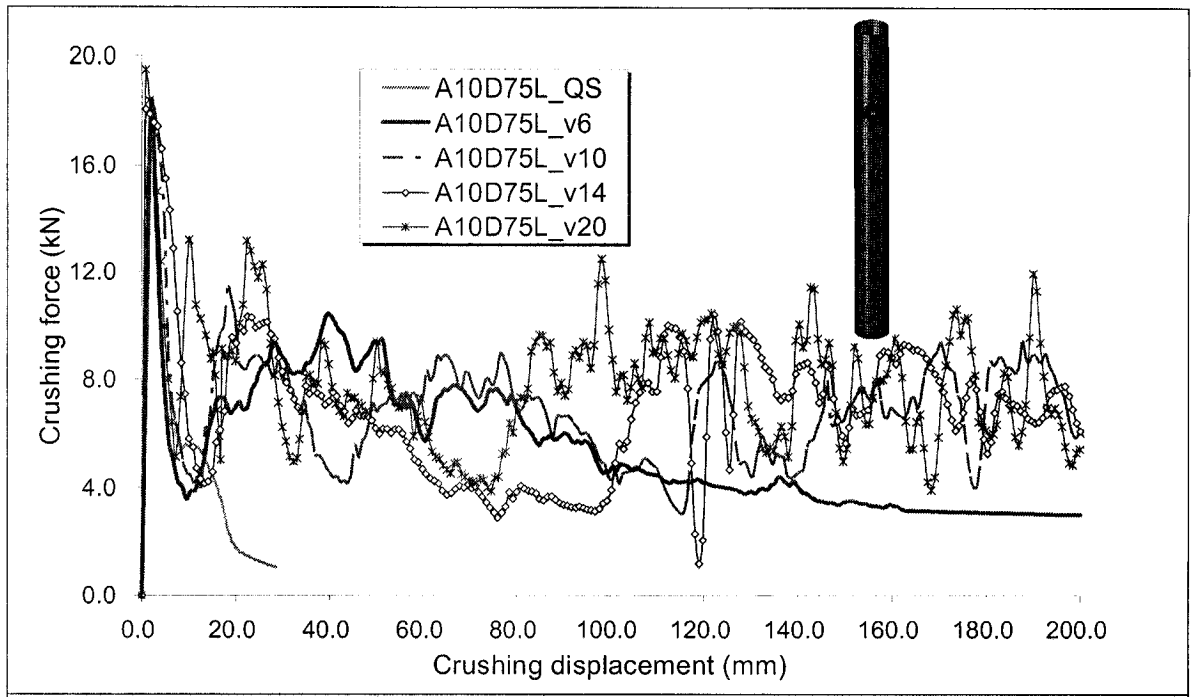

(c) 10D aluminum tube without cutout at 75% height

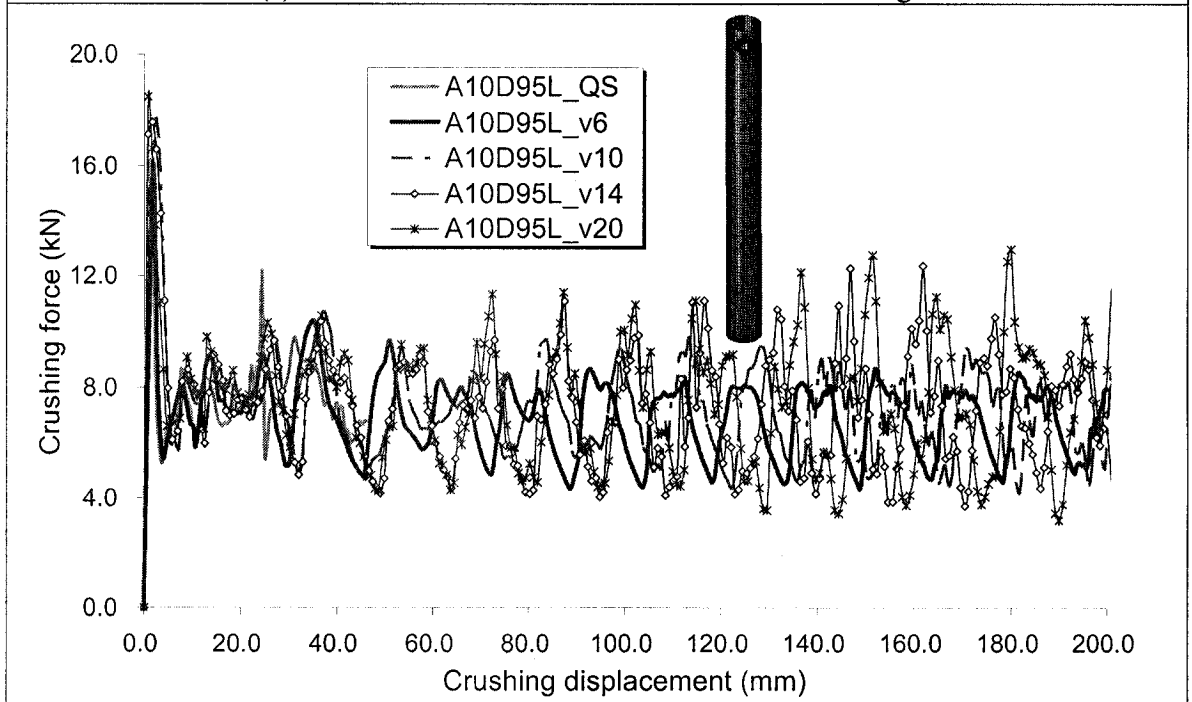

(d) 10D aluminum tube with a cutout at 95% height

Figure 4-6: Crushing response of the 10D aluminum tubes with and without a cutout subject to quasi-static and dynamic crushing

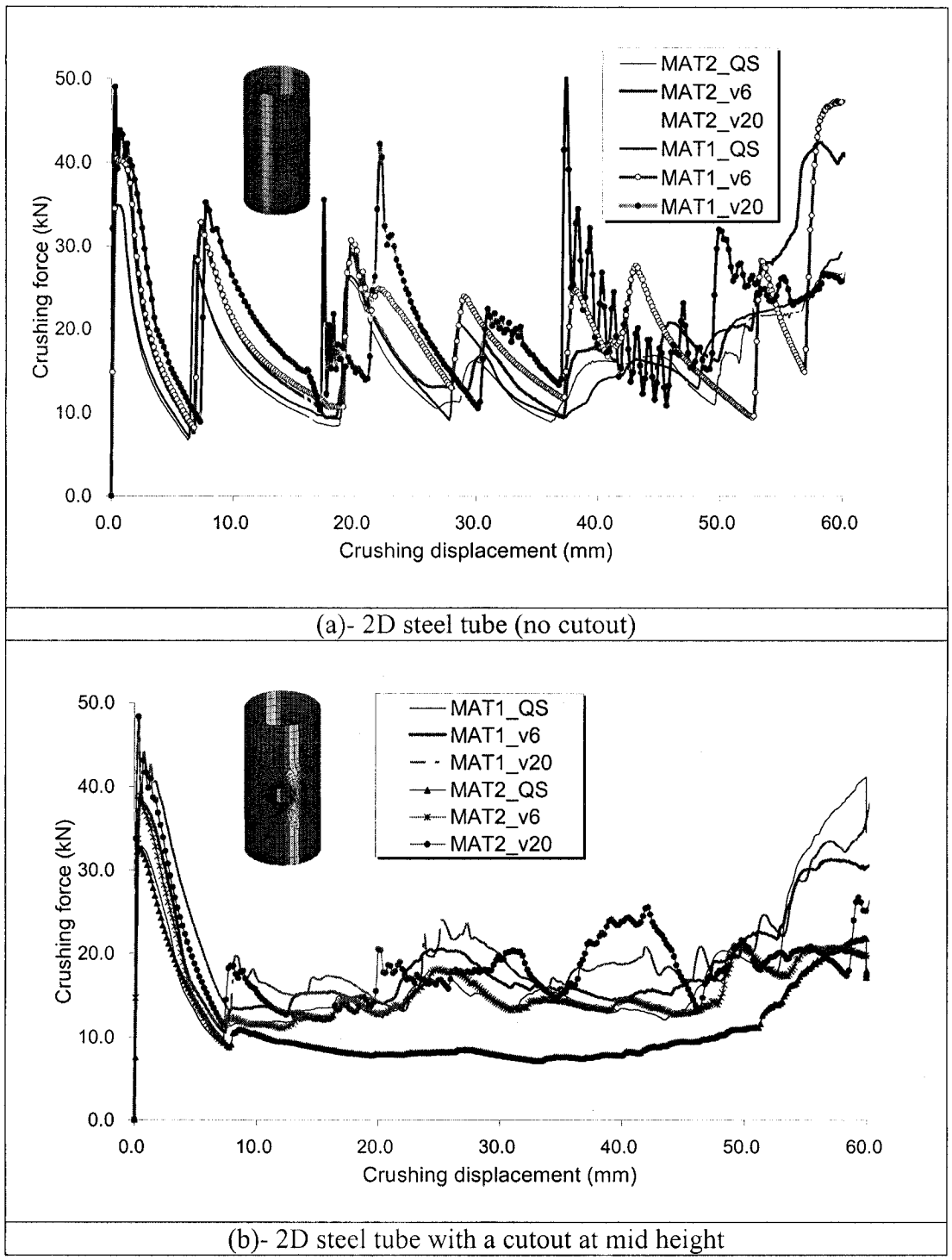

(a)- 2D steel tube (no cutout)

(b)- 2D steel tube with a cutout at mid height

Figure 4-7: Crushing responses of the 2D steel tubes with and without a cutout subject to quasi-static and dynamic crushing

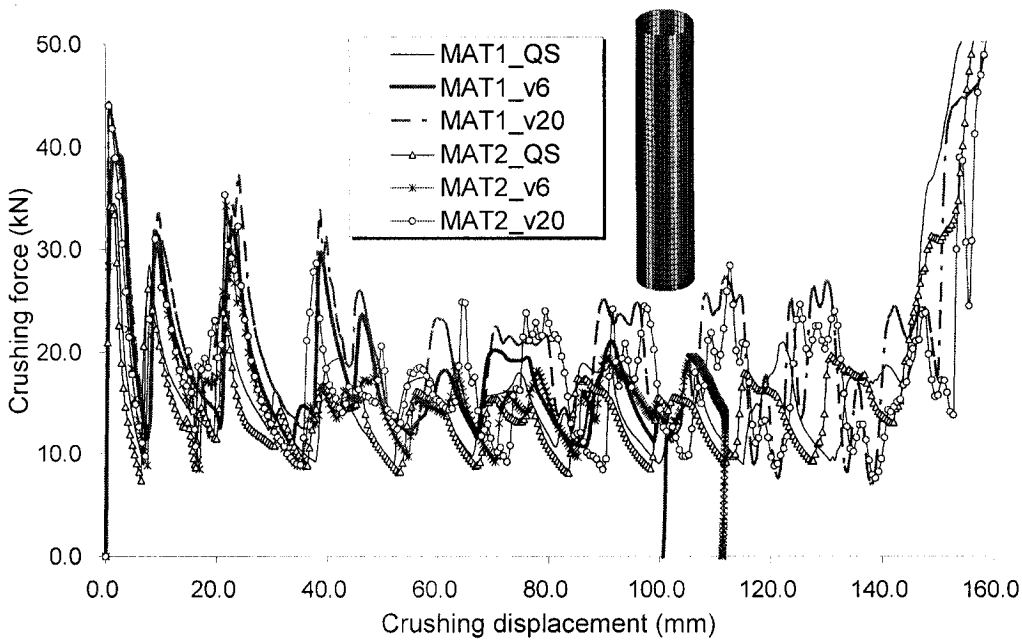

(a)- 5D steel tube (no cutout)

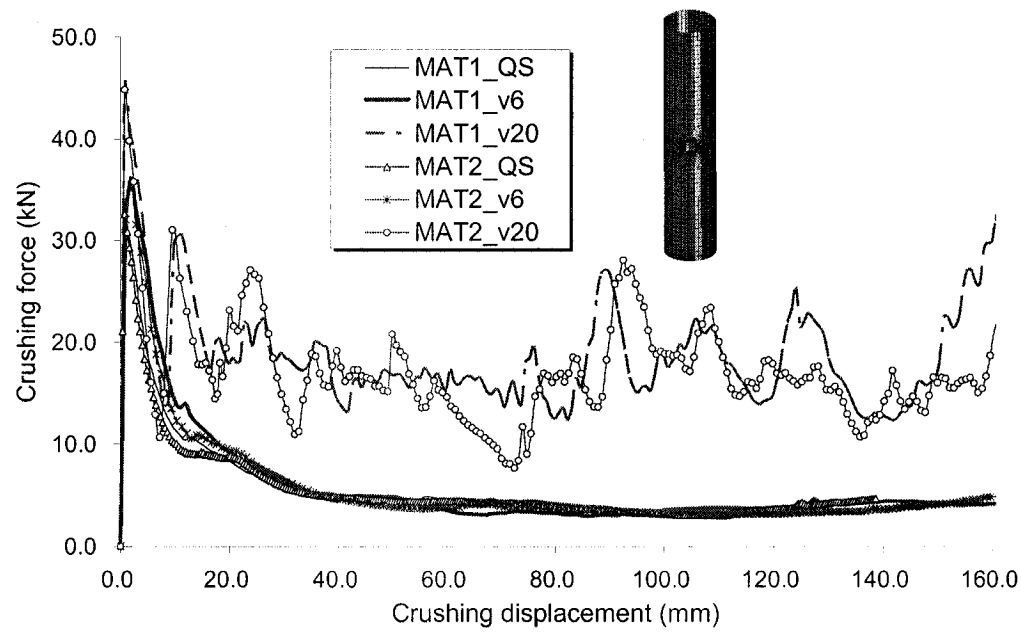

(b)- 5D steel tube with a cutout at mid height

--- (c) to be continued at next page

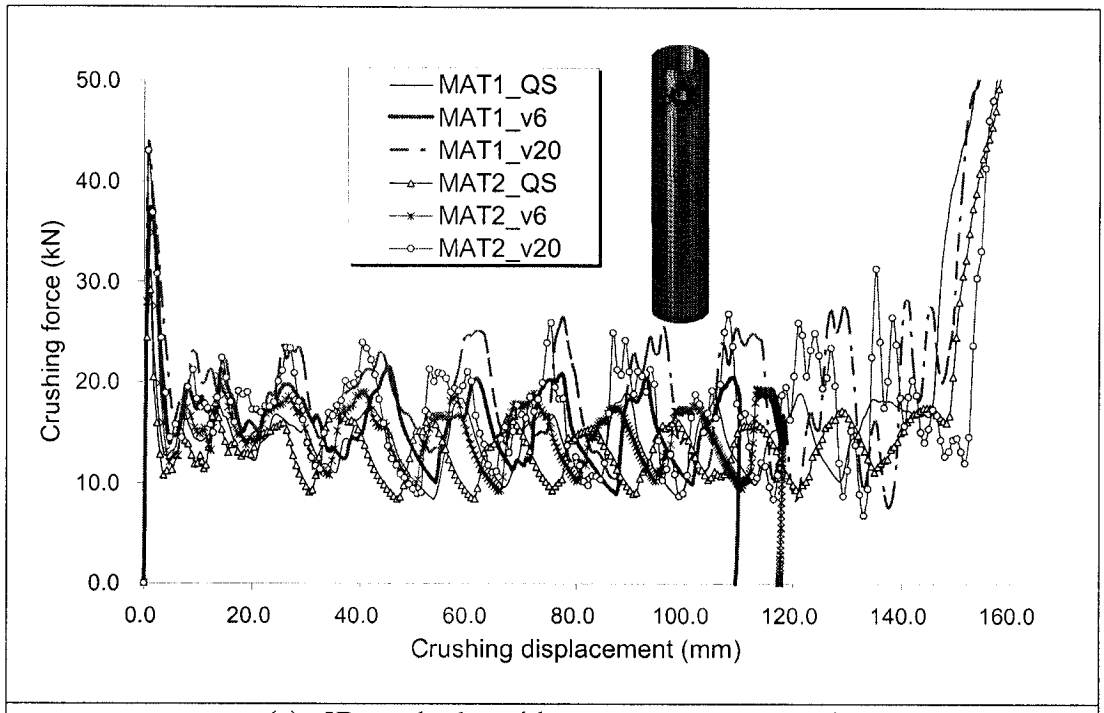

(c)- 5D steel tube with cutout at near top end

Figure 4-8: Crushing responses of the 5D steel tubes with and without a cutout subject to quasi-static and dynamic crushing

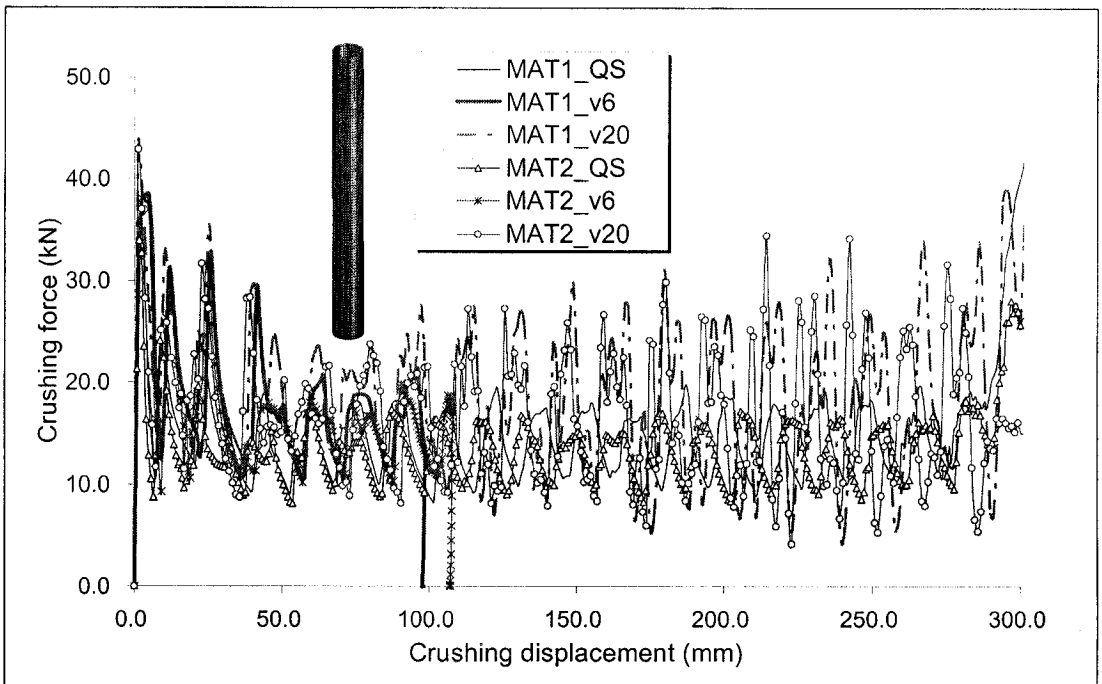

(a)- 10D steel tube (no cutout)

(b) and (c) on next page

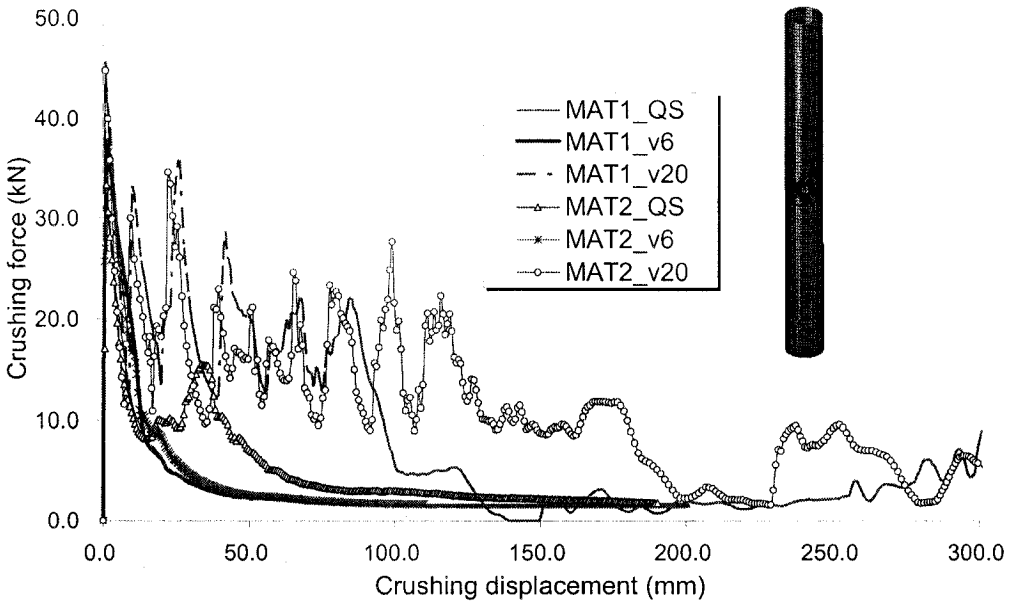

(b)- 10Dsteel tube with a cutout at mid height

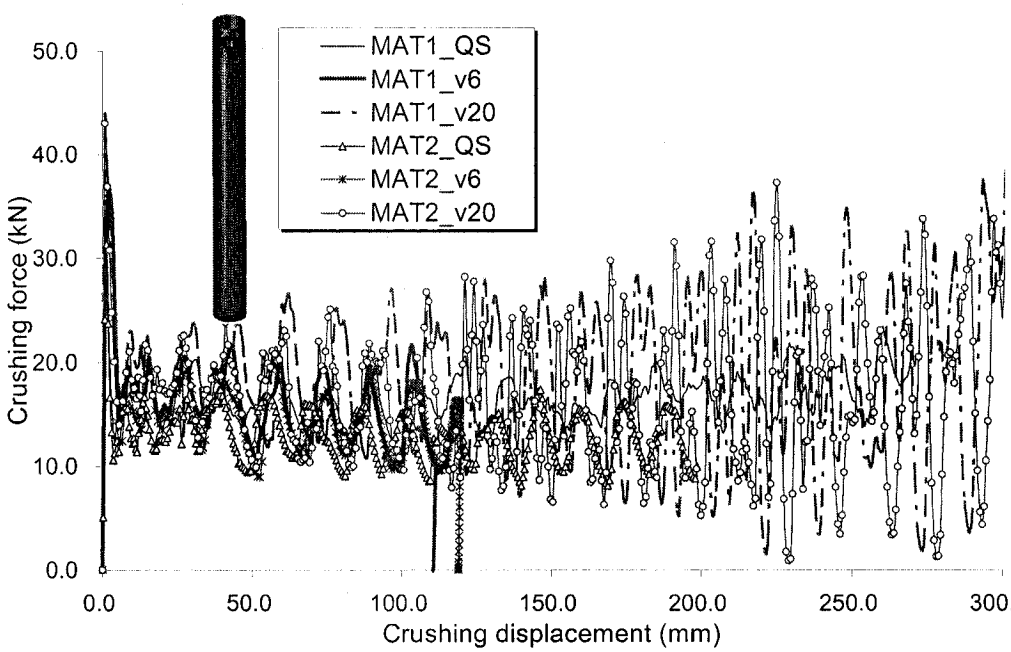

(c)- 10Dsteel tube with a cutout at near top end

Figure 4-9: Crushing responses of the 10D steel tubes with and without a cutout subject to quasi-static and dynamic crushing

Table 4-1: Summary of numerical crushing analysis on aluminum tubes

Tube Length	cutout location	Loading condition	response time* (ms)	Absorbed Energy * (J)	Peak crushing force-P/ (KN)	SEA (J/Kg)*	Mean crushing force-Pm* (KN)	crushing mode
2D	none	Q-S	none	504.00	19.10	20886.48	8.26	PC2
2D	none	D_v=6	10.80	507.00	19.33	21010.80	8.33	PC2
2D	none	D_v=10	6.16	498.00	19.54	20637.83	8.14	PC2
2D	none	D_v=14	4.36	462.00	19.62	19145.94	7.42	PC2
2D	none	D_v=20	3.03	546.00	20.84	22627.02	8.81	PC2
2D	L0=0.50L	Q-S	none	479.00	17.97	19850.44	7.40	PC3
2D	L0=0.50L	D_v=6	10.66	474.00	18.85	19643.23	7.60	PC3
2D	L0=0.50L	D_v=10	6.14	391.00	18.42	16203.60	6.46	PC3
2D	L0=0.50L	D_v=14	4.33	458.00	18.99	18980.17	7.58	PC3
2D	L0=0.50L	D_v=20	3.02	412.00	20.68	17073.87	7.01	PC3
5D	none	Q-S	none	1040.00	18.41	17239.63	7.32	PC2
5D	none	D_v=6	28.38	1040.00	19.07	17239.63	7.25	PC2
5D	none	D_v=10	14.95	1070.00	19.23	17736.93	7.44	PC2
5D	none	D_v=14	10.36	1160.00	19.25	19228.82	8.11	PC2
5D	none	D_v=20	7.08	1140.00	19.33	18897.29	8.07	PC2
5D	L0=0.50L	Q-S	none	446.00	17.24	7393.15	3.19	GB
5D	L0=0.50L	D_v=6	28.30	1050.00	17.13	17405.40	7.46	PC1
5D	L0=0.50L	D_v=10	14.72	1090.00	18.21	18068.46	7.66	PC1
5D	L0=0.50L	D_v=14	10.28	1080.00	18.22	17902.69	7.68	PC1
5D	L0=0.50L	D_v=20	7.12	1090.00	19.50	18068.46	7.67	PC2
5D	L0=0.70L	Q-S	none	821.00	17.18	13609.36	6.01	GB &PC2
5D	L0=0.70L	D_v=6	23.90	788.00	18.22	13062.34	5.81	GB &PC2
5D	L0=0.70L	D_v=10	14.58	985.00	17.48	16327.92	6.97	PC1
5D	L0=0.70L	D_v=14	10.11	887.00	18.06	14703.42	6.38	GB &PC2
5D	L0=0.70L	D_v=20	6.34	823.00	19.75	13642.52	6.04	GB &PC2
5D	L0=0.90L	Q-S	none	1033.00	16.75	17123.59	7.38	PC2
5D	L0=0.90L	D_v=6	28.08	993.00	17.28	16460.53	7.03	PC2
5D	L0=0.90L	D_v=10	14.88	1090.00	17.87	18068.46	7.72	PC2
5D	L0=0.90L	D_v=14	10.28	1040.00	17.64	17239.63	7.37	PC2
5D	L0=0.90L	D_v=20	7.12	1080.00	18.49	17902.69	7.64	PC2
10D	none	Q-S	none	1420.00	17.65	11769.36	7.00	PC2
10D	none	D_v=6	46.20	1440.00	16.72	11935.13	7.07	PC2
10D	none	D_v=10	22.00	1610.00	19.06	13344.14	7.94	PC4
---To be continued								

Table 4.1 Continued

10D	none	D_v=14	15.04	1630.00	19.13	13509.90	7.98	PC4
10D	none	D_v=20	10.20	1610.00	18.95	13344.14	7.95	PC2
10D	L0=0.50L	Q-S	none	980.00	17.49	8122.52	4.91	GB
10D	L0=0.50L	D_v=6	39.60	608.00	18.64	5039.28	3.31	PC2-->GB
10D	L0=0.50L	D_v=10	21.20	1220.00	18.46	10111.71	6.09	PC1-->GB
10D	L0=0.50L	D_v=14	14.94	1540.00	18.61	12763.96	7.58	PC1
10D	L0=0.50L	D_v=20	10.10	938.00	19.49	7774.41	4.63	PC2-->GB
10D	L0=0.75L	Q-S	none	952.58	16.97	8140.64	4.91	GB
10D	L0=0.75L	D_v=6	41.22	1100.00	18.20	9117.11	5.50	PC1-->GB
10D	L0=0.75L	D_v=10	30.56	1380.00	18.10	11437.83	6.75	PC1-->GB
10D	L0=0.75L	D_v=14	14.46	1390.00	18.06	11520.71	6.92	PC1-->GB
10D	L0=0.75L	D_v=20	10.20	1600.00	19.50	13261.25	7.89	PC2
10D	L0=0.95L	Q-S	none	1523.61	16.20	12623.07	7.60	PC2
10D	L0=0.95L	D_v=6	45.80	1400.00	16.04	11603.60	6.92	PC2
10D	L0=0.95L	D_v=10	21.68	1460.00	17.73	12100.89	7.21	PC2
10D	L0=0.95L	D_v=14	14.88	1470.00	17.58	12183.78	7.32	PC2
10D	L0=0.95L	D_v=20	10.20	1520.00	18.49	12598.19	7.53	PC2

Note:

Loading Condition:

Q-S: Quasi-Static;
D_v=6: Dynamic crushing (v= 6 m/s);
D_v=10: Dynamic crushing (v=10 m/s);
D_v=14: Dynamic crushing (v= 14 m/s);
D_v=20: Dynamic crushing (v=20 m/s);

* These values are calculated based on 60mm crushing distance for 2D (80mm) tubes; likewise, 100mm for 5D (200mm) tubes, and 200mm for 10D (400mm) tubes.

Crushing modes:

GB - Global Buckling;
PC1- initial folding occurred around the cutout. The folding then occurred on the top part of the shell, and finally the bottom part folded;
PC2 - initial folding occurred at the loaded end, and propagated downwards;
PC3 - initial folding occurred simultaneously at the loaded end and around the cutout;
PC4 - initial folding occurred at both top and bottom end, and folding continued progressively

Table 4-2: Summary of numerical crushing analysis on steel tubes

Tube Length	material type	strain rate effect	cutout location	Loading condition	response time* (ms)	Absorbed Energy (J)*	Peak crushing force –*PI* (KN)	SEA (J/kg)*	Mean crushing force-*Pm** (KN)	crushing mode
2D	MAT1	yes	none	Q-S	none	995.00	34.93	14182.47	16.49	PC2
2D	MAT1	yes	none	D_v=6	12.48	1200.00	47.41	17104.48	20.02	PC2
2D	MAT1	yes	none	D_v=20	3.05	1300.00	50.89	18529.86	21.13	PC2
2D	MAT2	yes	none	Q-S	none	954.00	34.85	13598.07	15.75	PC3
2D	MAT2	yes	none	D_v=6	12.15	1160.00	42.44	16534.33	19.48	PC3
2D	MAT2	yes	none	D_v=20	3.05	1240.00	48.91	17674.63	20.17	PC3
2D	MAT2	no	none	D_v=20	3.04	917.00	42.64	13070.68	14.95	PC3
2D	MAT1	yes	L0=0.50L	Q-S	none	1050.00	32.90	14966.42	17.40	PC2
2D	MAT1	yes	L0=0.50L	D_v=6	12.21	1140.00	39.20	16249.26	19.20	PC2
2D	MAT1	yes	L0=0.50L	D_v=20	3.03	1270.00	48.76	18102.25	20.91	PC2
2D	MAT2	yes	L0=0.50L	Q-S	none	680.00	32.50	9692.54	11.39	PC2
2D	MAT2	yes	L0=0.50L	D_v=6	11.90	958.00	38.93	13655.08	15.95	PC2
2D	MAT2	yes	L0=0.50L	D_v=20	3.05	1150.00	48.39	16391.80	18.95	PC2
2D	MAT2	no	L0=0.50L	D_v=20	3.01	832.00	38.29	11859.11	13.69	PC2
5D	MAT1	yes	none	Q-S	none	1540.00	34.48	8780.30	15.15	PC2
5D	MAT1	yes	none	D_v=6	32.20	1790.00	39.23	10205.68	16.63	PC2
5D	MAT1	yes	none	D_v=20	5.16	2060.00	44.33	11745.08	20.14	PC2
5D	MAT2	yes	none	Q-S	none	1390.00	34.27	7925.08	13.61	PC2
5D	MAT2	yes	none	D_v=6	25.80	1630.00	38.77	9293.44	15.66	PC2
5D	MAT2	yes	none	D_v=20	5.13	1820.00	44.00	10376.72	17.83	PC2
5D	MAT2	no	none	D_v=20	5.10	1450.00	33.95	8267.17	14.24	PC2
5D	MAT1	yes	L0=0.50L	Q-S	none	634.20	32.82	3615.89	7.27	GB
5D	MAT1	yes	L0=0.50L	D_v=6	14.90	716.00	36.20	4082.27	7.49	GB
5D	MAT1	yes	L0=0.50L	D_v=20	5.12	1910.00	45.35	10889.86	18.62	PC3
5D	MAT2	yes	L0=0.50L	Q-S	none	647.00	32.61	3688.87	6.47	GB
5D	MAT2	yes	L0=0.50L	D_v=6	18.20	710.00	35.31	4048.06	6.72	GB
5D	MAT2	yes	L0=0.50L	D_v=20	5.12	1800.00	44.83	10262.69	17.58	PC3
5D	MAT2	no	L0=0.50L	D_v=20	5.12	1450.00	33.72	8267.17	14.12	PC3
5D	MAT1	yes	L0=0.90L	Q-S	none	1420.00	31.21	8096.12	13.98	PC2
5D	MAT1	yes	L0=0.90L	D_v=6	26.20	1630.00	37.33	9293.44	15.86	PC2
5D	MAT1	yes	L0=0.90L	D_v=20	5.16	1930.00	43.59	11003.88	18.97	PC2
5D	MAT2	yes	L0=0.90L	Q-S	none	1350.00	29.21	7697.02	13.37	PC2
5D	MAT2	yes	L0=0.90L	D_v=6	24.40	1530.00	36.98	8723.29	15.00	PC2
5D	MAT2	yes	L0=0.90L	D_v=20	5.16	1750.00	43.03	9977.62	17.21	PC2
5D	MAT2	no	L0=0.90L	D_v=20	5.12	1350.00	32.05	7697.02	13.25	PC2
--To be continued										

Table 4.2 Continued

10D	MAT1	yes	none	Q-S	none	2940.00	34.14	8381.20	14.59	PC2
10D	MAT1	yes	none	D_v=6	34.60	1800.00	38.49	5131.35	18.24	PC2
10D	MAT1	yes	none	D_v=20	10.56	3820.00	43.60	10889.86	18.76	PC2
10D	MAT2	yes	none	Q-S	none	2670.00	33.97	7611.50	13.24	PC2
10D	MAT2	yes	none	D_v=6	37.20	1800.00	37.98	5131.35	16.67	PC2
10D	MAT2	yes	none	D_v=20	10.50	3470.00	42.89	9892.09	17.12	PC2
10D	MAT2	no	none	D_v=20	10.38	2700.00	31.84	7697.02	13.32	PC2
10D	MAT1	yes	L0=0.50L	Q-S	none	651.20	33.48	1856.41	3.26	GB
10D	MAT1	yes	L0=0.50L	D_v=6	none	712.00	37.67	2029.73	3.56	GB
10D	MAT1	yes	L0=0.50L	D_v=20	10.28	2180.00	45.33	6214.63	10.73	PC3-->GB
10D	MAT2	yes	L0=0.50L	Q-S	none	1030.00	33.35	2936.27	5.15	GB
10D	MAT2	yes	L0=0.50L	D_v=6	none	763.00	37.61	2175.12	3.82	GB
10D	MAT2	yes	L0=0.50L	D_v=20	9.80	2890.00	44.81	8238.66	14.65	PC3->GB
10D	MAT2	no	L0=0.50L	D_v=20	10.36	2690.00	33.69	7668.51	13.29	PC2
10D	MAT1	yes	L0=0.95L	Q-S	none	3230.00	32.25	9207.91	15.76	PC2
10D	MAT1	yes	L0=0.95L	D_v=6	40.00	1790.00	36.57	5102.84	16.27	PC2
10D	MAT1	yes	L0=0.95L	D_v=20	10.56	3710.00	43.59	10576.27	18.32	PC2
10D	MAT2	yes	L0=0.95L	Q-S	none	2600.00	31.37	7411.94	12.80	PC2
10D	MAT2	yes	L0=0.95L	D_v=6	41.00	1800.00	36.32	5131.35	15.00	PC2
10D	MAT2	yes	L0=0.95L	D_v=20	10.48	3350.00	43.03	9550.00	16.66	PC2
10D	MAT2	no	L0=0.95L	D_v=20	10.36	2600.00	32.05	7411.94	12.89	PC2

Note:

Loading Condition:

Q-S: Quasi-Static;
D_v=6: Dynamic crushing (v= 6 m/s);
D_v=10: Dynamic crushing (v=10 m/s);
D_v=14: Dynamic crushing (v= 14 m/s);
D_v=20: Dynamic crushing (v=20 m/s);

* These values are calculated based on 60mm crushing distance for 2D (80mm) tubes; likewise, 100mm for 5D (200mm) tubes, and 200mm for 10D (400mm) tubes.

Crushing modes:

GB - Global Buckling;
PC1- initial folding occurred around the cutout. The folding then occurred on the top part of the shell, and finally the bottom part folded;
PC2 - initial folding occurred at the loaded end , and propagated downwards;
PC3 - initial folding occurred simultaneously at the loaded end and around the cutout;
PC4 - initial folding occurred at both top and bottom end, and folding continued progressively

4.5.1 Comparisons of experimental and numerical simulations

Figure 4.10 shows the numerical and experimental crushing force versus crushing displacement response for the quasi-static crushing of the 5D aluminum tubes without and with a cutout near their loaded end ($L_0 = 0.90L$). Good agreement is observed between the numerical simulations and experimental results.

The numerical and experimental crushing response of 5D aluminum tubes without a cutout is shown in Figure 4.11. Again, good agreement is observed. The numbers of circumferential and axial waves are six and four, respectively, in both numerical and experimental results.

Figure 4.12 illustrates the crushing behaviors of 5D aluminum tubes with a cutout at its mid-height obtained from the numerical simulation and experimental tests. The crushing profile (both the isometric and plan views) at 80mm crushing distance obtained from the numerical simulation and experimental testing are compared. Similar circumferential and axial wave forms in the crushed tubes are observed between numerical and experimental results. The crushing force versus time and force versus crushing displacement responses are also shown in this figure. Good agreements are also observed in these comparisons.

Behaviors of the 5D aluminum tubes with a cutout at its 70% height ($L_0 = 0.70L$) obtained from numerical simulation and experimental test are illustrated in Figure 4.13. The tubes are crushed in a global buckling mode in both numerical and experimental observations. Good agreements are also observed in the crushing load versus time and crushing load versus crushing displacement response.

Finally, the response of the 5D aluminum tubes with a cutout near their top end ($L_0 = 0.90L$) captured through numerical simulation and testing are shown in Figure 4.14, with good agreement in the results.

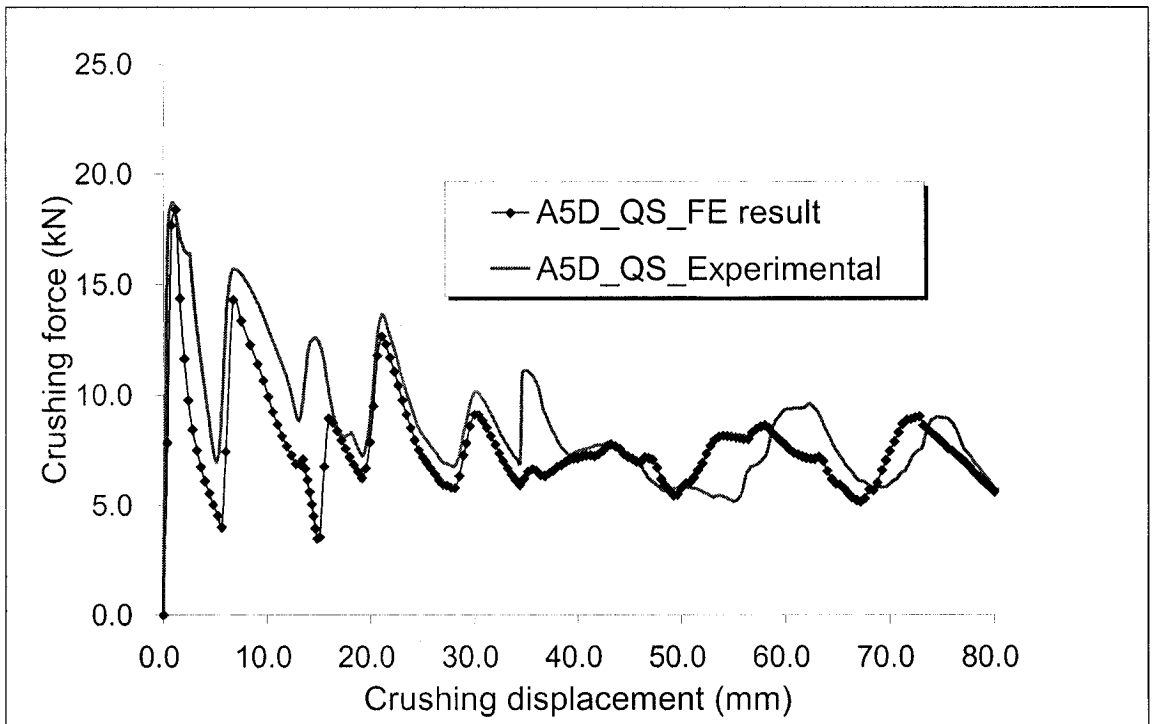

(a) 5D aluminum with no cutout

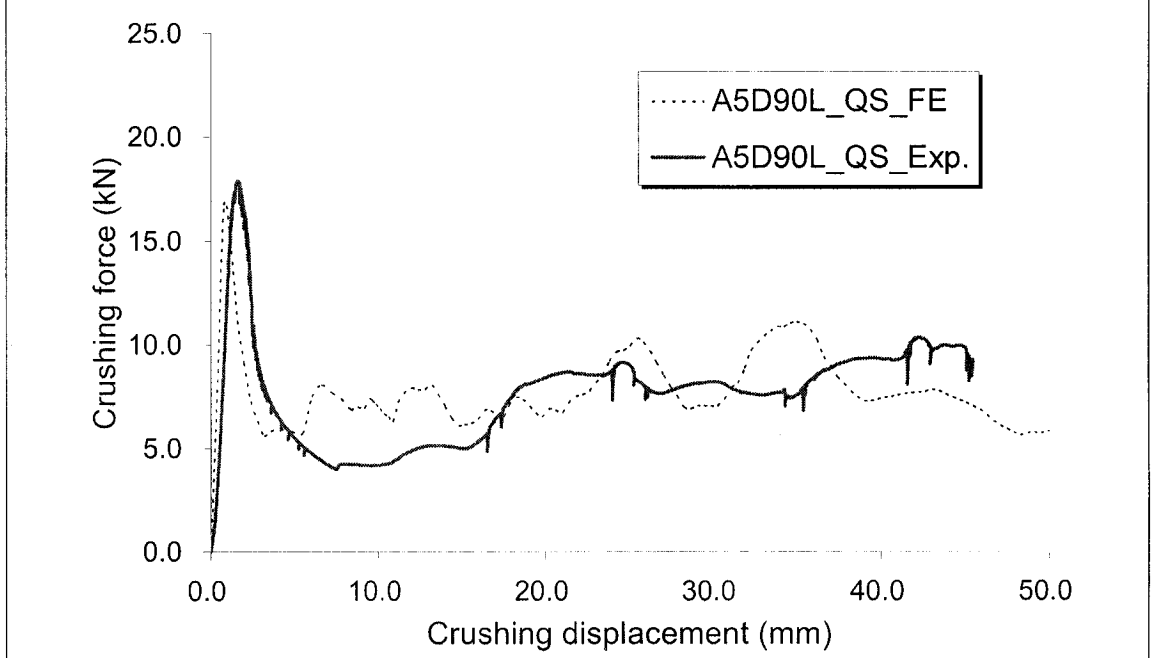

(b) 5D aluminum tube with cutout near top end

Figure 4-10: Numerical and experimental crushing force versus crushing distance responses of the 5D aluminum tubes with and without a cutout near top end subject to quasi-static crushing

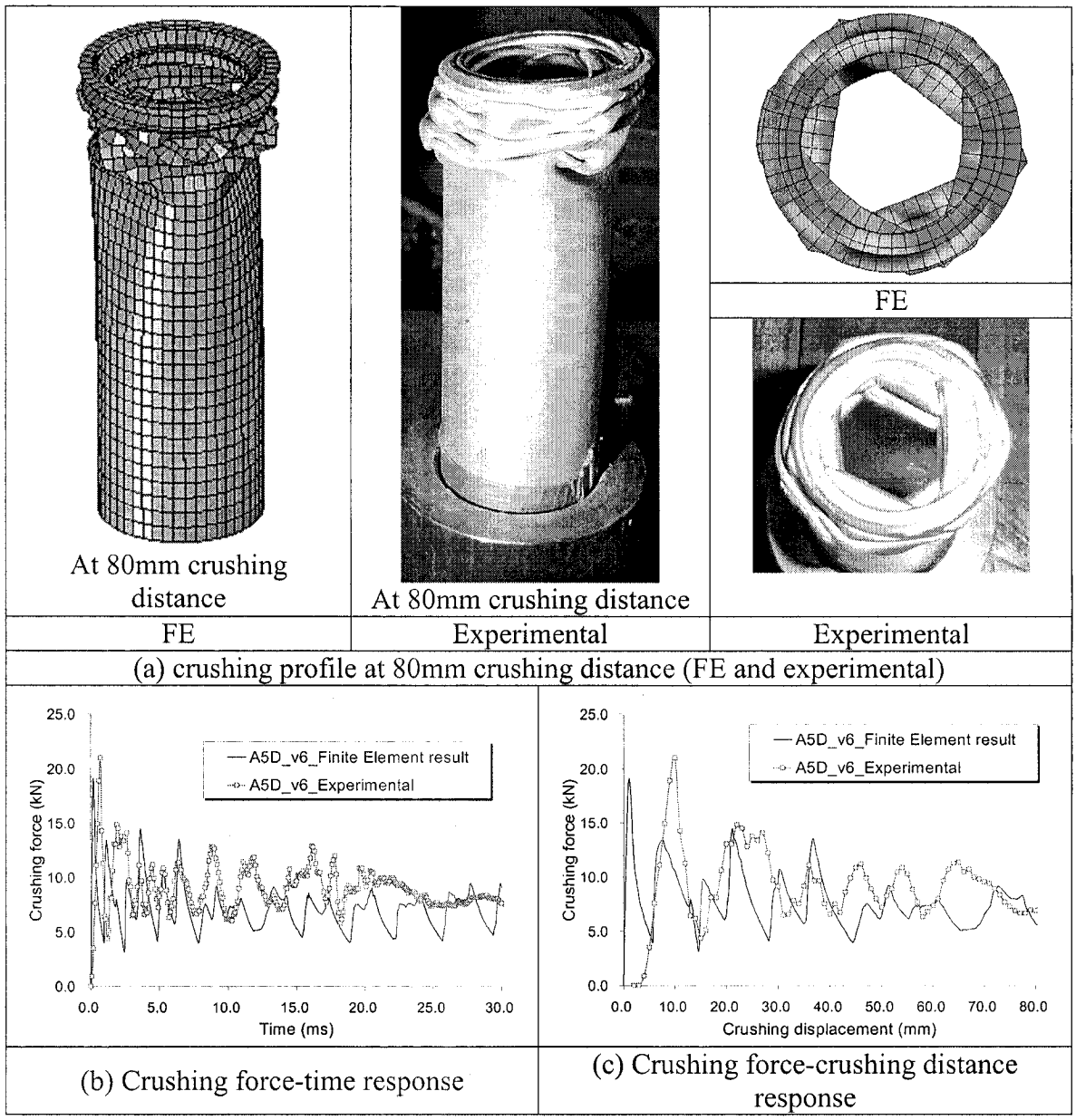

Figure 4-11: Comparison of the numerical and experimental results for the 5D aluminum tube subject to dynamic crushing (v=6 m/s)

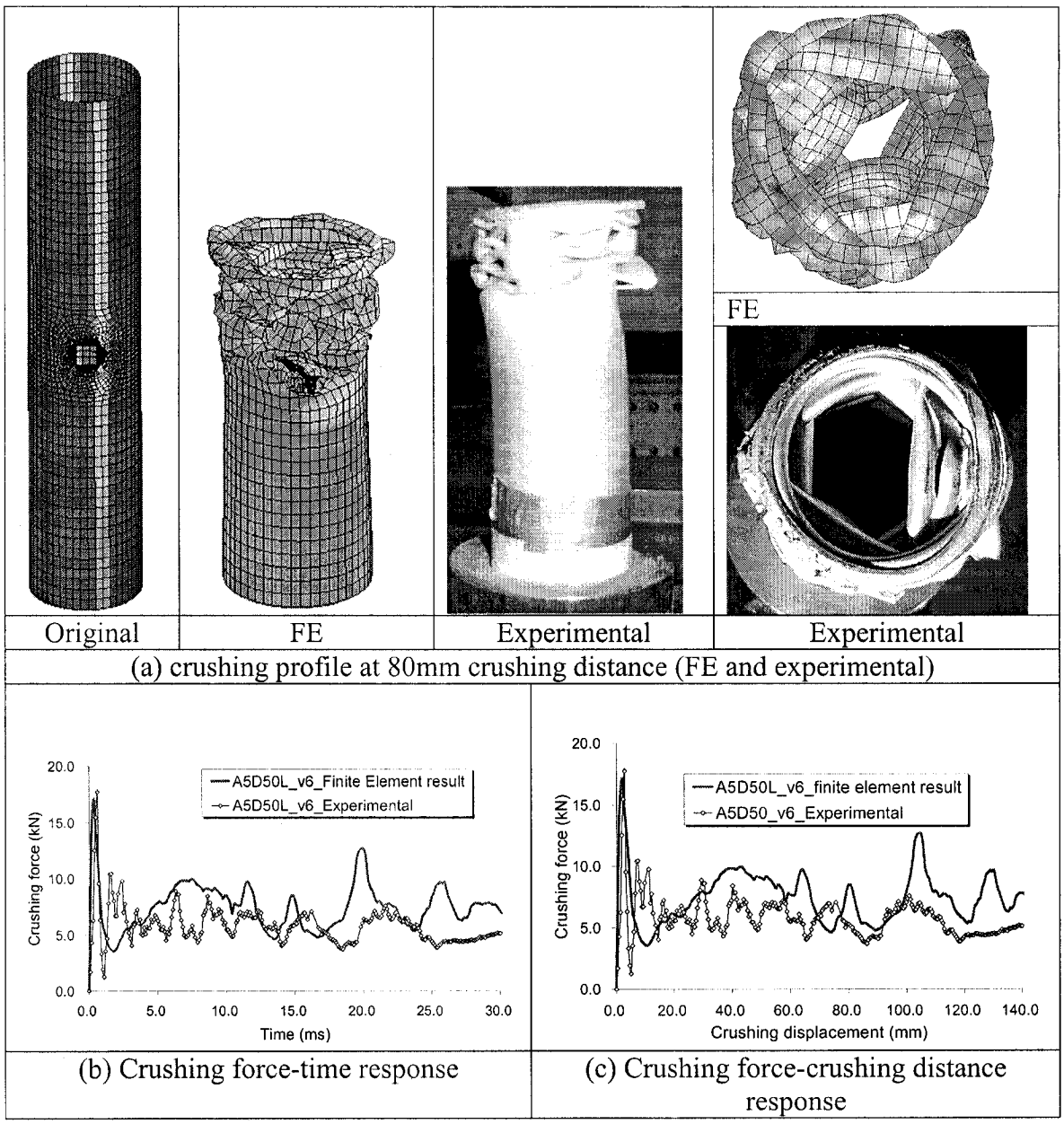

Figure 4-12: Comparison of the numerical and experimental results for the 5D aluminum tube with a cutout at its mid-height subject to dynamic crushing (v=6 m/s)

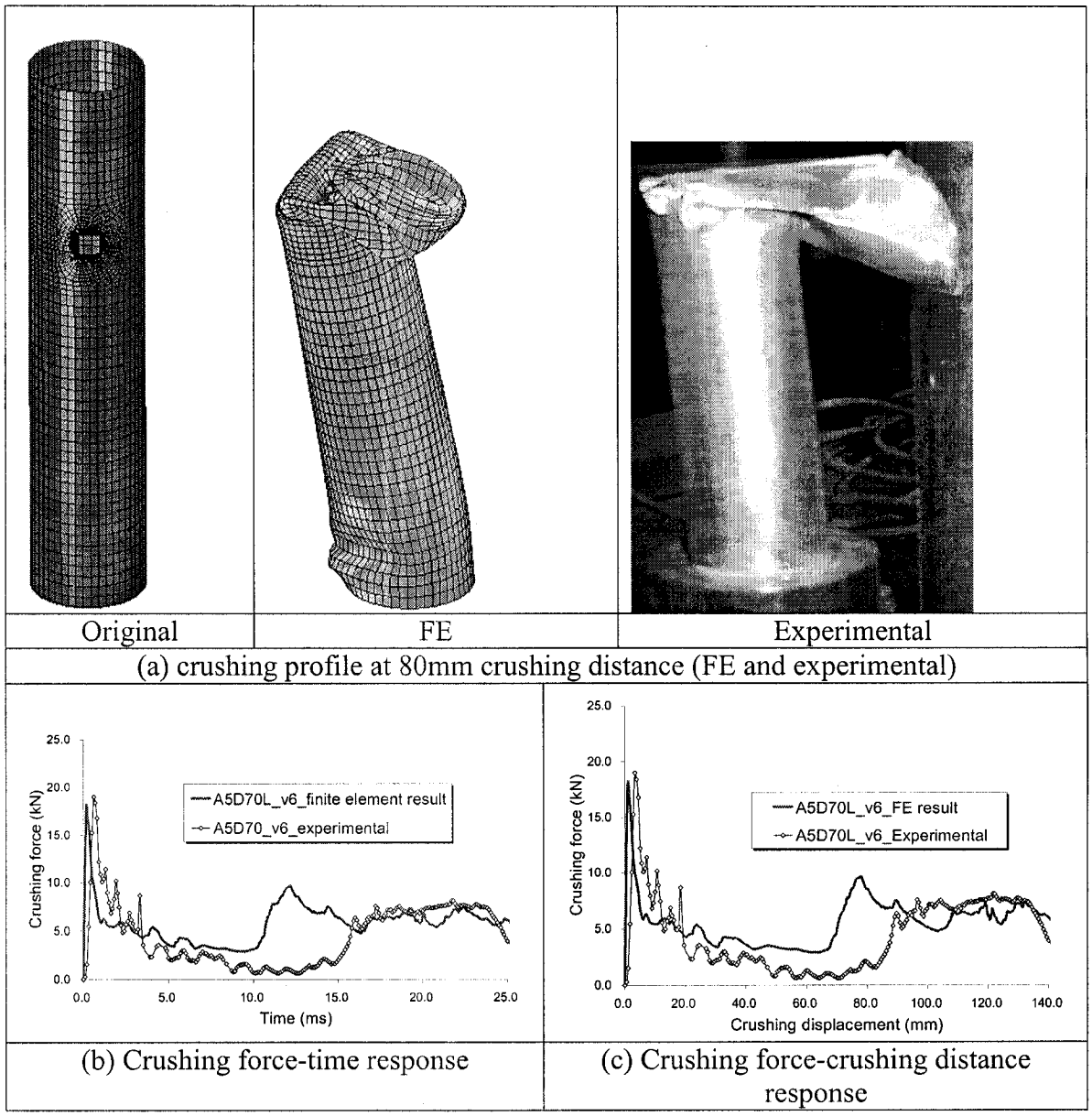

Figure 4-13: Comparison of the numerical and experimental results for the 5D aluminum tube with a cutout at $L_0 = 0.70L$ subject to dynamic crushing (v= 6m/s)

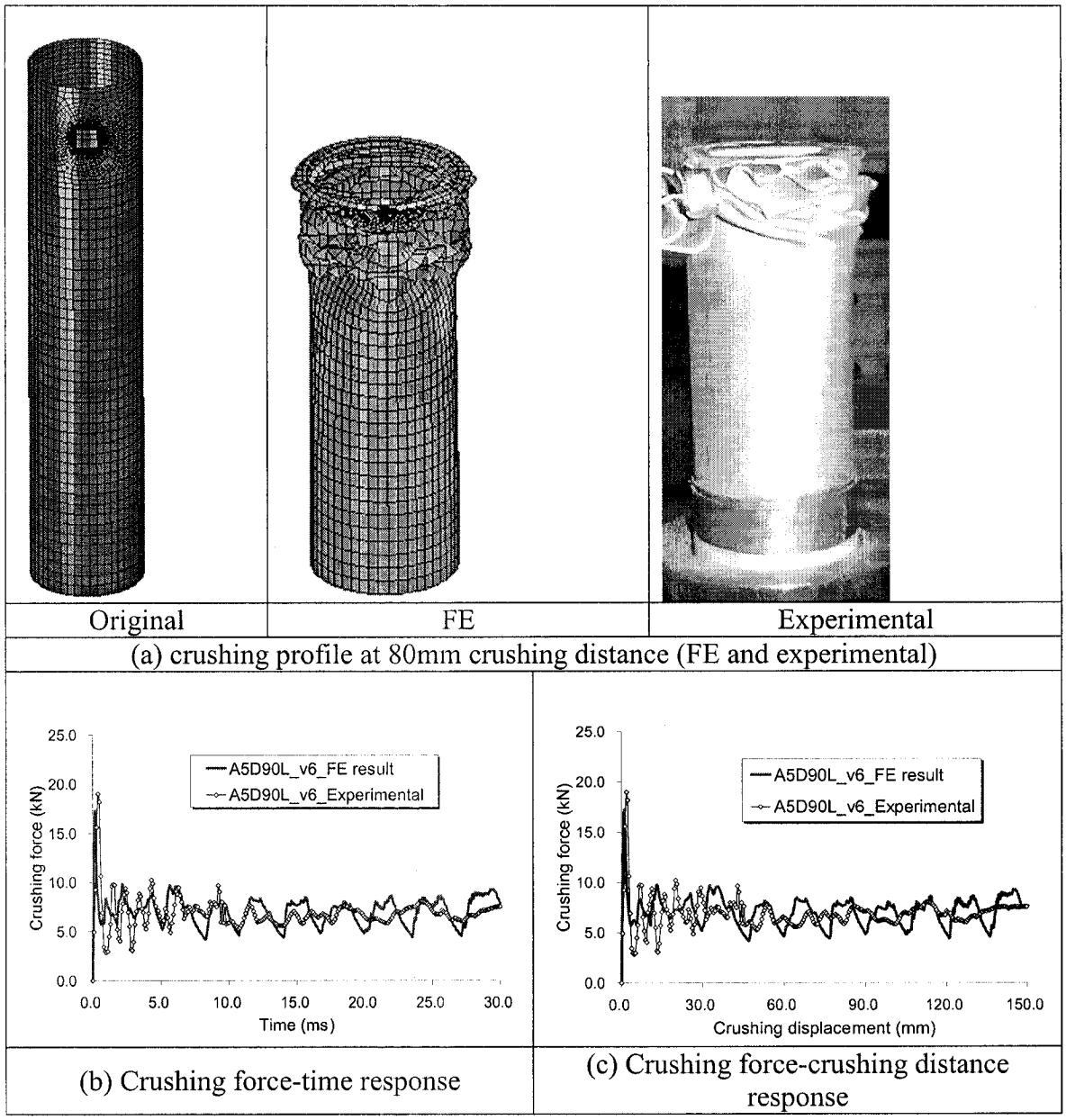

Figure 4-14: Comparison of the numerical and experimental results for the 5D aluminum tube with a cutout near top end ($L_0 = 0.90L$) subject to dynamic crushing (v=6 m/s)

4.5.2 Aluminum tubes

Figure 4.4 shows the crushing responses of the 2D aluminum tubes with and without a cutout subject to quasi-static and dynamic impact loadings. The magnitudes of the peak crushing force at the formation of each wrinkle (also called the corner crushing load) in the tubes without a cutout, as expected, are higher than those in tubes with a cutout; moreover, the higher the impact velocity, the higher the corner crushing load in the tubes without a cutout. However, it is also observed from Figure 4.4 that the corner crushing load in 2D tubes with a cutout at its mid height is less sensitive to the change in velocity than in tubes without a cutout. The crushing load goes steadily after the initial peak load, be it with less fluctuation, until the occurrence of bottoms-out, i.e., the tube is fully crushed. It can be seen from Table 4.1 that the peak crushing force for the 2D tubes with and without a cutout slightly increased with the increase of impact velocity. However, the variation of mean crushing force in tubes with and without a cutout is found to be irregular with respect to the change in impact velocity. In general, the presence of a cutout reduced the mean crushing force by about 10%. The 2D tubes without a cutout were crushed in PC2 mode, whereas the tubes with a cutout crushed in a PC3 mode.

Figure 4.5 illustrates the crushing response of 5D aluminum tubes with and without a cutout subject to quasi-static and dynamic impact loadings. As stated previously, three different locations of cutout were considered. Not surprisingly, the tubes without a cutout progressively crushed in a PC2 mode, and in general the energy absorption capacity increases with the increase of impact velocity. It is found from Table 4.1 that the peak crushing force increases with the increase in loading velocity for tubes with and without a cutout. It is also found from Figure 4.5 and Table 4.1 that the worst situation is created when the cutout is located at mid-height of the tubes, and when the tube is subject to quasi-static crushing, the corresponding crushing mode is a global buckling mode. Obviously, the presence of a cutout reduces the energy absorption capacity of the tubes. The negative influence of the cutout is alleviated as the cutout is moved from the tubes' mid-height to near the top end or when the tubes are subject to dynamic crushing rather than quasi-static crushing. Interestingly, in all cases of dynamic crushing, the cutout location of $L_0 = 0.70L$ created the worst situation, in comparison to tubes with the cutout

located at either $L_0 = 0.50L$ or $L_0 = 0.90L$. This phenomenon is also observed in the experimental results. The mean crushing force, absorbed energy and SEA in $L_0 = 0.50L$ and $L_0 = 0.90L$ were very close to each other in the dynamic crushing, although they exhibited different crushing modes. The tubes with a cutout at $L_0 = 0.50L$ were crushed essentially in a PC1 mode, while the tubes with a cutout at $L_0 = 0.90L$ were all crushed in a PC2 mode. By comparison, the tubes without a cutout and tubes with a cutout at $L_0 = 0.90L$, showed that when the cutout was located near the upper end, their peak crushing force was reduced, while less influence was observed on the mean crushing force and SEA in the tubes. This is indeed a preferred situation when designing energy absorbers.

The crushing responses of the 10D aluminum tubes with and without a cutout subject to quasi-static and dynamic impact loadings are shown in Figure 4.6 and summarized in Table 4.1. For the 10D tubes without a cutout, as the impact velocity increased from 0 to 20 m/s, the corresponding absorbed energy, peak and mean crushing forces are first increased, followed by a decreasing trend. The maximum energy absorption (EA) capacity was observed when the impact velocity was at 14 m/s. Correspondingly, the crushing mode changed from PC2 to PC4 and back to PC2 as the loading velocity was increased. The same trend applies to the 10D tubes with a cutout at mid-height, in terms of the variation observed in their energy absorption capacity as a function of the variation in impact velocity. The maximum EA capacity also occurred when the impact velocity was at 14m/s, and the crushing mode in this case was observed as progressive crushing (PC1) mode. The final failure mode of the other tubes with a cutout at their mid-height was a global buckling mode; however, their pre global buckling mode differed. In this case, the pre global buckling modes were a PC1 mode for v=10 m/s, and PC2 mode for v=6 m/s and 20 m/s. In the 10D tubes with a cutout located at $L_0 = 0.75L$ and $0.95L$, their EA capacity increased as the impact velocity increased. In tubes with a cutout at $L_0 = 0.75L$, the crushing mode changed gradually from a global buckling mode to a progressive crushing mode, as the impact velocity increased from 0 to 20 m/s. On the other hand, the tubes with a cutout at $L_0 = 0.95L$ crushed in a progressive crushing

(PC2) mode, regardless of the impact velocity. By comparison, when considering the tubes without a cutout and tubes with a cutout at $L_0 = 0.95L$, it is found that when the cutout was located near the upper end, the peak crushing force was reduced, while it had less influence on the energy absorption capacity of the tubes. This finding conforms to that observed in the 5D aluminum tubes.

4.5.3 Steel tubes

As stated in section 2, two types of steel materials, namely MAT1 and MAT2, were considered in the numerical part of the research. MAT1 and MAT2 have the same yield strength, but different strain hardening ratio. The strain rate effect was accounted when modeling the steel. One of the objectives of this study is to determine how the energy absorption capability is related to the variation of strain hardening ratio.

Figure 4.7 shows the crushing response of the 2D steel tubes with and without a cutout made of MAT1 and MAT2 materials, subject to quasi-static and dynamic impact loadings. It is shown in Figure 4.7 that there is a remarkable difference between quasi-static crushing and dynamic crushing for the steel tubes without a cutout, which is because of the strain rate effect. The peak and mean crushing forces in the dynamic crushing are much higher than those in the quasi-static crushing. With the increase of impact velocity, the corner crushing load grows larger, and reaches to almost the same magnitude as the initial peak crushing forces, particularly in the tubes made of MAT1 which has higher strain hardening ratio. Interestingly, it is found that the 2D tubes made of MAT1, with a cutout at their mid-height, could absorb more energy under quasi-static crushing than the counterparts with no cutout, although lower peak crushing force is attained because of the cutout. However, this phenomenon did not occur in tubes made of MAT2, where both peak and mean crushing forces for the tubes with a cutout are lower than those in the tubes without a cutout under dynamic crushing. With the increase of impact velocity under dynamic crushing, the reduction effect due to the cutout is alleviated, as shown in Table 4.2. With the presence of a cutout in the 2D tubes, the tubes made of MAT1 have much more EA capacity than the tubes made of MAT2. In general, the cutout in the 2D tubes has very small effect on the EA capability of tubes, and with some positive effect in some cases (tubes made of MAT1 under quasi-static crushing).

All of the tubes without a cutout are crushed in a progressive crushing mode (PC2) and the tubes with a cutout at their mid-height are crushed in a PC3 crushing mode.

Figure 4.8 shows the crushing response of the 5D steel tubes with and without a cutout made of MAT1 and MAT2, subject to the quasi-static and dynamic impact loading. For the 5D tubes without a cutout, tubes made of MAT1 exhibited more EA capacity than the MAT2 tubes. It was observed, the higher the impact velocity, the higher the peak and mean crushing forces, the absorbed energy and specific energy absorption (SEA). For the 5D tubes with a cutout at their mid-height ($L_0 = 0.50L$), the quasi-static crushing modes for both types of materials are global buckling mode. Even at relatively low impact velocities, the tubes are also crushed in a global buckling mode. As the impact velocity was increased from 6 m/s to 20 m/s, the crushing mode changed from a global buckling mode to a progressive crushing mode (PC3). The EA capacity also increased remarkably as the impact velocity increased from 6 m/s to 20 m/s. For the 5D tubes with a cutout near their top end ($L_0 = 0.90L$), the crushing modes for both quasi-static and dynamic crushing events were all progressive crushing modes (PC2). In every loading case, by moving the location of the cutout from mid-height to near the top end, the EA capacity of the tubes was increased significantly. Unlike the case of the 2D tubes, the presence of the cutout in the 5D tubes always reduced the EA capacity regardless of the cutout location.

Figure 4.9 shows the crushing response of the 10D steel tubes with and without a cutout made of MAT1 and MAT2 materials, subject to quasi-static and dynamic impact loadings. All the tubes without and those with a cutout near the top end ($L_0 = 0.95L$) were crushed in a progressive crushing mode (PC2). It is noted that under a dynamic crushing loading with an impact velocity of 6 m/s, all tubes without a cutout and with a cutout near the top end ($L_0 = 0.95L$) absorbed a similar amount of energy (1800J). This is believed to be due to the fact that the total energy input in the system was 1800J ($0.5mv^2 = 0.5 \times 100 \times 6^2$). As seen from Figures 4.9a and 4.9c, it takes more crushing displacement for a MAT2 tube to absorb the 1800 J input energy. This is observed in both cases of tubes without a cutout (Figure 4.9a) and with a cutout near the upper end (Figure 4.9c). It should be noted that in all tubes, except those subject to an impact

velocity of v=6 m/s, the crushing energy and the mean crushing force were calculated based on a 200 mm crushing displacement in the force versus displacement curve. However, as seen in Figures 4.9a and 4.9c, when the tube is subject to an impact velocity of 6 m/s, the crushing displacement does not reach 200 mm (in fact, approximate 98-120mm); therefore, in these cases, the crushing energy and mean crushing force are calculated from the crushing displacements seen on the figures (i.e. 98-120mm). In the 10D tubes with a cutout at their mid-height, the crushing modes were essentially all in a global buckling mode, with the exception that in the dynamic impact case, with a velocity of 20 m/s, the tubes were first crushed in a progressive crushing mode (PC3), and finally collapsed in a global buckling mode, as shown in Figure 4.9 (see also Table 4.2). In general, it was observed that the relationship between the EA capacity and cutout location, and the impact velocity of the 10D tubes was similar to that in the 5D tubes.

Moreover, to further demonstrate the influence of strain rate effect in steel, all the MAT2 steel tubes subject to dynamic crushing with an impact velocity of 20 m/s, were considered with and without the strain rate effect. It is seen from Table 4.2 that there are significant differences between the comparable case studies, in terms of the peak crushing force and energy absorption capacity. When the strain rate effect is taken into account, the peak crushing force and the energy absorption capacity became significantly higher than when there was no such effect.

4.6 Prediction of mean and peak crushing forces

The crushing behavior and response of the aluminum and steel tubes subjected to quasi-static and dynamic axial compressive loading were presented in the previous sections. It was found that the energy absorption was relative to the tube length, material properties, cutout location and impact velocities. The research reported here demonstrated very good agreement between the results from the experiments and numerical analyses. This observation encouraged us to conduct systematic numerical simulations and to develop appropriate empirical equations based on the result obtained. In this section, a series of empirical equations were developed by means of linear and/or nonlinear regression analysis on the data that was reported in Section 4. These empirical

equations may be used to predict the peak and mean crushing forces of aluminum or steel tubes with a cutout along different locations, subject to both quasi-static compression and dynamic impact loadings with various impact velocities.

4.6.1 Equations for aluminum tubes

From this study, it was found that equation (4.3) could be used to predict the mean crushing force of aluminum tubes very well. Empirical equations were also developed for the aluminum tubes without a cutout, subject to both quasi-static and dynamic crushing load conditions. Under quasi-static crushing, the mean crushing forces for tubes of various lengths could be predicted by:

$$P_m = 4\pi Rt\sigma_u \left(\frac{2t}{R}\right)^{0.7} \left(1.01 - 0.0179\frac{L}{2R}\right) \tag{4.6}$$

Whereas under a dynamic crushing condition, the mean crushing force of aluminum tubes could be evaluated by the following equation, which considers the variation of both tube length and impact velocity.

$$P_m = 4\pi Rt\sigma_u \left(\frac{2t}{R}\right)^{0.7} \left(1.01 - 0.0179\frac{L}{2R}\right)(0.968 + 0.00654V) \tag{4.7}$$

For aluminum tubes with a cutout at various locations, the mean crushing forces for quasi-static and dynamic crushing conditions could be predicted by equation (4.8) and (9), respectively.

Under quasi-static crushing:

$$P_m = 4\pi Rt\sigma_u \frac{C_N}{C}\left(\frac{2t}{R}\right)^{0.7} \left(1.01 - 0.0179\frac{L}{2R}\right)\left(0.2326 + 0.9506\frac{L_0}{L}\right) \tag{4.8}$$

Under dynamic crushing:

$$P_m = 4\pi Rt\sigma_u \frac{C_N}{C}\left(\frac{2t}{R}\right)^{0.7} \left(1.01 - 0.0179\frac{L}{2R}\right)(0.968 + 0.00654V)\left(0.732 + 0.287\frac{L_0}{L}\right) \tag{4.9}$$

Under a quasi-static crushing condition, the reference peak crushing force may be calculated by $P_I = 2\pi tR\sigma_0$, because the crushing initiation force is proportional to the net section yielding at the crushing front. That said, the peak crushing force is also a function of the impact velocity, as shown by the results obtained from the numerical simulations

reported in Tables 4.1 and 4.2. For aluminum tubes with and without a cutout, the peak crushing force could be predicted by:

$$P_{I\_A} = \pi Rt(\sigma_0 + \sigma_u)\frac{C_N}{C}\left(1.02 - 0.00931\frac{L}{2R}\right)\left(1.04 - 0.129\frac{L_0}{L}\right)(0.994 + 0.00188V) \tag{4.10}$$

In equation (4.8~4.10) C_N is the net circumference of the tubes where the cutout is located, and C is the overall circumference of the tubes (without a cutout). The ratio of C_N over C describes the reduction effect of a cutout. Equations (4.6~4.10) are developed based on linear regression analysis and apply to fixed-free supported tubes with L/D ratios between 2~10, impact velocities of between 6~20 m/s and the cutout location in the interval of $0.50L \le L_0 \le 0.95L$. From the model summary of regression analyses, it was found that the R-Square value for equations (4.6~4.10) are all above 90%, thus signifying pretty good fit of the model.

4.6.2 Equations for steel tubes

It is known that steel is a strain rate-sensitive material, thus sensitive to the variation in impact velocity. In this study, it was found that a model developed based on combining Jones [13] and Magee and Thornton [4] models could be used to predict the mean crushing force in steel tubes, subject to low or intermediate-velocity (up to 20 m/s) axial impact, with good accuracy, the model can be represented by:

$$P_m = 4\pi Rt\sigma_u\left(\frac{2t}{R}\right)^{0.7}\left[1 + \left(\frac{V_0}{4RD}\right)^{1/q}\right] \tag{4.11}$$

Based on equation (4.11), nonlinear regression analysis is conducted to develop the empirical equations predicting the mean and peak crushing forces of steel tubes subject to quasi-static compression and dynamic impact loading. For steel tubes without a cutout, the mean crushing force can be predicted by:

$$P_m = 4\pi Rt\sigma_u\left(\frac{2t}{R}\right)^{0.7}\left(0.951 - 0.0149\frac{L}{2R}\right)\left(1.42 - 0.371\frac{\sigma_u}{\sigma_0}\right)\left[1 + \left(\frac{V_0}{4RD}\right)^{1/q}\right] \tag{4.12}$$

For steel tubes with a cutout, the mean crushing force can be predicted by:

$$P_m = 4\pi Rt\sigma_u \frac{C_N}{C}\left(\frac{2t}{R}\right)^{0.7}\left\{0.39864+\frac{L_0}{L}\left(\frac{L}{2R}\right)^{-0.55206}\left(\frac{\sigma_u}{\sigma_0}\right)^{-0.11721}\left[1+\left(\frac{V_0}{4RD}\right)^{1/q}\right]\right\} \tag{4.13}$$

The same approach can also be used to determine the peak force (crushing initiation force) of the tubes subject to either quasi-static compression or dynamic axial impact. Since the peak crushing force is a function of material properties and impact velocity, the following equation can be used to produce a base value for determining the peak crushing forces of steel tubes of various lengths with or without a cutout:

$$P_{I\_Sref} = 2\pi tR\sigma_0\left[1+\left(\frac{V_0}{4RD}\right)^{1/q}\right] \tag{4.14}$$

For steel tubes without a cutout, the peak crushing force can be predicted by:

$$P_{I\_S} = 2\pi tR\sigma_0\left(1.22-0.0153\frac{L}{2R}\right)\left(0.999+0.0893\frac{\sigma_u}{\sigma_0}\right)\left[1+\left(\frac{V_0}{4RD}\right)^{1/q}\right] \tag{4.15}$$

For steel tubes with a cutout, the peak crushing force can be predicted by:

$$P_{I\_S} = 2\pi tR\sigma_0\frac{C_N}{C}\left\{1+0.624881\left(\frac{L_0}{L}\right)\left(\frac{L}{2R}\right)^{-0.43694}\left(\frac{\sigma_u}{\sigma_0}\right)\left[1+\left(\frac{V_0}{4RD}\right)^{1/q}\right]\right\} \tag{4.16}$$

As can be seen both the mean and peak crushing forces are function of the tubes' length/radius ratio, material's strain hardening ratio and strain rate parameters, and the impact velocity. The summary of regression analyses showed that the developed equations (4.12-4.13 and 4.15-4.16) can be used to predict the mean and peak crushing forces quite well from the independent parameters considered (L_0/L, $L/2R$, σ_u/σ_0 and V_0). These equations apply to steels tubes confined by the following conditions:

$2 \le L/D \le 10, 1.32 \le \sigma_u/\sigma_0 \le 1.65$, $0.50 \le L_0/L \le 0.95$ and $6.0 \le V_0 \le 20.0 m/s$

If the impact velocity approaches zero, then equations (4.11-4.16) automatically produce the corresponding quasi-static crushing values.

4.7 Conclusions

Quasi-static and dynamic crushing response and energy absorption capacity of aluminum and steel tubes with and without a cutout were studied numerically and experimentally. The influence of location of cutout on the energy absorption capacity of tubes having various length/radius ratios, subject to various impact loading conditions, was investigated, both numerically and experimentally. Very good agreements were observed between numerical and experimental results. The numerical studies also investigated the response of tubes made of strain rate insensitive (aluminum) and sensitive (steel) materials.

The results revealed that in quasi-static crushing, the energy absorption efficiency of both aluminum and steel tubes was improved when the cutout location was moved from mid-height to their top end. In general, when the cutout was located at the mid-height, the tubes were crushed in a global buckling mode; conversely, when the cutout is located near the top end, the tubes crushed in a progressive crushing mode.

Under dynamic impact conditions, as the impact velocity increased, the negative influence of the cutout was decreased. However, this trend was not observed for the specific case of 5D aluminum tubes with a cutout located at $L_0 = 0.70L$ when subject to dynamic crushing, and the 2D steel tubes with a cutout at their mid-height, subject to quasi-static crushing.

Empirical equations for predicting the mean and peak crushing forces of aluminum and steel tubes with and without a cutout were developed based on combining the approaches used by Jones [13] and Magee *et al.* [4]. These equations were based on linear and nonlinear fit to the results obtained from the parametric numerical study conducted in this research.

4.8 Acknowledgements

The financial support of the Natural Sciences and Engineering Council of Canada (NSERC) in the form of Discovery Grants to the second and third authors in support of this work is gratefully acknowledged.

4.9 References

[1] Alghamdi A.A.A. (2001), Collapsible impact energy absorbers: an overview, *Thin-Walled Structures* 39: 189–213.

[2] Yamashita M., Gotoh M. and Sawairi Y. (2003), Axial crush of hollow cylindrical structures with various polygonal cross-sections Numerical simulation and experiment, *Journal of Materials Processing Technology* 140: 59–64.

[3] Alexander J.M. (1960), An approximate analysis of the collapse of thin cylindrical shells under axial loading, *Quarterly Journal of Mechanics and applied Mathematics* 13: 10-15.

[4] Magee C.L. and Thornton P.H. (1978), Design consideration in energy absorption by structural collapse, *SAE Technical Paper No.* 780434.

[5] Zhao H. and Abdennadher S. (2004), On the strength enhancement under impact loading of square tubes made from rate insensitive metals, *International Journal of Solids and Structures* 41: 6681–6697.

[6] Schneider F. and Jones N. (2004), Impact of thin-wall high strength steel structural section, *Proceedings of the Institution of Mechanical Engineers 218 (D): Journal of Automobile Engineering*, 131-158.

[7] Dipaolo B.P., Monteiro P.J.M. and Gronsky R. (2004), Quasi-static axial crush response of a thin-wall, stainless steel box component, *International Journal of Solids and Structures* 41: 3707–3733.

[8] Wang B. and Lu G. (2002), Mushrooming of circular tubes under dynamic axial loading, *Thin-Walled Structures* 40: 167–182.

[9] Mantena P.R. and Mann R. (2003), Impact and dynamic response of high-density structural foams used as filler inside circular steel tube, *Composite Structures* 61: 291–302.

[10] Bouchet J., Jacquelin E. and Hamelin P. (2000), Static and dynamic behavior of combined composite aluminum tube for automotive applications, *Composites Science and Technology* 60: 1891-1900.

[11] Mamalis A.G.., Manolakos D.E., Ioannidis M.B., Kostazos P.K. (2003), Crushing of hybrid square sandwich composite vehicle hollow bodyshells with reinforced core subjected to axial loading: numerical simulation, *Composite Structures* 61: 175–186.

[12] Marsoleka J. and Reimerdes H.G. (2004), Energy absorption of metallic cylindrical shells with induced non-axisymmetric folding patterns, *International Journal of Impact Engineering* 30: 1209–1223.

[13] Jones N., *Structural Impact*, Cambridge University Press, 1997.

[14] Kormi K., Webb D.C. and Montague P. (1993), Crash behavior of circular tubes with large side openings, *International Journal of Mechanical Science* 35 (3/4): 193-208.

[15] Sahu S.K. and Datta P.K. (2002), Dynamic stability of curved panels with cutouts, *Journal of Sound and Vibration* 251(4): 683-696.

[16] Sahu S.K. and Datta P.K. (2003), Dynamic Stability of Laminated Composite Curved Panels with Cutouts, *Journal of Engineering Mechanics ASCE* Nov 2003 1245-1253.

[17] Han H.P., Taheri F., Cheng J.Q. and Pegg N. (2006), Numerical and experimental investigations of the response of aluminum cylinders with a cutout subject to axial compression, *Thin Wall Structures* 44: 254–270.

[18] LS-DYNA keyword user's manual, V970, LSTC, Livermore, CA, 2005.

[19] El-Hage H.H. (2004), A numerical study on the quasi-static axial crush characteristics of square aluminum and aluminum-composite hybrid tubes, *PhD thesis*, University of Windsor.

[20] Olovsson L., Simonsson K. and Unosson M. (2005), Selective mass scaling for explicit finite element analyses, *International Journal for Numerical Methods in Engineering* 63: 1436–1445.

4.10 Appendix A: Crushing profiles of the tubes with a cutout

This section is a supplementary part to Sections 4.5.2 and 4.5.3 in Chapter 4. As discussed in the above mentioned sections, the crushing mode of both aluminum and steel tubes are sensitive to the change of impact velocities. The detailed crushing profiles of these tubes are provided in this appendix. To assess the effect of the impact velocities, the crushing modes at same crushing displacement are compared for different length of tubes. For 2D tubes, the crushing profiles of the tubes are recoded at 40mm crushing displacement. Likewise, the crushing profiles of the 5D and 10D tubes are recoded at 80 mm and 160 mm crushing displacement, respectively.

4.10.1 Aluminum tubes

Figure 4.15 show the crushing profiles of the 2D aluminum tubes without a cutout at various loading conditions. It is seen that the crushing mode tends to be more symmetric axially as the velocity of crushing load increases from zero to 20 m/s.

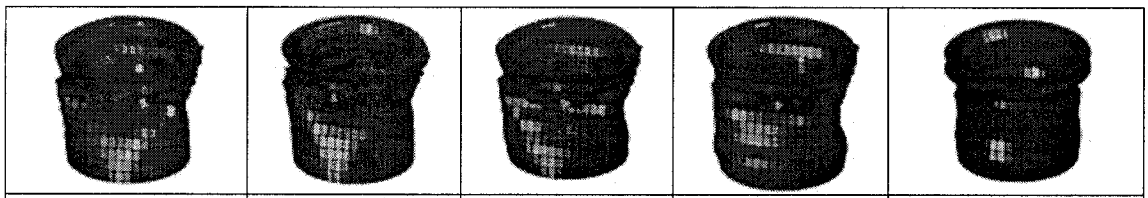

Figure 4-15: Crushing profiles of 2D aluminum tubes without a cutout

Likewise, the crushing profiles of 2D aluminum tubes with a cutout at their mid-height, subject to impact loading of various velocities are shown Figure 4.16. It is observed from Figure 4.16 that large deformation occurs mostly near the top end when the crushing velocity is low, whereas large inward deformation arises near the cutout when the velocity of crushing load is increased.

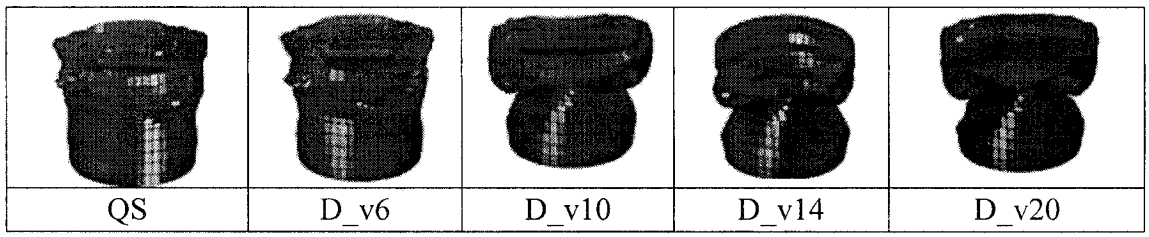

Figure 4-16: Crushing profiles of 2D aluminum tubes with a cutout at their mid-height

The crushing profiles of 5D aluminum tubes without a cutout, subject to crushing loading at various impact velocities are shown in Figure 4.17. It is observed from Figure 4.17 that the folding the tubes only occurs near the top end when the tube is subject to quasi-static crushing and dynamic 6 m/s dynamic crushing load. The folding of the tubes occurs simultaneously at the top and bottom end when it is subject to 10-14 m/s dynamic crushing, most obviously when subject to 14 m/s dynamic crushing load. As the velocity of the dynamic crushing load is increased up to 20 m/s, the folding of tubes occurs mostly near the top end, with very small radial deformation near the bottom end, and the crushing mode is in a more accordion type.

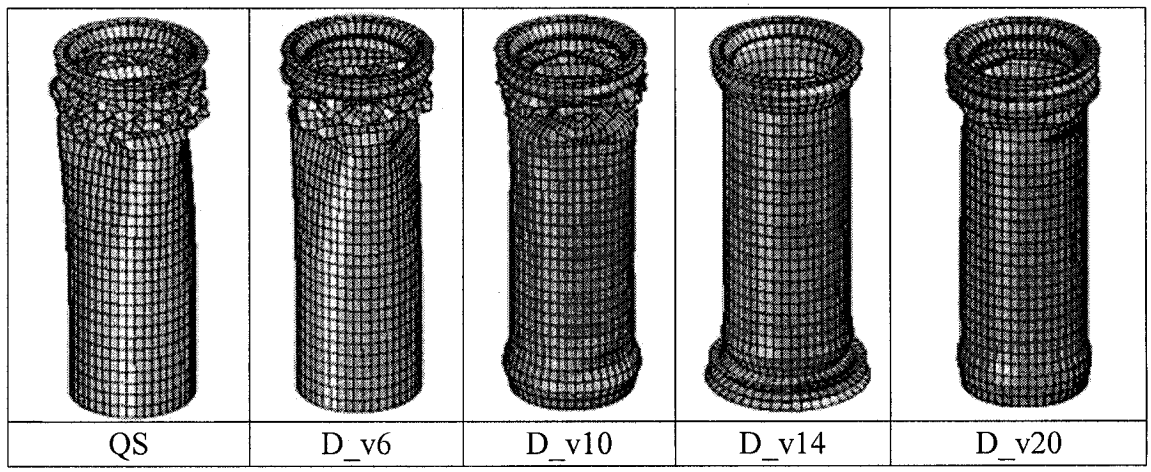

Figure 4-17: Crushing profiles of 5D aluminum tubes without cutout

Figures 4.18-4.20 show the crushing profiles of 5D aluminum tubes with a cutout at three different locations, subject to quasi-static and dynamic crushing loadings of various impact velocities. For 5D aluminum tubes with a cutout at its mid-height, a global buckling mode is observed in quasi-static crushing case, whereas a more stable crushing

mode is observed when the tube is subject to dynamic crushing load. Large deformation initially occurs near the cutout in relatively low velocity (6-10 m/s) dynamic crushing, whereas folding forms firstly at the top end when the velocity of dynamic crushing load is between 14-20 m/s. It is observed from Figure 4.19 that the crushing modes are all in global buckling mode in all loading conditions when the cutout is located at its 70% height. The crushing modes are all in progressive crushing mode in all loading conditions when the cutout is located near the top end, as shown in Figure 4.20.

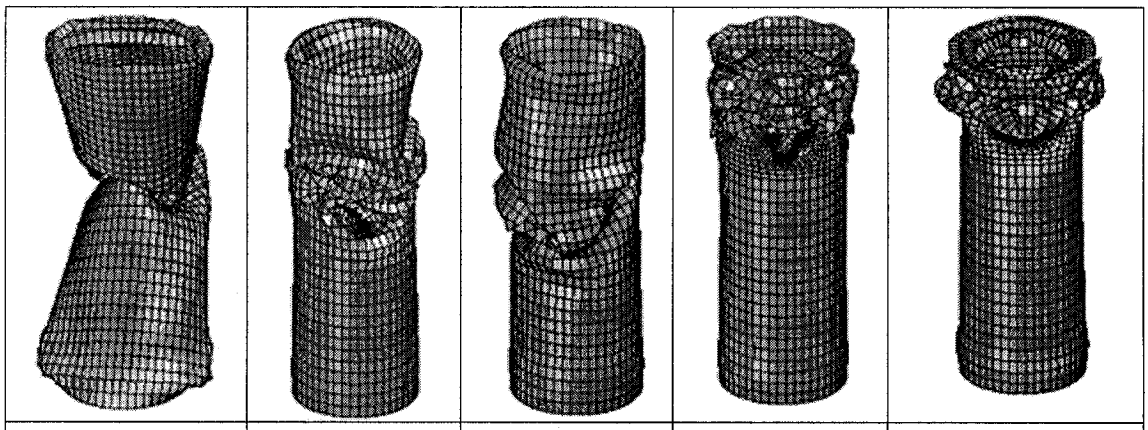

Figure 4-18: Crushing profiles of 5D aluminum tubes with a cutout at their mid height

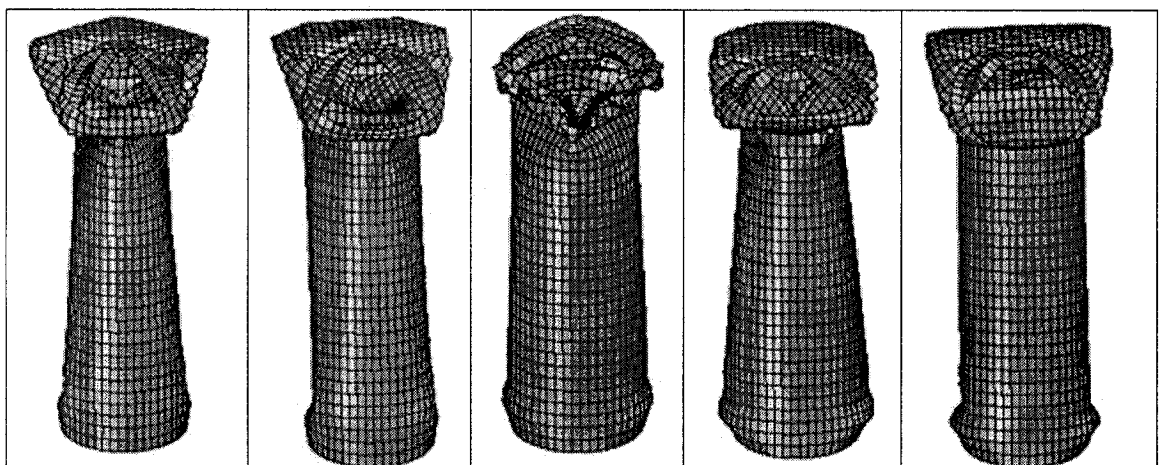

Figure 4-19: Crushing profiles of 5D aluminum tubes with a cutout at $L_0 = 0.70L$

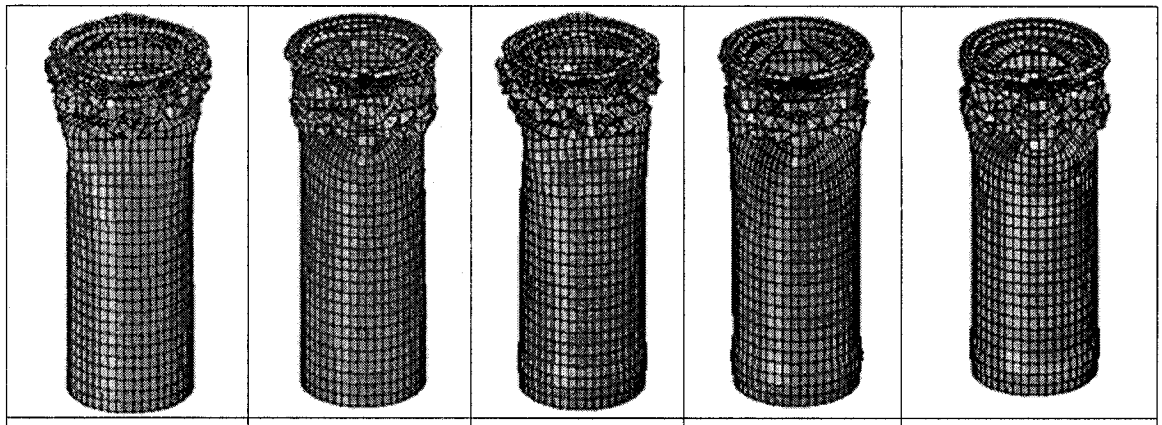

Figure 4-20: Crushing profiles of 5D aluminum tubes with a cutout at $L_0 = 0.90L$

Similar results for 10D aluminum tubes are illustrated in Figures 4.21-4.24. The analogous phenomena of transition of folding initiation from top end, to simultaneously top and bottom end, then to top end, is observed in 10 aluminum tube without cutout, as shown in Figure 4.21.

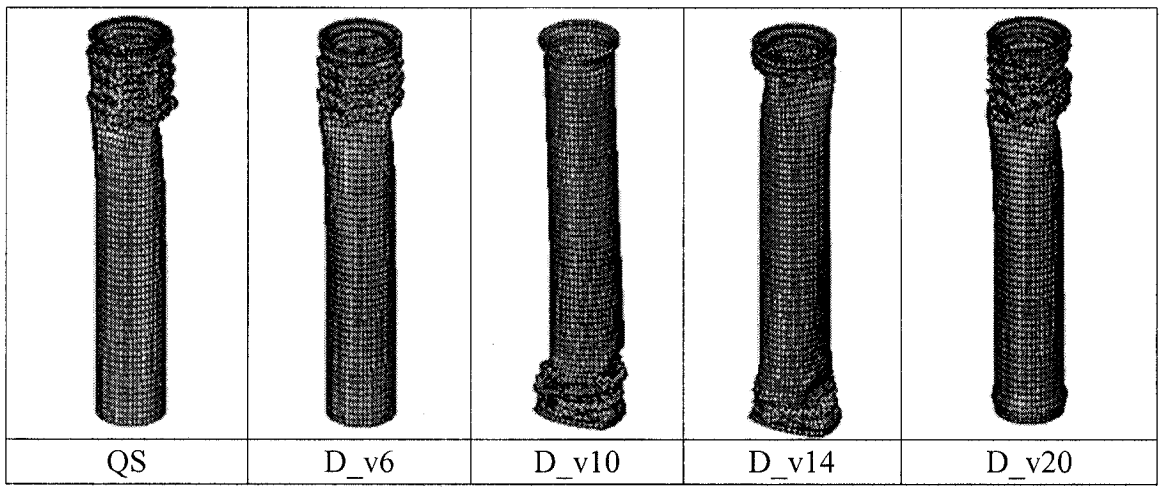

Figure 4-21: Crushing profiles of 10D aluminum tubes without cutout

When the cutout is located at the mid-height of the 10D aluminum tube, the crushing modes are all in global buckling mode, as shown in Figure 4.22. When the cutout is located at its 75% height (see Figure 4.23), the crushing mode is in global buckling mode in quasi-static and relatively low velocity (6-14 m/s) dynamic crushing. The crushing mode turns to be a progressive crushing mode, as the velocity of the

dynamic crushing load is increased to 20 m/s. the crushing modes are all in progressive crushing mode when the cutout is located near the top end, as shown in Figure 4.24.

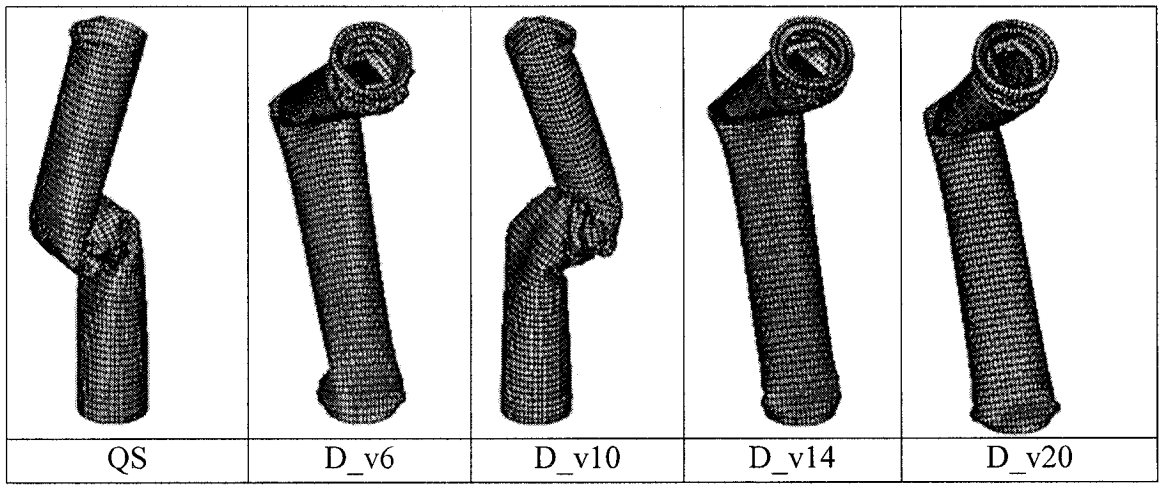

Figure 4-22: Crushing profiles of 10D aluminum tubes with a cutout at $L_0 = 0.50L$

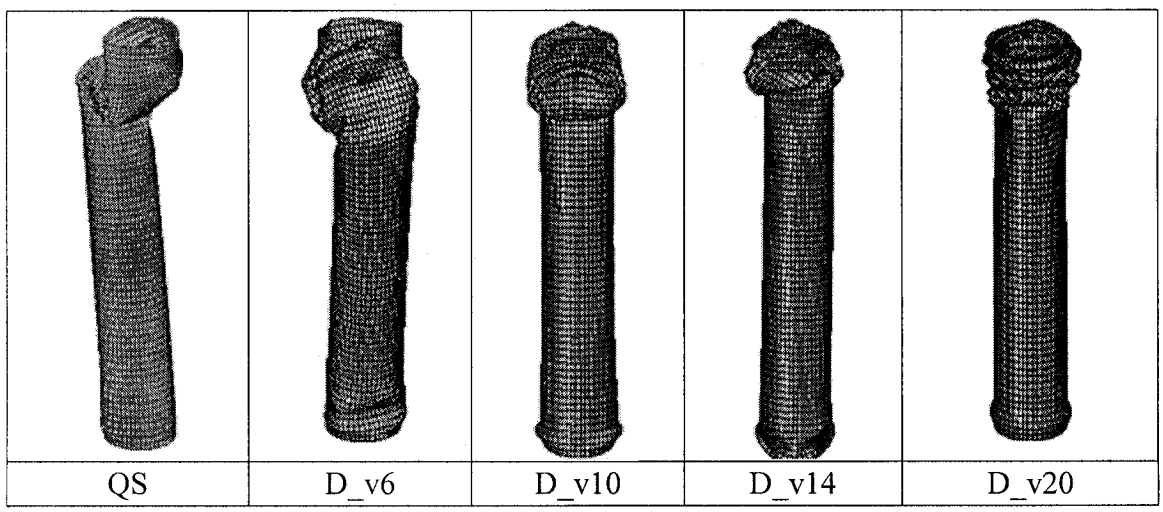

Figure 4-23: Crushing profiles of 10D aluminum tubes with a cutout at $L_0 = 0.75L$

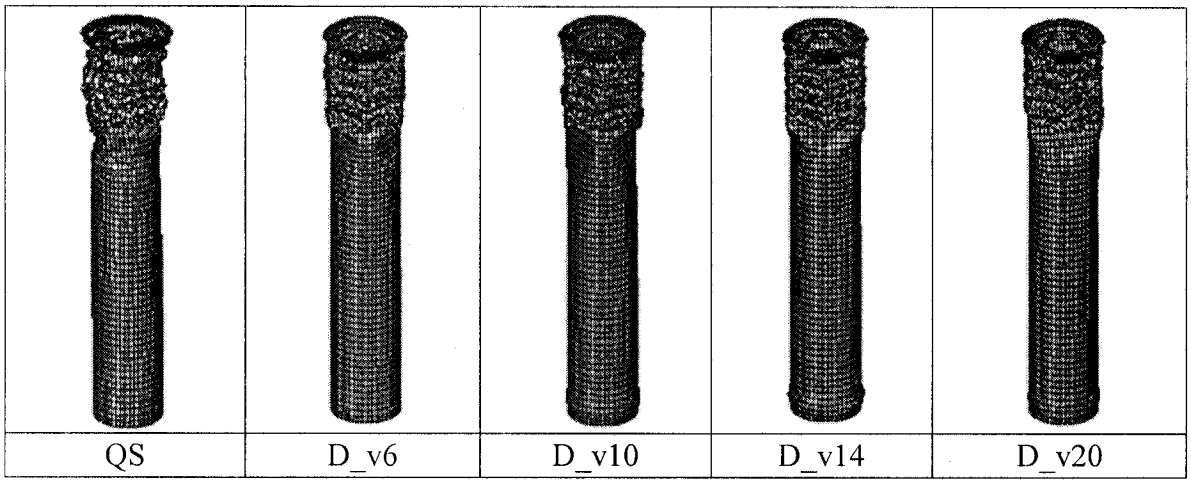

Figure 4-24: Crushing profiles of 10D aluminum tubes with a cutout at $L_0 = 0.95L$

4.10.2 Steel tubes

The crushing profiles for steel tubes made of MAT 2 are presented in this section, shown in Figures 4.25-4.32. Owing to the similarity between steel tubes made of MAT 1 and MAT 2, the crushing profiles of steel tubes made of MAT 1 will not be discussed.

Figures 4.25-4.26 show the crushing profiles of the 2D steel tubes without and with a cutout at its mid-height, subject to quasi-static and dynamic crushing loadings. It is seen that the 2D steel tubes are crushed in a more accordion type when the crushing velocity is increased from zero to 20 m/s.

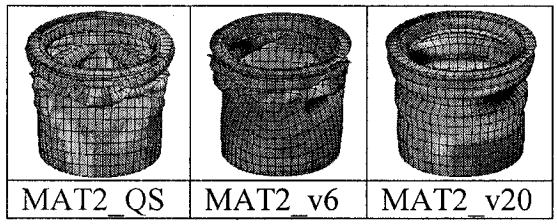

Figure 4-25: Crushing profiles of 2D steel tubes without cutout

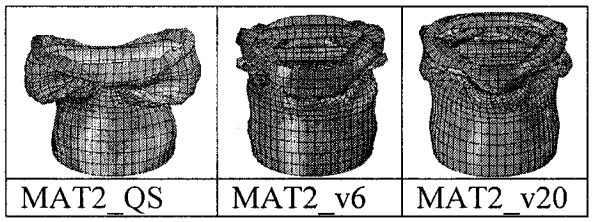

Figure 4-26: Crushing profiles of 2D steel tubes with a cutout at their mid height

The crushing profiles of 5D steel tubes without a cutout, with a cutout at its mid height and near top end, are illustrated in Figures 4.27-4.29. Similar conclusion can be drawn as from the aluminum 5D tubes.

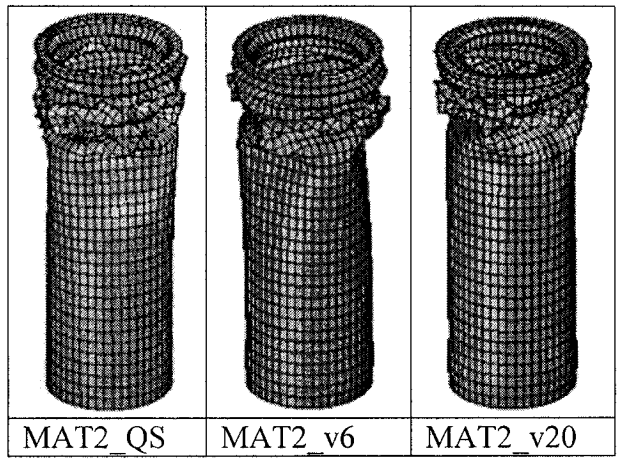

Figure 4-27: Crushing profiles of 5D steel tubes without cutout

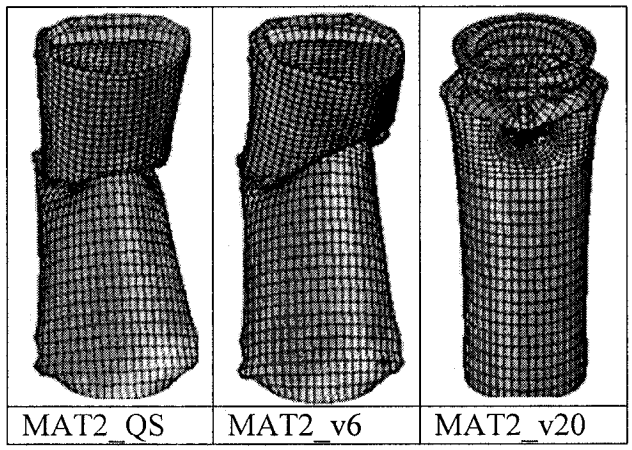

Figure 4-28: Crushing profiles of 5D steel tubes with a cutout at $L_0 = 0.50L$

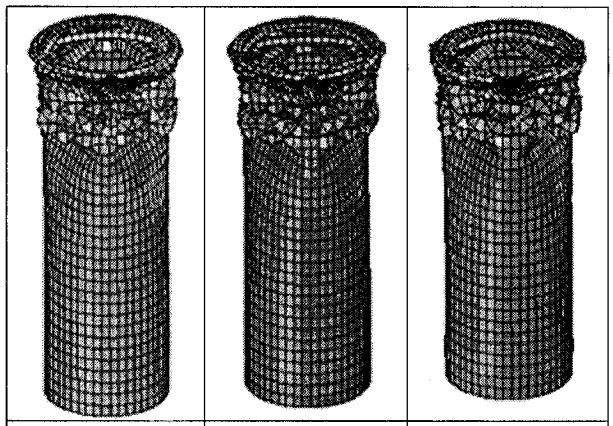

Figure 4-29: Crushing profiles of 5D steel tubes with a cutout at $L_0 = 0.90L$

Likewise, the crushing profiles for 10D steel tubes without and with a cutout at two different locations, subject to quasi-static crushing and dynamic crushing with velocity of 6 m/s and 20 m/s, are shown in Figures 4.30-4.32. Unsurprisingly, the tubes without a cutout and with a cutout near the top end are crushed in a progressive crushing mode in all loading conditions. It is noted from Figure 4.30 and 4.32 that when the velocity of dynamic crushing load is 6 m/s, the tubes are not crushed up to the crushing displacement of 160 mm. The reason is that the energy input to the tube (1800 J) is not sufficiently high to crush the tube by 160 mm distance, as has been discussed in Section 4.5.3 of Chapter 4. It is also observed from Figure 4.31 that when the cutout is located at the mid-height of the 10D steel tube, the tube is crushed in a global buckling mode, broken into two segments at mid-height when subject to quasi-static crushing; whereas the tube is crushed into three-segment global buckling mode when subject to dynamic crushing of 6 m/s. the crushing mode is mix of global buckling and progressive crushing initiated at the loaded end when the tube is subject to dynamic crushing of 20 m/s.

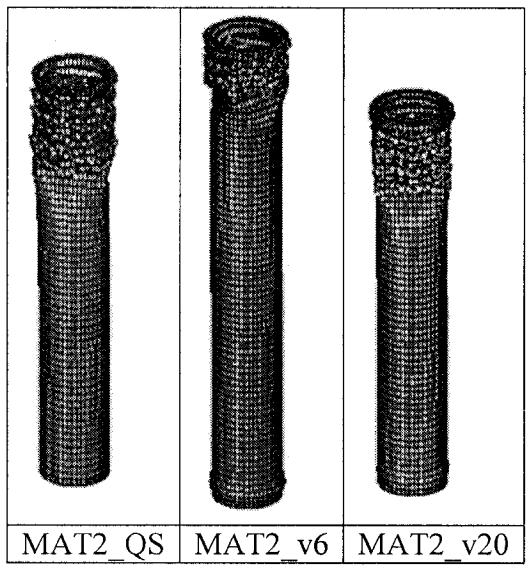

Figure 4-30: Crushing profiles of 10D steel tubes without cutout

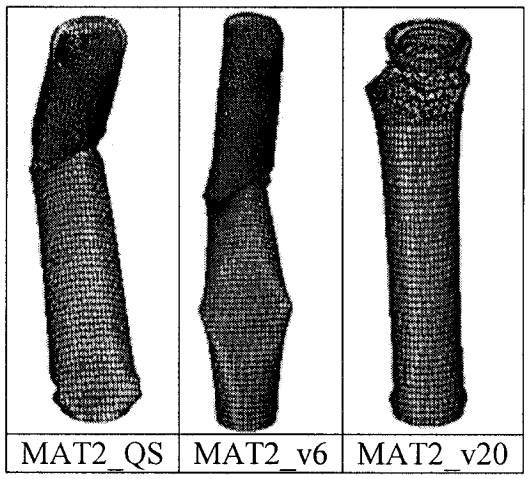

Figure 4-31: Crushing profiles of 10D steel tubes with a cutout at $L_0 = 0.50\text{L}$

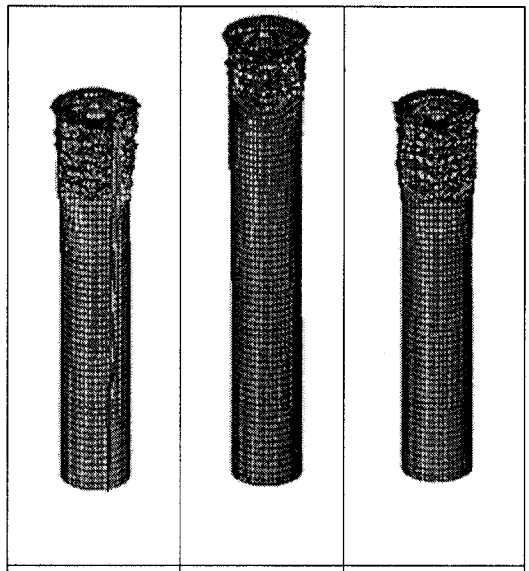

Figure 4-32: Crushing profiles of 10D steel tubes with a cutout at $L_0 = 0.95L$

4.11 Appendix B: Verification of empirical equations in section 4.6

More numerical simulations on aluminum and steel tubes with a cutout at random locations, subject to impact loadings of arbitrary velocity within the specified range, are carried out to verify the empirical equations that have been developed from the available numerical results. Table 4.3 tabulates the comparison of mean and peak crushing forces predicted by empirical equations (4.6~4.16) and numerical simulation. The cases that have been selected in this verification study include 5D and 10D aluminum and steel tubes, having a cutout at their 80% height, subject to quasi-static and dynamic crushing of 8 m/s and 16 m/s. The empirical mean and peak crushing forces calculated from equations (4.6-4.16) are in most cases within 8 percent of the numerical results, i.e., the empirical predictions are reasonably close to the numerical prediction.

Table 4-3: Comparison of numerically and empirically predicted mean and peak crushing forces

Material	Type of tube	Loading condition	Mean crushing force (KN)			Peak crushing force (KN)		
			Empirical	Numerical	% Difference	Empirical	Numerical	% Difference
Aluminum	5D80L	QS	7.18	6.95	3.31%	17.04	16.97	0.41%
	5D80L	D_v=8m/s	7.10	6.78	4.72%	17.30	17.95	-3.62%
	10D80L	QS	6.48	6.35	2.05%	16.23	16.75	-3.10%
	10D80L	D_v=16m/s	6.73	7.01	-3.99%	16.72	17.52	-4.57%
Steel (MAT2)	5D80L	QS	9.87	10.60	-6.89%	36.39	34.11	6.68%
	5D80L	D_v=8m/s	11.21	11.50	-2.52%	39.11	42.11	-7.12%
	10D80L	QS	8.48	8.55	-0.82%	34.05	32.50	4.77%
	10D80L	D_v=16m/s	9.52	9.81	-2.96%	36.35	38.61	-5.85%

Chapter 5 A Numerical Study on the Axial Crushing Response of Hybrid Pultruded and $\pm 45^{\circ}$ Braided Tubes

Haipeng Han[a], Farid Taheri [a], Neil Pegg[b], and You Lu[a]

[a]Department of Civil Engineering, Dalhousie University, 1360 Barrington Street, Halifax, NS B3J 2Z1

[b]Defense Research and Development Canada – Atlantic, 9 Grove Street, Dartmouth, NS, B2Y 3Z7

Accepted for publication in the Journal of "**Composite Structures**" in April 2006

5.1 Abstract

A comprehensive numerical investigation was carried out to evaluate the response and energy absorbing capacity of hybrid composite tubes made of unidirectional pultruded tube over wrapped with $\pm 45^{0}$ braided fiber-reinforced plastic (FRP). The numerical simulation characterized the crushing behaviors of these tubes subject to both quasi-static compression and axial dynamic impact loadings. Two types of braided FRP, glass and carbon fibers, were considered. Parametric studies were also conducted to examine the influence of the tube's length, thickness and type of braid, as well as the loading conditions on the crushing behavior of the tubes.

It was observed that although the pultruded tube, which had the highest stiffness among the tubes considered, produced the highest magnitude of energy absorption capacity, it exhibited a non-symmetric failure mode followed by a longitudinal splitting. On the other hand, the hybrid tubes exhibited a more desirable, accordion type failure mode, therefore they are considered to be more suitable candidates as energy absorbing structural members in service conditions.

Keyword: Energy Absorber, pultruded tube, braiders, crushing, finite element

5.2 Introduction

Many practical engineering systems have requirements for absorbing various levels of energy during impact events. Different types of energy absorbers have been developed based on energy dissipation due to friction, shearing, bending, crushing and plastic deformation, to name a few. They are fabricated largely from metallic materials.

Due to the superior strength-to-weight ratio and unmatched design and manufacturing flexibility, composite materials are becoming more popular in replacing conventional materials by offering significant weight reduction and safety. Pultrusion is a process for producing continuous and prismatic shaped composite components, and is one of the most cost-effective processes in the composite industry. As a result, high strength pultruded composite sections are widely used in civil infrastructures, automobiles, aerospace structures, submarines and in mining and oil & gas applications. Due to their relatively high strength and stiffness in the longitudinal direction, tubular pultruded sections may be considered as effective energy absorbers when subjected to quasi-static or dynamic axial loadings, especially when weight saving is a design constraint.

A large number of experimental and theoretical studies have been conducted in the past to examine the progressive collapse mode of metallic thin-walled tubes under the axial compressive loading. The latest review of crushing response of steel tubes can be found in [1]. The increased interest in using fiber-reinforced polymer composite (FRPC) for light weight structures has also prompted research on investigating the axial crushing performance of composite tubes [2-12]. Most of the early research studies, whether considering quasi-statically or dynamically applied loading, have been experimental in nature. The previous researches studied the crushing behavior of composite tubes made of carbon/epoxy, glass/epoxy, glass/vinyl ester, graphite/epoxy and sandwich materials. The tubes considered were fabricated by hand lay-up, pultrusion, filament winding, weaving and stitching. The geometry of the tubes included circular, elliptical, square and cone shapes. The studies considered the crushing modes and the energy absorption capacity of the tubes. Virtually all the previous studies investigated the influence of the stacking sequence on the crushing behaviors of the composite components, and some [4, 7 and 8], also considered the influence of the vertex angle in the cone shaped tubes.

Moreover, in consideration of performance of light weight energy absorbers, several numerical and experimental works [13-16] have also studied the crushing behaviors and energy absorption capability of hybrid tubes comprising of metal tubes with filament wound composite overwrap.

There have been several works that have taken advantage of hybridization of composite materials as a new concept in the design of energy absorbers [17-25]. Again, most of these studies have been conducted experimentally and have considered only the crushing resulting from quasi-static loading. The use of biaxially braided composite tubes, combination of biaxially and triaxially braided tubes, and hybrid of filament wound laminated tubes with different combinations of carbon and glass fibers were also reported in [17-20]. It was found that tri-axial hybrids could provide enhanced specific energy absorption attributes through the combination of transverse shearing, bending, crushing, and local accordion type buckling modes. Segmented and non-segmented composite tubes were discussed as another way of hybridization by Abosbaia *et al.* [21]. The segmented composite tube consisted of three different material regions. It was found that segmented composite tubes made of carbon fiber fabric and cotton fiber fabric exhibited good energy absorption capability as well as stable load-carrying capacity. A good example on the numerical simulation of hybrid composite tube can be found in [22]. In that study, Mamalis *et al.* [22] investigated the collapse of square sandwich composite vehicle hollow body shells with reinforced core. The crushing behavior and energy absorption efficiency of hybrid and non-hybrid natural fiber composite solid cones were also presented by Mahdi and his co-workers in [23]. The most relevant studies to the subject considered in our investigation are perhaps the work of Saito *et al.* [24] and that reported by Okano *et al.* [25]. These two studies demonstrated that braided/pultruded hybrid composites, produced in the form of rods, exhibited superior response, in terms of energy absorption capability, in comparison to the unidirectional pultruded rods. It was also shown that the braiding angle of 30°, together with the use of a flexible resin could produce the most optimized rod for absorbing energy. These works have demonstrated that hybridization could be used not only to enhance the energy absorption capacity, but also to provide predictable sequences of stable crushing modes.

In pultrusion process, it is rather difficult to place the fibers in an angular orientation, despite the high productivity rate associated with this process. Braiding technology is also a cost-effective manufacturing process. The hybridization of pultrusion and braiding is highly promising due to the ease of manufacturing. To the authors' knowledge, no work has considered the crushing response of such cost-effective hybrid FRPC tubes. A comprehensive numerical investigation was therefore carried out to study the crushing performance of hybrid pultruded/braided FRPC tubes. Two types of braiding, namely, carbon and glass fiber epoxy braiding were investigated. In this numerical study, the characteristics of such tubes, subject to both quasi-static and dynamic axial crushing loadings, were studied. Two tube lengths (L=5D and L=10D) were considered. The results provided by this work would enhance the data needed for the effective design of composite structural components for energy absorption applications.

5.3 Features in numerical modeling

The LS-DYNA [26] code was used in conducting all the simulations. Before conducting an extensive numerical modeling of the hybrid tubes, a preliminary study was conducted to gain a basic understanding of the response of pultruded tubes. Due to similarity of the numerical procedures, however, the modeling of the hybrid tubes only is described here. A few studies (such as the one by El-Hage [15]) have considered the crashworthiness simulation procedures of aluminum-composite hybrid tubes. As stated, Mamalis *et al.* [22] also numerically investigated the crashing behaviors and energy absorption characteristics of thick-walled square tubular crashworthy bodyshells made of hybrid sandwich composite panels with integral FRP hollow cylindrical inserts. However, as stated earlier, simulation studies on hybrid FRPC tubes have not been conducted in the past.

The geometric configuration of the hybrid tube is shown in Figure 5.1. The central diameter of the pultruded pipe is 40 mm and its wall thickness is 3.174 mm. The pultruded tubes are made of high strength glass fiber sections manufactured by Creative Pultrusion Inc (PA, USA). The braiding thickness is either 0.3 mm or 1.0 mm, depending

on the type of the braiding (i.e., either light fabric or medium fabric). Both glass and carbon fiber braids were considered. Two tube lengths were modeled in this study; namely, 5D (200 mm long) and 10D (400 mm long) tubes. The biaxial carbon and glass fiber braidings are manufactured by A & P Technologies (OH, USA). Four different tube combinations were analyzed in the numerical simulation, namely, HPG1, HPG2, HPC1 and HPC2. Here HPG1 refers to the hybrid of pultruded tube with the glass fiber braiding of 0.3 mm thickness, and HPG2 refers to the combination of the pultruded and glass fiber braiding of 1.0 mm thickness. The same rule applies for HPC1 and HPC2, where glass (G) is replaced by carbon (C).

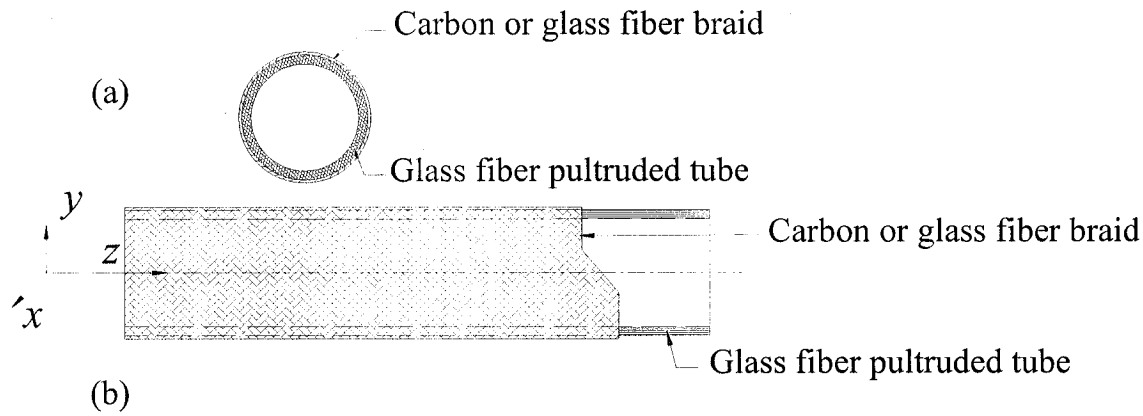

Figure 5-1: Configuration of the hybrid of pultruded and composite braided tubes

5.3.1 Element type used in the simulation

The Belyschko-Tsay quadrilateral element was used to model both the pultruded tube and composite braids. The meshed shell elements were located at the mid-plane of each tube (i.e., on the mid-plane of the pultruded tube and the overwrap), which were separated by a small gap equal to the average thickness of the two walls. Contact algorithms were used to connect the pultruded tube shell element and the braided shell elements, so as to properly simulate the interaction between the two sub-components. The pultruded tube was modeled as 2 layers of 0^0 lamiae, and the braid by 4 layers of $\pm 45^0$ lamiae. The integration points representing different layers of certain stacking orientations were located evenly through the thickness. Consequently 6 integration points

through the thickness were needed to model the hybrid material. The model for the 5D hybrid tube was comprised of a total of 4900 elements connected with 5017 nodes.

5.3.2 Material model

The constitutive material model 54 of LS-DYNA was selected to model both the pultruded tube and the braided one. Material model 54 has the option of using either the Tsai-Wu failure or the Chang-Chang failure criterion for assessing lamina failure. The Chang-Chang criterion is the modification of the Hashin's failure criterion to account for nonlinear shear stress-strain behavior. The criterion also accounts for the post-failure degradation, so that the post failure behavior of the laminate could be considered by the failure of each successive lamina. The post failure conditions in the Material 54 model [26] are slightly different from the original Chang-Chang equations, thus accounting for four types of failure (i.e., tensile fiber mode, compressive fiber mode, tensile matrix mode and compressive matrix mode). According to this model, if fiber breakage and/or fiber matrix shear failure occurs in a lamina, both the lamina's transverse modulus and minor Poisson's ratio are reduced to zero, but the change in the longitudinal modulus and shear modulus follows the Weibull distribution. On the other hand, if matrix failure occurs either in tension or compression, then the transverse modulus and minor Poisson's ratio are reduced to zero, while the longitudinal modulus and shear modulus remain unchanged.

The mechanical properties of the pultruded tube, as well as the glass fiber/epoxy and carbon fiber/epoxy braids in the principle directions are given in Table 5.1. These glass/epoxy properties are adopted from the data sheet provided by the suppliers. The carbon fiber/epoxy material properties are taken from the experimental investigation reported in [27]. The parameters DFAILT and DFAILC of the software are used to assume that the material behaves in an elastic-perfectly plastic manner after the maximum tensile or compressive strain has reached. The parameters FBRT and YCFAC account for the strength reduction in tension and compression, respectively, in the fiber direction after failure of the matrix.

Table 5-1: Mechanical properties of the pultruded tube, glass/epoxy and carbon/epoxy braids in principle directions

Material type		Pultruded tube	Glass/ Epoxy braid	Carbon/ Epoxy braid
Density (Kg/m^3)	ρ	1795	1975	1512
Longitudinal Modulus (GPa)	E_{11}	20.6	30.9	118.0
Transverse Modulus (GPa)	E_{22}	6.9	8.3	5.5
In-plane shear modulus (GPa)	G_{12}	2.9	2.8	4.8
Out-of-plane shear modulus (GPa)	G_{23}	2.9	3.0	4.8
Minor Poisson's ratio	ν_{21}	0.1172	0.0866	0.0127
Longitudinal tensile strength (MPa)	S_L^+	226.9	798.0	1095.0
Longitudinal compressive strength (MPa)	S_L^-	500.0	480.0	712.9
Transverse tensile strength (MPa)	S_T^+	51.6	27.1	26.4
Transverse compressive strength (MPa)	S_T^-	113.4	140.0	84.4
In-plane shear strength (MPa)	S_{LT}	48.3	36.8	84.3
Maximum strain for fiber tension	DFAILT	2.3%	2.3%	2.3%
Maximum strain for fiber compression	DFAILC	1.4%	1.4%	1.4%
Reduction factor for tensile strength in the fiber direction after matrix failure	FBRT	1.0	1.0	1.0
Reduction factor for compressive strength in the fiber direction after matrix failure	YCFAC	3.0	3.0	3.0

5.3.3 Boundary constraints and the Contact algorithm

5.3.3.1 Quasi-static loading case

In the modeling of quasi-static crushing, the bottom end of the hybrid tube was assumed to be built-in, thus all degrees of freedom at this location were constrained. The upper end was free and subjected to compression by a loading plate. The loading plate was modeled as a rigid plate, and its mass was assumed to be 100 kg. As shown in [15], the masses of both loading plate and tube could be scaled up for the purpose of computation efficiency, while still maintaining a quasi-static condition. In this study, the density of the loading plate and tube were therefore scaled-up by a factor of 1000. It was observed that the ratio of the total kinetic energy (KE) to the total internal energy was less than 5% over the period of the crushing process, thus enforcing a quasi-static

condition. The loading plate was displaced using LS-DYNA's *BOUNDARY_PRESCRIBED _MOTION_RIGID command at a constant rate of 100 mm/sec. Two types of contact algorithms were used to simulate the boundary conditions in quasi-static crushing. The first one was to simulate the interface between the loading plate and the upper end of the hybrid tube using the command *CONTACT_CONSTRAINT_NODES_ TO_SURFACE. The interface force between the loading plate and the tube was then extracted to provide the force-displacement response. The other algorithm was used to prevent the tube from drifting on its lower end. This was done by employing the *RIGIDWALL_GEOMETRIC_FLAT command, by which a flat rigid surface was defined in the location beneath the tube. This would ensure that the tube would always stay on the top of this rigid surface in the event the bottom end of the tube starts folding.

5.3.3.2 Dynamic axial impact case

In the modeling of the dynamic axial crushing, the same boundary conditions as described above were applied. The tube was impacted by the loading plate with certain downward velocities. The initial velocity of the loading plate was imposed by the command *INITIAL_VELOCITY_RIGID_BODY.

In both the quasi-static and dynamic crushing simulations, two other contact algorithms were also used to model the behavior of the hybrid tube. One was a self-contact algorithm to prevent interpenetration during the progressive folding of the tube using the command *CONTACT_AUTOMATIC_SINGLE_SURFACE, which was also used to simulate the interaction between the pultruded and braided tubes. A contact algorithm was used to tie the pultruded tube to the braided tubes, by the command *CONTACT_TIEBREAK_NODES_ONLY. The contact algorithm accounts for both normal and shear forces at the interface. The tiebreak criterion in this algorithm follows the following relationship [26].

$$\left(\frac{f_n}{NFLF}\right)^2+\left(\frac{f_s}{SFLF}\right)^2 \geq 1.0 \qquad (5.1)$$

where f_n is the normal force at the interface; f_s is the shear force at the interface; NFLF is the normal force at the bond failure and SFLF is the shear force at the bond failure.

In this study, the values of both NFLF and SFLF were assumed to be 100 N, which is related to the mechanical properties of the resin [15]. A parametric study was also conducted to study the effect of this failure force as will be discussed later. It suffices to state that the variation of the failure force has minor influence on the crushing pattern, as well as the energy absorption capability of the tubes.

5.4 Results and discussion

5.4.1 Preliminary study - the pultruded tube

A preliminary study was conducted to study the crushing behavior and energy absorption capability of the 5D composite tubes having the same thickness, but with different stacking sequences. Both the quasi-static compression and dynamic impact were considered in this preliminary study. In the modeling of the dynamic crushing of tubes, the initial velocity of the loading plate was assumed as 6 m/s. The quasi-static and dynamic axial crushing responses of these tubes are plotted in Figure 5.2a and 5.2b, in which the distance is referred to the distance that is traveled by the loading plate. The plots illustrate the crushing responses within the first 80 mm distance from the top end of the tube. Five different stages during the dynamic crushing response of the pultruded tubes with $[0]_4$ and $[\pm 45]_2$ lay-ups are shown in Figure 5.2c and 5.2d. The energy absorption capacities of these tubes are illustrated in Figure 5.3. Figure 5.3a shows the absolute energy absorption by the tubes, and Figure 5.3b illustrates the normalized energy absorption with reference to the effective flexural stiffness $\overline{D}_{11}$ of the tubes. The effective flexural stiffness is defined by equation (5.2), which accounts for the nonsymmetric laminate and integrates the effect of axial stiffness A_{11}, the bending-extensional coupling stiffness B_{11} and the flexural stiffness D_{11}.

$$\overline{D}_{11} = \frac{A_{11}D_{11} - B_{11}^2}{A_{11}} \tag{5.2}$$

The general specifications of the model and their responses are summarized in Table 5.2. As can be seen from Table 5.2, for the same thickness, the $[0]_4$ pultruded tube

exhibits the highest energy absorption capability, in both quasi-static and dynamic crushing events, although it shows the lowest peak crushing force among all the tubes considered. At a first glance, one would therefore select the $[0]_4$ pultruded tube as an effective design for an energy absorber. However, as alluded by [2], and also illustrated by Figures 5.2c and 5.2d, the pultruded tube would crush in an asymmetric manner, or in a splitting mode. These two characteristics are not desirable when considering an energy absorber. On the other hand, it is seen that the $[\pm 45]_2$ tube is crushed in a symmetric manner in a rather perfect local buckling mode. It is also shown in Figure 5.3b that after normalized with the effective flexural stiffness, the $[\pm 45]_2$ tube possesses the highest value of the normalized energy absorption, which again demonstrates the merit of the $[\pm 45]_2$ tube. It is therefore concluded that combining these two lay-ups might produce an energy absorber that would possess both the described attributes (i.e., a combined symmetric and local buckling failure modes with high energy absorption capacity).

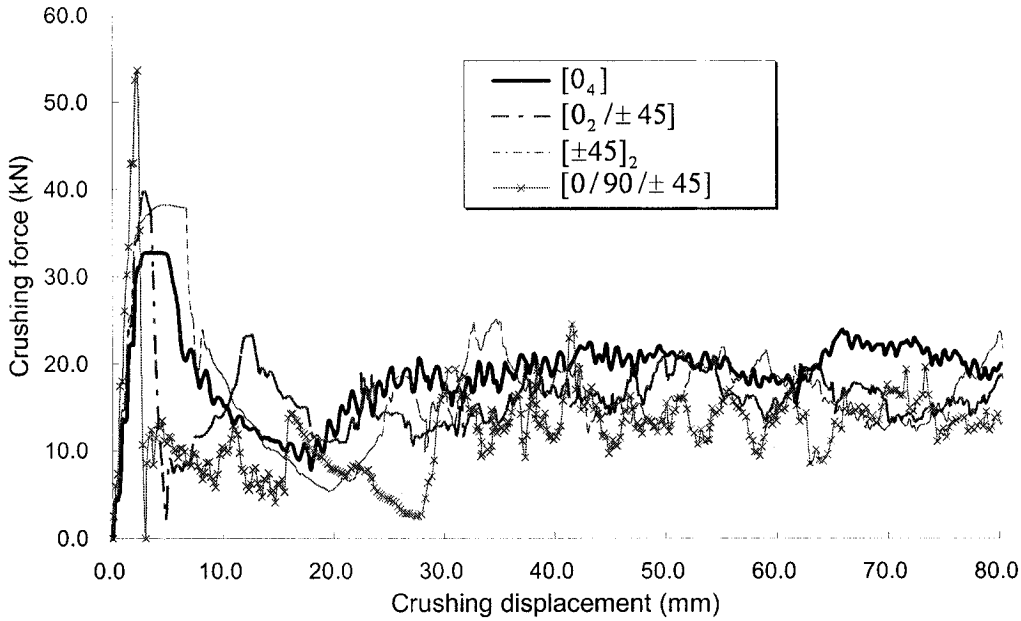

(a) Plot of crushing force vs. crushing displacement in quasi-static crushing

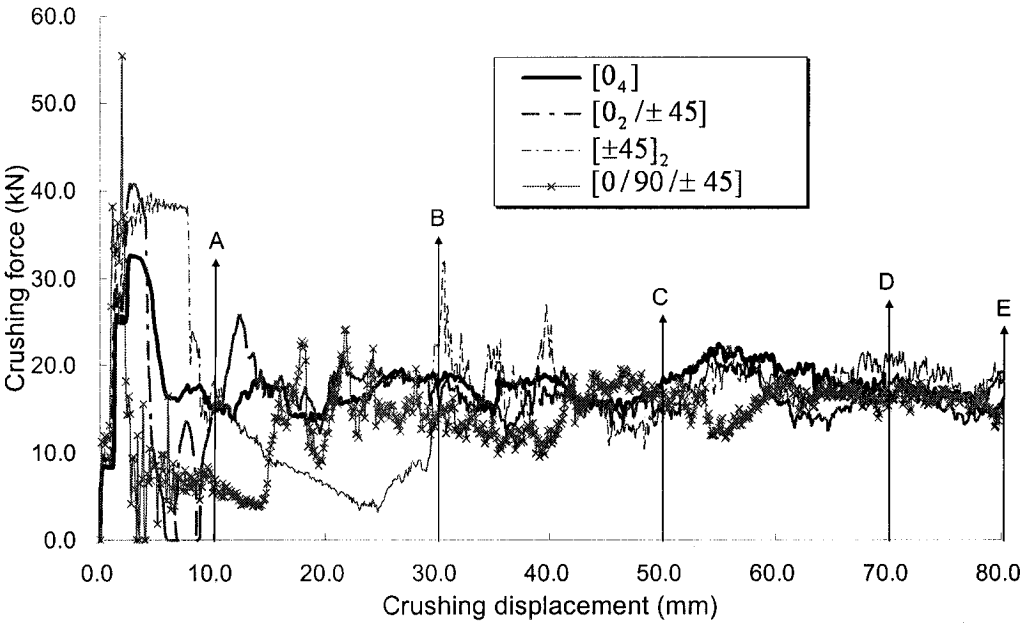

(b) Plot of crushing force vs. crushing displacement in dynamic crushing (v=6m/s)

---(c) and (d) on next page

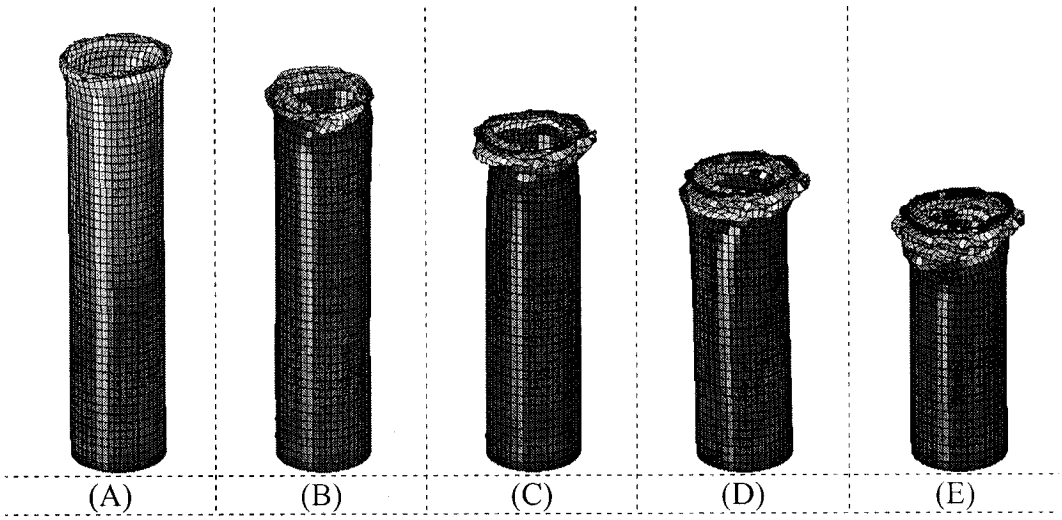

(c) Crushing profiles of $[0_4]$ tube at designated crushing displacement in (b)

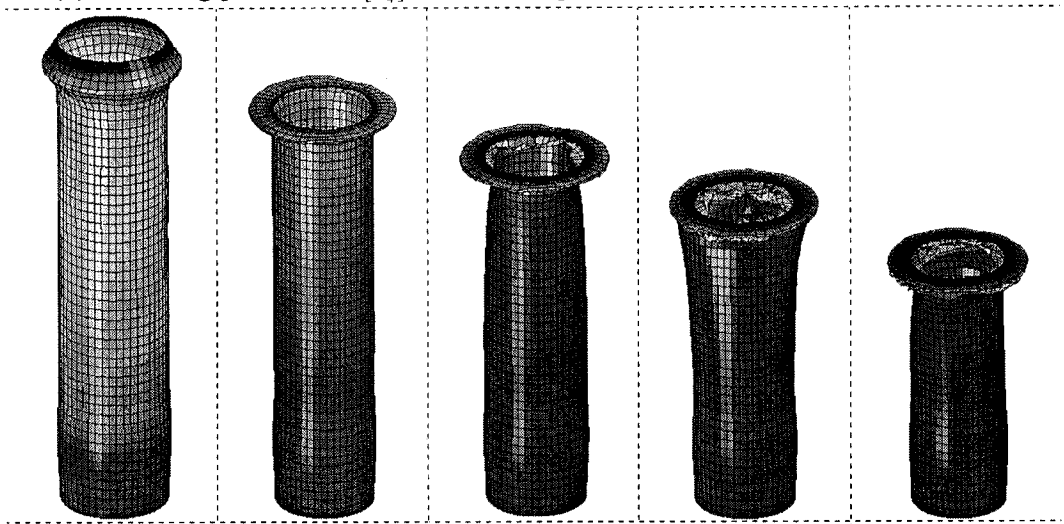

(d) Crushing profiles of $[\pm 45]_2$ tube designated crushing displacement in (b)

Figure 5-2: Crushing response of the composite tubes with the same thickness and different stacking sequences subject to quasi-static and dynamic crushing (v=6 m/s)

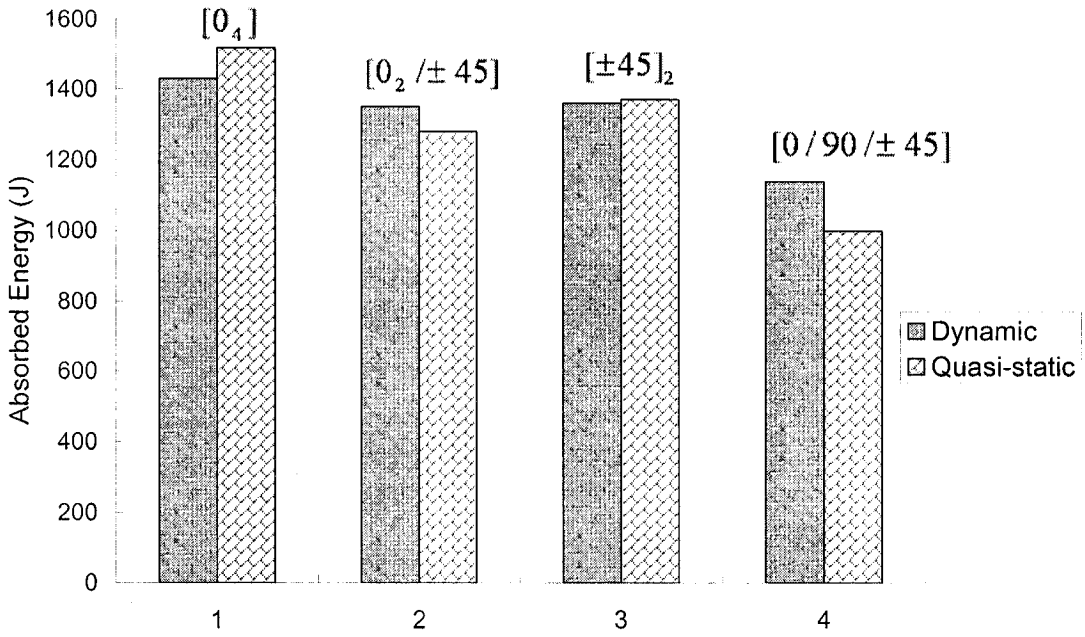

(a) Absolute energy absorption by tubes of same thickness and different stacking sequences

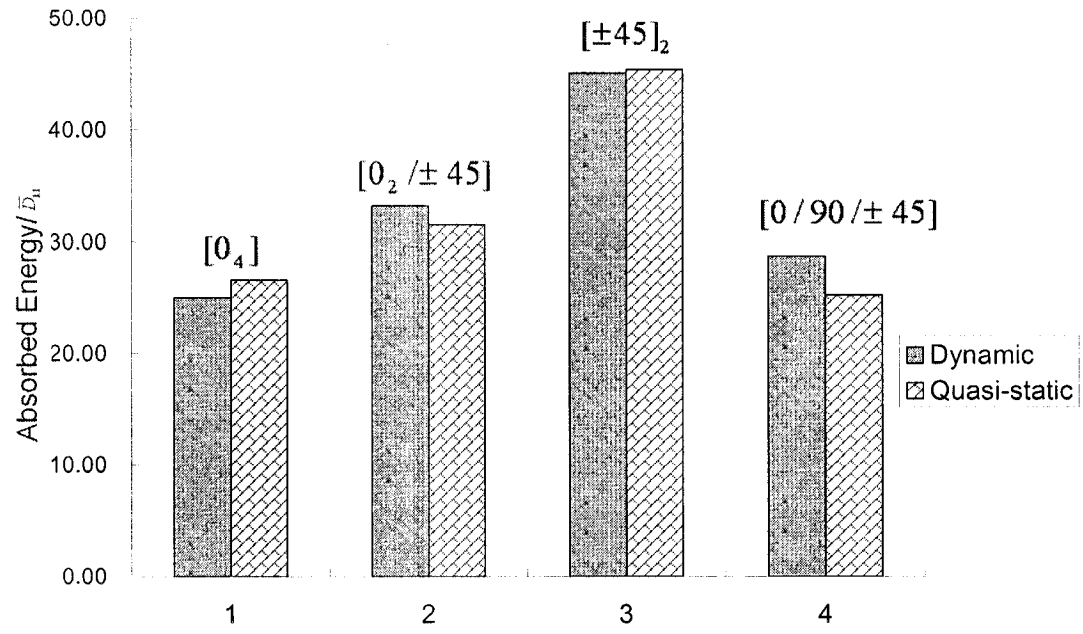

(b) Normalized energy absorption with reference to the effective flexural stiffness

Figure 5-3: Energy absorption capacities of the composite tubes with the same thickness and different stacking sequences subject to quasi-static and dynamic crushing (v=6 m/s)

Table 5-2: Summary on the axial crushing forces of the composite tubes with the same thickness and various stack sequences

Stacking sequence	Loading condition	Absorbed Energy-E (J)*	Peak crushing force-F_I (KN)	Average crushing force-F_{AVI} (KN)
$[0]_4$	Quasi-static	1430	32.63	17.74
	Dynamic	1520	32.75	18.92
$[0_2/\pm 45]$	Quasi-static	1350	40.86	16.70
	Dynamic	1280	39.87	15.99
$[\pm 45]_2$	Quasi-static	1360	39.92	17.26
	Dynamic	1370	38.25	17.00
$[0/90/\pm 45]$	Quasi-static	1140	55.41	14.46
	Dynamic	1000	53.66	12.37
* Note:	Absorbed energy for all tubes is calculated based on 80 mm axial crushing displacement			

5.4.2 Results of the hybrid tubes

In a real crash event, the crushing distance should not progress through the entire length of the energy absorber. Therefore, only the first portion of the crushing displacement curve is used to evaluate the energy absorption capacity of the tubes. For all of the 5D (intermediate length) tubes, the peak crushing force (or crushing initiation force, F_I) is taken from data of the entire crushing event, whereas the absorbed energy and mean crushing force are evaluated for the first 80 mm of crushing distance. For all 10D (long) tubes, the same procedure is repeated, except data for the first 110 mm crushing distance is reported (as opposed to the 80 mm distance for the 5D tubes). Both quasi-static and dynamic axial crushing are simulated for all hybrid tubes. In the simulation of dynamic crushing, two different velocities (i.e., 6 m/s and 14 m/s), were used for the 100 kg loading plate. For all hybrid tubes, the crushing responses of the corresponding pultruded tube without braiding, subject to both quasi-static and dynamic loads, were also simulated and considered. The summary of the results for all hybrid tubes, as well as the corresponding pultruded tubes (without braiding) are given in Table 5.3.

Table 5-3: Summary of the crushing characteristic of the pultruded and composite braid hybrid tubes

Tube Length	Braid type	Braid thickness (mm)	Loading condition	Absorbed Energy (J)*	Peak crushing force (F_i)	Average crushing force (F_{avi})	Energy increase (%)
5D	None	None	Q-S	1520	32.75	18.92	
5D	None	None	D_v=6	1430	32.64	17.74	
5D	None	None	D_v=14	1413	32.1	17.47	
5D	Glass fiber	0.30	Q-S	1650	35.09	20.55	8.55
5D	Glass fiber	0.30	D_v=6	1590	34.8	19.9	11.19
5D	Glass fiber	0.30	D_v=14	1530	33.65	18.85	8.28
5D	Glass fiber	1.00	Q-S	1930	42.1	24	26.97
5D	Glass fiber	1.00	D_v=6	1950	42	24.4	36.36
5D	Glass fiber	1.00	D_v=14	1950	41	22.4	38.00
5D	Carbon fiber	0.30	Q-S	1630	38.2	20.3	7.24
5D	Carbon fiber	0.30	D_v=6	1700	37.9	20.8	18.88
5D	Carbon fiber	0.30	D_v=14	1740	37.42	21.4	23.14
5D	Carbon fiber	1.00	Q-S	2060	54.4	25.5	35.53
5D	Carbon fiber	1.00	D_v=6	2070	55.1	25.8	44.76
5D	Carbon fiber	1.00	D_v=14	2150	54.7	26.3	52.16
10D	None	None	Q-S	1950	32.7	17.9	
10D	None	None	D_v=6	1340	32.8	9.56	
10D	None	None	D_v=14	1300	32.48	11.6	
10D	Glass fiber	0.30	Q-S	2050	33.5	18.5	5.13
10D	Glass fiber	0.30	D_v=6	2060	34.8	18.6	53.73
10D	Glass fiber	0.30	D_v=14	2010	33.28	18.02	54.62
10D	Glass fiber	1.00	Q-S	2420	41.9	22	24.10
10D	Glass fiber	1.00	D_v=6	2490	40.3	22.5	85.82
10D	Glass fiber	1.00	D_v=14	2320	40.3	20.8	78.46
10D	Carbon fiber	0.30	Q-S	2000	36.4	18.2	2.56
10D	Carbon fiber	0.30	D_v=6	2100	33.4	19	56.72
10D	Carbon fiber	0.30	D_v=14	2130	33.7	19	63.85
10D	Carbon fiber	1.00	Q-S	2759	53.8	25	41.49
10D	Carbon fiber	1.00	D_v=6	2660	54.8	24.4	98.51
10D	Carbon fiber	1.00	D_v=14	2810	45.4	25.1	116.15
Note:	**Q-S**: Quasi-static; **D_v=6**: Dynamic crushing (v= 6m/s); **D_v=14**: Dynamic crushing (v=14 m/s); Absorbed energy and mean crushing force are calculated based on 80 mm axial crushing displacement for 5D (200 mm) tubes, and 110 mm for 10D (400 mm) tubes						

As seen from Table 5.3, for both 5D and 10D pultruded tubes (P_5D and P_10D), the peak crushing forces (F_1) are very similar in the three loading conditions considered. The energy absorption capability of the 5D pultruded tubes (P_5D in Table 5.3) in the quasi-static case is slightly higher than that of the dynamic loading cases (1520 J compared to 1430 J and 1413 J). However, in the long pultruded tubes (P_10D in Table 5.3), the value in the quasi-static case is significantly greater than those in dynamic load cases (i.e., 1950 J compared to 1340 J and 1300 J) within the same crushing distance.

5.4.2.1 Glass fiber epoxy pultruded and braided hybrid tubes

Two different thicknesses (0.3 mm and 1.0 mm) of braids were used to overwrap the pultruded tubes to form the hybrid tubes. Figures 5.4a and 4b show the crushing response of the 5D and 10D hybrid tubes, namely HPG1_5D and HPG1_10D (the tubes with 0.3 mm thick glass fiber overwrap). Figures 5.4a and 5.4b show that there is a considerable transition in the force-crushing distance curves for both quasi-static and dynamic crushing events. It is also observed that the peak crushing forces are almost within the same magnitude under both loading conditions in both HPG1_5D and HPG1_10D. It is also seen from Figure 5.4b that the crushing forces were reached in two stages in all HPG1_10D tubes. As seen, after the first spike in crushing initiation force, the crushing force drops dramatically down to 5 KN. After the crushing distance of 20 mm, the folding force will remain relatively constant. As seen from Table 5.2, by using the 0.3 mm glass fiber overwrap, the energy absorption capability of the 5D tubes was increased by 8.55% in quasi-static crushing, and by 11.19% and 8.28% in the 6 m/s and 14 m/s dynamic crushing case, respectively. In the 10D tubes, however, the energy absorption capacities were increased by 5.13% in quasi-static crushing, and 53.73% and 54.62% for the dynamic impact events with velocities of 6 m/s and 14 m/s, respectively. Although the energy absorption capacities were improved remarkably in the above tubes, with the presence of the glass fiber braidings, the peak crushing force only increased by a very small magnitude, particularly in the 10D tubes. This is a desirable attribute for an effective energy absorber. For example, if such a component is used as an energy absorber in a race car, or in an aircraft landing gear, it would absorb considerable energy, exerting less force to the occupants of the vehicle.

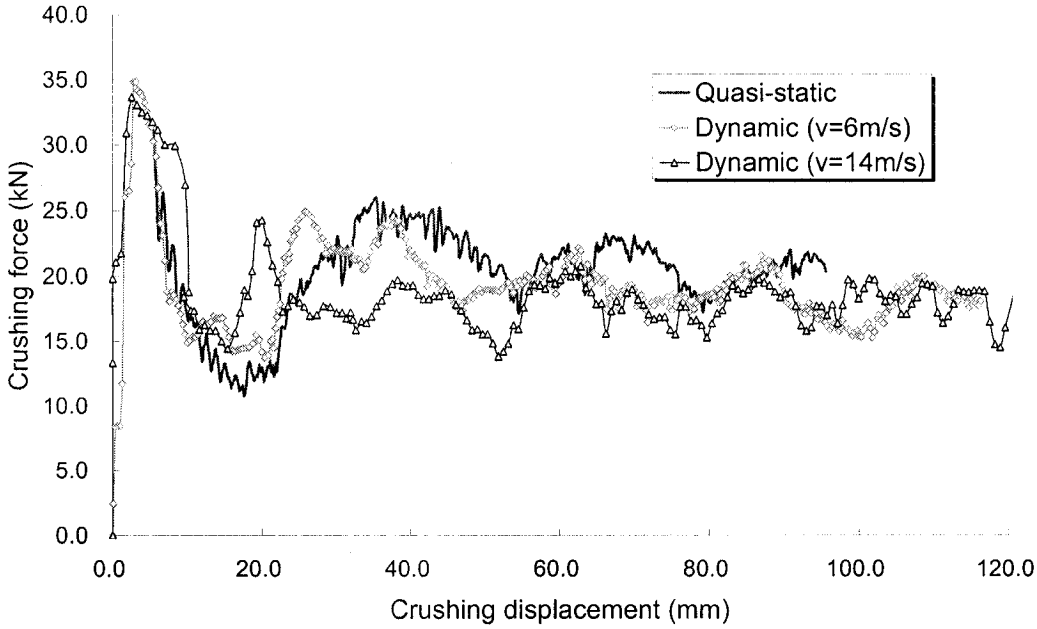

(a)- HPG1_5D

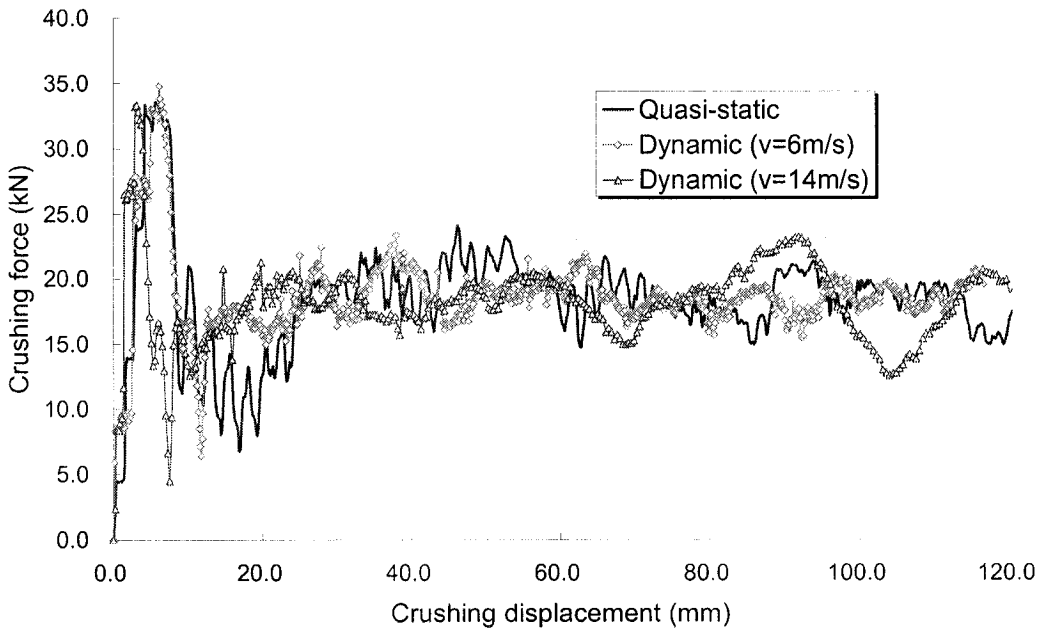

(b)- HPG1_10D

---(c) and (d) to be continued on next page

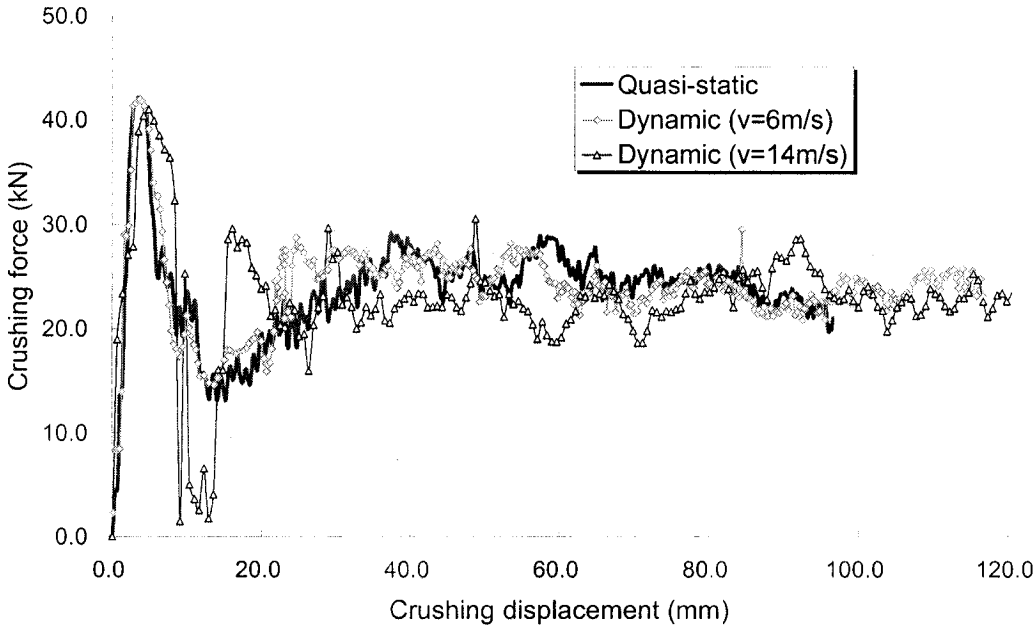

(c)- HPG2_5D

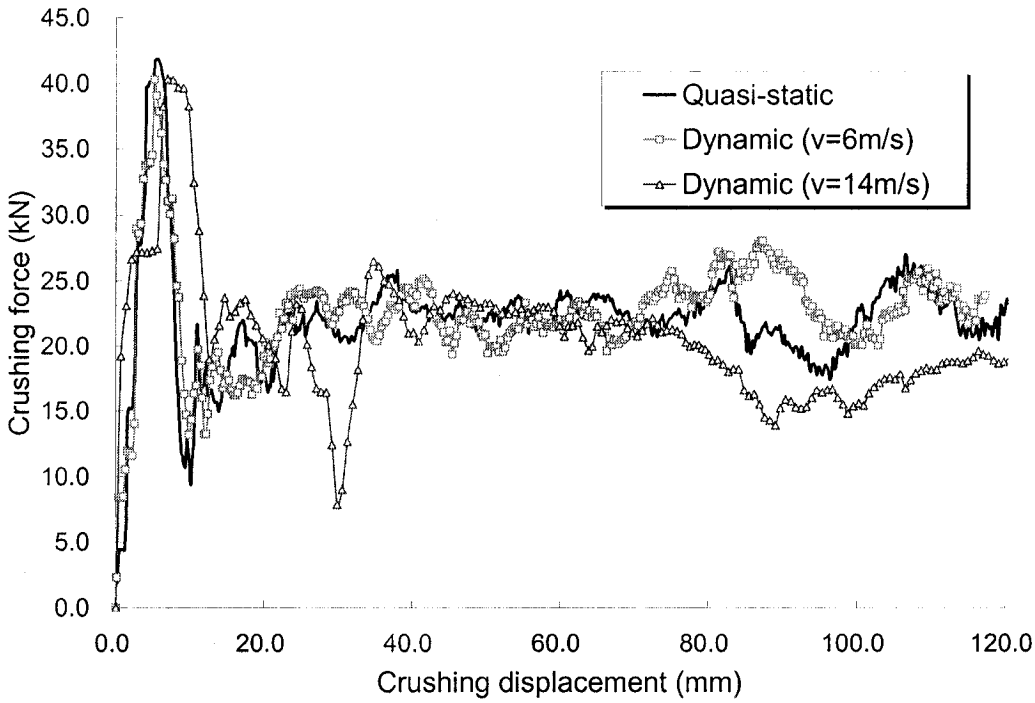

(d)- HPG2_10D

Figure 5-4: Plot of crushing force vs. crushing displacement of the hybrid tubes with glass fiber braids subject to various loading conditions

Figures 5.4c and 5.4d illustrate the crushing response of 5D and 10D hybrid tubes, namely the HPG2_5D and HPG2_10D tubes, with 1.0 mm thick glass fiber braid. It is evident from these two figures that for both 5D and 10D tubes, the responses from quasi-static crushing and dynamic crushing with 6 m/s velocity are very similar, when considering the peak and mean crushing forces, as well as the energy absorption capacities. There is however more significant fluctuation in the dynamic crushing with 14 m/s velocity in both 5D and 10D tubes, particularly at the early stage of the events. Figure 5.5 shows the response of the hybrid tubes (HPG2_5D) at six stages during the event. With the presence of glass fiber braiding, the hybrid tubes are crushed in a more stable manner, that is, in a local buckling mode (see Figure 5.5). As can be seen from the results summarized in Table 5.3, the 1.0 mm glass fiber braid could be used to effectively enhance the energy absorption capacities of the 5D hybrid tubes (in this case by 26.97%, 36.36% and 38.00% for the quasi-static, and the 6 m/s and 14 m/s dynamic crushing cases, respectively). Similarly, the energy absorption capacities of the 10D tubes were improved by 24.10%, 85.82% and 78.46%, for the quasi-static, and the dynamic crushing with the velocities of 6 m/s and 14 m/s, respectively.

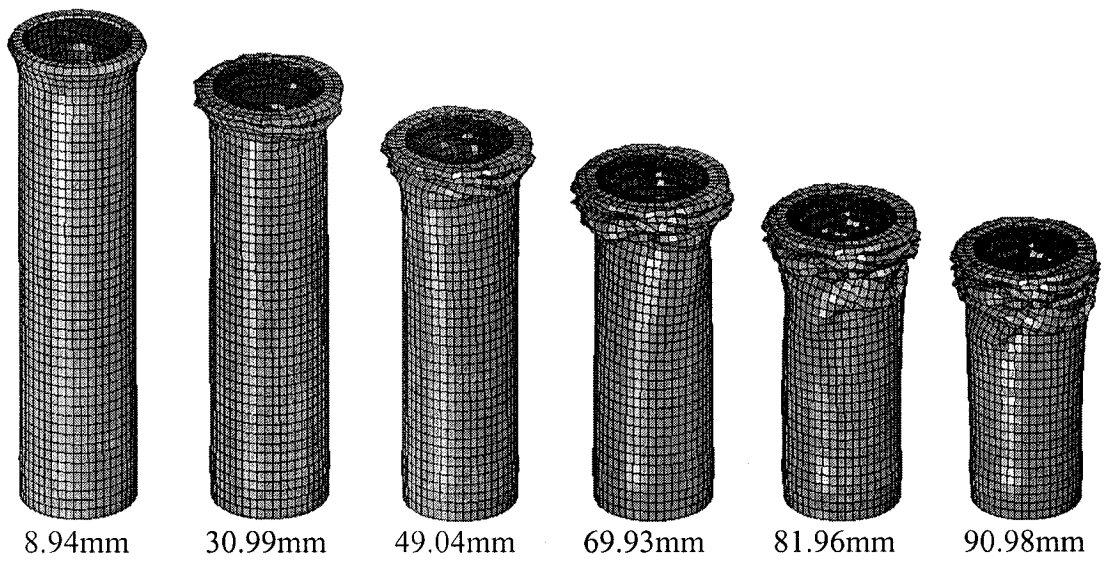

Figure 5-5: Crushing profiles of the HPG2_5D tube at different stages of the dynamic crushing event (v=6 m/s)

5.4.2.2 Glass fiber epoxy pultruded and carbon fiber braided hybrid tubes

The crushing response of the 5D and 10D hybrid tubes having 0.3 mm thick carbon braiding are shown in Figures 5.6a and 5.6b, respectively. Figures 5.6c and 5.6d also show the crushing response of the 5D and 10D hybrid tubes having 1.0 mm thick carbon braiding, respectively. The overall comparison of these 4 case studies indicates that for the 5D hybrid tubes, the responses from all three loading conditions are quite similar. However, the responses of the 10D hybrid tubes become unstable with the increase in crushing speed, as shown in Figures 5.6b and 5.6d. A more erratic fluctuation in load-distance is also observed in Figures 5.6b and 5.6d for the 10D hybrid tubes when subjected to 14 m/s impact. With the presence of the carbon fiber braiding, the energy absorption capacities of the 5D and 10D pultruded tubes are improved by up to 63.85% for the 0.3 mm thick braider and 116.15% for the 1.0 mm thick braiding, respectively, in dynamic crushing with a velocity of 14 m/s.

As expected, the carbon fiber braid enhances the crushing response of the pultruded tubes much more than the glass fiber braid, because the carbon fiber has a much larger longitudinal modulus than the glass fiber. However, as summarized in Table 5.3, in some cases the carbon fiber braid offered either similar capacity, or in some cases even lower capacity than that produced by glass fiber braid of the same thickness. This is believed to be due to the fact that the carbon epoxy braidings have lower transverse modulus, transverse compressive strength and minor Poisson's ratio than the equivalent glass epoxy. Figure 5.7 shows the crushing response of HPC2_5D at six progressive crushing stages corresponding to the 6 m/s dynamic crushing event. A brittle failure associated with the fiber or matrix compressive failure is observed in the hybrid tubes with carbon fiber braidings (Figure 5.7). It is postulated that the large mismatch of the Poisson's ratio between the glass fiber pultruded tube and the carbon fiber braid could also adversely impact the positive attribute of carbon fiber braids. However in most cases, the carbon fiber braid could enhance the energy absorption capacity of the tubes more remarkably than that achieved by glass fiber braid of the same thickness, noting that the crushing mode may be relatively unfavorable. As summarized in Table 5.3, in the 5D hybrid tubes, the 0.3 mm carbon fiber braid improved the energy absorption capacity by 7.24-23.14%, whereas the glass fiber braid increased it by 8.28-11.19%.

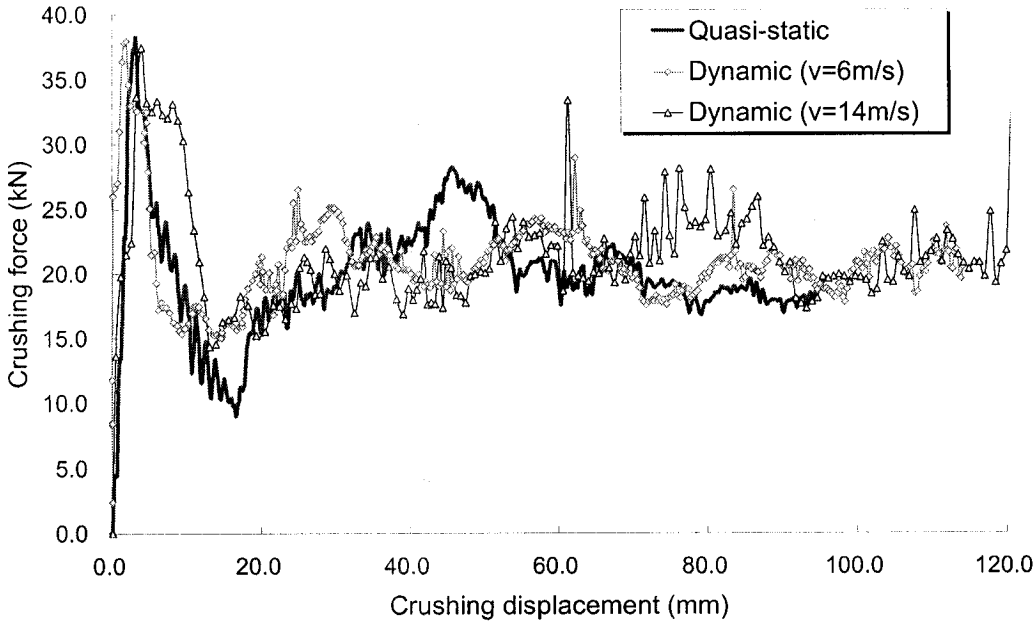

(a)- HPC1_5D

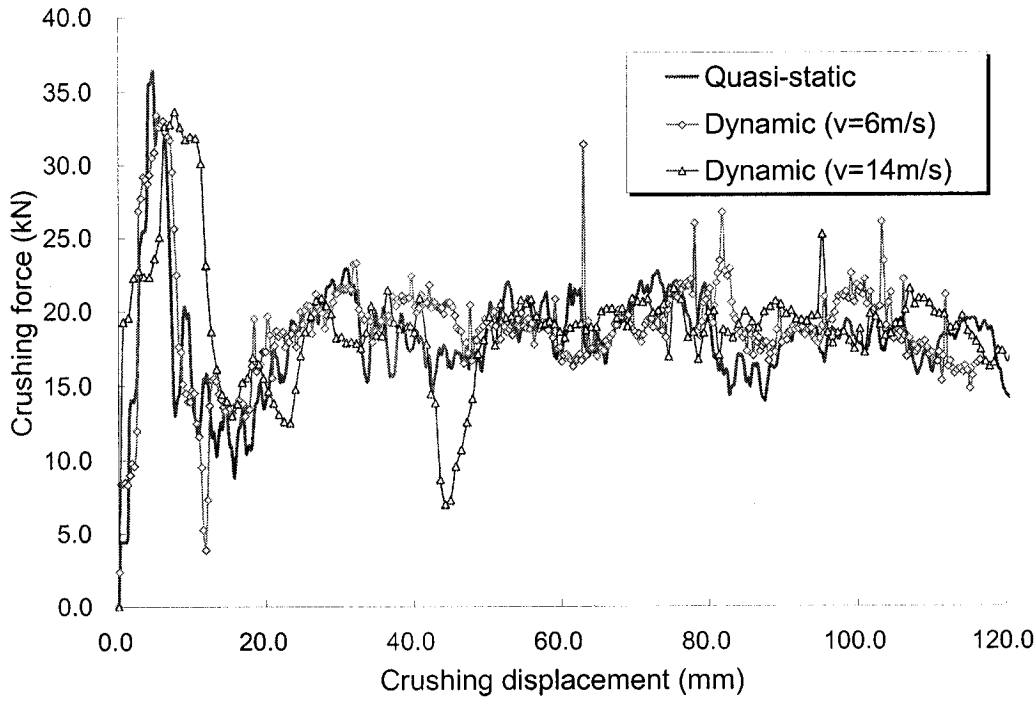

(b)- HPC1_10D

---(c) and (d) on next page

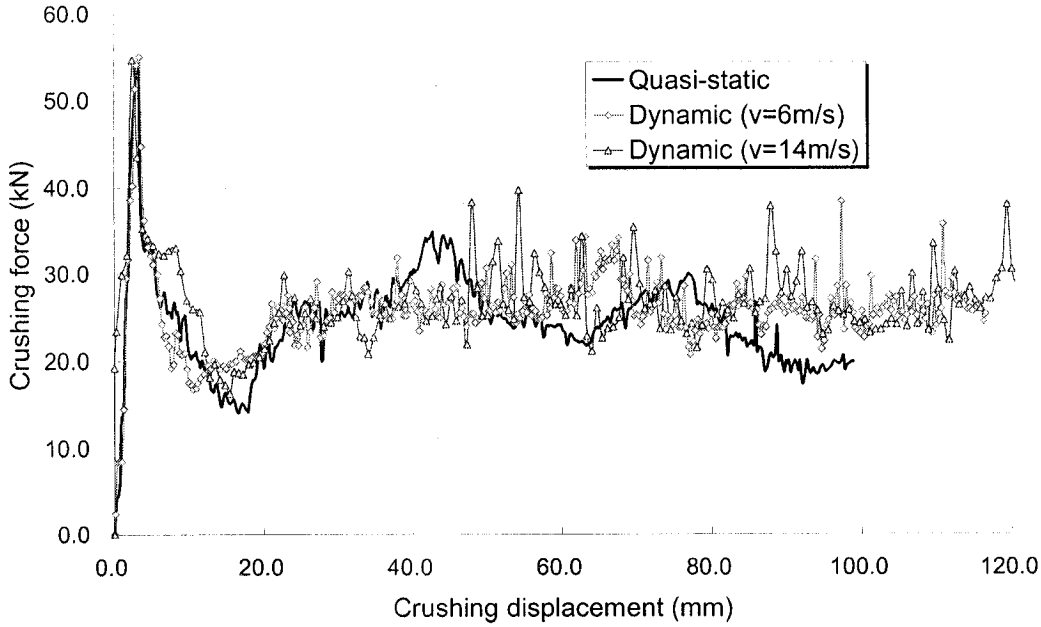

(c)- HPC2_5D

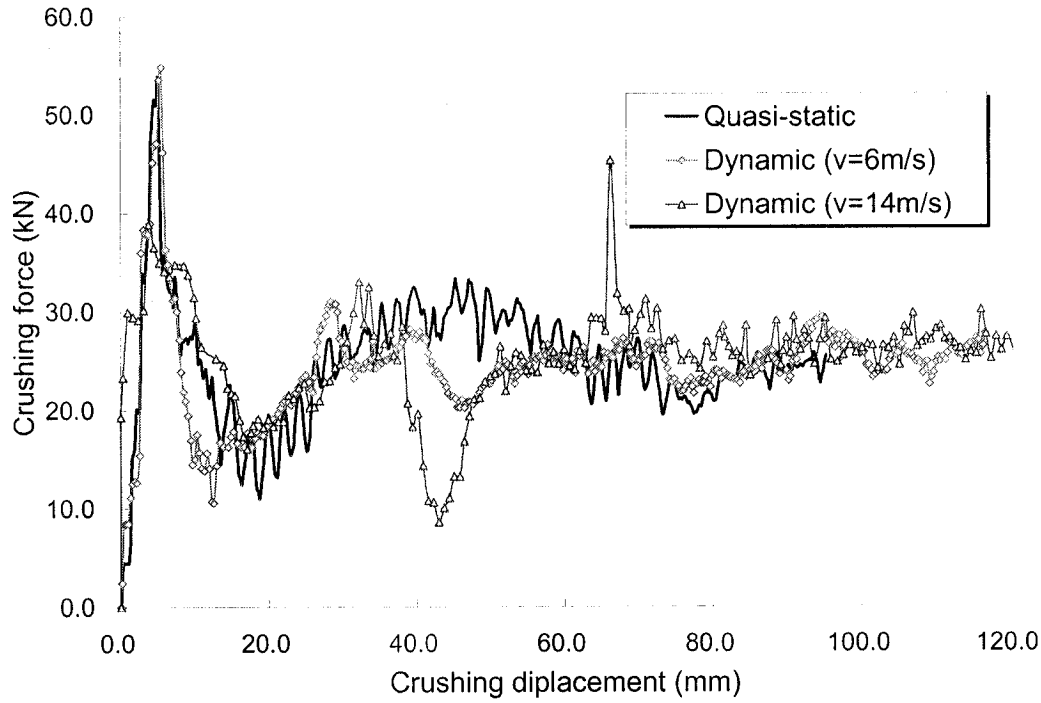

(d)- HPC2_10D

Figure 5-6: Plot of crushing force vs. crushing displacement of the hybrid tubes with carbon fiber braids subject to various loading conditions

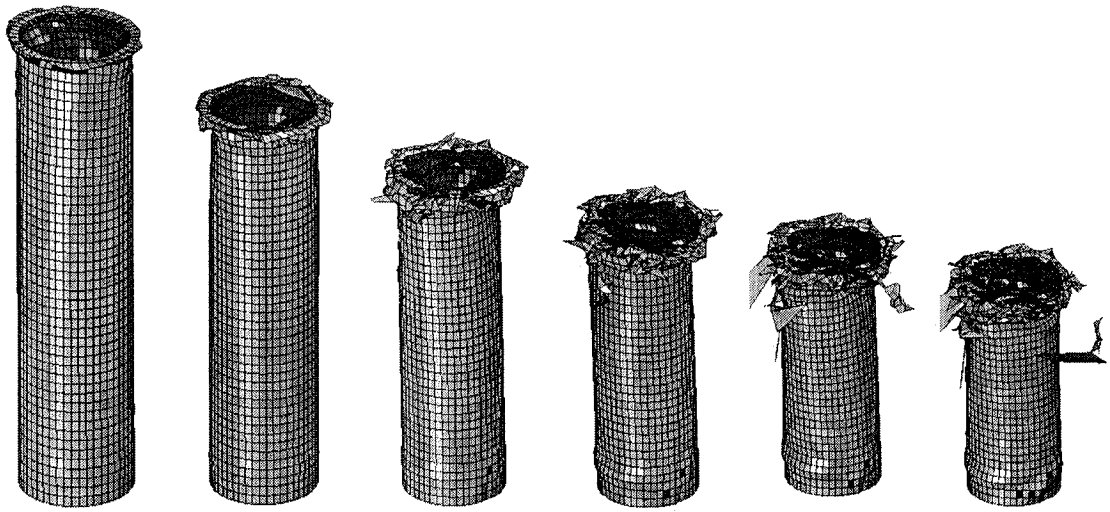

Figure 5-7: Crushing profiles of the HPC2_5D tube at different stages of the dynamic crushing event (v=6 m/s)

5.4.2.3 Influence of the loading condition and tube length

Figures 5.8 and 5.9 illustrate the enhancement in energy absorption in the 5D and 10D hybrid tubes compared with the corresponding 5D and 10D pultruded tubes. For the 5D hybrid tubes, the comparison of the static and dynamic crushings shows that although the folding (or local buckling ripples) did not form within the same crushing distance, overall however, the folding patterns were very similar, and the peak crushing forces were almost the same in both the quasi-static and dynamic cases. Moreover, the crushing behavior of the 10D hybrid tubes was observed to be more sensitive to the impact speed; the higher the impact velocity, the more unstable the response.

In tubes with the same type of braiding, the crushing behavior of the tube with thicker braid is more unlikely to be a perfect progressive local buckling mode than the one with thinner braid, although the one with thicker braid could absorb more energy.

Comparing the tubes having the same thickness of either glass fiber or carbon fiber braids, it was observed that the behavior of the tubes with carbon fiber braid was more unstable compared to the one with glass fiber braid, particularly in the longer tubes.

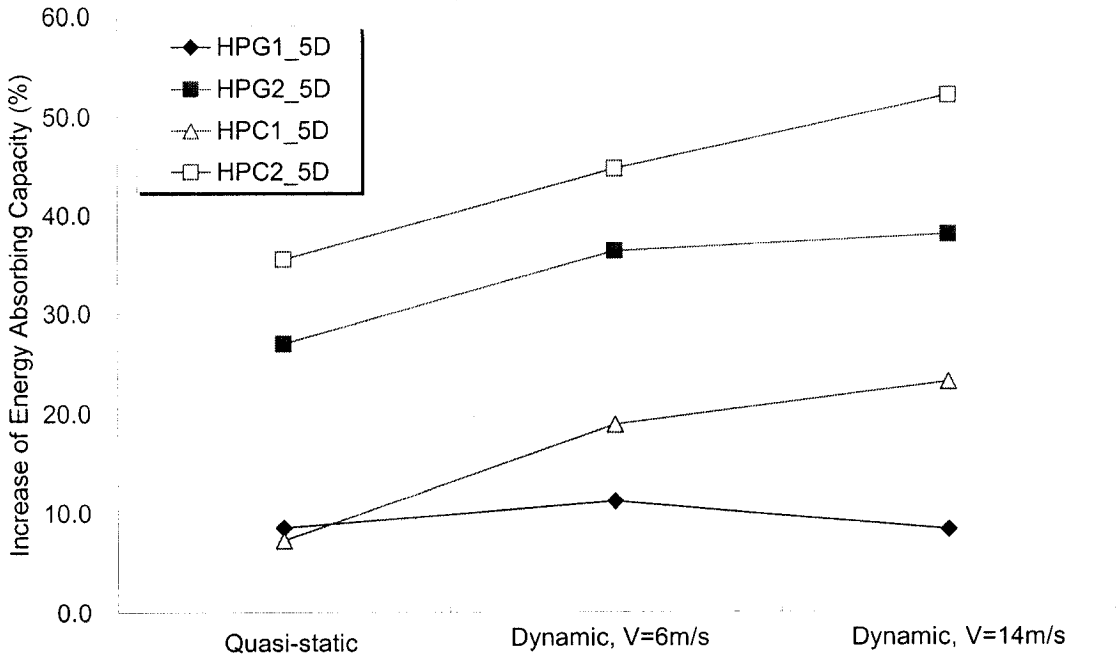

Figure 5-8: Enhancement in energy absorption capacity of the 5D hybrid tubes compared to the 5D pultruded tube

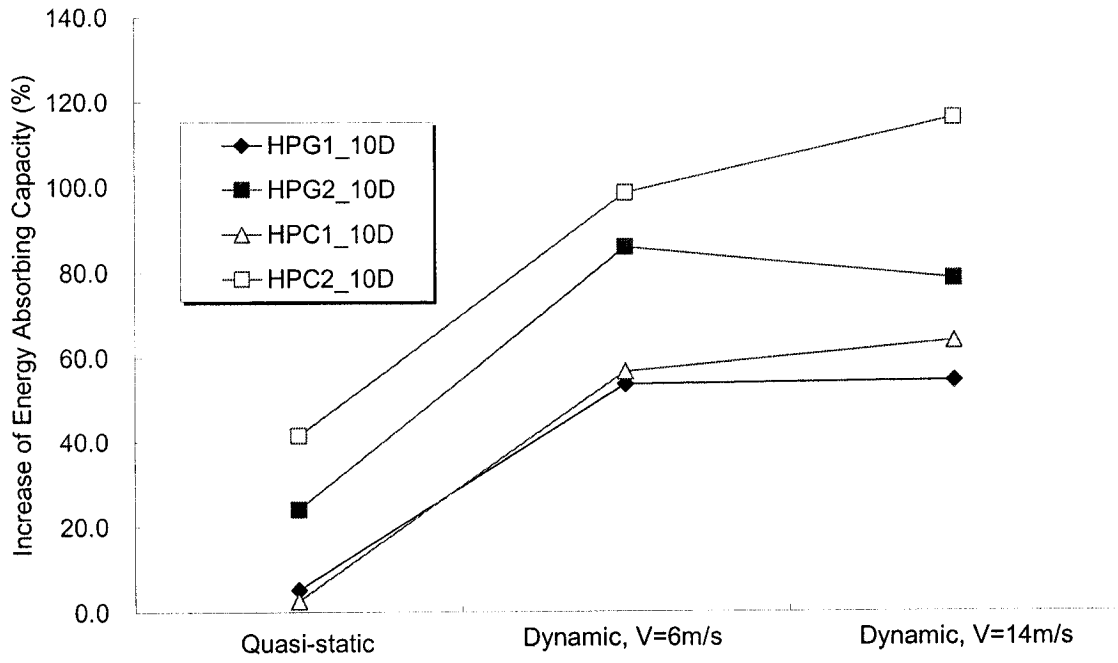

Figure 5-9: Enhancement in energy absorption capacity of the 10D hybrid tubes compared to the 10D pultruded tubes

The numerical results indicate that braiding overwraps could be used to effectively enhance the crushing characteristic and energy absorbing capability of the tubes. The energy absorption capacity of the pultruded tubes was decreased with the increase in impact speed. However, with the presence of the braidings, the tubes could absorb more energy as the impact velocity was increased, particularly in the long hybrid tubes. Therefore, the contribution of braiding is much more significant at high impact velocities than in quasi-static crushing. This contribution is more pronounced at relatively high velocity impacts.

5.4.2.4 Influence of interface bonding between the pultruded and braided tubes

As stated, the bonding between the pultruded and braided tubes was modeled by the contact algorithm expressed by equation (5.1). In the simulations discussed so far, it was assumed that the value of the normal failure force (NFLF) and the shear failure force (SFLF) were the same. These failure forces are strongly dependent on the properties of the resin used in the bonding, and not to other factors. For example, vinyl ester resin has higher mechanical properties than polyester resin. As demonstrated by Bouchet *et al.* [14], for instance, even surface treatments of multi-material structures did not improve the specific energy absorption values of the tubes they considered. Three different values of failure forces (i.e., 100 N, 250 N and 500 N), were considered in the contact algorithm (see Equation 5.1) to evaluate the influence of this parameter. Figures 5.10a and 5.10b show the crushing response of the HPG1_5D and HPC1_5D tubes under a dynamic impact condition (v=6 m/s) with the above mentioned three failure forces. Figure 5.10c and 5.10d show that the HPG1_5D and HPC1_5D tubes behave similarly under a quasi-static loading condition. It is observed that under both quasi-static and dynamic loading conditions, the variation in failure force has insignificant influence on the crushing response and the energy absorption capacity of the hybrid tubes. Therefore, the failure force of 100 N was used in all simulations, whose results were presented earlier.

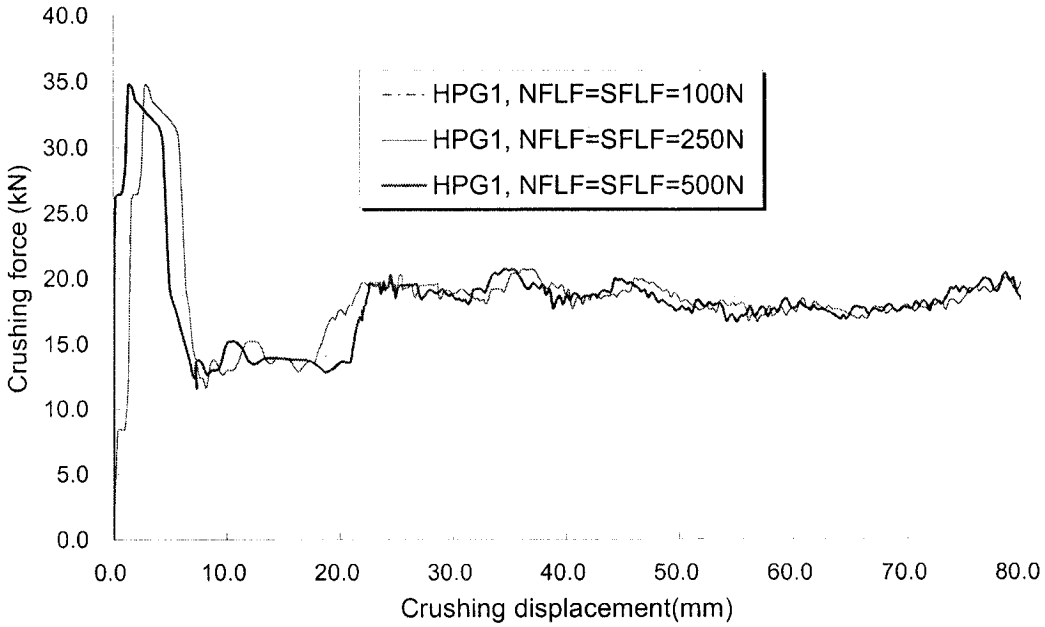

(a)- HPG1_5D_dynamic response

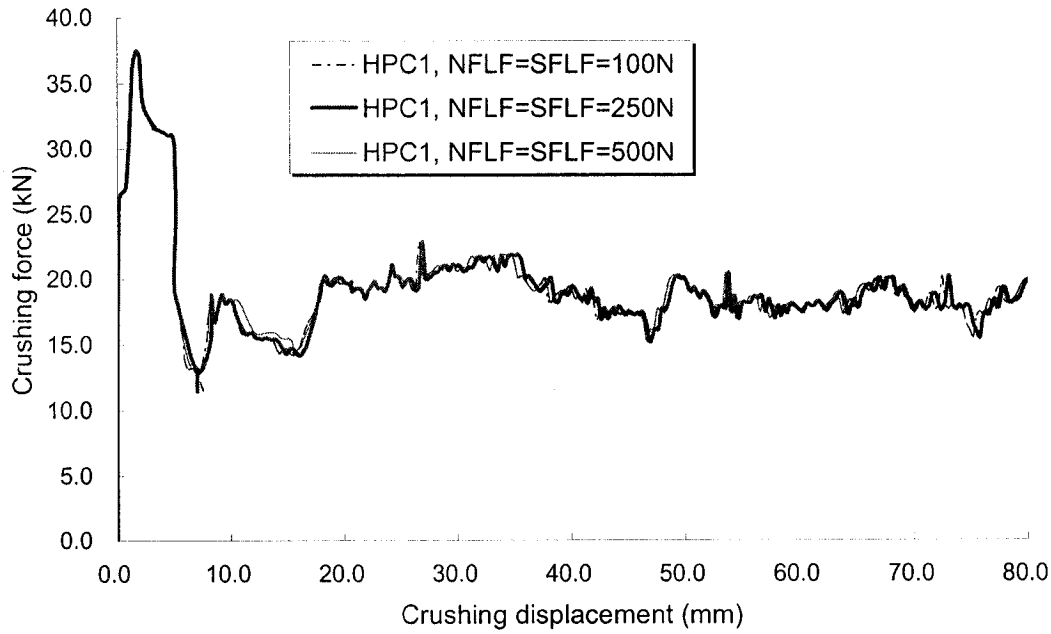

(b)- HPC1_5D_dynamic response

---(c) and (d) to be continued on next page

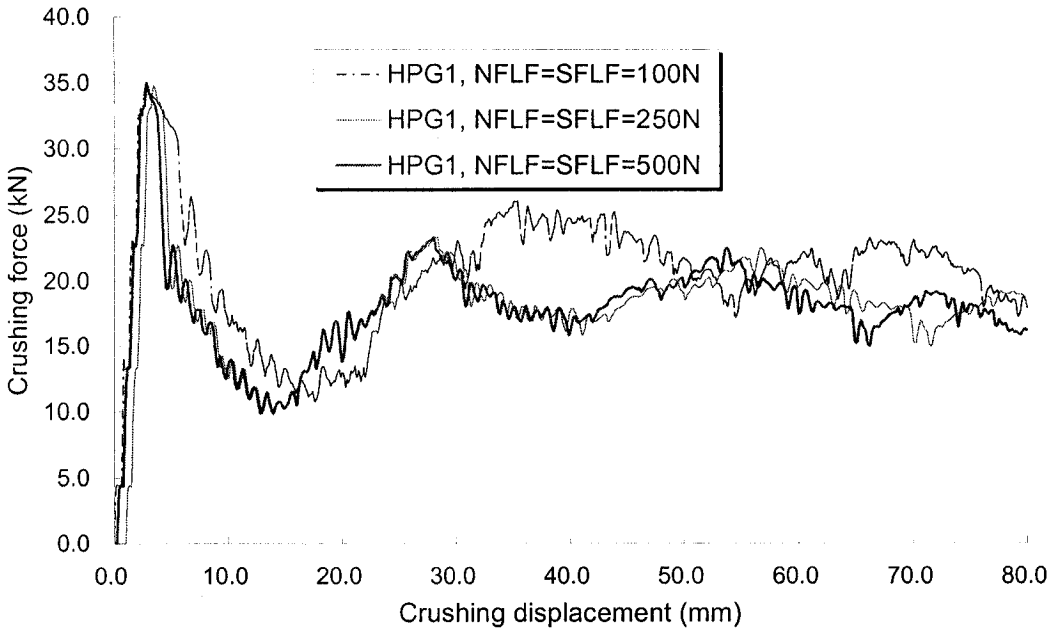

(c)- HPG1_5D_quasi-static response

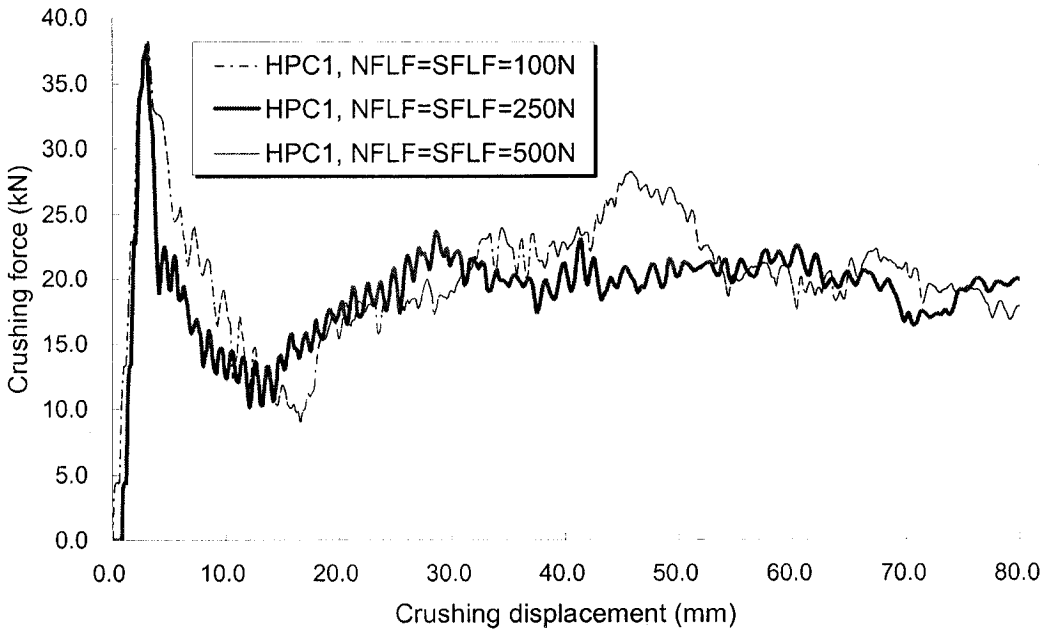

(d)- HPC1_5D_quasi-static response

Figure 5-10: Plot of crushing force vs. crushing displacement of the hybrid tubes with glass or carbon fiber braids and different interface bond failure forces (100 N, 250 N and 500 N), subject to quasi-static and dynamic crushing

5.5 Conclusions

In this study the hybrid tubes made of pultruded tube overwrapped by braiding were considered as a component with great potential in energy absorbing applications. From the results obtained through numerical simulations, it was found that overwrapping of braids over the pultruded tubes could be an effective means to enhance the energy absorption capacity and response of such tubes.

In the preliminary study, the $[0]_4$ pultruded tube was found to be able to absorb the highest magnitude of energy among all the tubes having the same thickness but with different stacking sequences. However, the pultruded tubes often crushed in unpredictable modes (such as asymmetric crushing and splitting modes). Therefore, both glass and carbon fiber braidings were employed in this investigation to enhance the energy absorption capacity and response of the pultruded tubes. A parametric study was conducted to consider two types of tube lengths and two types of braid thicknesses. The response of the hybrid tubes under quasi-static and impulse forces under 6 m/s and 14 m/s velocities were also simulated. It was found that the response of the hybrid tubes was sensitive to tube length, braid thickness and loading conditions. Interesting insights were obtained by examining the interaction of the studied parameters. Most significantly, it was observed that while the carbon fiber braid could increase the energy absorption capacity very effectively, it did not produce the desirable local buckling failure mode. Moreover, the thinner braid (0.3 mm) was found to produce a more local buckling failure mode in comparison to the thicker braid (1.0 mm). Furthermore, braids were found to be most useful in dynamic axial impact, because the higher the impact velocity, the more contribution the braid offers.

In the future, an experimental investigation will be conducted to ascertain the integrity of the numerical results. The future work will also consider different combinations of pultrution and braid tubes, such as high strength carbon fiber pultrution tubes with glass or carbon fiber braids.

5.6 Acknowledgement

The financial support of Natural Sciences and Engineering Council of Canada (NSERC) in the form of Discovery Grants to the second and third authors in support of this work is gratefully acknowledged.

5.7 References

[1] Schneider F., Jones N., Impact of thin-walled high-strength steel structural sections, *Proceedings of the Institution of Mechanical Engineers*, part D – Journal of Automobile Engineering 218 (D2): 131-158 Feb 2004

[2] Farley G.L., Jones R.M., Crushing characteristics of continuous fiber reinforced composite tubes. *Journal of Composite Materials*, 26(1), 37–50, 1992

[3] Mamalis A.G., Yuan Y.B., Viegelahn G.L., Collapse of thin wall composite sections subjected to high speed axial loading, *International Journal of Vehicle Design*, Vol 13, No 5/6, 564-579, 1992

[4] Hamada H., Ramakrishna S., Sato H., Effect of fiber orientation on the energy absorption capability of carbon fiber/PEEK composite tubes, *Journal of Composite Materials*, Vol 30, No 8, 947-963, 1996

[5] Mamalis A.G., Manolakos D.E., Demosthenous G.A., Ioannidis M.B., The static and dynamic axial collapse of fiberglass composite automotive frame rails, Composite Structures 34 (1996) 77-90

[6] Schultz M.R., Hyer M.W., Static and Dynamic Energy-Absorption Capacity of Graphite-Epoxy Tubular Specimens, Mechanics of Composite Materials and Structures, 8, 231–247, 2001

[7] Mahdi E., Sahari B.B., Hamouda A.M.S., Khalid Y.A., An experimental investigation into crushing behavior of filament-wound laminated cone-cone intersection composite shell, Composite Structures 51 (2001) 211-219

[8] Velmurugan R., Gupta N.K., Solaimurugan S., Elayaperumal A., The effect of stitching on FRP cylindrical shells under axial compression, International Journal of Impact Engineering 30 (2004), 923–938

[9] Mamalis A.G., Manolakos D.E., Ioannidis M.B., Papapostolou D.P., On the crushing response of composite sandwich panels subjected to edgewise compression: experimental, Composite Structures 71 (2005) 246–257

[10] Mahdi E., Hamouda A.S.M., Mokhtar A.S., Majid D.L., Many aspects to improve damage tolerance of collapsible composite energy absorber devices, Composite Structures 67 (2005) 175–187

[11] Mamalis A.G., Manolakos D.E., Ioannidis M.B., Papapostolou D.P., On the experimental investigation of crash energy absorption in laminate splaying collapse mode of FRP tubular components, Composite Structures 70 (2005) 413–429

[12] Mamalis A.G., Manolakos D.E., Ioannidis M.B., Papapostolou D.P., On the response of thin-walled CFRP composite tubular components subjected to static and dynamic axial compressive loading: experimental, Composite Structures 69 (2005) 407–420

[13] Song H.W., Wan Z.M., Xie Z.M., Du X.W., Axial impact behavior and energy absorption efficiency of composite wrapped metal tubes, International Journal of Impact Engineering 24 (2000) 385-401

[14] Bouchet J., Jacquelin E., Hamelin P., Dynamic axial crushing of combined composite aluminum tube: the role of both reinforcement and surface treatments, Composite Structures 56 (2002) 87–96

[15] El-Hage H.H., A numerical study on the quasi-static axial crush characteristics of square aluminum and aluminum-composite hybrid tubes, PhD thesis, Department of Mechanical Engineering, University of Windsor, 2004

[16] Babbage J.M., Mallick P.K., Axial crush resistance of aluminum-composite hybrid tubes, Proceeding of 17th Annual Technical Conference of the American Society of Composite, Paper No. 070

[17] Chiu C.H. and Lu C.K., Crushing characteristics of 3-D braided composite square tubes, Journal of Composite Materials, Vol 31, No 22, 2309-2327, 1997

[18] Karbhari V.M., Hailer J.E., Rate and architecture effects on progressive crush of braided tubes, Composite Structures 43, 93-108, 1998

[19] Chiu C.H., Tsai K.H. and Huang W.J., Crush-failure modes of 2D triaxially braided hybrid composite tubes, *Composites Science and Technology* 59, 1713-1723, 1999

[20] Mahdi E., Hamouda A.M.S., Sahari B.B., Khalid Y.A., Effect of hybridization on crushing behavior of carbon/glass fiber/epoxy circular–cylindrical shells, *Journal of Materials Processing Technology* 132, 49–57, 2003

[21] Abosbaia A.A.S., Mahdi E, Hamouda A.M.S., Sahari B.B., Quasi-static axial crushing of segmented and non-segmented composite tubes, Composite Structures 60 (2003) 327–343

[22] Mamalis A.G., Manolakos D.E., Ioannidis M.B., Kostazos P.K., Crushing of hybrid square sandwich composite vehicle hollow bodyshells with reinforced core subjected to axial loading: numerical simulation, Composite Structures 61 (2003) 175–186

[23] Mahdi E., Hamouda A.S.M., Sen A.C., Quasi-static crushing behavior of hybrid and non-hybrid natural fiber composite solid cones, Composite Structures 66 (2004) 647–663

[24] Saito H., Chirwa E.C., Inai R., Hamada H., Energy absorption of braiding pultrusion process composite rods, Composite Structures 55 (2002) 407–417

[25] Okano M., Sugimoto K., Saito H., Nakai A., Hamada H., Effect of the braiding angle on the energy absorption properties of a hybrid braided FRP tube, *Journal of Materials-Design and Applications* 219 (L1): 59-66 Feb 2005

[26] LS-DYNA keyword user's manual, V970, LSTC, Livermore, CA, 2005

[27] Zhang Z., Investigation on dynamic pulse buckling and damage behavior of composite laminated beam subjected to axial impulse, *PhD thesis*, Faculty of Engineering, Dalhousie University, 2004

Chapter 6 Crushing behaviors and energy absorption efficiency of Hybrid Pultruded and $\pm 45^{\circ}$ Braided Tubes

Haipeng Han[a], Farid Taheri [a,*], Neil Pegg[b]

[a]Department of Civil and Resource Engineering, Dalhousie University,
1360 Barrington Street, Halifax, NS B3J 2Z1
[b]Defense Research and Development Canada – Atlantic,
9 Grove Street, Dartmouth, NS, B2Y 3Z7

Submitted to the Journal of "**Mechanics of Advanced Materials and Structures**" in July 2006

6.1 Abstract

A numerical and experimental investigation was carried out to evaluate the response and energy absorbing capacity of hybrid composite tubes made of unidirectional pultruded tube over wrapped with $\pm 45^{0}$ braided fiber-reinforced plastic (FRP). The numerical simulation characterized the crushing behaviors of these tubes subject to both quasi-static compression and axial dynamic impact loadings. Two types of FRP braids, that is, glass and carbon fibers braids were considered. Parametric studies were also conducted to examine the influence of the thickness and type of braid, as well as the loading conditions on the crushing behavior of the tubes. Due to its ease and controllability, quasi-static crushing tests were conducted to verify the numerical studies' findings. Very good agreement was observed between the finite element simulation and experiments.

It was observed that the presence of braids restrained the brittle crack propagation in pultruded tubes, thus reinforced the flexural behavior of the tube walls, and in turn improved their energy absorption capacity. Moreover, the hybrid tubes exhibited a more desirable, accordion type failure mode, therefore they are considered to be more suitable candidates as energy absorbing structural members in service conditions.

* To whom correspondence should be addressed, email: farid.taheri@dal.ca, Phone:1-902- 494-3935; fax: 1-902-484-6635

Keyword: Energy absorber, hybrid tube, pultruded tube, braids, crushing, finite element

6.2 Introduction

An energy absorber is a system that converts, totally or partially, kinetic energy into another form of energy. The aim of an energy absorber design is to alleviate the force that applies to the occupants of structures. Metallic energy absorbers collapse under crush or impact load by buckling and/or folding in accordion fashion with irreversible plastic deformation. Due to their superior strength-to-weight ratio, excellent corrosion resistivity and unmatched design and manufacturing flexibility, fiber reinforced polymer (FRP) composite materials are becoming more popular in replacing the conventional materials by offering significant weight reduction and safety, as well as tailorable failure mode. In comparison to metallic energy absorbers, most composite tubular energy absorbers are generally crushed in a brittle manner rather than in a ductile manner. The challenge is determining the specific energy absorption capacity for selecting materials, while maintaining safety and minimizing the overall economic cost.

Pultrusion is a process for producing continuous and prismatic shaped FRP components, and is one of the most cost-effective processes in composite industry. As a result, high strength pultruded composite sections are widely used in many engineering applications. Due to their relatively high strength and stiffness in the longitudinal direction, tubular pultruded sections may be considered as effective energy absorbers. A previous study by Han *et al.* [1] have shown that pultruded tube can absorb the highest energy when compared to composite tubes of the same thickness and but with other types of stacking sequences.

A large number of experimental and theoretical studies have been conducted in the past to examine the progressive collapse mode of metallic thin-walled tubes under the axial compressive loading. The increased interest in using FRP to lower structural weight has also prompted research into investigating the axial crushing performance of FRP tubes [2-12]. Most of the earlier studies, whether considering quasi-statically or dynamically applied loading, have been experimental in nature. Previous researchers

studied the crushing behavior of composite tubes made of carbon/epoxy, glass/epoxy, glass/vinyl ester, graphite/epoxy and sandwich FRP. The tubes considered were fabricated by hand lay-up, pultrusion, filament winding, weaving and stitching methods. The geometry of the tubes included circular, elliptical, square and cone shapes. The studies considered the crushing modes and the energy absorption capacity of the tubes. The crushing modes in composite tubes have been classified into three categories in reference [2]; these are: local buckling, transverse shear and laminar bending modes. It was also reported in [2] that it is very difficult to initiate a progressive crushing mode for very thin and thick-walled tubes. Transverse shearing mode is generally insensitive to strain rate. For Laminar bending crushing and local buckling modes, energy absorption capability can be influenced by changing the crushing speed.

Moreover, in consideration of performance of light weight energy absorbers, several numerical and experimental investigations [13-16] have also considered the crushing behavior and energy absorption capability of hybrid tubes comprising of metallic tubes with filament wound FRP overwraps.

There have been several other works that have taken advantage of hybridization of composite materials as a new concept in the design of energy absorbers [17-25]. For example, the use of biaxially braided composite tubes, combination of biaxially and triaxially braided tubes, and hybrid of filament wound laminated tubes with different combinations of carbon and glass fibers have been reported in [17-20]. It was found that tri-axial hybrids could provide enhanced specific energy absorption attributes through the combination of transverse shearing, bending, crushing, and local accordion type buckling modes. Segmented and non-segmented composite tubes were discussed as another way of hybridization by Abosbaia *et al.* [21]. The segmented composite tube consisted of three different material regions. It was found that segmented composite tubes made of carbon fiber fabric and cotton fiber fabric exhibited good energy absorption capability as well as stable load-carrying capacity. The crushing behavior and energy absorption efficiency of hybrid and non-hybrid natural fiber composite solid cones were also presented by Mahdi and his co-workers in [23]. The most relevant studies on the subject considered in our investigation are perhaps the work of Saito *et al.* [24] and Okano *et al.* [25]. These two studies demonstrated that braided/pultruded hybrid composites, produced in form of rods,

exhibited superior response in terms of energy absorption capability in comparison to the unidirectional pultruded rods. It was also shown that the braiding angle of 30°, together with the use of a flexible resin could produce the most optimized rod for absorbing energy. These works have demonstrated that hybridization could be used not only to enhance the energy absorption capacity, but also to provide predictable sequences of stable crushing modes.

In pultrusion process, it is rather difficult to place the fibers in an angular orientation, despite the high productivity rate associated with this process. Braiding technology is also a cost-effective manufacturing process. FRP tubes provide energy absorption capacity by combining various mechanisms, such as fiber fracture, delamination and splitting. However, a serious problem is that considerable energy absorption will be lost by such brittle failure, usually occurring parallel to fibers (splitting); therefore it is necessary to restrain the brittle crack propagation by providing lateral support (e.g. braids).

As can be seen, the hybridization of pultrusion and braiding is highly promising due to the ease of manufacturing. To the authors' knowledge, no work has considered the crushing response of such cost-effective hybrid FRP tubes experimentally. A comprehensive numerical and experimental investigation was therefore carried out to study the crushing performance of hybrid pultruded/braided FRP tubes. Two types of braiding, namely, carbon and glass fiber epoxy braidings were investigated. Experimental investigation was carried out first in this work. FRP tube specimens were fabricated and quasi-static crushing tests were conducted on both pultruded and hybrid tubes. Subsequently, a numerical study was conducted to characterize the crushing behavior and energy absorption efficiency of such tubes, subject to both quasi-static and dynamic axial crushing loadings. The results from the experimental investigation and numerical study will be compared and discussed. The results provided by this work would help designers to gain more confidence in designing such FRP structural components used for energy absorption applications.

6.3 Experimental investigation

An experimental investigation was conducted first to characterize the crushing behavior and energy absorption capacity of pultruded and hybrid tubes. The experimental program included fabrication and testing of the hybrid tubes.

The geometric configuration of the hybrid tube is shown in Figure 6.1. The central diameter of the pultruded tube is 40 mm and its wall thickness is 3.174 mm. the length of the tubes is 200mm (i.e., five time its diameter). The pultruded tubes are made of high strength glass fiber sections manufactured by Creative Pultrusion Inc (PA, USA). The braiding thickness is either 0.3 mm or 1.0 mm, depending on the type of the braiding (i.e., either light fabric or medium fabric). Both glass and carbon fiber braids were considered. The biaxial carbon and glass fiber braidings are manufactured by A & P Technologies (OH, USA). Four different tube combinations were manufactured and tested, namely, HPG1, HPG2, HPC1 and HPC2. Here HPG1 refers to the hybrid of pultruded tube with the glass fiber braiding of 0.3 mm thickness, and HPG2 refers to the combination of the pultruded and glass fiber braiding of 1.0 mm thickness. The same rule applies for HPC1 and HPC2, where glass (G) is replaced by carbon (C). The pultruded tube and the braids before manufacturing are shown in Figure 6.2.

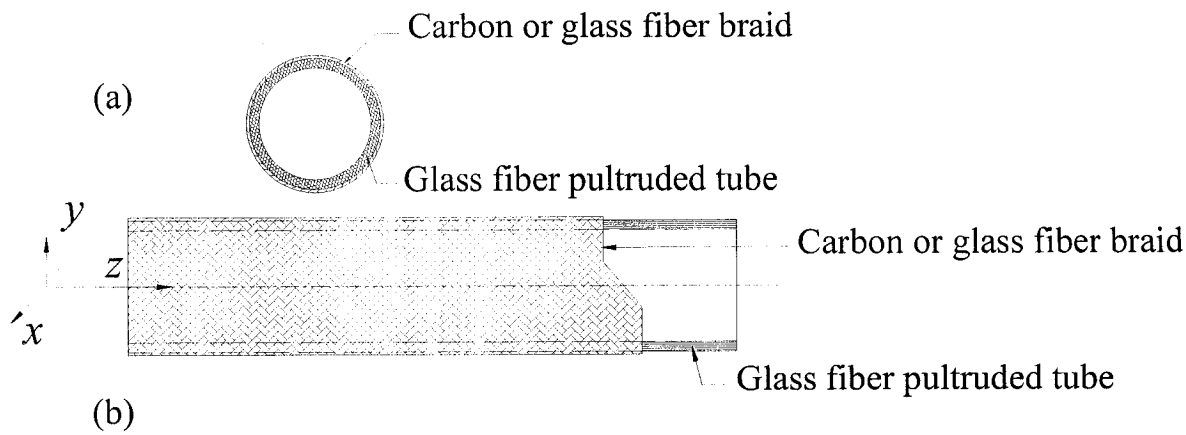

Figure 6-1: Configuration of the hybrid of pultruded and braided FRP tubes

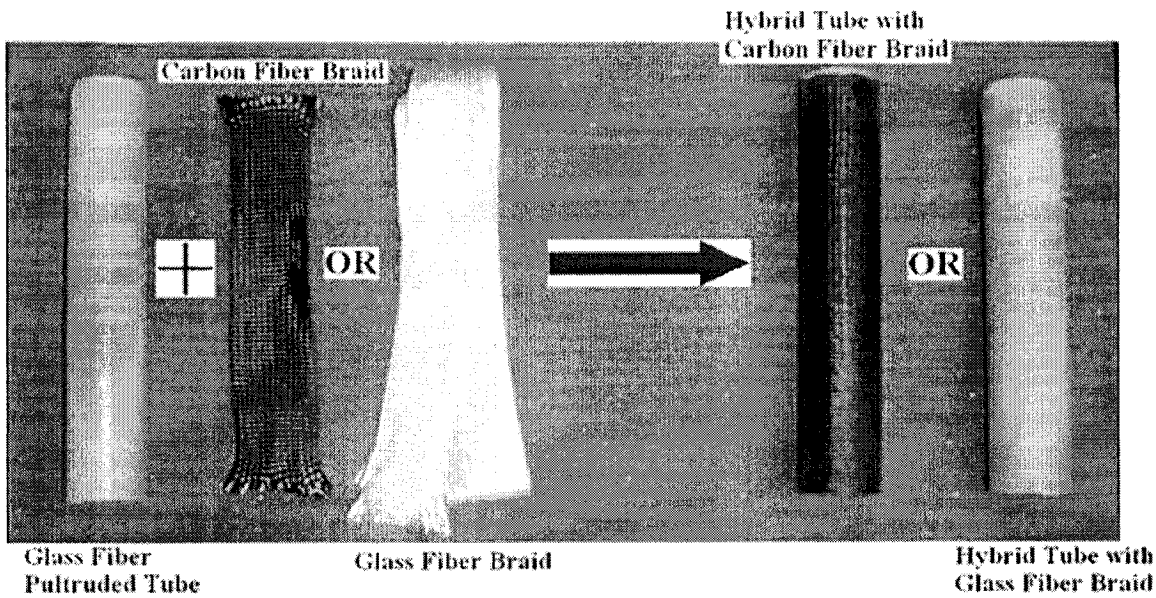

Figure 6-2: Samples of the pultruded tube, glass and carbon fiber braids

The West System 105-epoxy resin and 205-fast hardener (with weight ratio of 5:1) were used as the adhesive securing the interface between the pultruded tube and braids. The resin cures at room temperature. The weight ratio of glass/carbon fiber braid to epoxy resin was about 1:1. Caution was exercised to ensure that the resin was applied uniformly along the tube. Once the braids were fit on the pultruded tube with wet resin, the hybrid tube was placed in a pressure chamber under air pressure for 16 hours till the resin hardened (see Figure 6.3). The air pressure in the chamber was about 100 MPa, which prompted perfect bonding between the pultruded tube and braids.

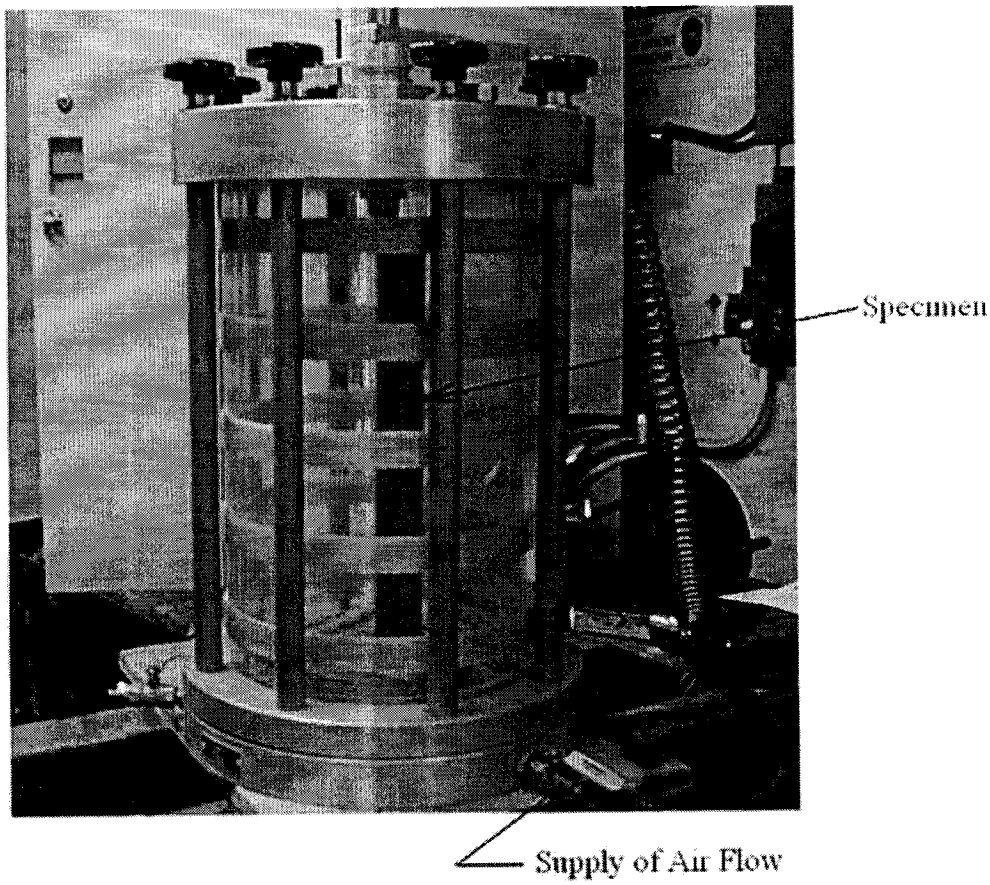

Figure 6-3: Pressure chamber used in consolidating the hybrid tubes

In comparison to steel, FRP materials have been found to be strain rate insensitive, particularly for thin-walled FRP tubes subject to low or intermediate velocity impact [3, 8]. It has also been reported [6] that the presence of 0° fibers lead to higher load ratios (the ratio of the peak crushing load to average crushing load). It was also observed that the specimens tested dynamically exhibited higher load ratios than similar specimens tested statically [6, 12]. In dynamic crushing test, however, more specialized and sensitive force and displacement transducers are used. The control of such transducers is rather difficult when using a conventional drop-weight impact system. Quasi-static crushing test is easy to perform and can generally be used to characterize the energy absorption capacity efficiently as long as the tube is subject to impact velocity up to an intermediate range (up to 18-24 m/s [3]). Quasi-static crushing tests were therefore only conducted in the experimental investigation. The crushing test was carried out by an

INSTRON 8500 universal testing machine, the crushing speed was 10mm/min, and the total crushing distance was 100 mm for all tubes. A 45-degree chamfer was created at the free end of each tube so as to trigger the initiation of local crushing and to ensure the progressive crushing in each tube. Crushing force versus crushing displacement response, as well as crushing profiles at various stages were recorded.

6.4 Finite element analysis

A few studies (such as the one by El-Hage [15]) have considered the crashworthiness simulation procedures of aluminum-composite hybrid tubes. As stated, Mamalis *et al.* [22] also numerically investigated the crashing behaviors and energy absorption characteristics of thick-walled square tubular crashworthy bodyshells made of hybrid sandwich composite panels with integral FRP hollow cylindrical inserts. However, as stated earlier, no simulation studies on hybrid FRPC tubes could be found. The LS-DYNA [26] code was used in conducting all the simulations carried out in our investigation.

6.4.1 Element type used in the simulation

The Belyschko-Tsay quadrilateral element was used to model both the pultruded tube and braided FRP tubes. The shell elements were located at the mid-plane of each tube (i.e., on the mid-planes of the pultruded tube and the overwrap), which were separated by a small gap equal to the average thickness of the two walls. An appropriate contact algorithm was used to connect the pultruded tube shell element and the braided shell elements, so as to properly simulate the interaction between the two sub-components. The pultruded tube was modeled as 2 layers of 0^0 laminae, and the braid tube by two layers of $\pm 45^0$ lamiae. The integration points representing different layers of certain stacking orientations were located evenly through the thickness. Consequently six integration points through the thickness were needed to model the hybrid material. The model for the hybrid tube was comprised of total of 4900 elements connected with 5017 nodes.

6.4.2 Material model

The constitutive material model 54 of LS-DYNA was selected to model both the pultruded tube and the braided one. Material model 54 has the option of using either the Tsai-Wu failure or the Chang-Chang failure criterion for assessing lamina failure. The Chang-Chang criterion is the modification of the Hashin's failure criterion to account for nonlinear shear stress-strain behavior. The criterion also accounts for the post-failure degradation, so that the post failure behavior of the laminate could be considered by the failure of each successive lamina. The post failure conditions in the Material-54 model [26] are slightly different from that prescribed by the original Chang-Chang equations; they account for four types of failure (i.e., tensile fiber mode, compressive fiber mode, tensile matrix mode and compressive matrix mode). According to this model, if fiber breakage and/or fiber matrix shear failure occurs in a lamina, both the lamina's transverse modulus and minor Poisson's ratio are reduced to zero, but the change in the lamina's longitudinal and shear moduli follows the Weibull distribution. On the other hand, if matrix failure occurs either in tension or compression, then the transverse modulus and minor Poisson's ratio are reduced to zero, while the longitudinal modulus and shear modulus remain unchanged.

The mechanical properties of the pultruded tube, as well as the glass fiber/epoxy and carbon fiber/epoxy braids in the principle directions are given in Table 6.1. These glass/epoxy properties are adopted from the data sheet provided by the suppliers. The carbon fiber/epoxy material properties are taken from the experimental investigation reported in [27]. The parameters DFAILT and DFAILC of the software are used to assume that the material behaves in an elastic-perfectly plastic manner after the maximum tensile or compressive strain has reached. The parameters FBRT and YCFAC account for the strength reduction in tension and compression, respectively, in the fiber direction after failure of the matrix.

Table 6-1: Mechanical properties of the pultruded tube, glass/epoxy and carbon/epoxy braids in the principle directions

Material type		Pultruded tube	Glass/ Epoxy braid	Carbon/ Epoxy braid
Density (Kg/m^3)	ρ	1795	1975	1512
Longitudinal Modulus (GPa)	E_{11}	20.6	30.9	118.0
Transverse Modulus (GPa)	E_{22}	6.9	8.3	5.5
In-plane shear modulus (GPa)	G_{12}	2.9	2.8	4.8
Out-of-plane shear modulus (GPa)	G_{23}	2.9	3.0	4.8
Minor Poisson's ratio	ν_{21}	0.1172	0.0866	0.0127
Longitudinal tensile strength (MPa)	S_L^+	226.9	798.0	1095.0
Longitudinal compressive strength (MPa)	S_L^-	500.0	480.0	712.9
Transverse tensile strength (MPa)	S_T^+	51.6	27.1	26.4
Transverse compressive strength (MPa)	S_T^-	113.4	140.0	84.4
In-plane shear strength (MPa)	S_{LT}	48.3	36.8	84.3
Fiber's maximum strain in tension	DFAILT	2.3%	2.3%	2.3%
Fiber's maximum strain in compression	DFAILC	1.4%	1.4%	1.4%
Reduction factor for tensile strength in the fiber direction after matrix failure	FBRT	1.0	1.0	1.0
Reduction factor for compressive strength in the fiber direction after matrix failure	YCFAC	3.0	3.0	3.0

6.4.3 Boundary constraints and the Contact algorithm

6.4.3.1 Quasi-static loading case

In the modeling of quasi-static crushing, the bottom end of the hybrid tube was assumed to be built-in, thus all degrees of freedom at this location were constrained. The upper end was free and subjected to compression by a loading plate. The loading plate was modeled as a rigid plate, and its mass was assumed to be 100 kg. As shown in [15], the masses of both loading plate and tube could be scaled up for maximizing computation efficiency, while still maintaining a quasi-static condition. In this study, the density of the loading plate and tube were therefore scaled-up by a factor of 1000. It was observed that the ratio of the total kinetic energy (KE) to the total internal energy was less than 5% over the period of the crushing process, thus enforcing a quasi-static condition. The

loading plate was displaced using LS-DYNA's *BOUNDARY_PRESCRIBED _MOTION_RIGID command at a constant rate of 100 mm/sec. Two types of contact algorithms were used to simulate the boundary conditions in quasi-static crushing. The first one was to simulate the interface between the loading plate and the upper end of the hybrid tube using the command *CONTACT_CONSTRAINT_NODES_ TO_SURFACE. The interface force between the loading plate and the tube was then extracted to provide the force-displacement response. The other algorithm was used to prevent the tube from drifting on its lower end. This was done by employing the *RIGIDWALL_GEOMETRIC_FLAT command, by which a flat rigid surface was defined in the location beneath the tube. This would ensure that the tube would always stay on the top of this rigid surface in the event that the bottom end of the tube starts folding.

6.4.3.2 Dynamic axial impact case

In the modeling of the dynamic axial crushing, the same boundary conditions as described above were applied. The tube was impacted by the loading plate with certain downward velocities. The initial velocity of the loading plate was imposed by the command *INITIAL_VELOCITY_RIGID_BODY.

In both the quasi-static and dynamic crushing simulations, two other contact algorithms were also used to model the behavior of the hybrid tube. One was a self-contact algorithm to prevent interpenetration during the progressive folding of the tube using the command *CONTACT_AUTOMATIC_SINGLE_SURFACE, which was also used to simulate the interaction between the pultruded and braided tubes. A contact algorithm was used to tie the pultruded tube to the braided tubes, by the command *CONTACT_TIEBREAK_NODES_ONLY. The contact algorithm accounts for both normal and shear forces at the interface. The tiebreak criterion in this algorithm follows the following relationship [26].

$$\left(\frac{f_n}{NFLF}\right)^2+\left(\frac{f_s}{SFLF}\right)^2 \geq 1.0 \qquad (6\text{-}1)$$

where f_n is the normal force at the interface; f_s is the shear force at the interface; NFLF is the normal force at the bond failure and SFLF is the shear force at the bond failure.

In this study, the values of both NFLF and SFLF were assumed to be 100 N, which is related to the mechanical properties of the resin. Our previous study [1] has shown that the assumed failure forces can reasonably reflect the real situation, and that the variation of the failure force had minor influence on the crushing pattern, as well as the energy absorption capability of the tubes. A similar experimental study [14] also found that the influence of surface treatments of multi-material structures was insignificant on the specific energy absorption values.

6.5 Discussions

It was shown in a previous study [1] that a pultruded tube with fibers oriented along the tube's length offered the highest energy absorption capacity among the composite tubes that were tested (tubes had the same thickness, but different stacking sequences). However, it was also observed that the pultruded tube crushed in an asymmetric manner, or in a splitting mode. Moreover, by comparing the $[0]_4$ and $[\pm 45]_2$ lay-ups tubes, it was seen that the $[\pm 45]_2$ tube crushed in a symmetric manner, in a rather perfect local buckling mode. It was therefore concluded that combining these two lay-ups would produce an energy absorber that would possess both the described attributes (i.e., a combined symmetric and local buckling failure modes with high energy absorption capacity).

6.5.1 Numerical results and discussion

In a real crash event, the crushing distance should not progress through the entire length of the energy absorber. Therefore, only the first portion of the crushing displacement curve is used to evaluate the energy absorption capacity of the tubes. For all tubes simulated, the peak crushing force (or crushing initiation force, F_I) is taken from data of the entire crushing event, whereas the absorbed energy and mean crushing force are evaluated from the first 80 mm of the crushing distance. Both quasi-static and dynamic axial crushing were simulated for all tubes. In the simulation of the dynamic crushing, two different velocities (i.e., 6 m/s and 14 m/s), were used for the 100 kg loading plate. For all hybrid tubes, the crushing responses of the corresponding pultruded

tube without braiding, subject to both quasi-static and dynamic loads, were also simulated and considered. The summary of the results for all hybrid tubes, as well as the corresponding pultruded tubes (without braiding) are provided in Table 6.2.

Table 6-2: Summary of the crushing characteristics of the pultruded and hybrid tubes

Type of Tube	Braid type	Model name	Braid thickness (mm)	Loading condition	Absorbed Energy (J)*	Peak crushing force (F_I)	Mean crushing force (F_{avi}) *	Energy increase (%)
Pultruded	None	P_only	None	Q-S	1520	32.75	18.92	N/A
Pultruded	None	P_only	None	D_v=6	1430	32.64	17.74	N/A
Pultruded	None	P_only	None	D_v=14	1413	32.1	17.47	N/A
Hybrid	Glass fiber	HPG1	0.30	Q-S	1650	34.39	20.55	8.55
Hybrid	Glass fiber	HPG1	0.30	D_v=6	1590	34.27	19.9	11.19
Hybrid	Glass fiber	HPG1	0.30	D_v=14	1530	33.65	18.85	8.28
Hybrid	Glass fiber	HPG2	1.00	Q-S	1930	42.1	24	26.97
Hybrid	Glass fiber	HPG2	1.00	D_v=6	1950	42	24.4	36.36
Hybrid	Glass fiber	HPG2	1.00	D_v=14	1950	41	22.4	38.00
Hybrid	Carbon fiber	HPC1	0.30	Q-S	1630	38.2	20.3	7.24
Hybrid	Carbon fiber	HPC1	0.30	D_v=6	1700	37.9	20.8	18.88
Hybrid	Carbon fiber	HPC1	0.30	D_v=14	1740	37.42	21.4	23.14
Hybrid	Carbon fiber	HPC2	1.00	Q-S	2060	54.4	25.5	35.53
Hybrid	Carbon fiber	HPC2	1.00	D_v=6	2070	55.1	25.8	44.76
Hybrid	Carbon fiber	HPC2	1.00	D_v=14	2150	54.7	26.3	52.16
Note:	**Q-S**: Quasi-static; **D_v=6**: Dynamic crushing (v= 6m/s); **D_v=14**: Dynamic crushing (v=14 m/s); * The absorbed energy and mean crushing force are calculated based on 80 mm axial crushing displacement for all tubes							

As seen from Table 6.2, for the pultruded tubes, the peak crushing force (F_I) is very similar in the three loading conditions considered. The energy absorption capability of the pultruded tubes in the quasi-static case is slightly higher than that of the dynamic loading cases (1520 J compared to 1430 J and 1413 J).

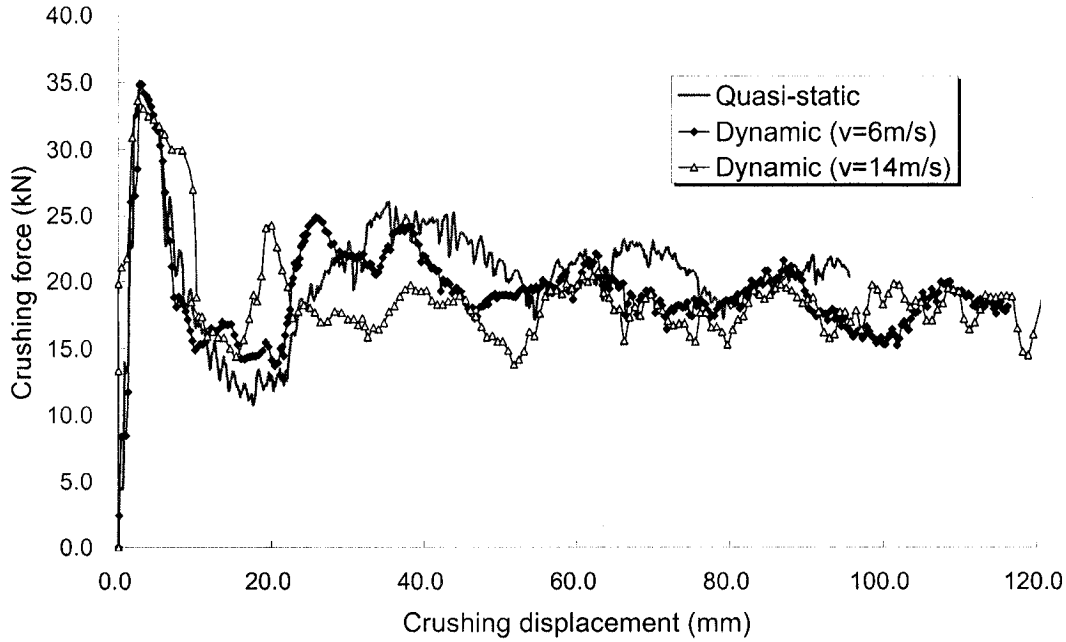

(a)- HPG1

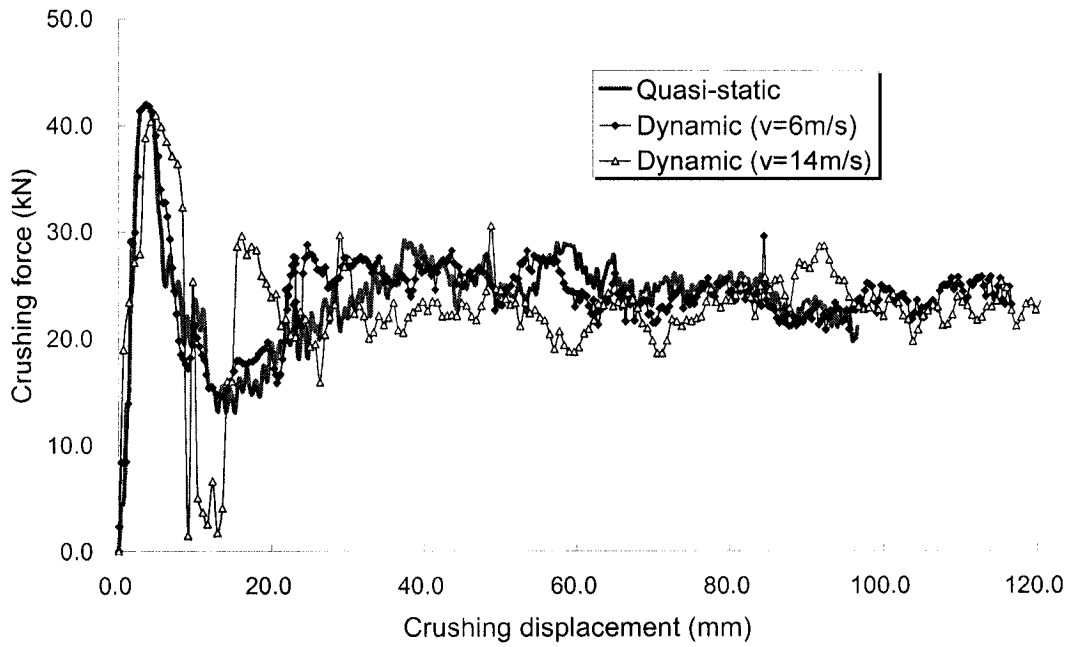

(b)- HPG2

(c) and (d) on next page

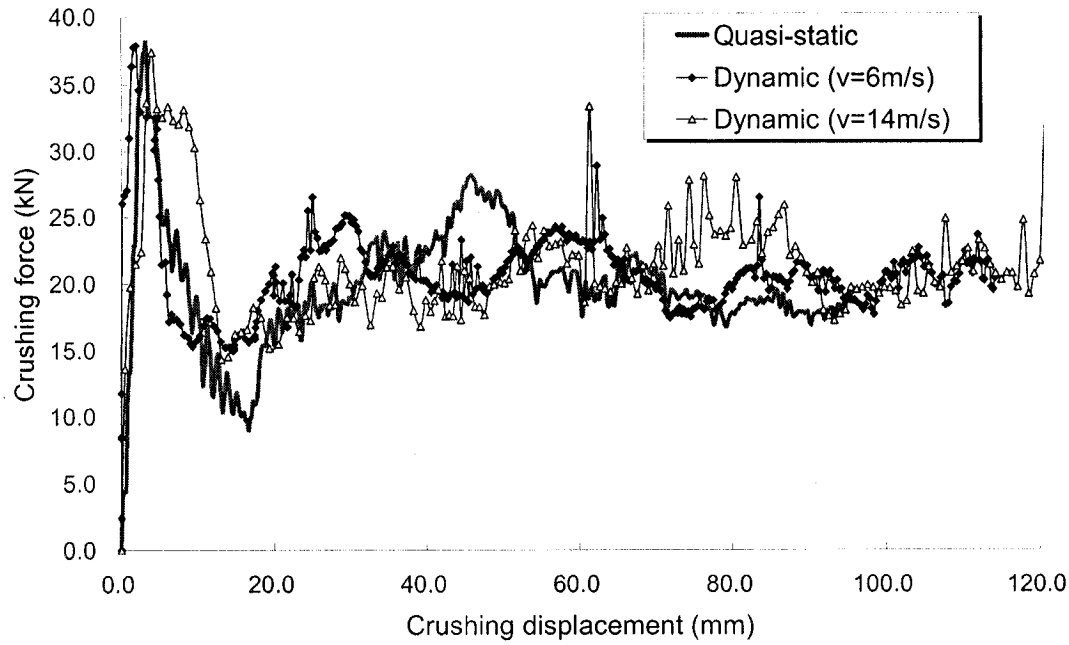

(c)- HPC1

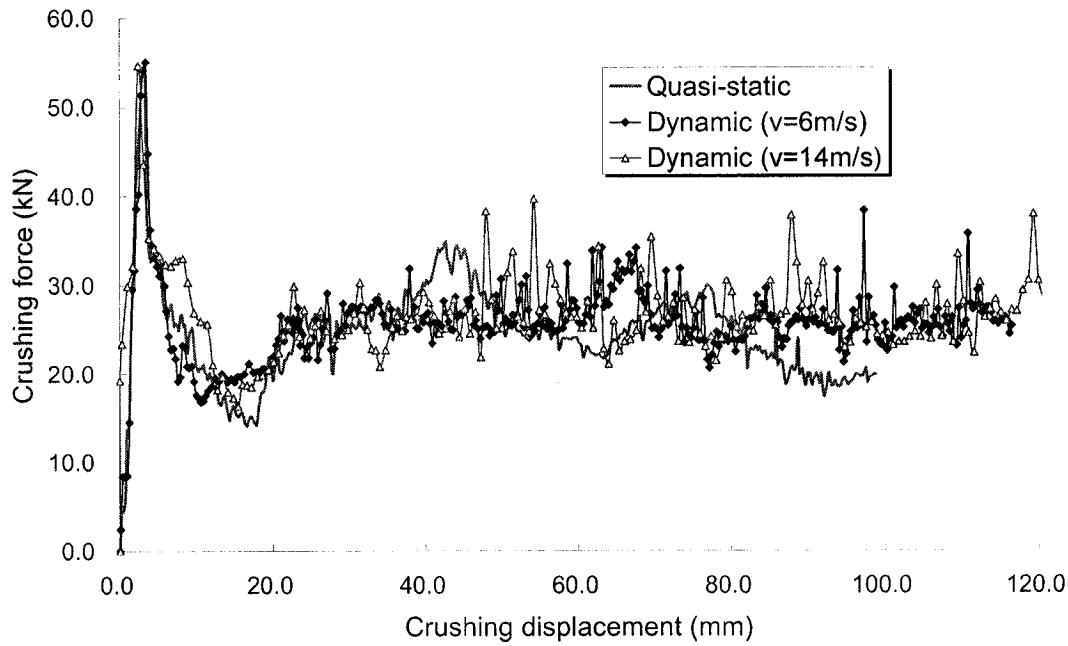

(d)- HPC2

Figure 6-4: Plot of crushing force vs. crushing displacement of the hybrid tubes (HPG1, HPG2, HPC1 and HPC2) subject to various loading conditions

6.5.1.1 Numerical results of the hybrid tubes

Two different thicknesses of braids (0.3 mm and 1.0 mm) were used to overwrap the pultruded tubes to form the hybrid tubes. Figure 6.4 shows the numerical crushing force versus crushing displacement response of the hybrid tubes, namely HPG1, HPG2, HPC1 and HPC2. It is observed that the peak crushing forces are almost within the same magnitude under the three loading conditions in all hybrid tubes. As seen from Table 6.2, by using the 0.3 mm glass fiber overwrap, the energy absorption capability of the HPG1 tubes was increased by 8.55% in quasi-static crushing, and by 11.19% and 8.28% in the 6 m/s and 14 m/s dynamic crushing cases, respectively. Although the energy absorption capacities were improved remarkably in the above tubes, with the presence of the glass fiber braidings, the peak crushing force only increased by a very small magnitude (less than 5%). This is a desirable attribute for an effective energy absorber. For example, if such a component is used as an energy absorber in a race car, or in an aircraft landing gear, it would absorb considerable amount of energy, but exerting minor force to the occupants of the vehicle.

It is evident from Figure 6.4b that for HPG2 tube, the responses from quasi-static crushing and dynamic crushing with 6 m/s velocity are very similar, when considering the peak and mean crushing forces, as well as the energy absorption capacities. There is however more significant fluctuation in the dynamic crushing with 14 m/s velocity in HPG2 tubes, particularly at the early stage of the events. Figure 6.5 shows the response of the hybrid tubes (HPG2) at six stages during the event. With the presence of glass fiber braiding, the hybrid tubes are crushed in a more stable manner (i.e., in a local buckling mode, as seen in Figure 6.5). As can be seen from the results summarized in Table 6.2, the 1.0 mm glass fiber braid could be used to effectively enhance the energy absorption capacities of the hybrid tubes (in this case by 26.97%, 36.36% and 38.00% for the quasi-static, and the 6 m/s and 14 m/s dynamic crushing cases, respectively).

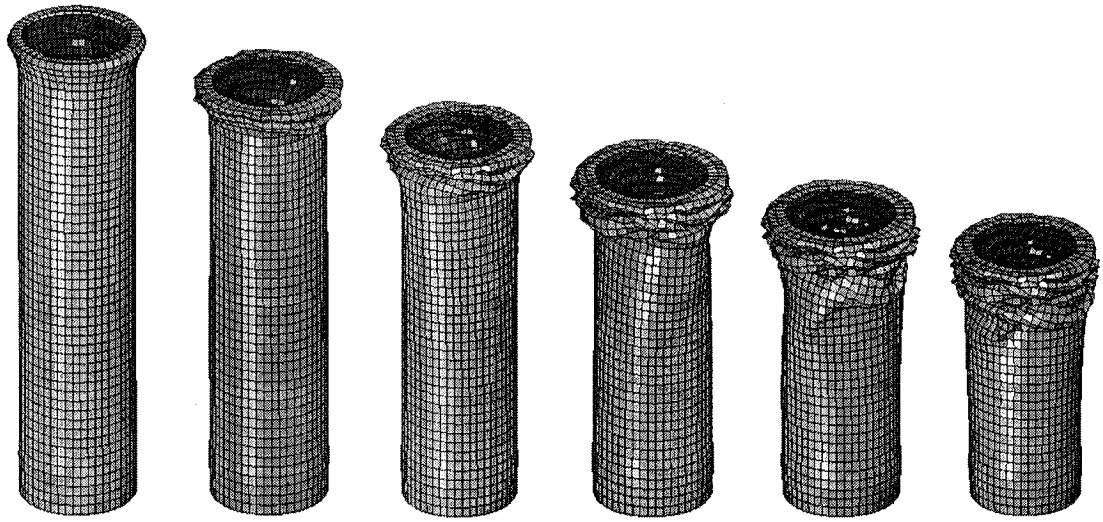

Figure 6-5: Crushing profiles of the HPG2 tube at different stages of the dynamic crushing event (v=6 m/s)

The crushing response of the HPC1 and HPC2 hybrid tubes are shown in Figures 6.4c and 6.4d, respectively. It is shown that for the HPC1 and HPC2 hybrid tubes, the responses from all three loading conditions are quite similar. With the presence of the carbon fiber braiding, the energy absorption capacities of the pultruded tubes are improved by up to 23.14% for the 0.3 mm thick braider and 52.16% for the 1.0 mm thick braiding, respectively, under dynamic crushing with velocity of 14 m/s.

As expected, the carbon fiber braid enhances the crushing response of the pultruded tubes much more remarkably than that offered by the glass fiber braid, because the carbon fiber has much larger longitudinal modulus in comparison to the glass fiber. However, as summarized in Table 6.2, in some cases the carbon fiber braid offered either similar capacity, or even lower capacity than that produced by the glass fiber braid of the same thickness. This is believed to be due to the fact that the carbon epoxy braidings have lower transverse modulus, transverse compressive strength and minor Poisson's ratio than the equivalent glass epoxy. Figure 6.6 shows the crushing response of the HPC2 tube at six progressive crushing stages corresponding to the 6 m/s dynamic crushing event. A brittle failure associated with the fiber or matrix tensile failure is observed in the hybrid tubes with carbon fiber braidings (Figure 6.6). It is postulated that the large mismatch of the Poisson's ratio between the glass fiber pultruded tube and the

carbon fiber braid could have also adversely impacted the positive attribute of carbon fiber braids. However, in most cases, the carbon fiber braid could enhance the energy absorption capacity of the tubes more remarkably than that achieved by glass fiber braid of the same thickness, noting that the crushing mode may be relatively unfavorable. As summarized in Table 6.2, the 0.3 mm carbon fiber braid improved the energy absorption capacity by 7.24-23.14%, whereas the glass fiber braid increased it by 8.28-11.19%.

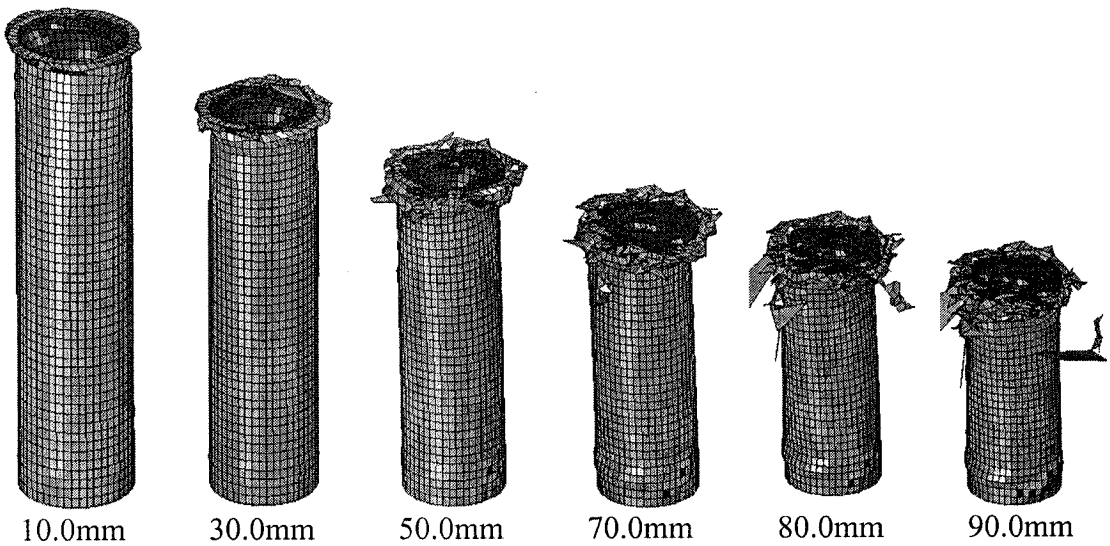

Figure 6-6: Crushing profiles of the HPC2 tube at different stages of the dynamic crushing event (v=6 m/s)

6.5.1.2 Influence of the braid type and loading condition

The comparison of the quasi-static and dynamic crushing behaviors of the hybrid tubes (see Figure 6.4) indicates that although the folding (or local buckling ripples) did not form within the same crushing distance, overall however, the folding patterns were very similar, and the peak crushing forces were almost the same in both the quasi-static and dynamic cases.

In tubes with the same type of braiding, the crushing behavior of the tube with thicker braid is more unlikely to be a perfect progressive local buckling mode than the one with thinner braid, although the one with thicker braid could absorb more energy.

Comparing the tubes having the same thickness of either glass fiber or carbon fiber braids, it was observed that the behavior of the tubes with carbon fiber braid was more unstable compared to the one with glass fiber braid.

The numerical results indicate that braiding overwraps could be used to effectively enhance the crushing characteristic and energy absorbing capability of the tubes. The energy absorption capacity of the pultruded tubes was decreased with the increase in impact speed, as tabulated in Table 6.2. However, with the presence of the braids, the tubes could absorb more energy as the impact velocity was increased. Therefore, the contribution of braiding is much more significant at high impact velocities than in quasi-static crushing. The enhancement in energy absorption in the hybrid tubes compared with the corresponding pultruded tubes under three different loading conditions is illustrated in Figure 6.7. It is seen that the contribution of braid is more pronounced at relatively high velocity impacts.

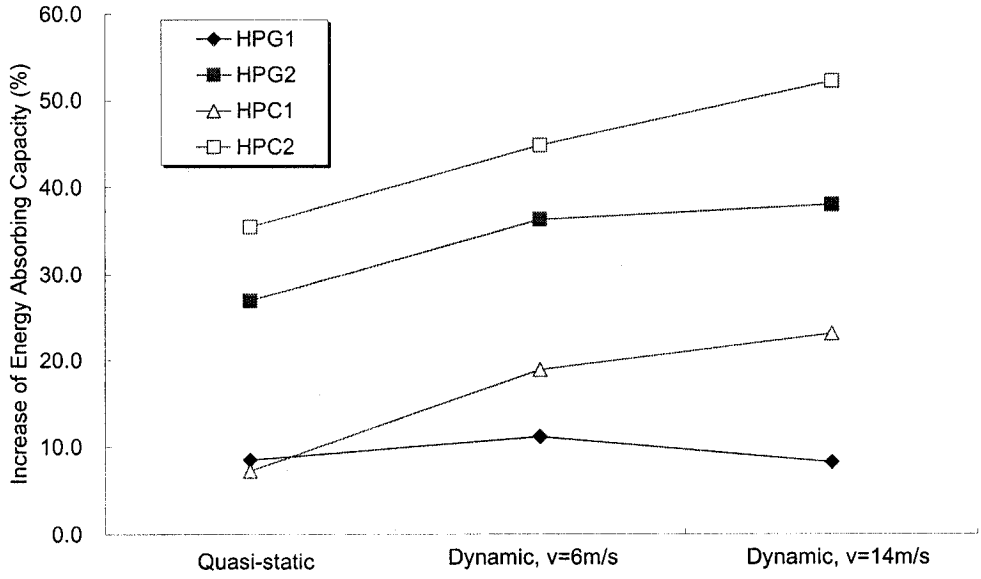

Figure 6-7: Enhancement in energy absorption capacity of the hybrid tubes compared to the pultruded tube

6.5.2 Experimental verifications

It has been discussed in many relative studies [such as 2, 15 and 16] that the existence of a chamfer at the crush front can reduce the peak crushing forces, but not

necessarily the mean crushing forces. The purpose of introducing a trigger mechanism, such as a chamfer, is to ensure that a tube is crushed in a progressive crushing manner. Since this trigger mechanism was not used in the numerical studies, comparison of the peak crushing forces between the numerical and experimental would not be quite compatible. Therefore, only the mean crushing force is used as the indicator in assessing the energy absorption capacity of the pultruded and hybrid tubes.

Tests were first carried out on the pultruded tubes with and without chamfer. The crushing force versus crushing distance response obtained through these tests, and from finite element simulation are illustrated in Figure 6.8a. Interestingly, very good agreement was observed between the test results of the tubes without chamfer and the FEM simulations. It can be noted that although with the presence of chamfer, the peak crushing force is remarkably reduced; however, the mean crushing forces in the three different cases in Figure 6.8a are very close to each other. The actual crushing profiles at the crushing distance of 10 mm, 80mm and 100mm are shown in Figure 6.8b. It is seen that the crushing mode was essentially longitudinal splitting, with brittle crack propagation within the interfaces of the longitudinal fibers.

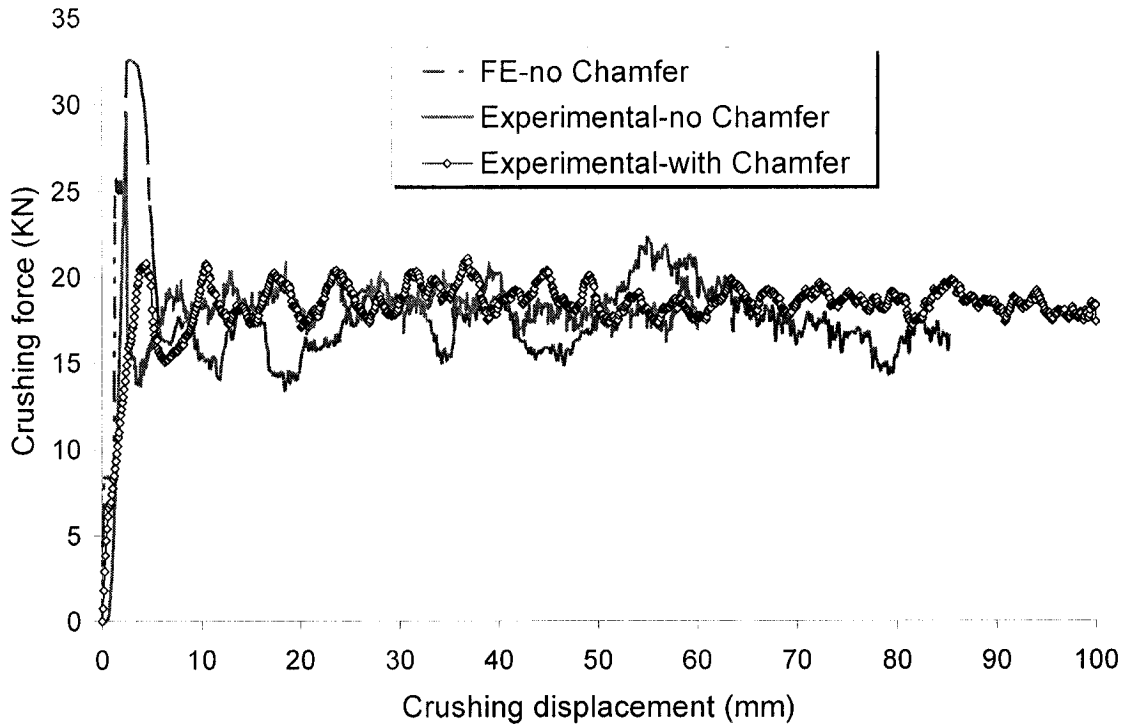

(a) Crushing force vs. crushing displacement curve

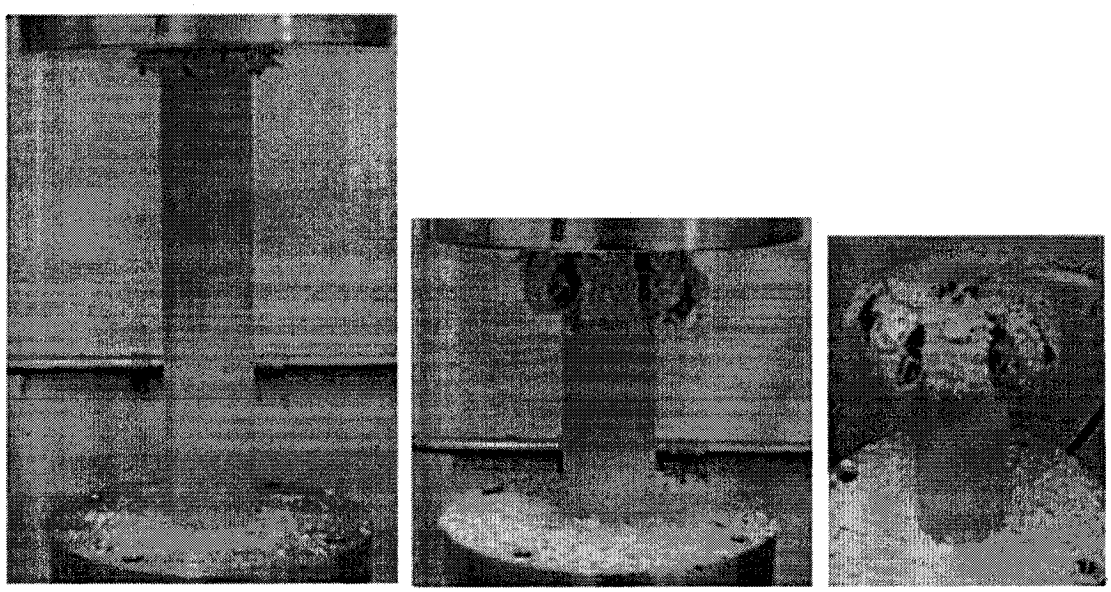

(b) Progressive crushing profiles in quasi-static crushing test

Figure 6-8: Comparison of FE and Experimental results for the pultruded tube

As stated earlier, all tested hybrid tubes were chamfered at the crushing front to ensure failure in a progressive crushing manner. Figure 6.9 shows the crushing force versus crushing distance response of HPG1 tube and its crushing profiles at the crushing displacement of 10 mm, 80mm and 100mm. As mentioned earlier, the chamfer was not modeled in the FE simulation; therefore, the peak crushing force is somewhat higher than that observed from the experiment; however, the mean crushing forces agree with each other very well. Likewise, Figures 6.10-6.12 show the results for HPG2, HPC1 and HPC2 tubes. The mean crushing forces of all tubes tested are summarized in Table 6.3. Very good agreements are observed for the mean crushing forces in all tubes tested between numerical and experimental studies. It was found from both numerical and experimental investigation that the energy absorption capacity of the hybrid tubes was significantly higher than that of the pultruded tube. The mean crushing force of the hybrid tubes increased with braid's thickness. It is also noticed from Figures 6.9b-6.12b that the failure in interface bond between the pultruded and braided components of the tube was observed during the crushing events. The pultruded tube failed in splitting mode eventually, whereas the braids failed in a self-compacting mode. However, the presence of the braids somewhat restrained the brittle crack propagation, thus reinforced the flexural behavior of the tube walls, and in turn improved the energy absorption capacity.

Table 6-3: Summary of the mean crushing force of the pultruded tube and hybrid tubes obtained from the numerical and experimental investigations

Type of tubes	**Mean Crushing Force** (kN)		**Increment of Mean Crushing force** (%)	
	FE	Experimental	FE	Experimental
Pultruded	18.9	18.6	N/A	N/A
HPG1	20.6	20.9	8.99%	12.37%
HPG2	24.0	24.6	26.98%	32.26%
HPC1	20.3	20.7	7.41%	11.29%
HPC2	25.5	26.2	34.92%	40.86%

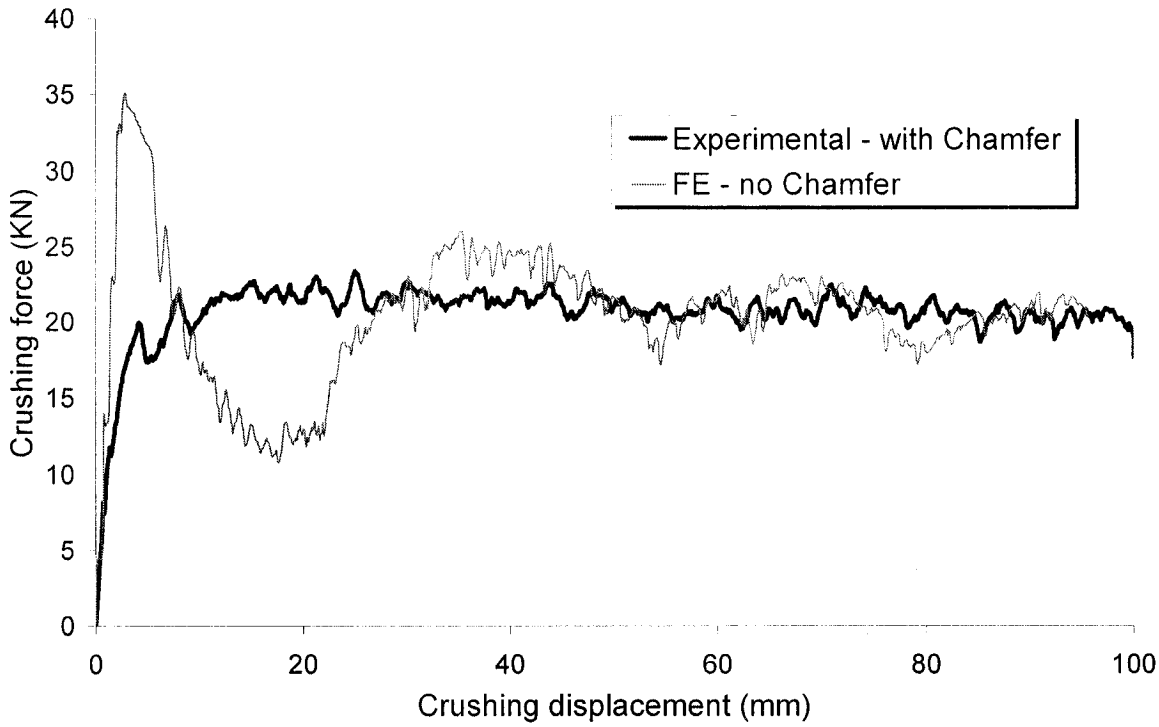

(a) Crushing force vs. crushing displacement curve

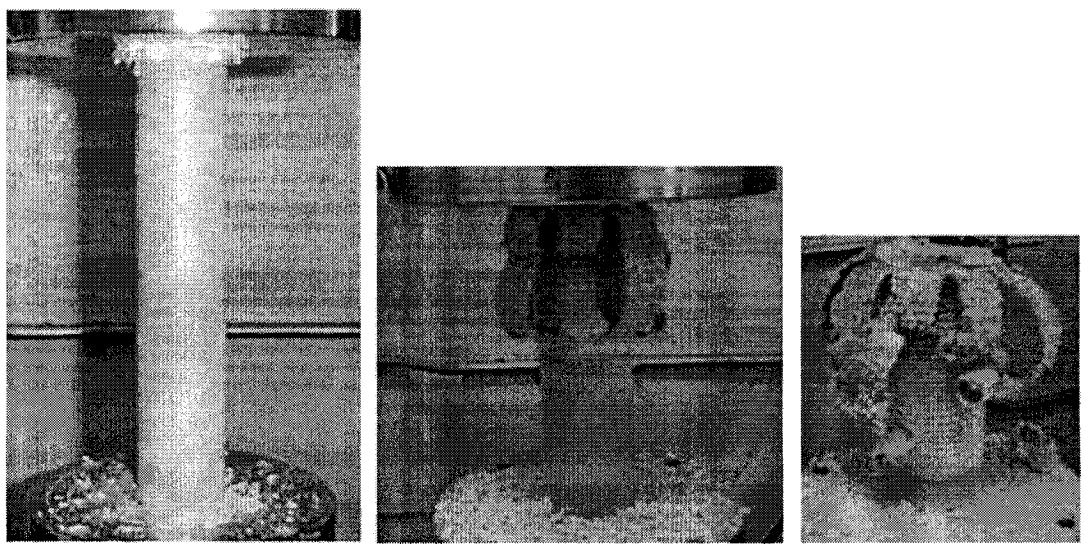

(b) Progressive crushing profiles in quasi-static crushing test

Figure 6-9: Comparison of FE and Experimental results for the HPG1 hybrid tube

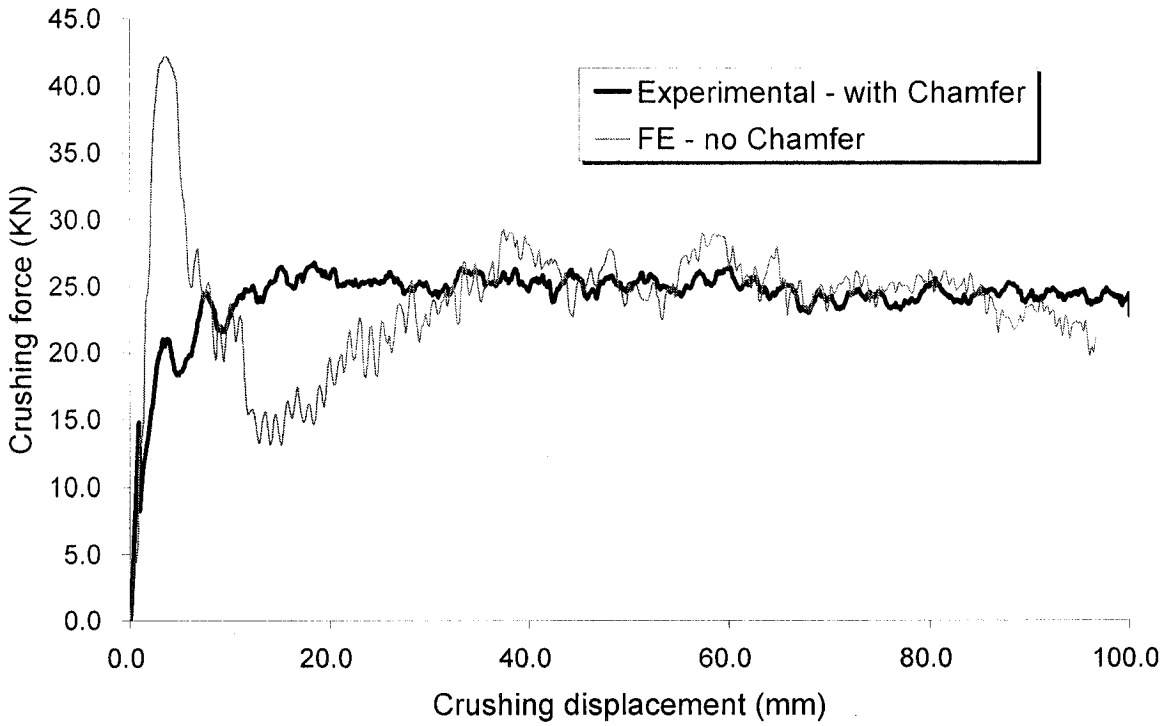

(a) Crushing force vs. crushing displacement curve

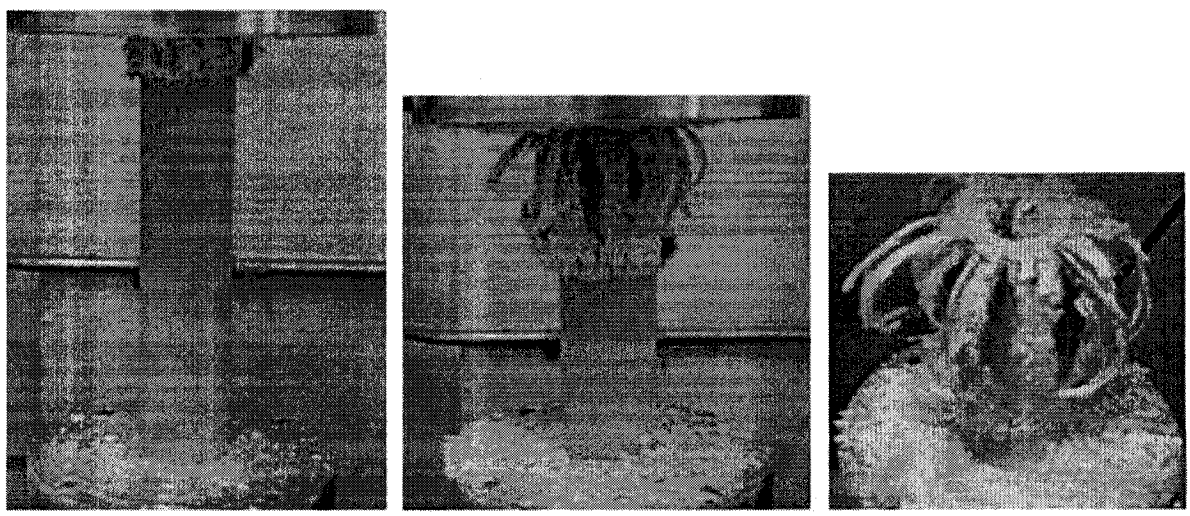

(b) Progressive crushing profiles in quasi-static crushing test

Figure 6-10: Comparison of FE and Experimental results for the HPG2 hybrid tube

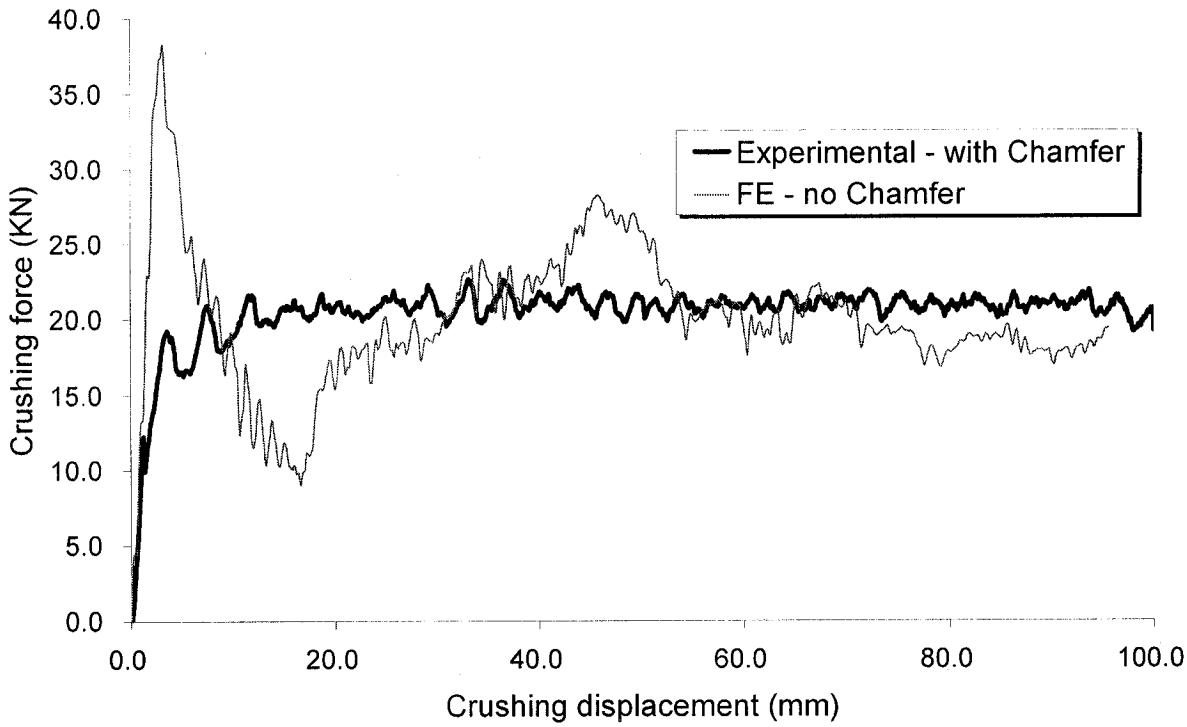

(a) Crushing force vs. crushing displacement curve

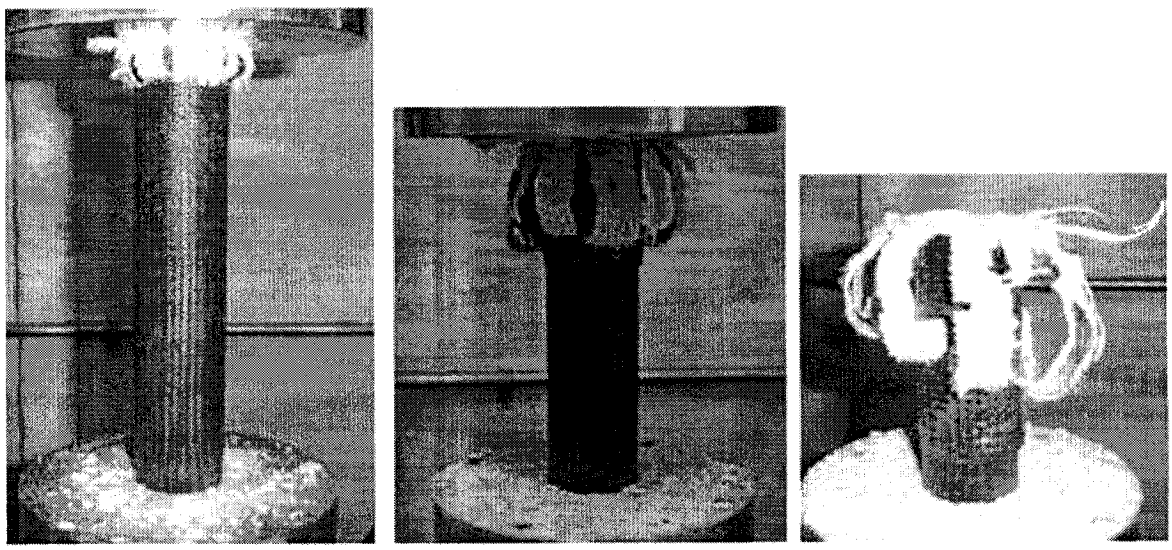

(b) Progressive crushing profiles in quasi-static crushing test

Figure 6-11: Comparison of FE and Experimental results for the HPC1 hybrid tube

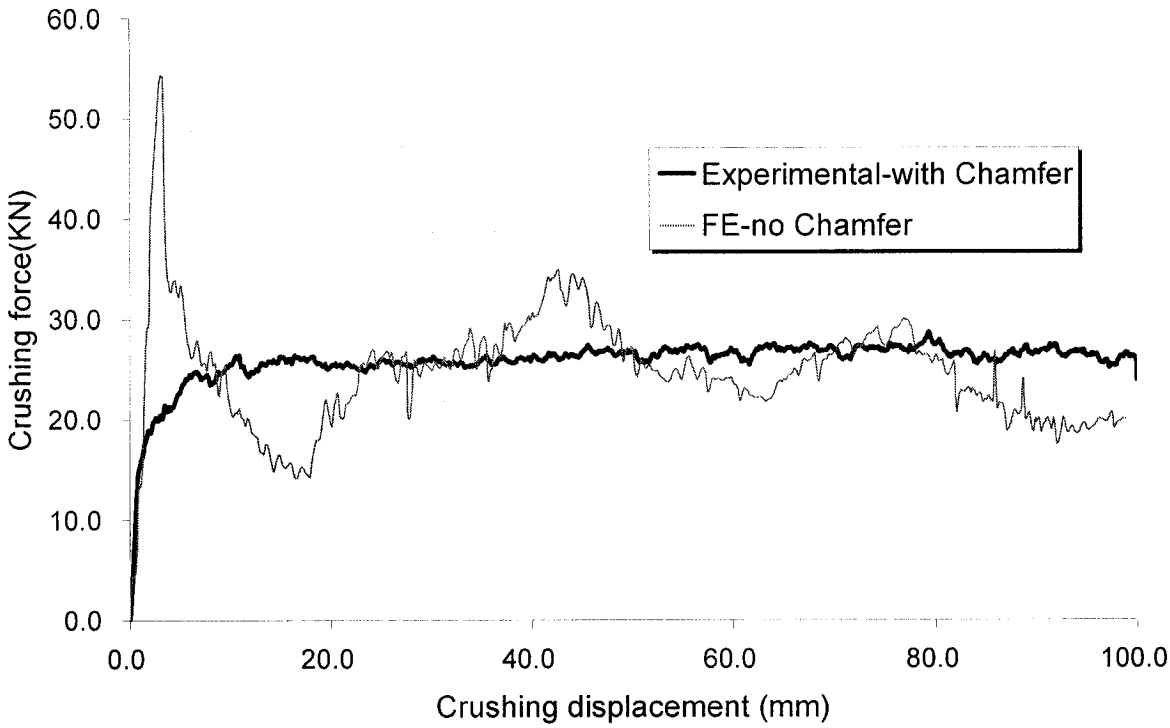

(a) Crushing force vs. crushing displacement curve

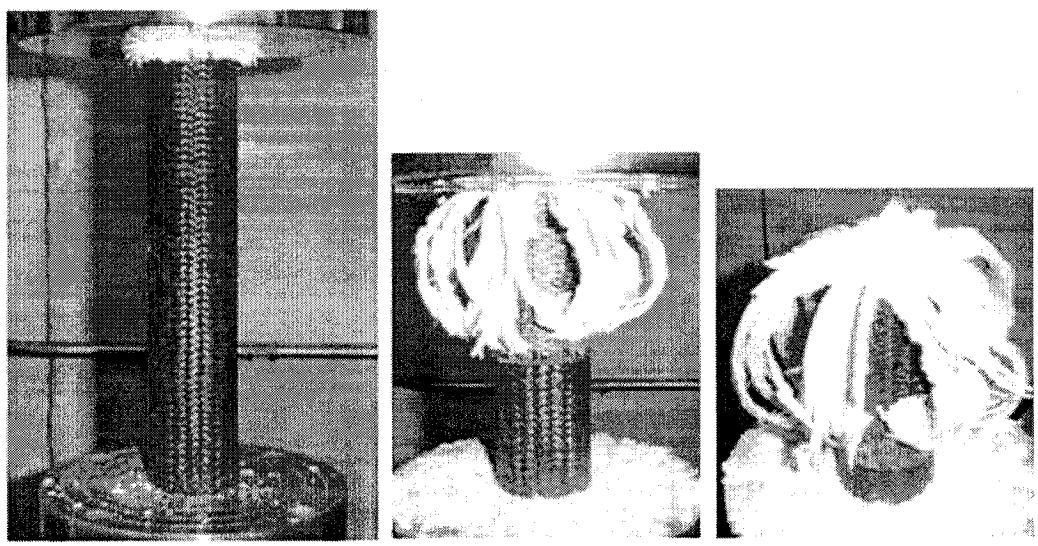

(b) Progressive crushing profiles in quasi-static crushing test

Figure 6-12: Comparison of FE and Experimental results for the HPC2 hybrid tube

Similar to the findings of the numerical studies, the energy absorption capacity of the HPC1 tube was found to be lower than that of the HPG1 tube, although carbon fiber braids are stronger than glass fiber braids. The plausible reason would be that the bonding between carbon braids and glass fiber pultruded tube is not as strong as the one between glass fiber braids and glass fiber pultruded tube. This could be due to the mismatch of the Poisson's ratios between glass fiber pultruded tube and carbon fiber braids as well as the difference between the so-called "mutual influence ratio" (the ratio of the longitudinal modulus to shear modulus [28]) coupled with the sudden burst of energy during the crushing event. Therefore, less energy absorption capacity is offered by the HPC1 tube. Moreover, it is noticed from Table 6.1 that the transverse modulus and transverse tensile strength of carbon/epoxy braid are slightly less than those of glass/epoxy braid, which is another reason that could explain the lower energy absorption capacity of the HPC1 tube.

6.6 Conclusions

In this study the hybrid tubes made of pultruded tube overwrapped by braiding were considered as a viable energy absorbing components. From the results obtained through the numerical simulations and experimental investigation, it was found that overwrapping of braids over the pultruded tubes could be an effective way to enhance the energy absorption capacity and response of such tubes.

A majority of the pultruded tubes studied in our earlier investigation crushed in unpredictable modes (such as asymmetric crushing and splitting modes), although they could absorb the highest amount of energy among the composite tubes having the same thickness, but with various stacking sequences [1]. Therefore, both glass and carbon fiber braidings were employed in this investigation to enhance the energy absorption capacity and response of the pultruded tubes. A parametric study was conducted to consider the two types of braids and two different braid thicknesses. The response of the hybrid tubes under quasi-static and impulse forces under 6 m/s and 14 m/s velocities were simulated in the numerical studies. It was found that the response of the hybrid tubes was sensitive to braid thickness and loading conditions. Interesting insights were obtained by examining the interaction of the considered parameters. Most significantly, it was observed that

while the carbon fiber braid could increase the energy absorption capacity very effectively, it did not produce the desirable local buckling failure mode. Moreover, the thinner braid (0.3 mm) produced a more distinct local buckling failure mode in comparison to the thicker braid (1.0 mm). Furthermore, braids were found to be most effective under dynamic axial impact, because the higher the impact velocity, the more contribution the braids offered. The computational results into response of the quasi-static crushing of the hybrid tubes were compared by the experimental investigation. Very good agreements were observed between the results of the numerical and experimental studies.

In the future, dynamic crushing tests will be conducted to further ascertain the integrity of the numerical results. The future work will also consider different combinations of pultrution and braid tubes, such as high strength carbon fiber pultruded tubes with glass or carbon fiber braids.

6.7 Acknowledgement

The financial support of Natural Sciences and Engineering Council of Canada (NSERC) in the form of Discovery Grants to the second and third authors in support of this work is gratefully acknowledged.

6.8 Reference

[1] Han H., Taheri F., Pegg N. and Lu Y. (2006), A numerical study on the axial crushing response of hybrid pultruded and braided tubes, Accepted for publication in *Composite Structures.*

[2] Farley G.L. and Jones R.M. (1992), Crushing characteristics of continuous fiber reinforced composite tubes. *Journal of Composite Materials* 26(1): 37–50.

[3] Mamalis A.G., Yuan Y.B. and Viegelahn G.L. (1992), Collapse of thin wall composite sections subjected to high speed axial loading, *International Journal of Vehicle Design* 13 (5/6): 564-579.

[4] Hamada H., Ramakrishna S. and Sato H. (1996), Effect of fiber orientation on the energy absorption capability of carbon fiber/PEEK composite tubes, *Journal of Composite Materials* 30 (8): 947-963.

[5] Mamalis A.G., Manolakos D.E., Demosthenous G.A. and Ioannidis M.B. (1996), The static and dynamic axial collapse of fiberglass composite automotive frame rails, *Composite Structures* 34: 77-90.

[6] Schultz M.R. and Hyer M.W. (2001), Static and Dynamic Energy-Absorption Capacity of Graphite-Epoxy Tubular Specimens, *Mechanics of Composite Materials and Structures* 8: 231–247.

[7] Mahdi E., Sahari B.B., Hamouda A.M.S. and Khalid Y.A. (2001), An experimental investigation into crushing behavior of filament-wound laminated cone-cone intersection composite shell, *Composite Structures* 51: 211-219.

[8] Gupta N.K. and Prasad E.G.L. (1999), Quasi-static and dynamic axial compression of glass/polyester composite hemi-spherical shells, *International Journal of Impact Engineering* 22: 757-774.

[9] Mamalis A.G., Manolakos D.E., Ioannidis M.B. and Papapostolou D.P. (2005), On the crushing response of composite sandwich panels subjected to edgewise compression: experimental, *Composite Structures* 71: 246–257.

[10] Mahdi E., Hamouda A.S.M., Mokhtar A.S. and Majid D.L. (2005), Many aspects to improve damage tolerance of collapsible composite energy absorber devices, *Composite Structures* 67: 175–187.

[11] Mamalis A.G., Manolakos D.E., Ioannidis M.B. and Papapostolou D.P. (2005), On the experimental investigation of crash energy absorption in laminate splaying collapse mode of FRP tubular components, *Composite Structures* 70: 413–429.

[12] Mamalis A.G., Manolakos D.E., Ioannidis M.B. and Papapostolou D.P. (2005), On the response of thin-walled CFRP composite tubular components subjected to static and dynamic axial compressive loading: experimental, *Composite Structures* 69: 407–420.

[13] Song H.W., Wan Z.M., Xie Z.M. and Du X.W. (2000), Axial impact behavior and energy absorption efficiency of composite wrapped metal tubes, *International Journal of Impact Engineering* 24:385-401.

[14] Bouchet J., Jacquelin E. and Hamelin P. (2002), Dynamic axial crushing of combined composite aluminum tube: the role of both reinforcement and surface treatments, *Composite Structures* 56: 87–96.

[15] El-Hage H.H., A numerical study on the quasi-static axial crush characteristics of square aluminum and aluminum-composite hybrid tubes, *PhD thesis*, Department of Mechanical Engineering, University of Windsor, 2004.

[16] Babbage J.M. and Mallick P.K. (2002), Axial crush resistance of aluminum-composite hybrid tubes, Proceeding of *17th Annual Technical Conference of the American Society of Composite*, Paper No. 070.

[17] Chiu C.H. and Lu C.K. (1997), Crushing characteristics of 3-D braided composite square tubes, *Journal of Composite Materials* 31(22): 2309-2327.

[18] Karbhari V.M. and Hailer J.E. (1998), Rate and architecture effects on progressive crush of braided tubes, *Composite Structures* 43: 93-108.

[19] Chiu C.H., Tsai K.H. and Huang W.J. (1999), Crush-failure modes of 2D triaxially braided hybrid composite tubes, *Composites Science and Technology* 59: 1713-1723.

[20] Mahdi E., Hamouda A.M.S., Sahari B.B. and Khalid Y.A. (2003), Effect of hybridization on crushing behavior of carbon/glass fiber/epoxy circular–cylindrical shells, *Journal of Materials Processing Technology* 132: 49–57.

[21] Abosbaia A.A.S., Mahdi E, Hamouda A.M.S. and Sahari B.B. (2003), Quasi-static axial crushing of segmented and non-segmented composite tubes, *Composite Structures* 60: 327–343.

[22] Mamalis A.G., Manolakos D.E., Ioannidis M.B. and Kostazos P.K. (2003), Crushing of hybrid square sandwich composite vehicle hollow bodyshells with reinforced core subjected to axial loading: numerical simulation, *Composite Structures* 61:175–186.

[23] Mahdi E., Hamouda A.S.M. and Sen A.C. (2004), Quasi-static crushing behavior of hybrid and non-hybrid natural fiber composite solid cones, *Composite Structures* 66: 647–663.

[24] Saito H., Chirwa E.C., Inai R. and Hamada H. (2002), Energy absorption of braiding pultrusion process composite rods, *Composite Structures* 55: 407–417.

[25] Okano M., Sugimoto K., Saito H., Nakai A. and Hamada H. (2005), Effect of the braiding angle on the energy absorption properties of a hybrid braided FRP tube, *Journal of Materials-Design and Applications* 219 (L1): 59-66.

[26] *LS-DYNA keyword user's manual*, V970, LSTC, Livermore, CA, 2005.

[27] Zhang Z. and Taheri F. (2004), Dynamic pulse-buckling behavior of quasi-ductile' carbon/epoxy and E-glass/epoxy laminated composite beams, *Composite Structures* 64 (3-4): 269-274.

[28] Taheri F., Shahin K. and Widiarsa I. (2002), On the parameters influencing the performance of reinforced concrete beams strengthened with FRP plates, Composite Structures 58 (2): 217-227.

Chapter 7 Local Buckling mitigation and Stress Analysis of Shape Memory Alloy Hybrid Composite Plate with and without a Cutout

Haipeng Han[a], Farid Taheri[a*], Neil Pegg[b], Zheng Zhang[c]
[a]Department of Civil Engineering, Dalhousie University, 1360 Barrington Street, Halifax, NS Canada B3J 2Z1
[b]Defense Research and Development Canada – Atlantic, 9 Grove Street, Dartmouth, NS, Canada B2Y 3Z7
[c]Technology & Solutions Division, Caterpillar Inc. Peoria, IL 61552 USA

Submitted to the Journal of "**Smart Materials and Structures**" in September 2006

7.1 Abstract

In this paper, the numerical model of a shape memory alloy hybrid composite (SMAHC) plate was constructed based on the effective coefficient of thermal expansion (ECTE) model for the shape memory alloy (SMA) material. The embedded SMA wires were modeled as an integrated composite layer in conjunction with the host composite lamina. The tailored design feature of laminated composite plates allows the flexibility of orientating the SMAHC layer along different directions. The response of the SMAHC plates with and without a central cutout, having certain geometric imperfections, subjected to an initial in-plane compressive loading and a subsequent elevated thermal load, were investigated numerically and experimentally. The positive attribute of the SMA material could be used to successfully suppress the post-buckling deflection of the SMAHC plate under an elevated temperature, when the SMA wires were properly oriented. The variation of stress concentration around the cutout of the SMAHC plate was also investigated. It was found from this study that the orientation of SMA wires had significant influence on the suppression of the lateral deflection. The extent of such positive attributes was found to be influenced by the boundary conditions of the SMAHC plate.

---

* To whom correspondence should be addressed, email: farid.taheri@dal.ca, Phone:1-902- 494-3935; fax: 1-902-484-6635

Keyword: Local buckling mitigation, stress concentration, Shape Memory Alloy Hybrid Composite (SMAHC), Cutout

7.2 Introduction

The enhancement in structural performance using shape memory alloys has been investigated for a variety of applications since their discovery in early 50's. Ever since, numerous researchers have investigated the use of SMA actuators for control of structural performance under static and dynamic loading conditions. SMA has also been used as thermally actuated devices in self-erecting structures, in damping or energy absorbing devices, in thermally actuated couplings and fasteners, and in various biomedical devices [1-4].

It is known that the combination of thermal loads and immovable in-plane boundaries imposed to a slender member could result in a thermoelectric instability, thus causing large thermal post-buckling deflection. Four plausible and distinct configurations for the use of SMA wires to control buckling of a structure are: embedding them in composite structure [5], surface bonding them to the host structures [6], connecting them externally to the structure [7], and inserting them in composite structures via sleeves [8].

Several works [9-12] have examined the use of SMA wires to control the buckling and postbuckling behavior of composite structures. Two major approaches have been used. In one approach, pre-strained SMA wires were fixed to an external support, which was independent of the boundary of the host structures, thus generating a large tensile stress in the component when SMA wires were activated. For example, Choi [9] utilized the recovery force of SMA to control the mid-span deflection of a composite beam, and improved the buckling capacity of the beam. Loughlan *et al.* [10] used the recovery force to substantially reduce the out-of-plan deflections, thus increasing the ultimate failure capacities of composite plates, although the activation of their SMA exerted a negative thermal load on the composite. Tsai and Chen [11] used the same principle to increase the dynamic stability of a composite beam. However, as pointed out by Birman [12], a potential drawback in this approach was the necessity of isolating the forces applied by

SMA fibers to the clamps from the supported structure. If this isolation is not done properly, then the beneficial effect of the approach would be negligible.

An entire new applications of SMA was created when Rogers and Robertshaw [13] introduced the idea of shape memory alloy hybrid composites (SMAHC). In this approach, the pre-strained SMA actuators were enclosed within a composite matrix and the boundaries of the structures served as mechanical constraints to the actuator. This approach relies on the inherent in-service elevated thermal environment for activating the actuator, without the need for any external auxiliary power source [14-17]. Along the same vein, Tylikowski [14] studied the dynamic stability of rotating shells reinforced with SMA fibers. In his study, SMA wires were oriented parallel to the shell axis on the inner and outer surfaces of a laminated shell. By activating the SMA fibers, the admissible angular velocity of the SMAHC shell was remarkably increased. Jia [15] utilized of the concept of the SMAHC and studied the behavior of the SMAHC plate subject to lateral quasi-static and impact loadings. Tawfik *et al.* [16] numerically analyzed the thermal post-buckling of SMA reinforced composite plates. In their study, it was assumed that the SMA was embedded along the longitudinal fiber direction (1-direction), a nonlinear finite element model based on the von Karman strain–displacement relation was utilized to study the effectiveness of SMA for enhancement of the flutter boundary, critical buckling temperature, post-buckling deflection and free vibration of an SMA-embedded panel. Likewise, Roh *et al.* [17] constructed a nonlinear finite element model based on the layer-wise theory and studied the thermal post-buckling responses of the SMAHC shell panels. Their numerical analysis showed that the recovery stresses produced by the SMA wires could enhance the stiffness of the structure, and the resulting SMAHC shell panel exhibited superior response in thermally induced post-buckling compared to the conventional composite panel. It was also shown that embedding SMA wires in a composite structure could prevent the unstable post-buckling behavior of the structure.

Although the phenomenological and micromechanics-based constitutive models have been successfully used in most previous works, these models are found to be limited in capturing the complex behavior of SMA materials and also difficult to be implemented in advanced structural analysis. A model known as the "effective coefficient of thermal

expansion (ECTE) model", implementable in most commercial finite element packages has been developed in the series of works conducted by Turner [18-21]. To the best of our knowledge, the application of this model for enhancing the buckling and postbuckling response of a SMAHC plate, hosting SMA wires, has not been considered. In this investigation, not only would we consider the above, but also the applicability of SMA in mitigating postbuckling behavior of the SMAHC plate with a cutout would be investigated.

It should be noted that the stress distribution in plates with discontinuities represents a significant interest from both fundamental mechanics and practical engineering perspectives. An exact solution for the stresses in an infinite SMA plate with a circular hole subjected to far-field biaxial tensile stresses was presented by Birman [22]. The solution was obtained by assuming plane stress, and was based on the two-dimensional version of the Tanaka constitutive law for shape memory materials. There have also been several numerical and experimental studies [23-24], in which the shape memory alloy/epoxy matrix composite was used to reduce the stress concentration at a crack tip in the shape memory alloy fiber-reinforced/epoxy intelligent composite. In these two studies, a new design concept was proposed in developing a composite material that would have high-performance mechanical properties. The influence of temperature, prestrain, as well as crack angle and domain size were studied. As stated, to the best of our knowledge, the influence of variation in the orientation of SMA wires on the stress concentration at the edge of a cutout in SMAHC plates subject to in-plane compression loading has not been investigated.

In this paper, a numerical model of a SMAHC plate, utilizing the ECTE constitutive model to represent the SMA material, was constructed in the ABAQUS finite element program. The SMAHC plate, with and without a cutout, and having certain geometric imperfections, was subject to in–plane pre-compression and was subsequently subject to a thermal load. Two types of boundary conditions for the plate were considered; one with four sides being simply supported (hereafter referred to as "SSSS"), and the other with two sides simply supported and two sides free (SSFF). With the shape memory effect under elevated temperature, the postbuckling response of the SMAHC plates with and without a cutout was characterized. The variation in stress concentration

factor at the edge of the cutout in the SMAHC plate in pre-buckling stage, at the onset of buckling and during postbuckling stage was also investigated. An experimental program was also carried out to verify the findings of the numerical study.

7.3 Constitutive modeling of SMAHC plate based on ECTE model

The ECTE constitutive models for SMA and SMAHC materials will be described in this section. Significant progress has been made in the areas of characterization and constitutive modeling of SMA materials and their integration into engineering applications. However, the development of conceptual structural components has been stymied by the lack of a robust analytical tool within a general purpose structural analysis environment. In the past, most of the structural concepts involving SMA materials have evolved by trial and error and/or by using excessively simplified modeling approaches.

An engineering model, referred to as ECTE, for SMA materials was recently developed based on the nonlinear thermoelasticity and a definition of an effective coefficient of thermal expansion [18]. The ECTE model has the advantages of being relatively simple to use, readily implementable in most commercial codes, and requires only the fundamental engineering properties as its input. The ECTE model does, however, have a more restrictive range of application than the phenomenological/micro-based models. The ECTE model has been used previously to analyze the static and dynamic response of the SMAHC beam and plate structures by a special purpose code [19-20] and a commercial finite element code [21].

There are various composite material types, structural fabrication techniques, and embedding strategies to integrate SMA actuators. Likewise, there are many micromechanical models for evaluating the effective composite properties and resulting constitutive equations for such hybrid composites. The case considered here is a laminated composite composed of unidirectional pre-impregnated (pre-preg) layers with SMA actuator wires embedded within the laminae. A representative volume element of an individual SMAHC lamina, with principal material coordinates 1 and 2, is shown schematically in Figure 7-1. This example is used for simplicity of illustration.

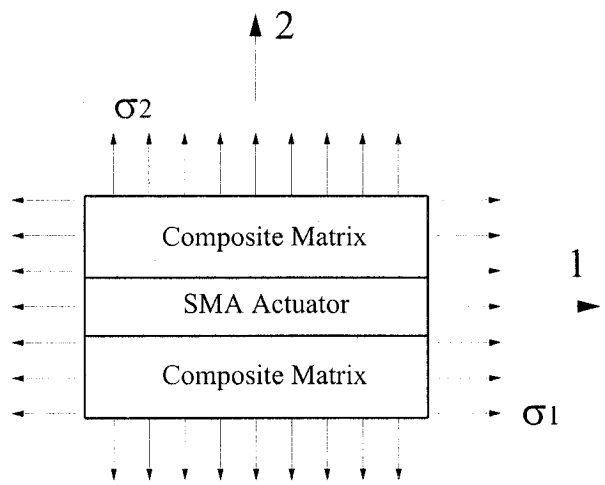

Figure 7-1: The representative volume element for the SMAHC lamina

The thermoelastic constitutive relations in the principal material coordinates for a thin orthotropic lamina under conditions of plane stress can be expressed in the following form

$$\begin{Bmatrix}\sigma_1\\ \sigma_2\\ \tau_{12}\end{Bmatrix}=\begin{bmatrix}Q_{11} & Q_{12} & 0\\ Q_{12} & Q_{22} & 0\\ 0 & 0 & Q_{66}\end{bmatrix}\left(\begin{Bmatrix}\varepsilon_1\\ \varepsilon_2\\ \gamma_{12}\end{Bmatrix}-\int_{T_0}^{T}\begin{Bmatrix}\alpha_1(\tau)\\ \alpha_2(\tau)\\ 0\end{Bmatrix}d\tau\right) \tag{7-1}$$

where $[Q]$ is the plane stress-reduced stiffness matrix, $\{\varepsilon\}$ is the total strain vector, and $\{\alpha\}$ is the vector of coefficients of thermal expansion. The stiffness terms are related to the effective engineering properties through the following equations:

$$Q_{11}=\frac{E_{11}}{1-\nu_{12}\nu_{21}} \tag{7-2}$$

$$Q_{12}=\frac{\nu_{12}E_{22}}{1-\nu_{12}\nu_{21}} \tag{7-3}$$

$$Q_{22}=\frac{E_{22}}{1-\nu_{12}\nu_{21}} \tag{7-4}$$

$$Q_{66}=G_{12} \tag{7-5}$$

To analyze the SMAHC structures, the estimation of the effective engineering properties for the lamina made of composite matrix and SMA actuator (the SMAHC

lamina) must be determined in order to make use of the constitutive relations described by equations (7-1~7-5). A mechanics of materials approach can be used as follows to develop the effective properties for such SMAHC lamina.

The most fundamental feature of the ECTE model is the axial constitutive relation of the SMA actuator, in which the non-mechanical (i.e., thermal and transformation) strain is represented by an effective thermal strain:

$$\sigma_{1a}(T) = E_a(T)\left[\varepsilon_1 - \int_{T_0}^{T} \alpha_{1a}(\tau)d\tau\right] \tag{7-6}$$

where $E_a(T)$ is the Young's modulus of the SMA material, ε_1 is the total axial strain, α_{1a} is the effective coefficient of thermal expansion, and the subscript a indicates that the quantity is specific to the actuator material. A measure of nonlinear CTE $\alpha_{1a}(T)$ over the temperature range of concern (T_0 to T) is necessary. It can be seen from Equation (7-6) that the ECTE model is intended to model thermally induced transformation phenomena, as opposed to a stress induced (pseudoelasticity) phenomenon. Equation (7-6) also implicitly indicates that the thermal strain is not only governed by the usual thermoelastic effects at temperatures below the austenite start temperature ($T < A_s$), but also is related to the recovery stress (σ_r), and actuator's Young's modulus at higher temperatures ($T \geq A_s$), as indicated by:

$$\sigma_r(T) = -E_a(T)\int_{T_0}^{T} \alpha_{1a}(\tau)d\tau \tag{7-7a}$$

or

$$\int_{T_0}^{T} \alpha_{1a}(\tau)d\tau = -\sigma_r(T)/E_a(T) \tag{7-7b}$$

Equation (7-7) implies that the measurement of the fundamental engineering properties (α_{1a} for $T < A_s$, σ_r and E_a for $T \geq A_s$) from experiments approximating the intended use condition (e.g., prestrain level and constraint) is all that is required to quantify the model. A similar constitutive expression can be written for the actuator in the transverse direction:

$$\sigma_{2a}(T) = E_a(T)\left[\varepsilon_2 - \int_{T_0}^{T} \alpha_{2a}(\tau)d\tau\right] \tag{7-8a}$$

or

$$\int_{T_0}^{T} \alpha_{2a}(\tau)d\tau = \varepsilon_2 - \sigma_{2a}(T)/E_a(T) \tag{7-8b}$$

where α_{2a} is not related to recovery stress, but is still nonlinear due to differing martensitic and austenitic properties. Note that it has been assumed that the Young's modulus for the SMA is directionally independent.

Similarly, the expressions for the composite matrix material, denoted by the subscript *m*, follow directly.

$$\sigma_{1m}(T) = E_{1m}(T)\left[\varepsilon_1 - \int_{T_0}^{T} \alpha_{1m}(\tau)d\tau\right] \tag{7-9a}$$

or

$$\int_{T_0}^{T} \alpha_{1m}(\tau)d\tau = \varepsilon_1 - \sigma_{1m}(T)/E_{1m}(T) \tag{7-9b}$$

and

$$\sigma_{2m}(T) = E_{2m}(T)\left[\varepsilon_2 - \int_{T_0}^{T} \alpha_{2m}(\tau)d\tau\right] \tag{7-10a}$$

or

$$\int_{T_0}^{T} \alpha_{2m}(\tau)d\tau = \varepsilon_2 - \sigma_{2m}(T)/E_{2m}(T) \tag{7-10b}$$

Given the above effective engineering properties of the SMA material and composite materials, one can construct the effective properties of a SMAHC lamina, based on the constitutive relation of rule of mixture [21], as follows:

$$E_1 = E_a v_a + E_{1m} v_m \tag{7-11}$$

$$E_2 = \frac{E_a E_{2m}}{E_a v_m + E_{2m} v_a} \tag{7-12}$$

$$\nu_{12} = \nu_a v_a + \nu_{12m} v_m \tag{7-13}$$

$$G_{12} = \frac{G_a G_{12m}}{G_a v_m + G_{12m} v_a} \tag{7-14}$$

$$\int_{T_0}^{T} \alpha_1(\tau)d\tau = \frac{E_a v_a \int_{T_0}^{T} \alpha_{1a}(\tau)d\tau + E_{1m} v_m \int_{T_0}^{T} \alpha_{1m}(\tau)d\tau}{E_a v_a + E_{1m} v_m} \tag{7-15}$$

$$\int_{T_0}^{T} \alpha_2(\tau)d\tau = \int_{T_0}^{T} [\alpha_{2a}(\tau)v_a + \alpha_{2m}(\tau)v_m]d\tau \qquad (7\text{-}16)$$

where v_a and v_m represent the volume faction of the SMA material and host composite material in the mixture. These effective engineering properties can be used in conjunction with Equations (7-1~7-5) to define the thermoelastic characteristics of a SMAHC lamina.

Note that the ECTE model is consistent with classical thermoelasticity, so the model can be readily implemented in any finite element code that has the capability for analyzing laminated composite materials with temperature dependent material properties.

7.4 Finite element modeling in ABAQUS

In the practical use of SMAHC structures, the SMA material can be embedded within or between specific lamina in the form of a ribbon. Alternatively, the SMA actuators can be embedded in the form of round wires, with diameter on the order of the lamina thickness. In both cases, the properties of combined SMAHC material can be formed by the Rule-of-Mixtures approach, defined by the relations presented in Equations (7-11~7-16). Then, the classical lamination theory can be used to develop the corresponding laminate stiffness coefficients, thermal forces, and thermal moments of the resulting SMAHC. An appropriate layered finite element could be used to model the laminated composite with conventional composite layers and individual SMAHC layers of various orientations. The property of the SMAHC layer would vary depending on the volume faction of the SMA materials; therefore, appropriate material properties should be input for the individual SMAHC layers.

ABAQUS, a commercially available FEM code, is capable of modeling laminated composite materials with temperature dependent material properties. In ABAQUS, this capability is available for many element types and solution procedures. A large variety of solution combinations can be achieved by making use of the multiple analysis steps (via the *STEP option) feature of the code within a single analysis input file. The *SHELL SECTION, COMPOSITE option is used to describe the material properties, fiber orientation and stacking sequence of fiber reinforced composites, which ties to the corresponding *MATERIAL card. The *ELASTIC, *EXPANSION, and *DENSITY

commands are then associated with each *MATERIAL option to fully prescribe the temperature dependent material properties. ABAQUS accepts thermal expansion data in terms of secant CTE values only, and does not support input of thermal strain.

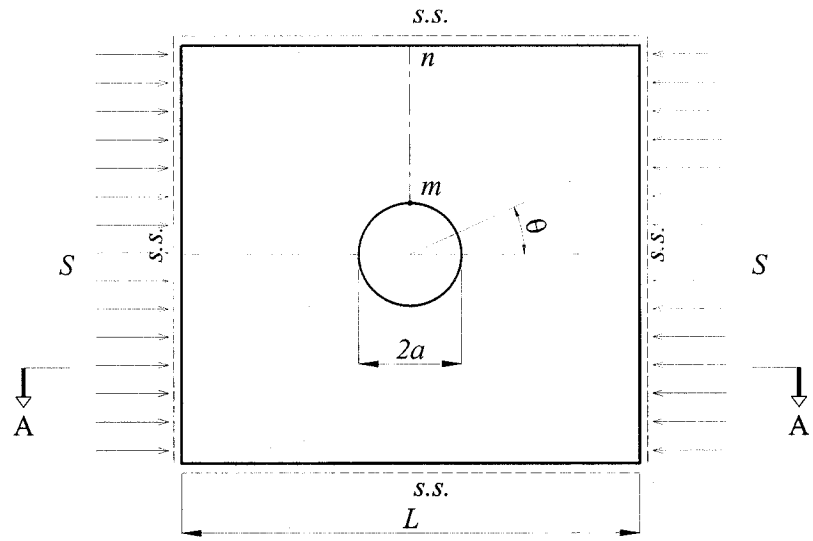

(a) Full SMAHC plate

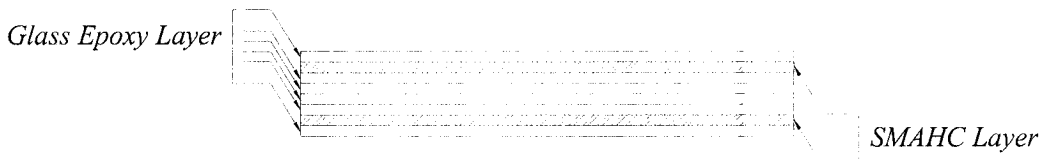

(b) Section A-A

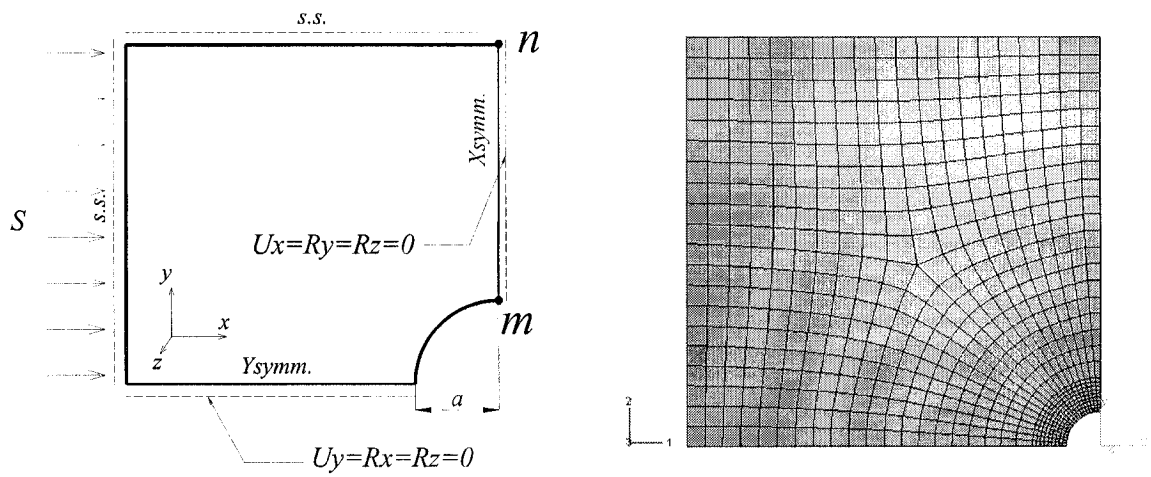

(c) Quarter-symmetric model

Figure 7-2: Architecture of the SMAHC plate with a cutout and its finite element model

The finite element models for the of $120\,\text{mm} \times 120\,\text{mm} \times 1\,\text{mm}$ SMAHC plates, with and without a cutout (diameter 10 mm) at its center, were constructed in ABAQUS. Due to the geometric symmetry, only a quarter symmetry of the plates were modeled in the analysis. Figure 7-2 shows the FE model of the SMAHC plate with a center cutout. The plate is simply supported on all edges (SSSS), and subject to an in-plane uniform distributed compression load along the x-axis. The same plates described earlier with two sides simply supported and two sides free (SSFF) were also analyzed. The lamination sequence of the plate was $[0/90/45/-45]_s$ that is, eight layers in total. Six of the layers were glass-epoxy layers and the other two were uniformly distributed mixture of SMA wires and glass/epoxy (SMAHC layer), as shown in Figure 7-2b. The thickness of both glass-epoxy layer and the SMAHC layer was 0.125 mm and the total thickness of the plate was therefore 1.0 mm. A volume fraction of 55.38% SMA was specified for the SMAHC layers. Equations (7-11~7-16) were used with the specified volume fractions and the properties of glass-epoxy and SMA material to generate effective properties for the SMAHC lamina. The effective engineering properties of the SMA materials fitting the ECTE model were taken from reference [21], as illustrated in Figure 7-3(a). It is observed from Figure 7-3 that the ECTE of SMA wires along the longitudinal direction - 1 (i.e., α_1) is negative over the temperature range of 75~300°F, with the most pronounced negative magnitude at the temperature of 140°F. This phenomenon is contradictory to conventional materials for which CTE is positive with the increase in temperature. It is also noticed that the elastic modulus of the SMA material increases by as much as three times of magnitude over the temperature range shown. Likewise, the properties of the glass-epoxy composite were obtained from [21], as illustrated in Figure 7-3(b). It is also observed that the CTE and the elastic modulus in the principle direction remain approximately constant in the temperature range (75~300°F). However, the CTE in the transverse direction increases with the elevation in temperature and the modulus in the transverse direction decreases over the temperature range. With the properties of SMA material and glass-epoxy composite, the effective engineering properties of the SMAHC layer is obtained using equations (7-11~7-16), as shown in Figure 7-4. Similar to the SMA material, the ECTE of the SMAHC lamina is also predominantly negative along the principle 1-direction, while it is positive along the 2-direction. The elastic modulus of the

SMAHC material also changes with increasing temperature. Therefore, the effective engineering properties of the SMAHC and those of the glass fiber/epoxy, were used in combination to construct the laminate properties of the plate model.

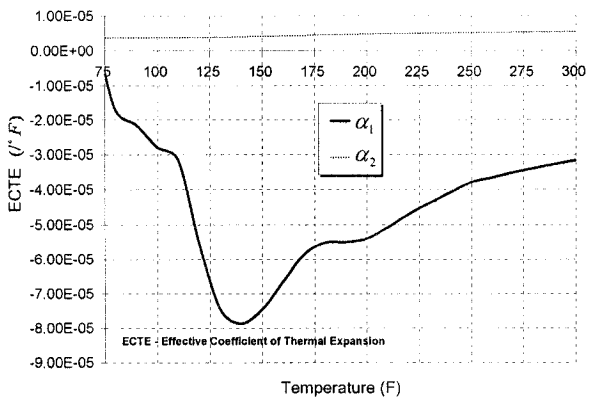

(i) ECTE

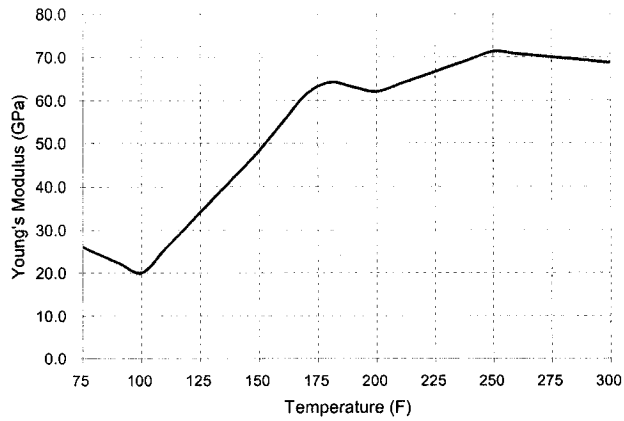

(ii) Young's Modulus

(a) Effective engineering properties of the SMA wires

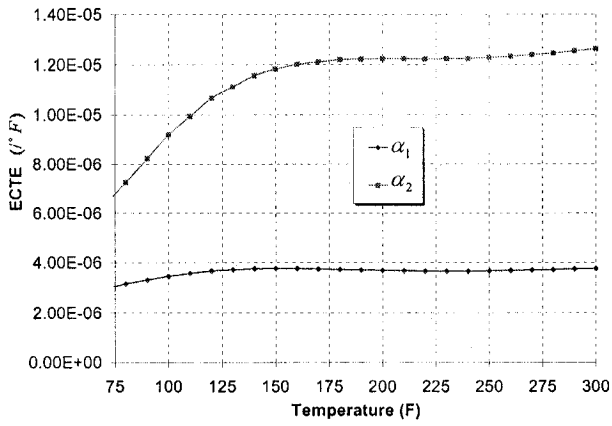

(i) ECTE

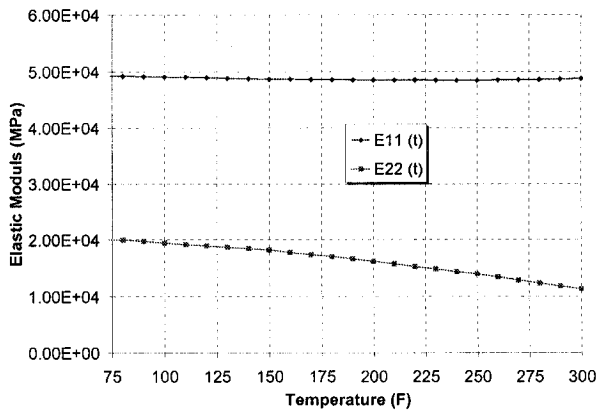

(ii) Elastic Modulus

(b) Effective engineering properties of the glass fiber/epoxy composite

Figure 7-3: Effective engineering properties of (a) the SMA wire and (b) glass fiber/epoxy composite

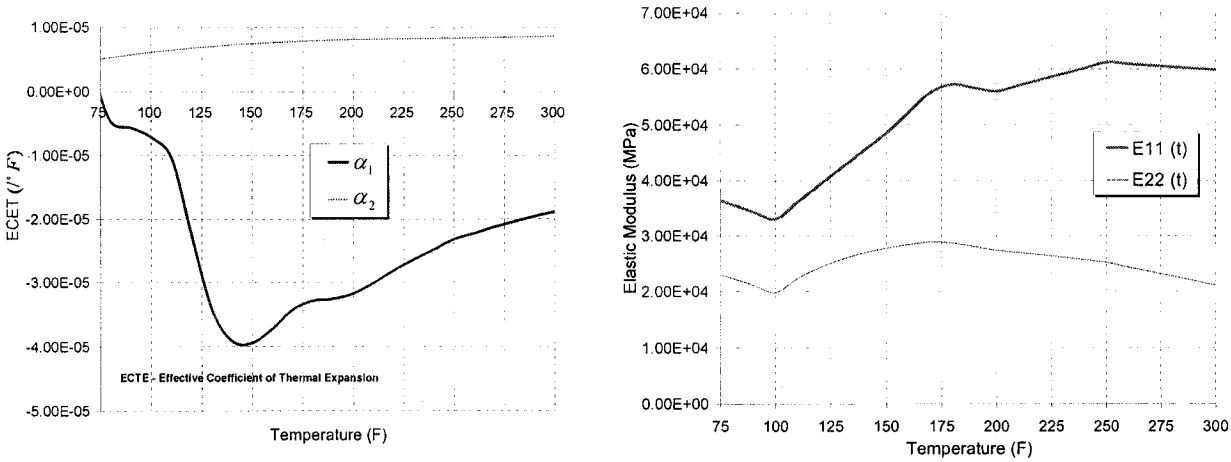

(i) ECTE (ii) Elastic Modulus

Figure 7-4: Effective engineering properties of the SMAHC lamina

Eigenvalue buckling analyses were conducted first for both SMAHC plate with and without a cutout. Table 7-1 summarizes the results from the eigenvalue buckling analyses. It is observed that the highest and lowest first buckling loads were obtained when the SMAHC layer was oriented at -45° and 0° orientation, respectively, for the SSSS SMAHC plate. Whereas for the SSFF SMAHC plate, similar results were observed when the SMAHC layer was oriented at 90° and 45° direction, respectively. In general, it is found that the first buckling load of the SSSS plates is about 3~4 times that of the SSFF plate.

Table 7-1: Eigenvalue buckling analysis results of the SMAHC plates with and without a cutout

		Orientation of SMAHC layer				
Plate Type	**Plate Boundary Condition**	**No SMAHC layer**	**0°**	**90°**	**45°**	**-45°**
		Buckling capacity (N/mm)				
SMAHC plate without a cutout	SSSS	7.220	7.030	7.110	6.940	7.310
	SSFF	2.260	1.820	2.310	2.260	2.250
SMAHC plate with a central cutout	SSSS	6.820	6.630	6.720	6.550	6.900
	SSFF	2.100	1.697	2.148	2.096	2.097

A three-step nonlinear analysis was then conducted to assess the stability of the plates. In the first step, a static analysis was conducted under uniform pressure. The resulting deformation was obtained and then appropriately factored to generate the initial imperfection of the SMAHC plate. The magnitude of maximum imperfection was chosen to be 0.01 times the plate thickness. In the second step, a general nonlinear static analysis was conducted. For the SSSS plate, the uniformly distributed in-plane compression loading was increased from 0 to 17.5N/mm. The maximum load in this step was about 2.5 times of the first eigenvalue buckling load. For the SSFF plate, the in-plane compression load was increased from zero to approximately its first buckling load. In the last step, a nonlinear static analysis was conducted, in which the plate temperature was raised from its ambient temperature of 75°F to 300°F. In another words, during this step, the SMA material was activated with the elevated temperature. By properly orientating the SMA wires, the out-of-plane deflection of the SMAHC plate was controlled and alleviated. This analysis procedure therefore mimicked the real situation, in which the SMAHC plate would be subject to both in-plane compression and thermal loadings. During the analysis, the lateral deflections at the center of the plate for the SMAHC plate without a cutout and at the edge of the cutout (point ***m*** in Figure 7-2c) for the SMAHC plate with a cutout were recorded. The stress concentration factor for the plate with a cutout was evaluated by monitoring the variation of stress concentration along the center line of the plate (between points m-n shown in Figure 7-2c).

In this stage of the study, the influence of variation of SMA wires' orientation with angles of 0^{o}, 90^{o}, 45^{o} and -45^{o} was investigated, and compared with the case of the plate with no SMA inclusion.

7.5 Experimental investigation

7.5.1 Specimens preparation

The following steps were followed for specimen preparation: A glass fiber/epoxy plate was first made of two layers of thin bi-directional glass fiber matt (Dynatron/Bondo Corp., Atlanta, GA, USA), with one layer of matt oriented along the 0^{o} direction, and the

other layer along the 45° direction. The resulting laminate corresponds to a quasi-isotropic laminating sequence of [0/90/45/−45]. The room-cured epoxy resin (West System, Bay City, MI, USA) was used in making the plate in accordance to the vendor's recommended procedure. The thickness of the above glass fiber/epoxy plate was 0.50 mm (hereafter referred to as the "0.5mm plate"). A rectangular frame with two edges perforated with 1.0 mm diameter holes, uniformly spaced at 4 mm distance, was used to orient (wind) the SMA wires supplied by the Dynalloy Inc. (Costa Mesa, CA, USA). Another two sides of the frame were made of threaded rods, so that the distance between the two perforated bars could be adjusted, as shown in Figure 7-5a, to apply a slight pre-tension force to the wires. The diameter of the SMA wire was 0.152 mm and the reverse transform temperature (A_s) of the wire was 194°F. Once the wire was wound throughout the frame, the wire was straightened and tensioned slightly by adjusting the distance between the two perforated bars by the threaded bars, as shown in Figure 7-5a. The length of each wire, i.e., the distance between the two perforated bars was approximately 300mm, so that it allowed for the extra length to be grouped together and connected to a power supply. Two layers of the 0.50mm plates and SMA wires were used to manufacture the SMAHC plate. As shown in Figure 7-5b, the SMA wires were sandwiched between the two layers of the 0.5mm plates. The same resin used in forming the glass/epoxy laminate was also used to bond the two 0.5mm plates and the SMA wires together. With the procedure, two types of SMAHC plate were therefore fabricated, each identified by the orientation of the SMA wires. In the first type, the SMA wires were oriented at a 0° direction (i.e. parallel to the direction of loading). In the second type, the SMA wires were oriented at -45° direction. These two types of plates correspond to the two SMAHC plates considered in the numerical investigations. Once the resin bonding the two 0.5mm plates and the SMA wires was cured, the SMA wires were cut off from the winding frame, and grouped along the edge of the plate and were subsequently connected to a DC power supply. The final SMAHC plate specimen is shown in Figure 7-5c. The total thickness of the SMAHC plate is 1.15mm. The plate of the same thickness, but with no SMA wires was also fabricated for the comparative case study.

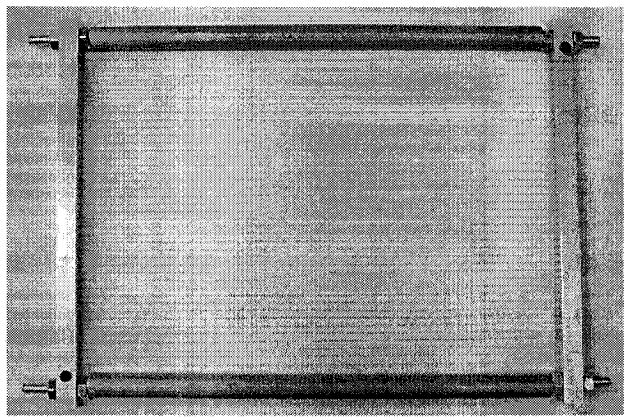

(a) Winding rack for the SMA wires

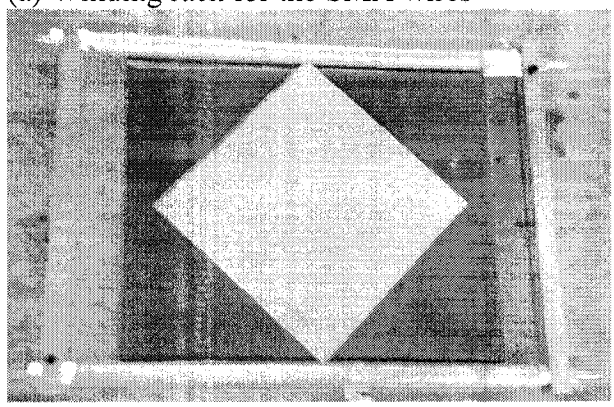

(b) Fabrication of the SMAHC plate

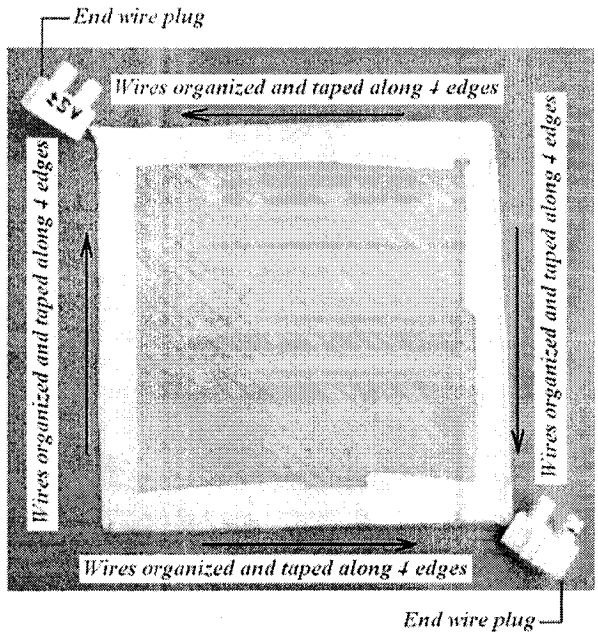

(c) The final SMAHC plate specimen

Figure 7-5: Manufacturing of the SMAHC plate specimen

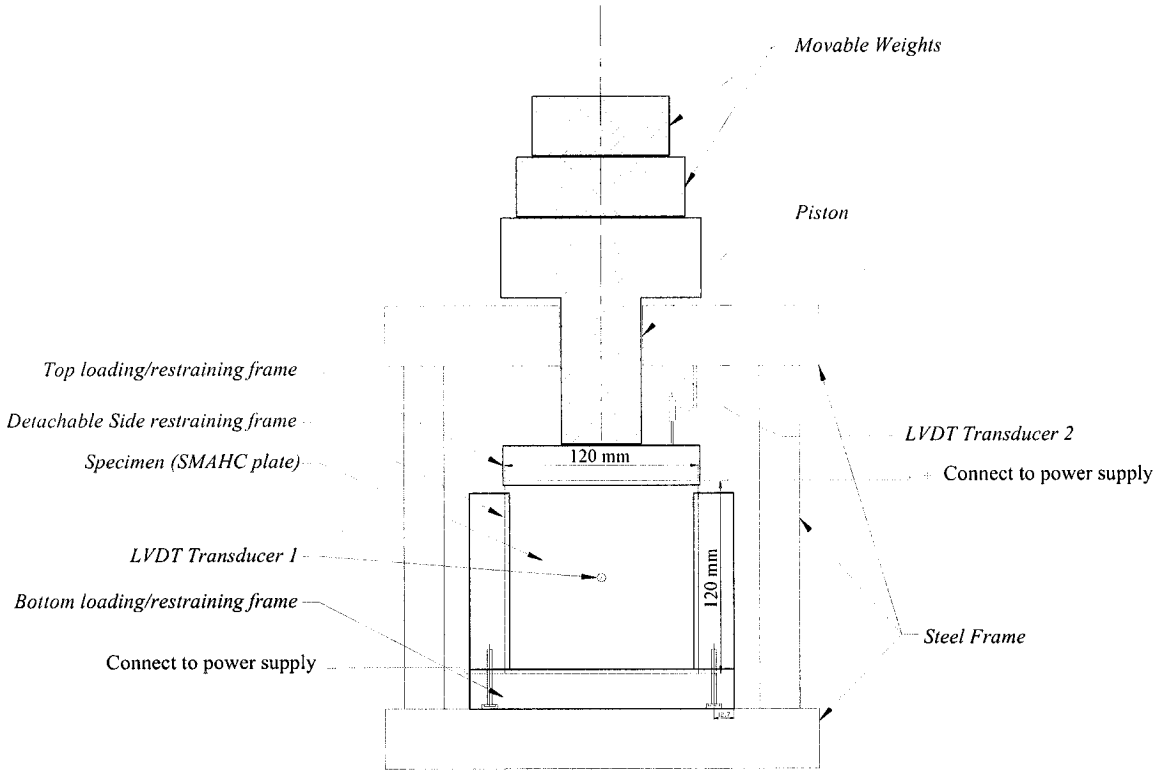

(a) Loading setup

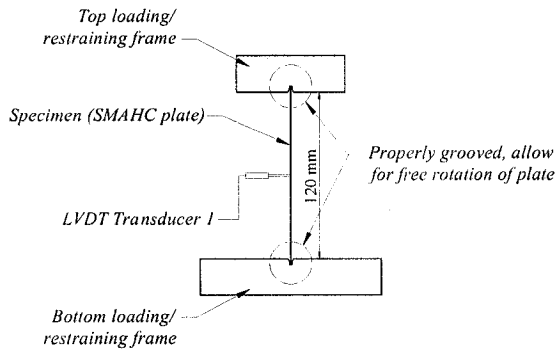

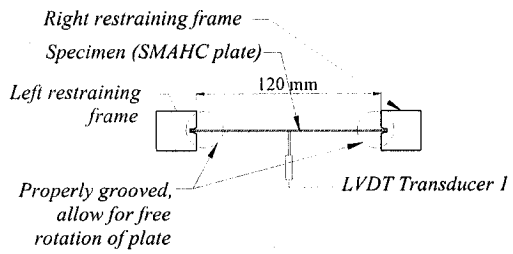

(b) Side view (c) Top view

Figure 7-6: Scheme of the experimental setup

7.5.2 Experimental setup and test procedure

The schematic experimental setup is illustrated in Figure 7-6. The steel loading frame was made of two steel plates and four threaded poles. A piston type loading ram

goes through the top steel plate. The fixture of the plate was made of 4 pieces of PVC blocks (a bottom piece, a top piece and two edge pieces). Each piece was grooved properly so that the edges of the plates were restrained against lateral displacement, but free to rotate (see Figures 7-6b and 7-6c). The two edge pieces were detachable, so that the test setup could accommodate both the SSSS and SSFF boundary conditions. Two LVDT transducers were used to measure the lateral deflection at the middle of the plates, as well as their axial displacement.

To evaluate the buckling capacity of the plate specimen with no SMA wires, the plate in the fixture was preliminarily tested in an Instron hydraulic universal testing machine. The test indicated that the buckling capacity was 7.1 N/mm for the SSSS plate, and 2.0 N/mm for the SSFF plate. This is very close to the results obtained numerically as tabulated in Table 7-1.

After the preliminary test results, the remaining tests were conducted by placing free weights (i.e., 100 kg and 25 kg for the SSSS and SSFF boundary conditions, respectively) on the loading piston shown in Figure 7-6a. The reason for applying weights in this manner was due to the fact that when the SMA wires would be actuated, the plate would tend to be stiffened, thereby pushing against the free weight. The weight was placed on the specimen first, and the readings of LVDT transducers were recorded before and after load application. A DC power supply was used to activate (heat) the SMA wires, as recommended by the supplier of the SMA wires. While keeping the plate loaded, the wires were activated by the power supply. The amount of voltage used to power the parallel SMA wires was 4.5 V. The reading of the axial displacement at the loaded end, and the lateral deflection at the center of the plates were recorded after the power was applied for 5 seconds. Eight SMA reinforced specimens were tested in this manner. The pure (non SMA reinforced) glass fiber/epoxy plates were also tested, and their deflections were similarly recorded. The test results are tabulated in Table 7-2.

Table 7-2: Experimental results (axial displacement and lateral deflection) of the plate specimens with and without a cutout

Test No	Boundary Condition	Orientation of SMA wires	Cutout	Axial displacement at the loaded end (mm)			Lateral deflection at the center of the plate (mm)		
				Initial	After load application	After heating for 5 seconds	Initial	After load application	After heating for 5 seconds
1	SSSS	no SMA	no	0.00	0.20	--	0.00	0.75	--
2	SSSS	no SMA	yes	0.00	0.40	--	0.00	1.50	--
3	SSSS	0^{o}	no	0.00	0.20	1.30	0.00	1.14	2.40
4	SSSS	0^{o}	yes	0.00	0.20	0.80	0.00	1.8	3.00
5	SSSS	-45^{o}	no	0.00	0.12	0.11	0.00	0.60	0.50
6	SSSS	-45^{o}	yes	0.00	0.20	0.19	0.00	1.32	1.00
7	SSFF	no SMA	no	0.00	0.20	--	0.00	1.56	--
8	SSFF	no SMA	yes	0.00	1.00	--	0.00	4.08	--
9	SSFF	0^{o}	no	0.00	0.12	7.10	0.00	1.50	20.05
10	SSFF	0^{o}	yes	0.00	1.10	13.0	0.00	2.43	40.30
11	SSFF	-45^{o}	no	0.00	0.20	5.70	0.00	1.86	15.00
12	SSFF	-45^{o}	yes	0.00	1.40	6.80	0.00	5.25	35.0

Note: SSSS: Four sides simply supported;
SSFF: Two sides simply supported and two sides free

7.6 Results and discussion

The results obtained from the numerical analyses described earlier are presented first. The buckling and postbuckling behaviors of the SMAHC plates with and without a cutout are discussed. The stress concentration around the cutout was also calculated for the SSSS SMAHC plate with a cutout. The correlation between the numerical and experimental results will also be discussed.

7.6.1 The SSSS SMAHC plate

Figure 7-7 illustrates the buckling and postbuckling response of the SSSS SMAHC plates subject to pre-compression loading and the subsequent thermal loading. Figure 7-7a shows the buckling and postbuckling response of the plates prior to activation of the SMA wires. The mid point deflection was normalized with respect to the thickness of the SMAHC plate and the load was normalized with respect to the first linear eigenvalue buckling load of the composite plate without SMAHC layers. It is noticed that the behavior of the SMAHC plate was not significantly sensitive to the orientation of the SMAHC layers in the pre-actuated stage. At the same loading level, the plate without SMAHC layers had the smallest magnitude of lateral deflection, and the SMAHC plate with the 0° oriented SMA wires had the largest deflection. The applied in-plane compression load was increased from zero to about 2.5 times the first eigenvalue buckling capacity of the plate. At the end of this stage, all plates are found to have similar levels of mid-span lateral deflection (approximately 3.4h). Figure 7-7b illustrates the postbuckling response of the SMAHC plate after being activated. It is seen that the variation of the lateral deflections of the SMAHC plates varies as a function of increasing temperature. It is also seen from Figure 7-7b that the mid-span lateral deflection initially increased when the temperature was elevated from 75°F to about 100°F in all cases, but it was then reduced after this stage, and then gradually increased as the temperature was increased. Figure 7-7b also shows that the mid-span deflection of the composite plate without SMA increased continuously with increase in temperature. The only exception was the plate with SMA oriented at 45°, whose deflection did not drop, though remained steady between the temperature range of 100-112°F. It should also be noted that the plate

with SMA oriented at -45° exhibited the highest drop in the lateral deflection in comparison to the other SMAHC plates (i.e., from 3.3 h to 1.6 h).

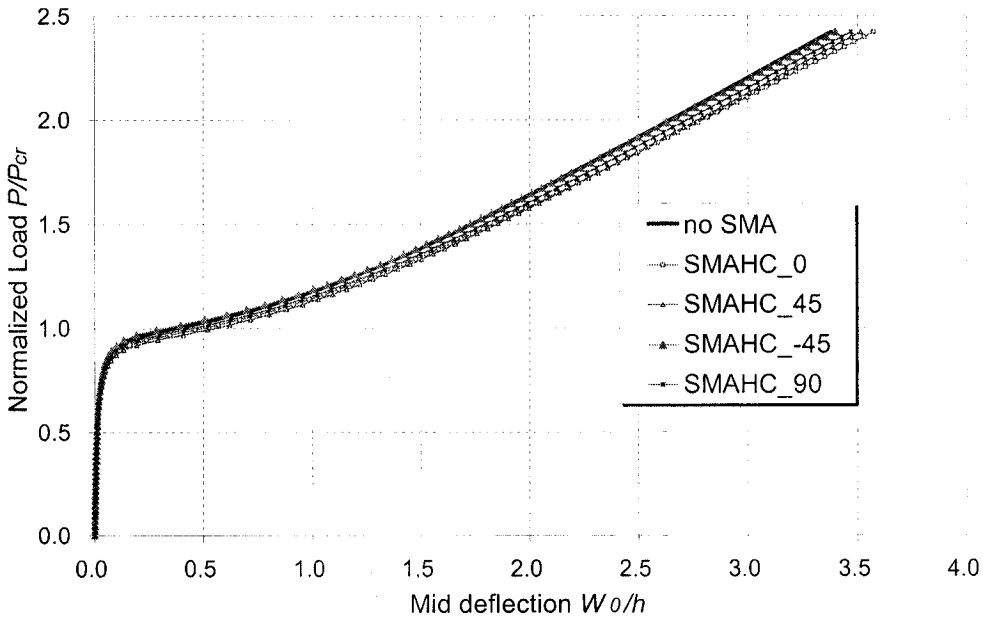

(a) Pre-actuation stage

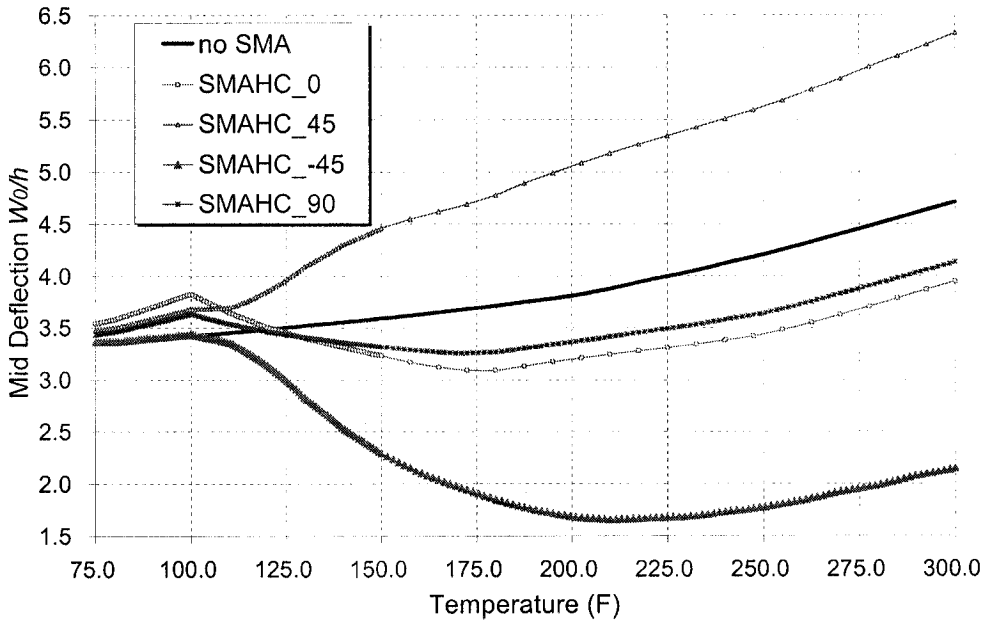

(b) Post-activation stage

Figure 7-7: Buckling and postbuckling of the SSSS SMAHC plate with an initial imperfection of 0.01h, (a) subject to pre-compression (b) after actuation of SMA wires

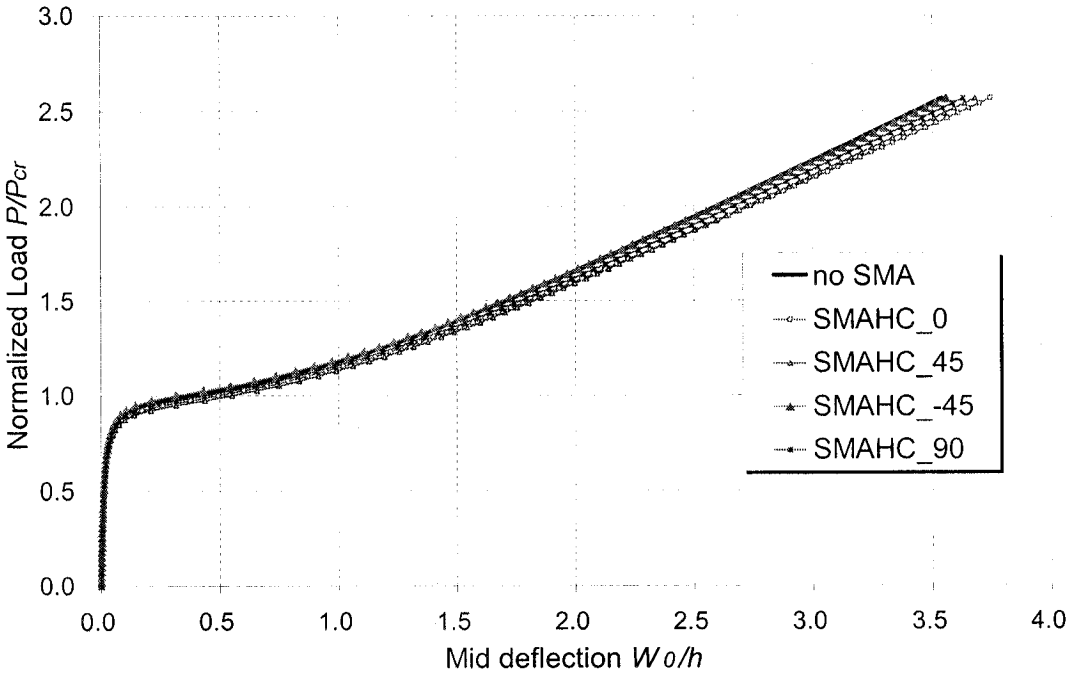

(a) Pre-actuation stage

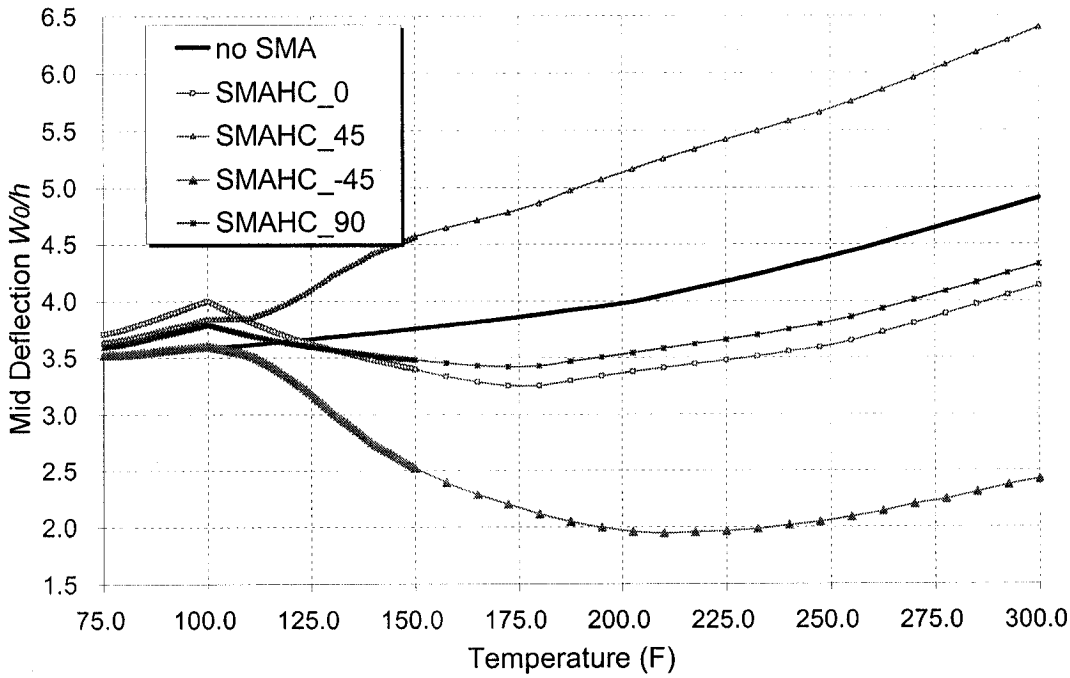

(b) Post-activation stage

Figure 7-8: Buckling and postbuckling of the SSSS SMAHC plate with a central cutout and an initial imperfection of 0.01h, (a) subject to pre-compression (b)) after actuation of SMA wires

Figure 7-8 shows the buckling and postbuckling response of the SSSS SMAHC plate with a central cutout and initial imperfection of 0.01h, subject to pre-compression and the subsequent thermal loading. The mid-span deflection was taken at the edge of the cutout (point ***m*** in Figure 7-2). Similar results were obtained for these plates, compared to the SMAHC plate without a cutout. The presence of the cutout, however, slightly increased the magnitude of the lateral deflections.

7.6.2 The SSFF SMAHC plate

Similar study was also conducted on the SSFF plate. The numerical results of the plate without a cutout are shown in Figure 7-9, and the results for the plate with a central cutout are illustrated in Figure 7-10.

It is seen from both Figures 7-9a and 7-10a that there is no difference in the normalized load-deflection behavior between the different cases in the pre-compression stage. However, mid span deflections varied remarkably at elevated temperature in both plates with and without cutout, as shown in Figure 7-9b and 7-10b. It can be observed from Figure 7-9b and 7-10b that the mid span deflection increased dramatically as temperature increased from 75° F to about 100° F, when the SMA wires were oriented at 0° direction. The deflection magnitude then decreases rather significantly after the temperature was increased beyond 100° F. In both plates (without and with a central cutout), the magnitude of the mid span deflection became much larger when the wires were oriented at 45° and -45°. For the plate without a cutout, the magnitude of the lateral deflections in the plate with SMA wires oriented at 45° and -45° were larger than the plate with no SMA wires, after the temperature of 120° F. The reverse observations were noted in the plate with a central cutout. During the entire loading procedure, it appears that the SMA wires provided no positive contribution when oriented at 90°, as expected. Overall, the presence of the SMA wires in the glass fiber/epoxy plate produced no beneficial effect in suppressing the lateral deflection of the SSFF plate at elevated temperature.

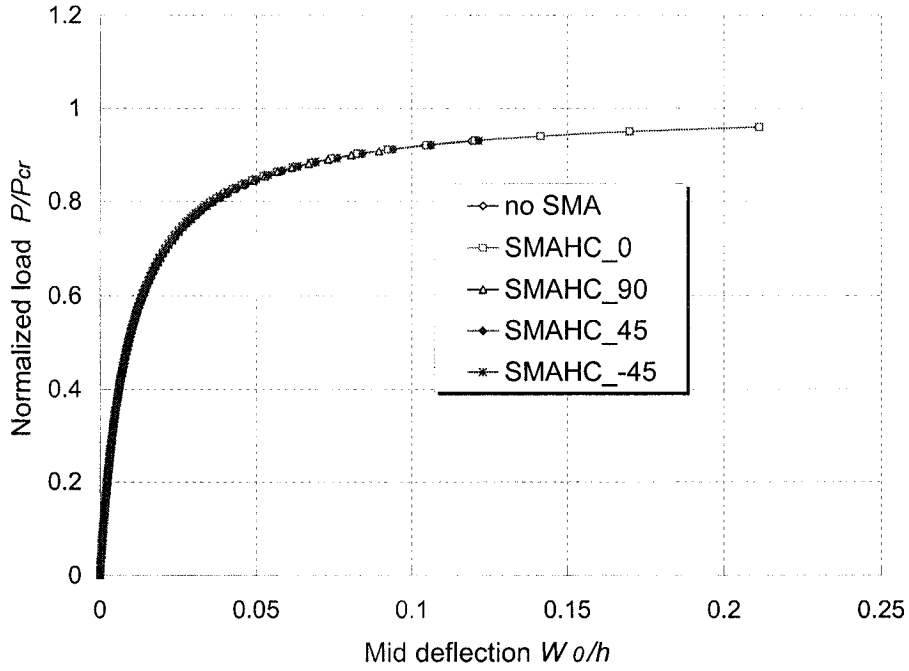

(a) Pre-actuation stage

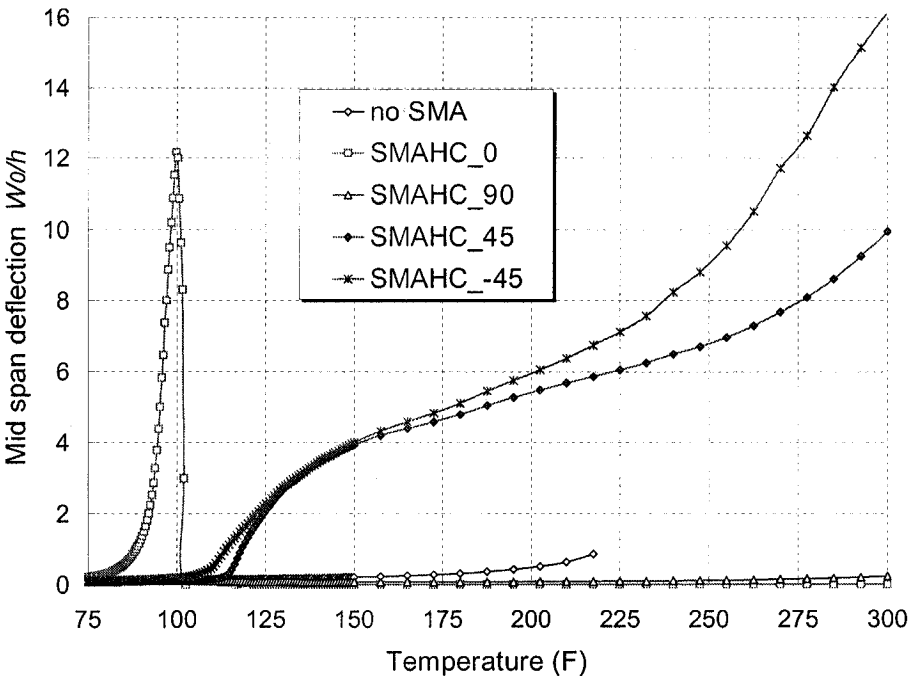

(b) Post-activation stage

Figure 7-9: Buckling and postbuckling of the SSFF SMAHC plate with an initial imperfection of 0.01h, (a) subject to pre-compression (b) at after actuation of SMA wires

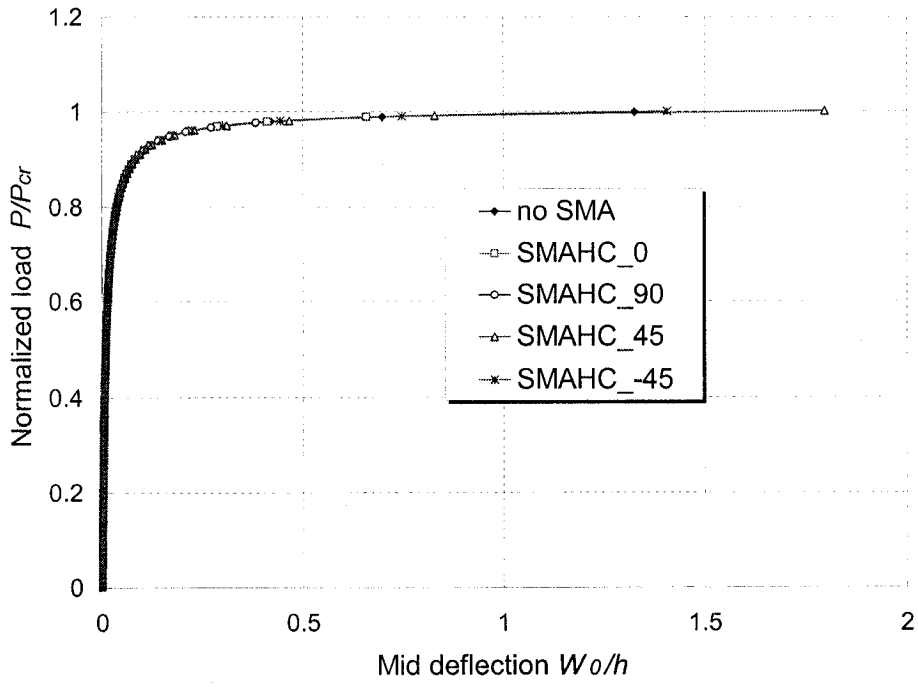

(a) Pre-actuation stage

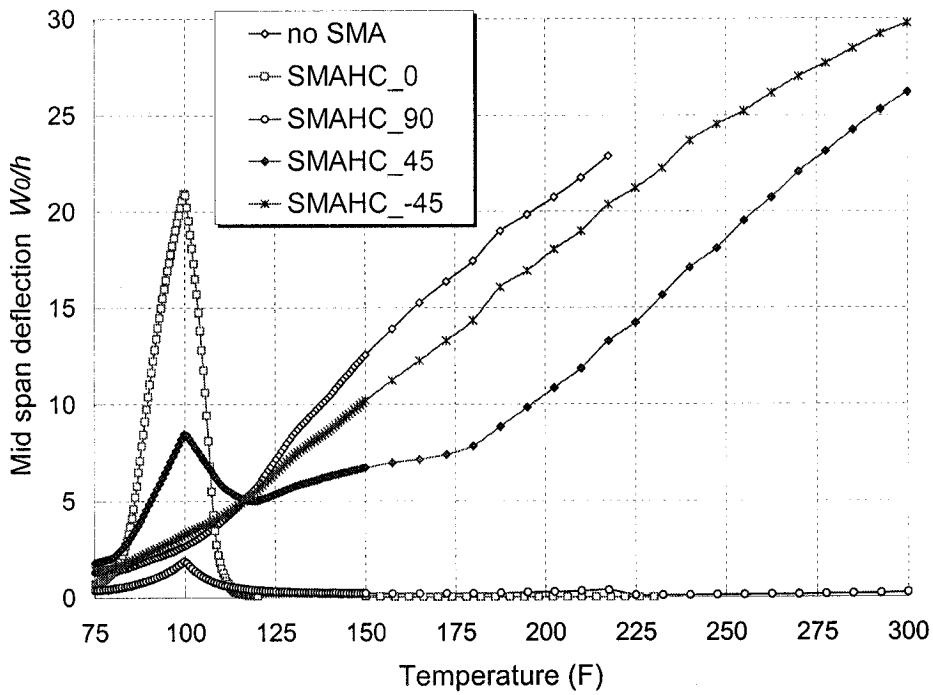

(b) Post-activation stage

Figure 7-10: Buckling and postbuckling of the SSFF SMAHC plate with a central cutout and an initial imperfection of 0.01h, (a) subject to pre-compression (b) at after actuation of SMA wires

7.6.3 Stress concentration factor in the SMAHC plate with a cutout

For an isotropic plate with a cutout, the distribution of the normal stress along line ***m-n*** (in reference to Figure 7-2c) would be in a parabolic manner, as defined by the following relation [25]:

$$\sigma_{x(m-n)} = -\frac{S}{2}(2+\frac{a^2}{y^2}+3\frac{a^4}{y^4}) \text{ for } y \geq a \tag{7-17}$$

where $\sigma_{x(m-n)}$ is the normal stress along line ***m-n***, S is the uniformly applied stress at the edge of the plate, a is the radius of cutout and y is the coordinate along the centerline of the plate and normal to the direction of stress.

In isotropic materials, the stress concentration factor approaches 3 at the boundary of the cutout ($y = a$). For a plate made of anisotropic materials, however, the distribution of stress concentration (K_t^{∞}) along line ***m-n*** can be described by [26]:

$$K_t^{\infty} = 1+\frac{1}{2}\left(\frac{a}{y}\right)^2+\frac{3}{2}\left(\frac{a}{y}\right)^4-\frac{n-2}{2}\left(5\left(\frac{a}{y}\right)^6-7\left(\frac{a}{y}\right)^8\right) \tag{7-18}$$

At the boundary of cutout ($y = a$), $K_t^{\infty} = 1+n$

$$\text{where } n = \sqrt{2\left(\frac{E_{xx}}{E_{yy}}-\nu_{xy}+\frac{E_{xx}}{2G_{xy}}\right)} \tag{7-19}$$

in which E_{xx}, E_{yy} are the major and minor moduli of elasticity, respectively, G_{xy} is the in-plane shear modulus and ν_{xy} is the major Poisson's ratio of the plate.

$$\text{or } n = \sqrt{\frac{2}{A_{22}}\left(\sqrt{A_{11}A_{22}-A_{12}}+\frac{A_{11}A_{22}-A_{12}^2}{2A_{66}}\right)} \tag{7-20}$$

where A_{ij} are the axial stiffness terms (see [26]).

In this study, the stress concentration factor is obtained by taking the ratio of the von Mises stress at point ***m*** versus point ***n*** (see Figure 7-2). It is noted that equation (7-18) applies to the entire composite plate. By substituting the mechanical properties of the glass-epoxy into equation (7-19), one would obtain the stress concentration factor of

2.414, at the edge of the pure glass-epoxy plate with a central cutout. The stress concentration factor at each layer was also found to be very close to the value noted above. In this study, the variation of response of the stress concentration factor in each layer is investigated for the plate hosting the SMA wires in comparison to the plate without SMA. All SMAHC plates investigated in this section were assumed to have an imperfection of 0.001h.

Figures 7-11~7-15 show the stress concentration factor (SCF) of each layer at point ***m*** in the SMAHC plate when the SMA layer oriented at various angles. It is shown in Figures 7-11a~7-15a that the stress concentration factor remains constant during pre-buckling stage, in all cases. The SCFs deviate from one another after the onset of buckling. Immediately after the onset of buckling, the SCFs in the first and second layers increased and then eventually decreased as the applied load was gradually increased to $2.5\,P_{cr}$ (where P_{cr} is the first eigenvalue buckling capacity). Whereas, the SCF in the 8^{th} layer dramatically decreased immediately after the onset of buckling and then kept increasing with decreasing at the final loading stage. At the end of the pre-activated stage, the SCF in all layers decreased from the initial level of about 2.65 to slightly lower than 1. In the pre-activated stage, the highest SCF occurred in the outer layer in all cases, regardless of the orientation of the SMA wires.

It is seen from Figures 7-11b~7-15b that the SCFs fluctuated significantly as the temperature was elevated. In the composite plate with no SMA wires (Figure 7-11b), the SCFs in the two 0^{o} laminae was observed to be much lower than those in the other layers. Interestingly, it is seen from Figure 7-12b that the highest SCF (about 17.5) occurred at the temperature of approximately 150^{o} F. As can be seen from Figures 7-3 and 7-4, this is the temperature at which the actuation effect of the SMA is maximum. As the temperature is increased beyond 150^{o} F, the SCFs in all layers, except for the 0^{o} layers, remains almost constant (at the range of 0.8~1.0 overall). In the thermal loading stage, the highest SCF (about 1.2~2.0) is found in the SMAHC plate, in which the SMA wires are oriented at 45^{o} or -45^{o} direction (Figures 7-14b and 7-15b). Other than these two cases, it is seen that the SCF is below or near 1 during the thermal loading stage; otherwise indicating that there would be no stress concentration at the edge of cutout. It can be therefore concluded that the stresses in the plate are re-distributed during the onset

of buckling and the subsequent postbuckling stage in the SMAHC plates. Therefore, the stress concentration factor is reduced near the edge of the cutout. In particular, in the plates whose SMA wires are oriented at 0^{o} and 90^{o}, the SCF remains constant within each layer, as the temperature is increased from about 150^{o} F to 300^{o} F (see Figures 7-12b and 7-13b).

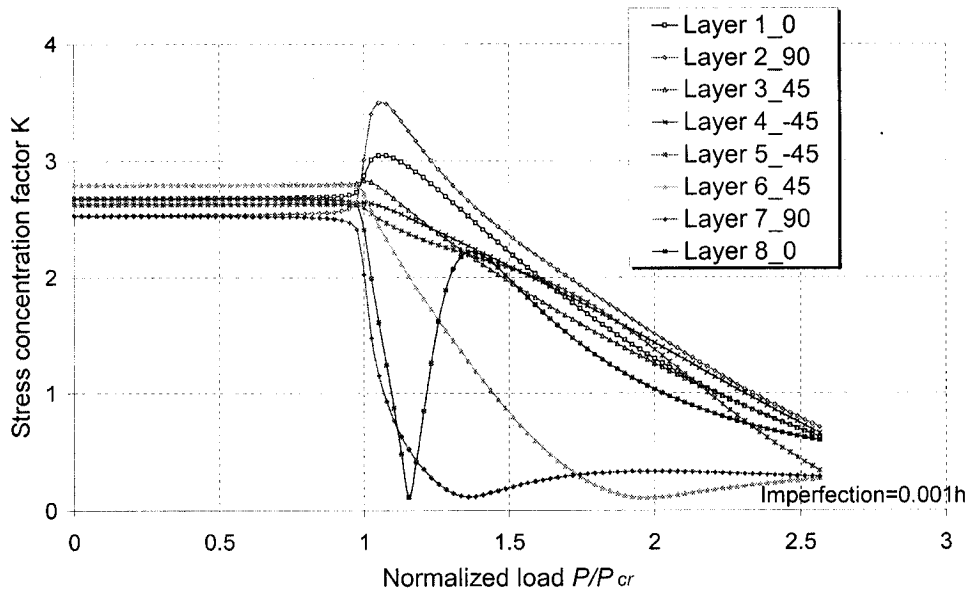

(a) Pre-actuation stage

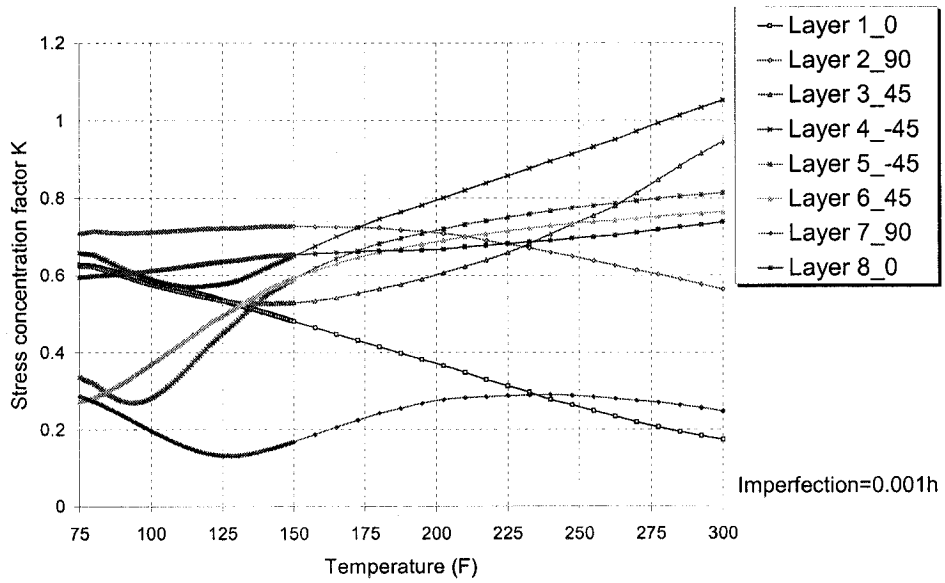

(b) Post-activation stage

Figure 7-11: Stress concentration factor at point *m* of the SSSS FRP plate with a central cutout, (a) subject to pre-compression (b) at elevated temperature (with no SMAHC laminar)

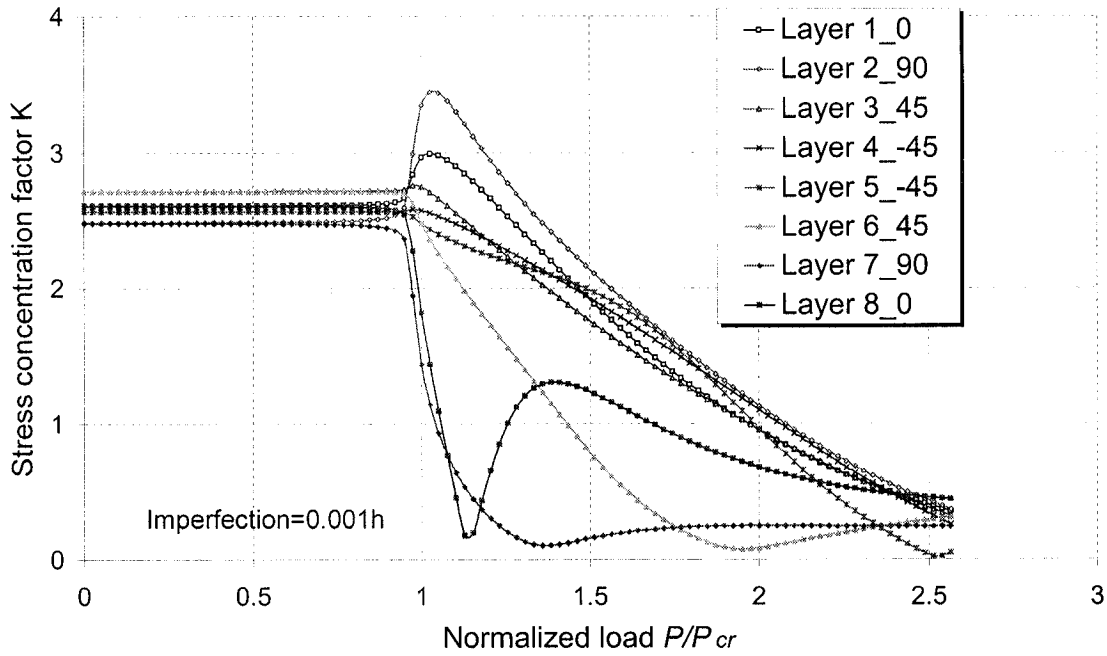

(a) Pre-actuation stage

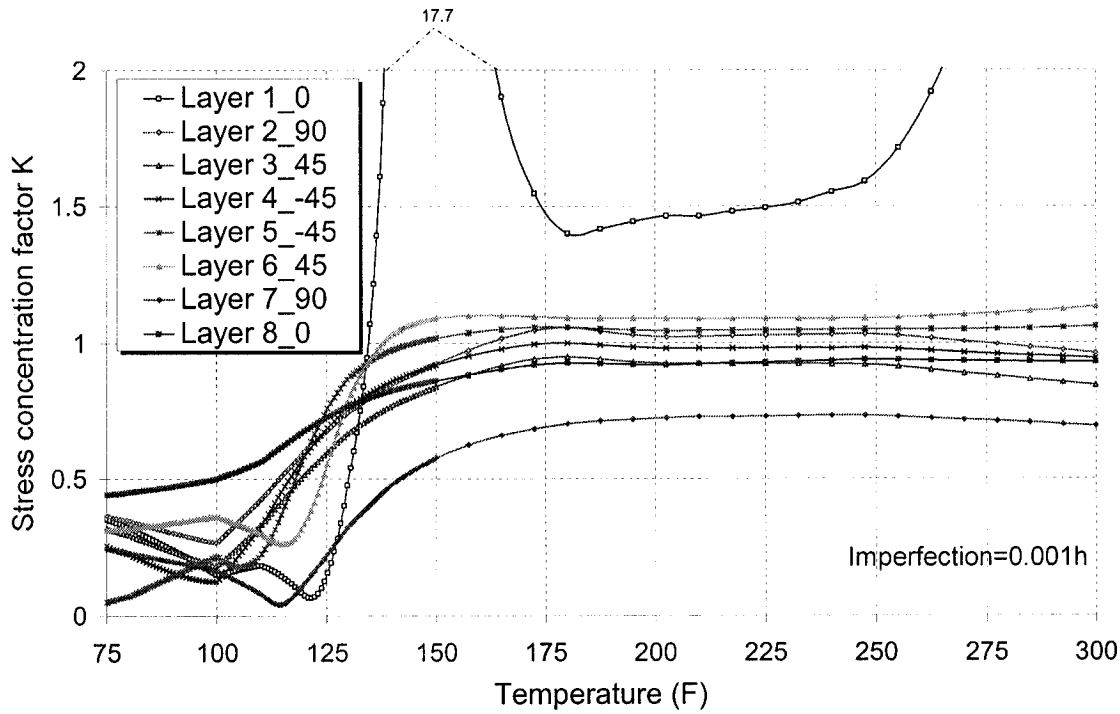

(b) at elevated temperature

Figure 7-12: Stress concentration factor at point *m* of the SSSS SMAHC plate with a central cutout, (a) subject to pre-compression (b) after actuation of SMA wires (with two SMAHC laminae at 0 ° direction)

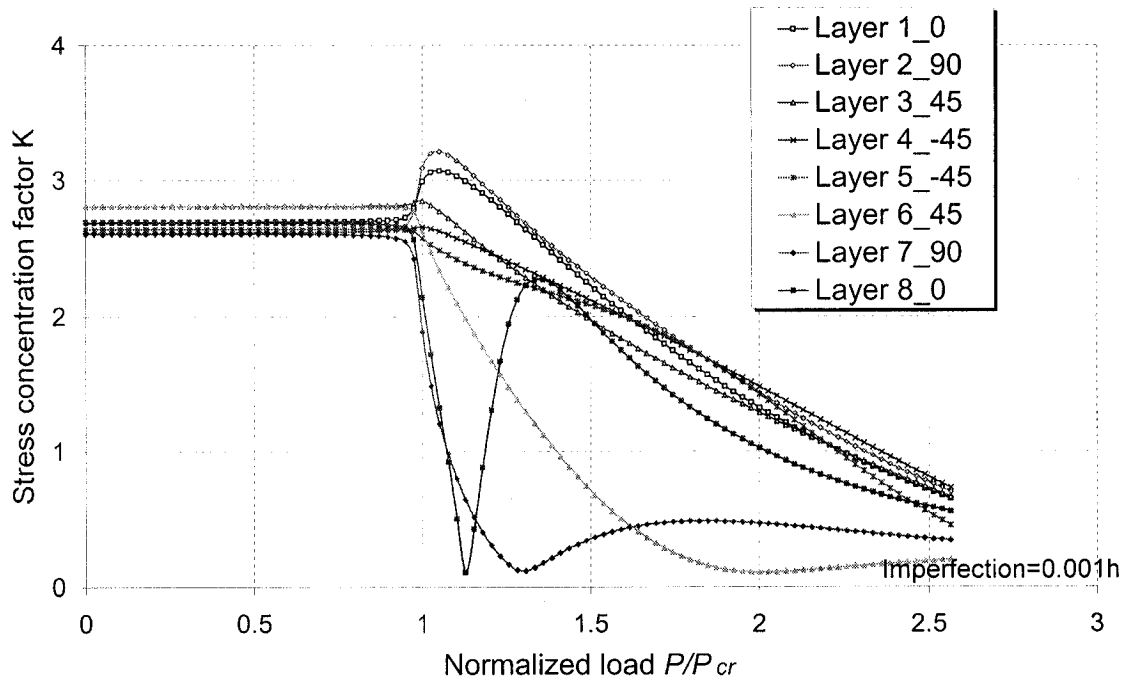

(a) Pre-actuation stage

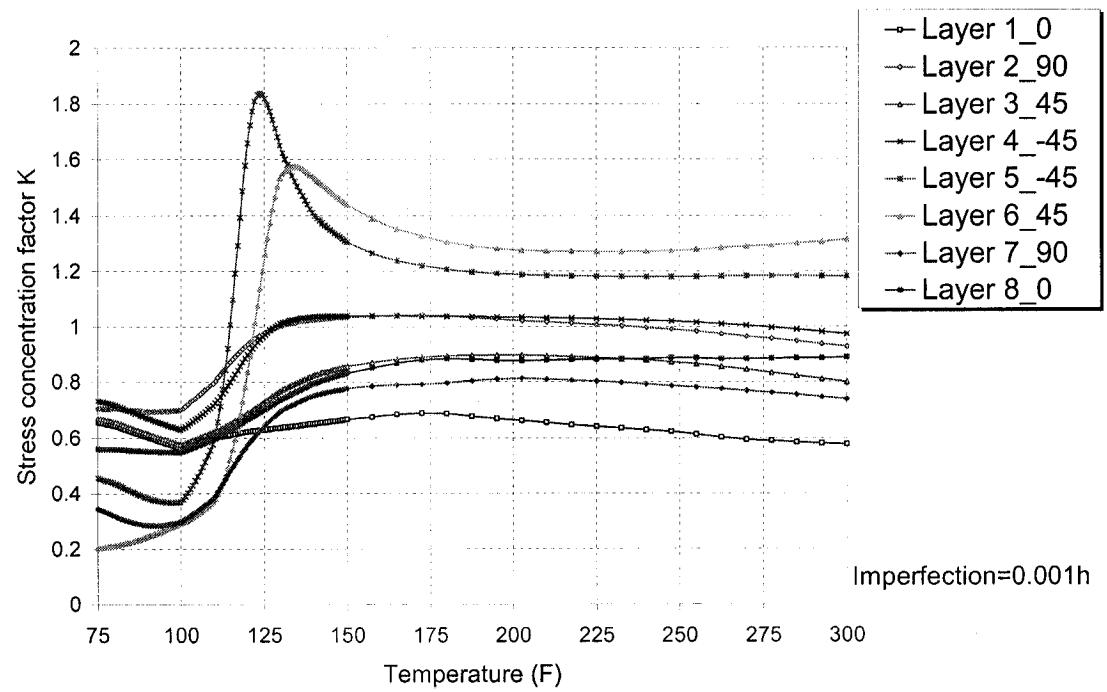

(b) Post-activation stage

Figure 7-13: Stress concentration factor at point *m* of the SSSS SMAHC plate with a central cutout, (a) subject to pre-compression (b) after actuation of SMA wires (with two SMAHC laminae at 90 ^{o} direction)

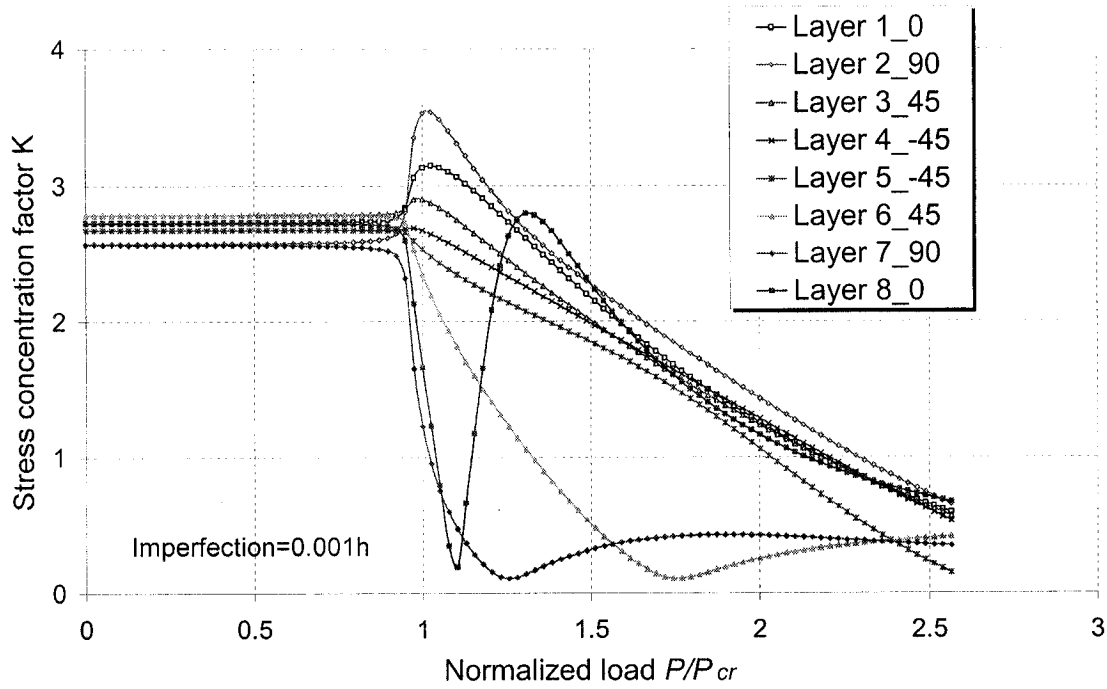

(a) Pre-actuation stage

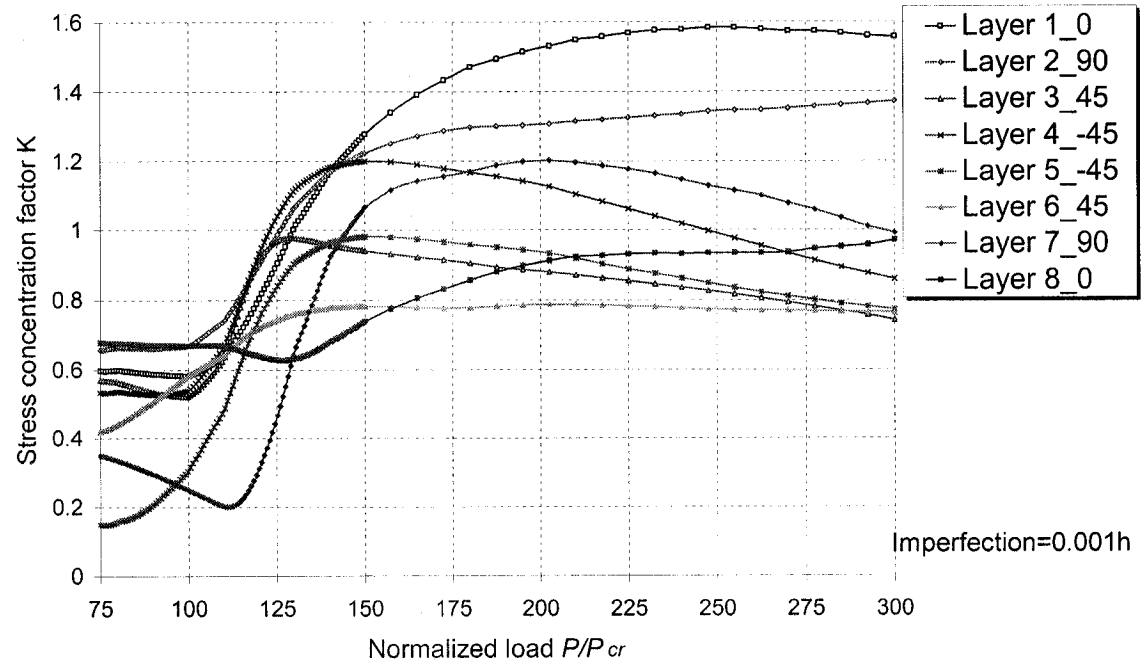

(b) Post-activation stage

Figure 7-14: Stress concentration factor at point *m* of the SSSS SMAHC plate with a central cutout, (a) subject to pre-compression (b) after actuation of SMA wires (with two SMAHC laminae at 45 ° direction)

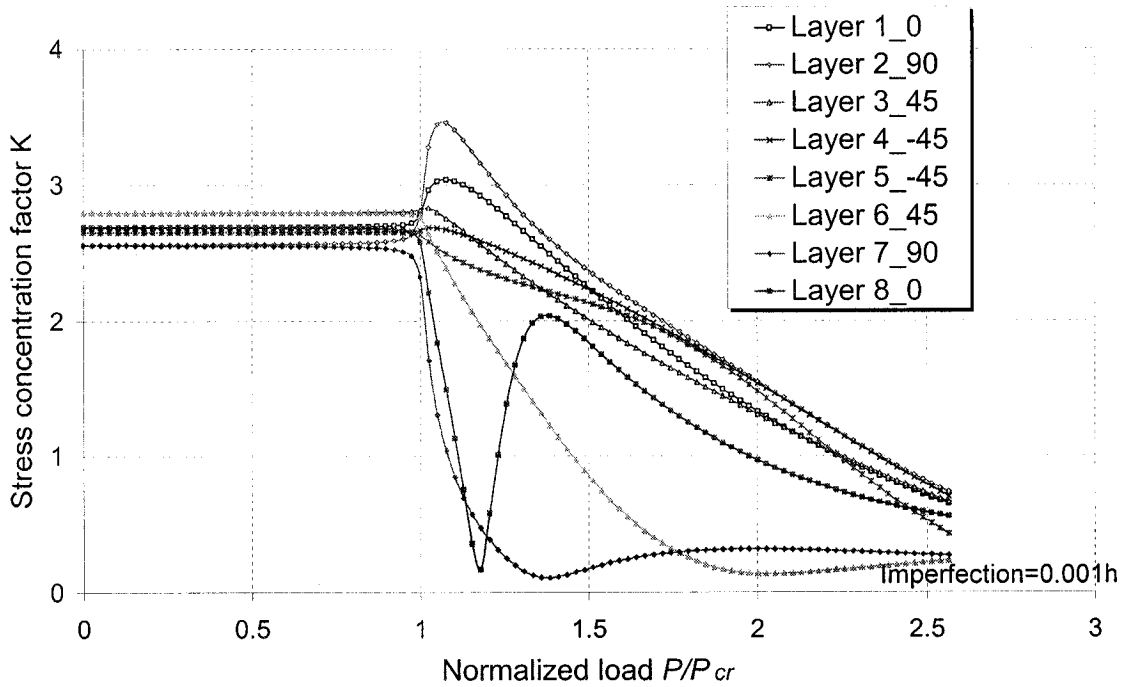

(a) Pre-actuation stage

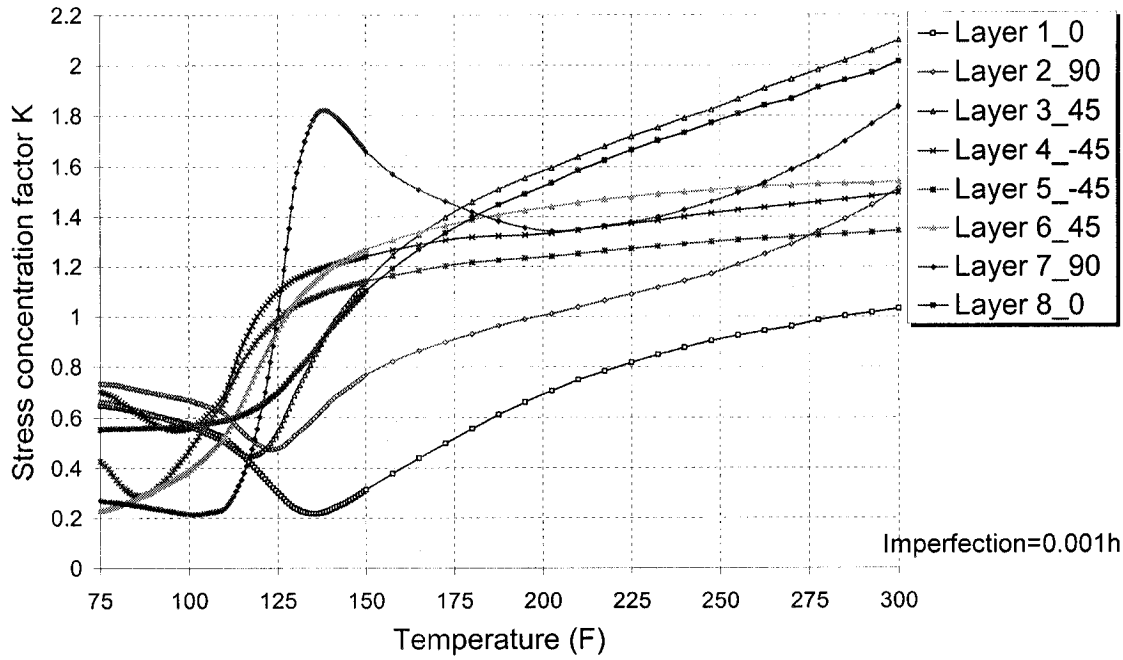

(b) Post-activation stage

Figure 7-15: Stress concentration factor at point *m* in the SSSS SMAHC plate with a central cutout, (a) subject to pre-compression (b) at after actuation of SMA wires (with two SMAHC laminae at -45 ^{o} direction)

7.6.4 Correlation between the numerical and experimental results

It is observed from the numerical study that the properly oriented SMA wires in a fiber reinforced composite plate could have beneficial effect on mitigating the postbuckling instability of the SSSS plates. The experimental program was carried out to verify the findings of the numerical study.

As shown from the numerical results, the optimum positive attribute of the SMA wires in mitigating the instability of the composite plate is achieved when the wires are oriented at -45° direction in the SSSS SMAHC plates. This trend was also confirmed by the experimental observations in that the SMA wires could maintain or reduce the lateral deflection of the SSSS plate when the wires were oriented at -45° direction (see Table 7-2). Other than for these plates, the beneficial effect of the SMA wires could not be observed in the other plates. It was also seen that the lateral deflection of the SSFF SMAHC plates actually increased when the SMA wires were activated during the test, particularly when the SMA wires were oriented at 0° angle. This phenomenon was also confirmed through the numerical simulation.

Overall, it is found that the numerical and experimental results agree with each other qualitatively, but not quantitatively. The reasons can be explained as follows:

Firstly, the engineering properties of the SMA wires used in the experimental investigation would not be exactly the same as those assumed in the numerical study, particularly the temperature related thermal expansion coefficient.

Secondly, there were two SMAHC laminae in the laminated plates in the numerical simulation, with an assumed volume faction 55.38% for the SMA wires in the two SMAHC laminae studied. However, due to fabrication related complexities, the volume faction of SMA material in the real specimens was only about 10%. The low volume ratio of SMA material resulted in its rather less significant beneficial effect in the SSSS plate specimens. Therefore, the beneficial effect of the SMA wires could only be seen in the plates with the wires oriented at -45° angle. In fact, the simulation with SMA wires of 10% volume ratio in the two SMAHC laminae also showed that the potential beneficial attribute would not be significant when the volume ratio is low.

Finally, it was noted that the length of each SMA wire was not exactly the same when they were bundled and connected to the DC power supply in parallel, particularly for those wires in the -45° direction. This would mean that the current would not have been equally distributed among the wires, thus producing variable actuation effect.

7.7 Conclusions

Utilizing of the ECTE model of the shape memory alloy material [18], the buckling and postbuckling behavior of the SMAHC plate with and without a cutout subject to in-plane pre-compression and the subsequent actuation of the SMA wires was investigated numerically and experimentally. It is found from this study that by orienting the SMA wires along proper direction in the laminate, the actuation property of SMA materials could be effectively harvested to suppress the instability (out-of-plane deflection) of FRP plates. For the four-side simply supported (SSSS) SMAHC plates, with the exception of the plate hosting SMA wires oriented at 45° direction, the SMA material was able to mitigate the instability of the SMAHC plates. The beneficial effect of SMA wires at -45° direction was found to be the most significant. It was also observed that such beneficial effect was not noteworthy in the SSFF SMAHC plates. In fact, the presence of SMA wires oriented at 0°, 45° and -45° angles in those plates increased the lateral deflection when the wires were activated.

The variation of stress concentration near the cutout in the four sides simply supported SMAHC plate during the pre-buckling, buckling and postbuckling stages was also investigated. It is found that the stress concentration factor (SCF) remained constant, at about 2.65, during the pre-buckling stage. It was then changed immediately at the onset of buckling and continued changing during the postbuckling stage. The variation of SCF as a function of orientation angle of the SMA wires were investigated and reported.

An experimental investigation evaluating the attribute of SMA wires was also conducted in this study. Although the numerical and experimental results were not in good agreement quantitatively due to several reasons described earlier, the observations obtained from numerical study could be qualitatively verified by the experimental

investigation. Good agreements were therefore observed when considering the orientation of the SMA wires and the boundary conditions of the SMAHC plates.

7.8 Acknowledgements

The financial support of the Natural Sciences and Engineering Council of Canada (NSERC) in the form of Discovery Grants to the second and third authors in support of this work is gratefully acknowledged.

7.9 References

[1] Buehler W.J. and Wiley R.C. (1962), TiNi-Ductile Intermetallic Compound, *Transactions of the American Society of Metals,* 55, 269-276.

[2] Wayman C.M. and Shimizu K. (1972), The Shape Memory ("Marmem") Effect in alloys, *Metal Science Journal,* 6: 175-183.

[3] Wayman C.M. (1980), Some Applications of Shape-Memory Alloys, *Journal of Metals,* June 1980: 129-137.

[4] Otsuka K. and Shimizu K. (1986), Pseudoelasticity and Shape Memory Effects in Alloys, *International Metals Reviews,* 31 (3): 93-114.

[5] Han H.P., Ang K.K., Wang Q. and Taheri F. (2006), Buckling enhancement of epoxy columns using embedded shape memory alloy spring actuators. *Composite Structures* 72: 200–211.

[6] Xu Z.J. (2002), Shape control of beam structures using shape memory alloy wire actuators, *M.Eng. Thesis*, National University of Singapore.

[7] Baz A. and Tampe L. (1989), Active control of buckling of flexible beams. In *proceeding of ASME Design Technical Conference*, Montreal, Canada, 211-218.

[8] Thompson S.P. and Loughlan J. (1995), The active buckling control of some composite column strips using piezoceramic actuators, *Composite Structures* 32(1-4): 59-67.

[9] Choi S., Lee J.J., Seo D.C. and Choi S.W. (1999), The active buckling control of laminated composite beams with embedded shape memory alloy wires, *Composite Structures* 47: 679-686.

[10] Loughlan J., Thompson S.P. and Smith H. (2002), Buckling control using embedded shape memory actuators and the utilization of smart technology in future aerospace platforms, *Composite Structures* 58:319–347.

[11] Tsai X.Y. and Chen L.W. (2002), Dynamic stability of a shape memory alloy wire reinforced composite beam, *Composite Structures* 56: 235–241.

[12] Birman V. (1997), Stability of functionally graded shape memory alloy sandwich panels, *Smart Materials and Structures* 6: 278–286.

[13] Rogers C.A. and Robertshaw H.H. (1988), "Shape Memory Alloy Reinforced Composites," *Engineering Science Preprints* 25, Society of Engineering Science, Inc., ESP25.8027.

[14] Tylikowski A. (1998), Dynamic stability of rotating composite shells with thermoactive shape memory alloy fibers, *Journal of Thermal Stresses* 21: 327-339.

[15] Jia H.Y. (1998), Impact Damage Resistance of Shape Memory Alloy Hybrid Composite Structures, *PhD thesis*, Virginia Polytechnic Institute and State University.

[16] Tawfik M., Ro J.J. and Mei C. (2002), Thermal post-buckling and aeroelastic behavior of shape memory alloy reinforced plates, *Smart Materials and Structures* 11: 297–307.

[17] Roh J.H., Oh I.K., Yang S.M., Han J.H. and Lee I. (2004), Thermal post-buckling analysis of shape memory alloy hybrid composite shell panels, *Smart Materials and Structures* 13: 1337–1344.

[18] Turner T.L. (2000), "A New Thermoelastic Model for Analysis of Shape Memory Alloy Hybrid Composites", *Journal of Intelligent Material Systems and Structures* 11: 382-394.

[19] Turner T.L. (2000), SMA hybrid composites for dynamic response abatement applications, Proceedings of the *7th International Conference on Recent Advances in Structural Dynamics*, 1, 453-465, the Institute of Sound and Vibration Research, University of Southampton, England.

[20] Turner T.L., Lach C.L. and Cano R.J. (2001), Fabrication and characterization of SMA hybrid composites, SPIE 8th Annual International Symposium on Smart Structures and Materials; Active Materials: Behavior and Mechanics, *SPIE Vol. 4333,* Paper No. 4333-60, Newport Beach, CA.

[21] Turner T.L. and Patel H.D. (2004), Analysis of SMA hybrid composite structures using commercial codes, *Smart Structures and Materials: Modeling, Signal Processing, and Control, Proceedings of SPIE* Vol. 5383, Paper No. 12, San Diego, CA.

[22] Birman V. (1999), Analysis of an infinite shape memory alloy plate with a circular hole subjected to biaxial tension, *International Journal of Solids and Structures* 36: 167-178.

[23] Shimamoto A., Ohkawara H. and Nogata F. (2004), Enhancement of mechanical strength by shape memory effect in TiNi fiber-reinforced composites, *Engineering Fracture Mechanics* 71: 737-746.

[24] Shimamoto A., Azakami T. and Oguchi T. (2003), Reduction of KI and KII by the Shape-memory Effect in a TiNi Shape-memory Fiber-reinforced Epoxy Matrix Composite, *Experimental Mechanics* 43 (1): 77-82.

[25] Timoshenko S., *Theory of elasticity*, McGraw-Hill Book Company Inc. 1934

[26] Lekhnistskii's G., Tsai W.S. and Cheron T., *Anisotropic plates*, Gordon and Breach Science Publishers, New York, 1968.

7.10 Appendix A: Influence of geometric imperfection of the SMAHC plate

As discussed in Sections 7.6.1 and 7.6.2, the SMAHC plates with and without a cutout have an initial imperfection of 0.01h. In order to verify the influence of geometric imperfection on the behavior of SMAHC plate, plates with two other magnitudes of imperfection, 0.1h and 0.001h were also analyzed.

Figures 7-16 and 7-17 show the buckling and postbuckling response of the SSSS SMAHC plate with the initial imperfection of 0.1h and 0.001h, respectively. Similar conclusions can be drawn as the plate with the imperfection of 0.01h discussed in Section 7.6.1. By comparing Figures 7-16(a) and 7-17(a), it is found that the feature of bifurcation becomes more and more obvious, as the initial imperfection of the plate become smaller. However, at the end of pre-compression stage, the SMAHC plates with all types of imperfections have similar level of lateral deflection (about 3.4h). Locating the SMAHC layer along -45° direction is found to be the most effective way in suppressing the lateral deflection in an elevated temperature environment. It is found that the magnitude of imperfection in the SMAHC plate has significant effect on the pre-buckling and buckling behaviors of the plate, but it has less influence on the postbuckling and thermal buckling behaviors of the SMAHC plate.

Similar results for the SSSS SMAHC plate with a cutout are shown in Figures 7-18 and 7-19. Likewise, the behaviors of the SSFF SMAHC plate with and without a cutout are illustrated in Figures 7-20 to 7-23. The same conclusion can be drawn from these results as those discussed in Section 7.6.2, with the only difference lying in Figure 7-23 (b). It is observed that for the SSFF plate with a cutout and very small imperfection (0.001h), the postbuckling deflection at elevated temperature is smaller in the plate with SMA than that in the plate without SMA, which is a beneficial effect.

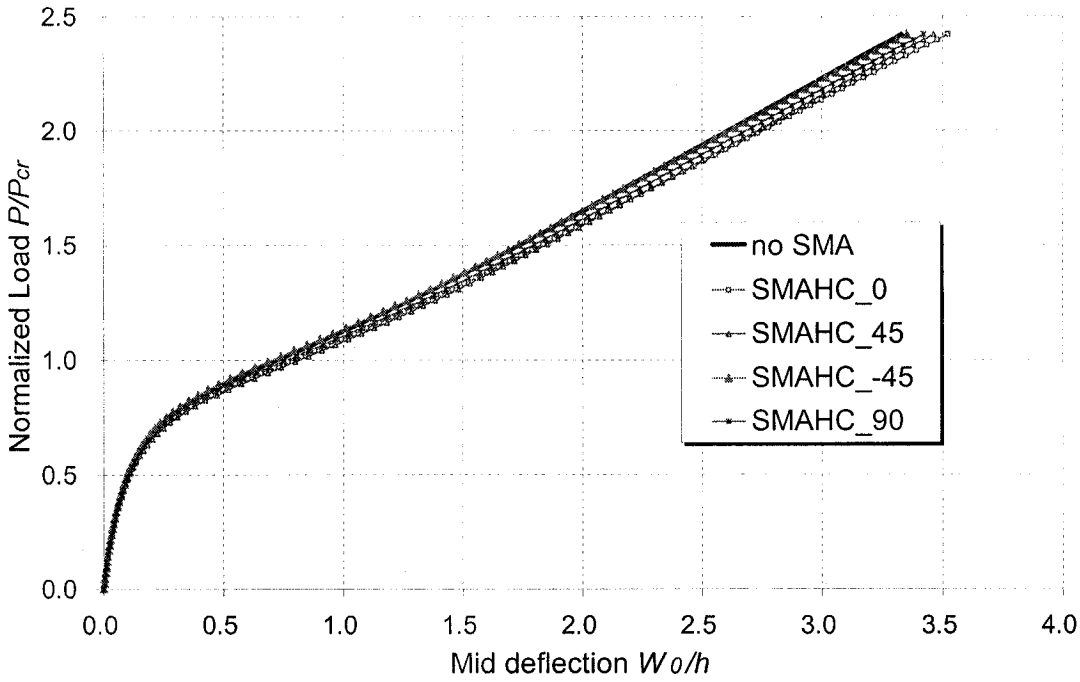

(a) Pre-actuation stage

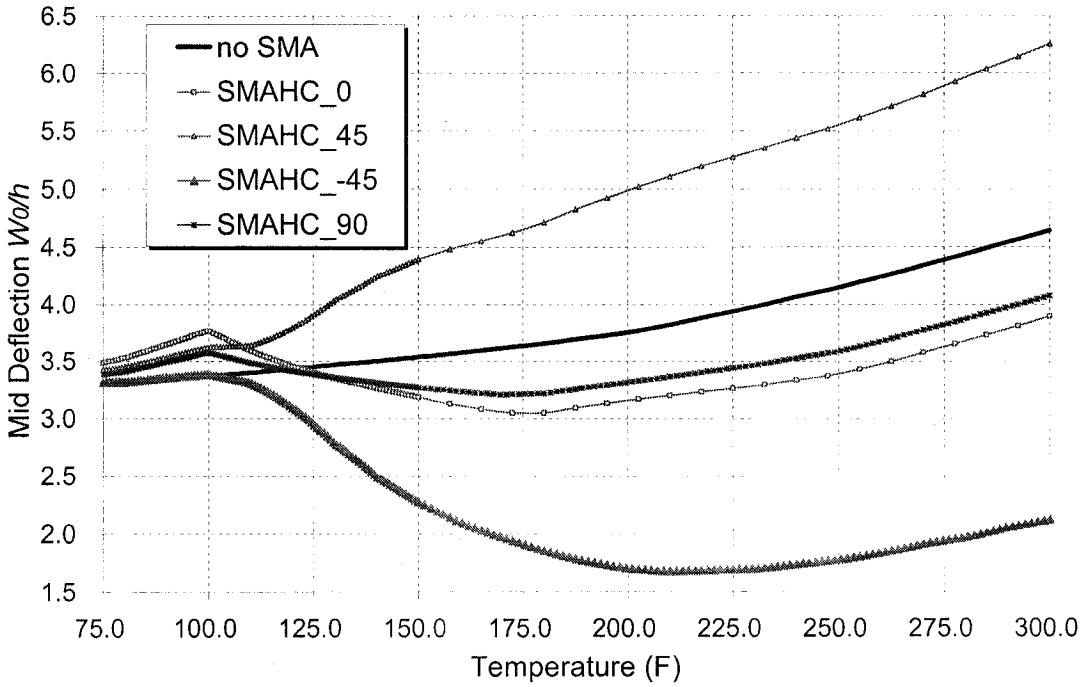

(b) Post-activation stage

Figure 7-16: Buckling and postbuckling of the SSSS SMAHC plate with an initial imperfection of 0.1h, subject to pre-compression and subsequent elevated temperature load

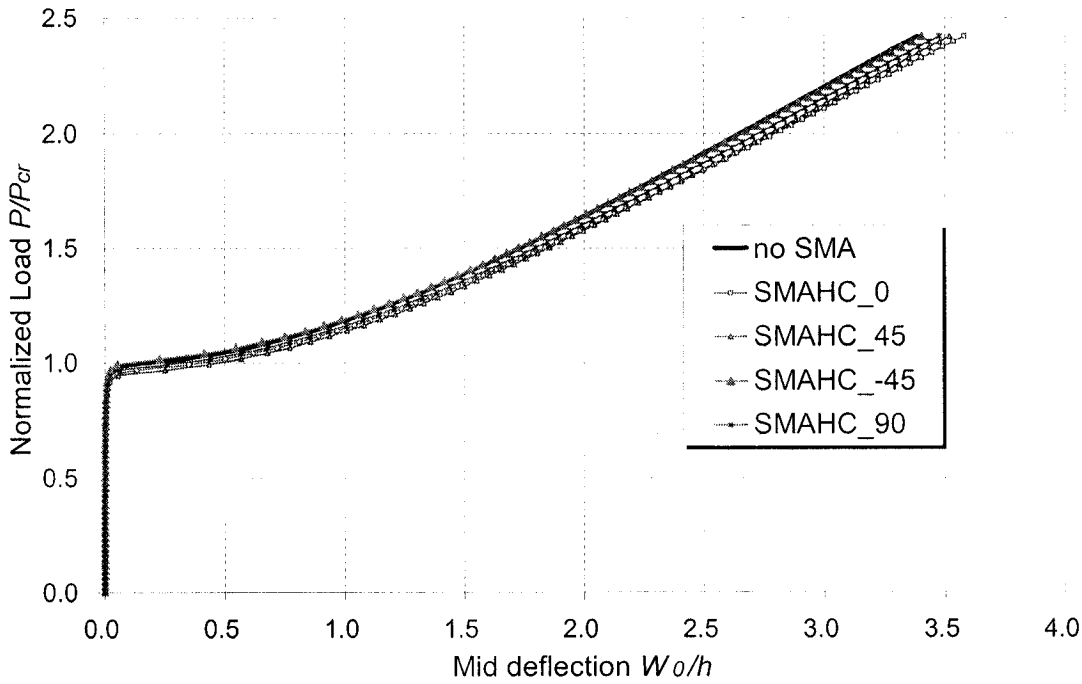

(a) Pre-actuation stage

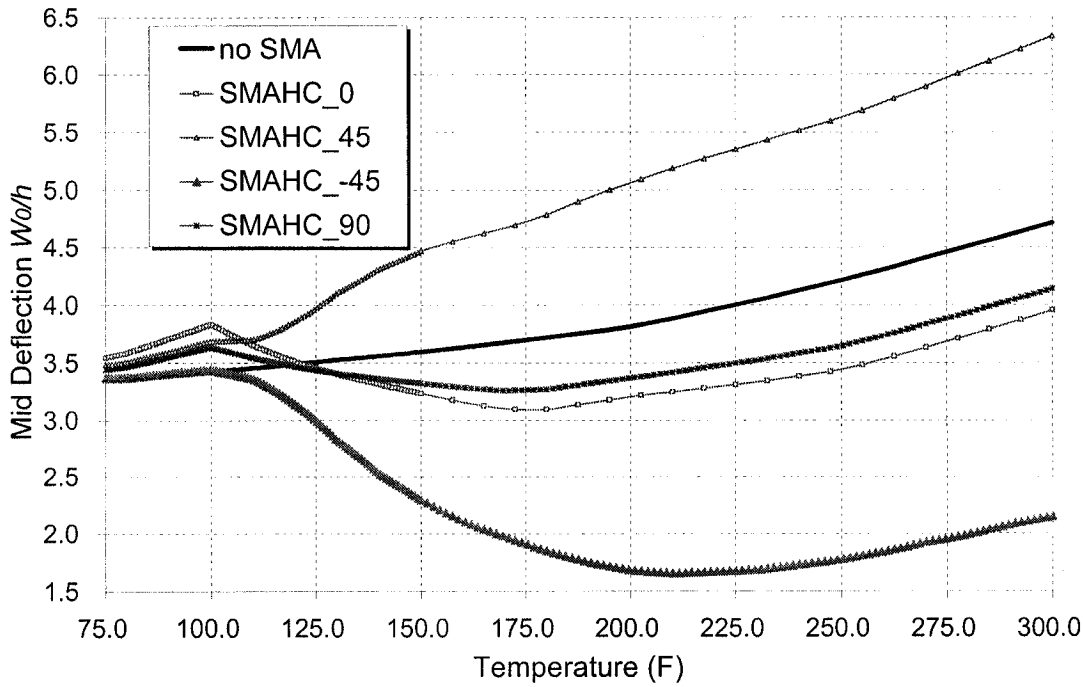

(b) Post-activation stage

Figure 7-17: Buckling and postbuckling of the SSSS SMAHC plate with an initial imperfection of 0.001h, subject to pre-compression and subsequent elevated temperature load

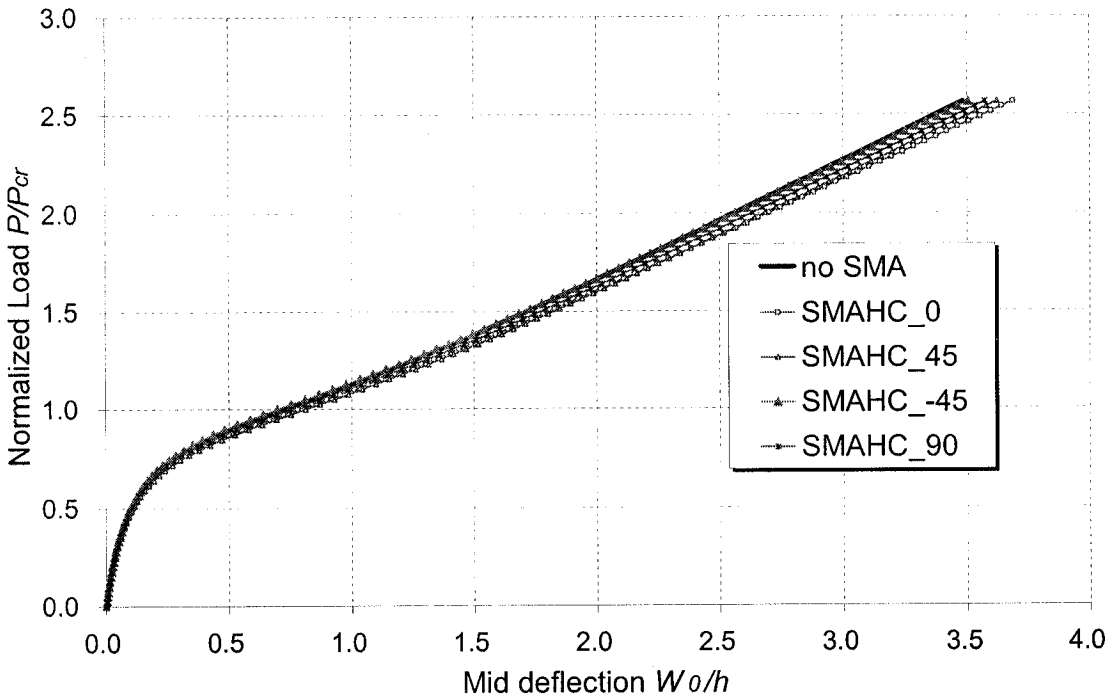

(a) Pre-actuation stage

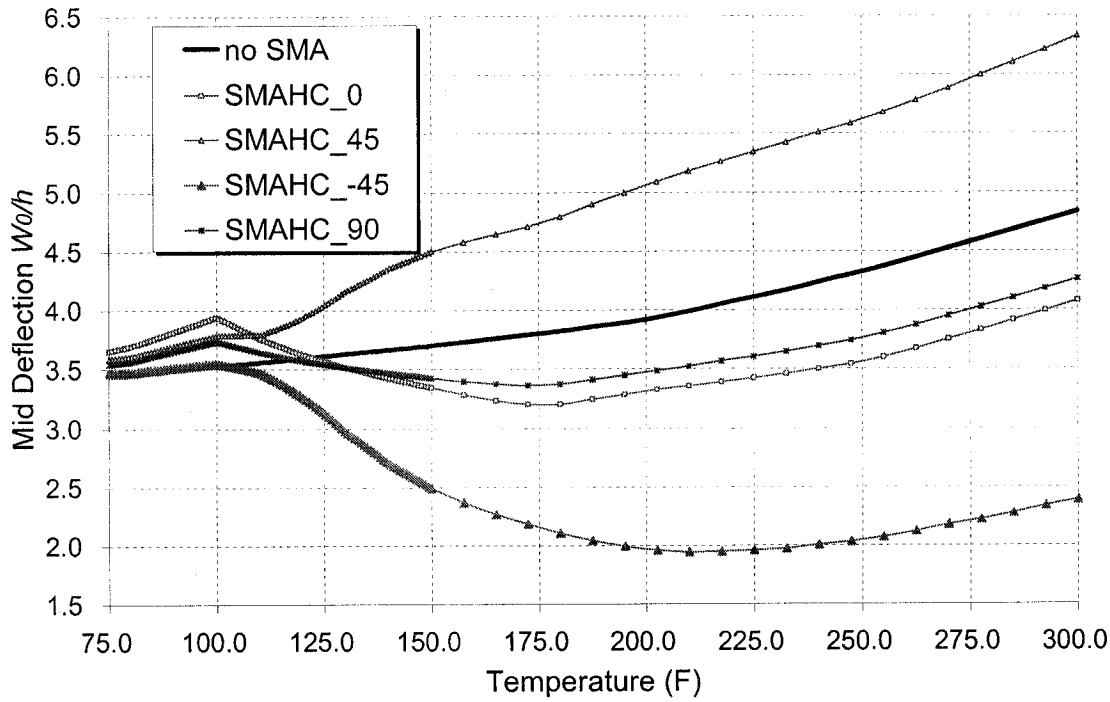

(b) Post-activation stage

Figure 7-18: Buckling and postbuckling of the SSSS SMAHC plate with a central cutout and an initial imperfection of 0.1h, subject to pre-compression and subsequent elevated temperature load

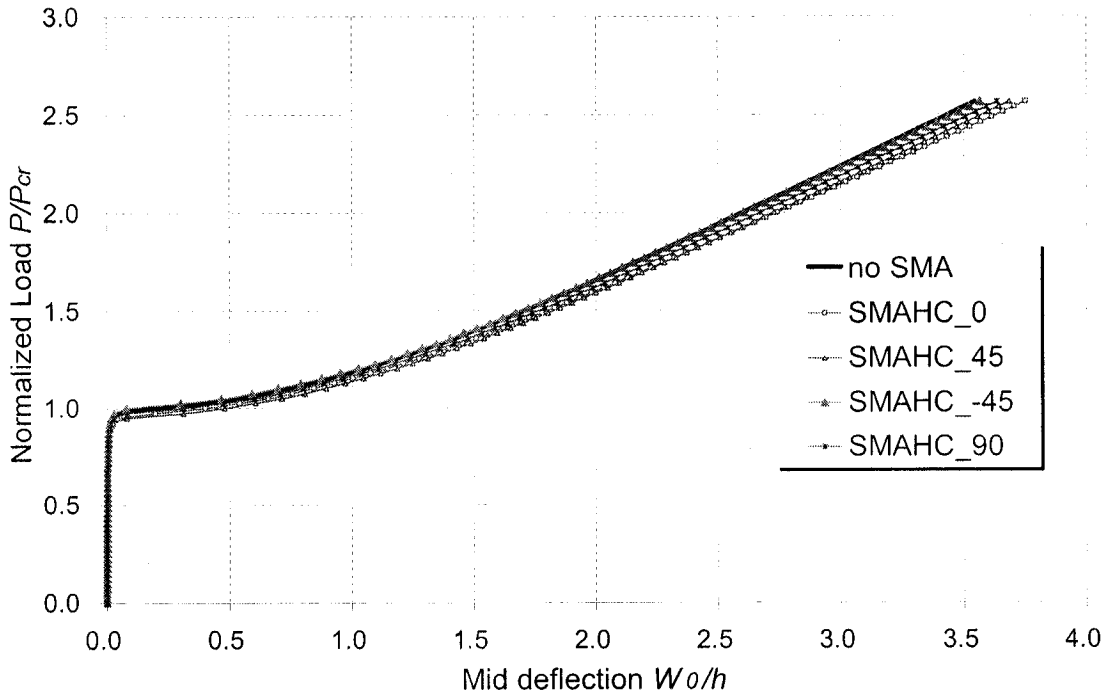

(a) Pre-actuation stage

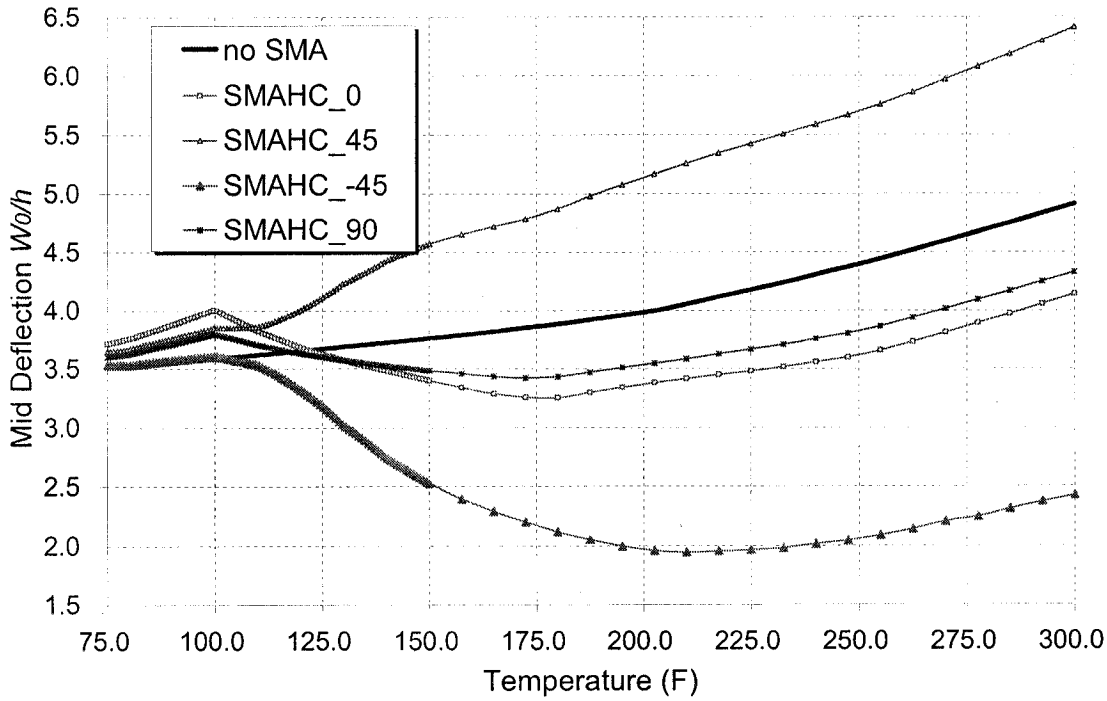

(b) Post-activation stage

Figure 7-19: Buckling and postbuckling of SSSS SMAHC plate with a central cutout and an initial imperfection of 0.001h, subject to pre-compression and subsequent elevated temperature load

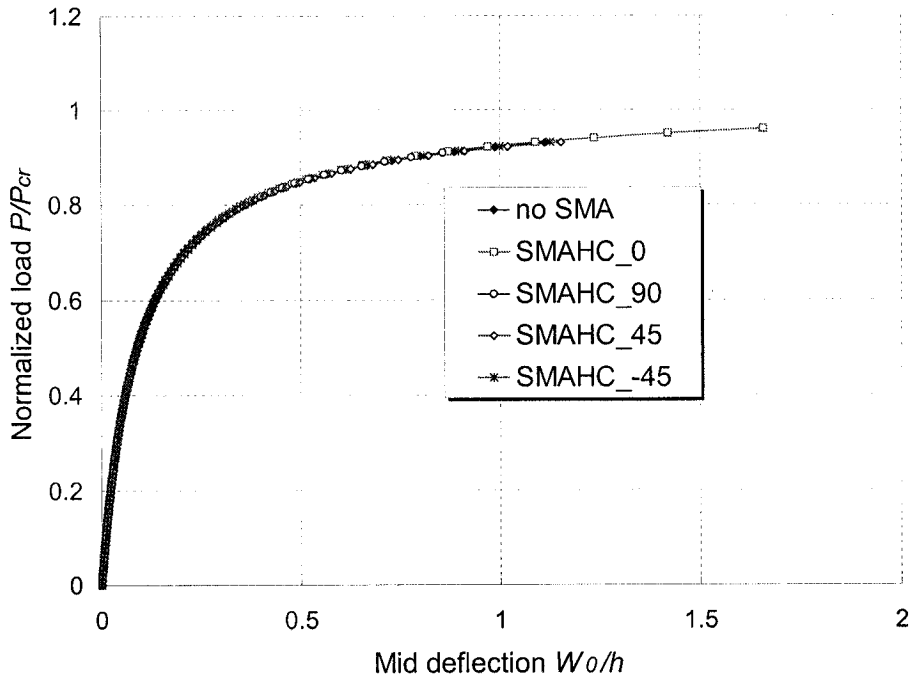

(a) Pre-actuation stage

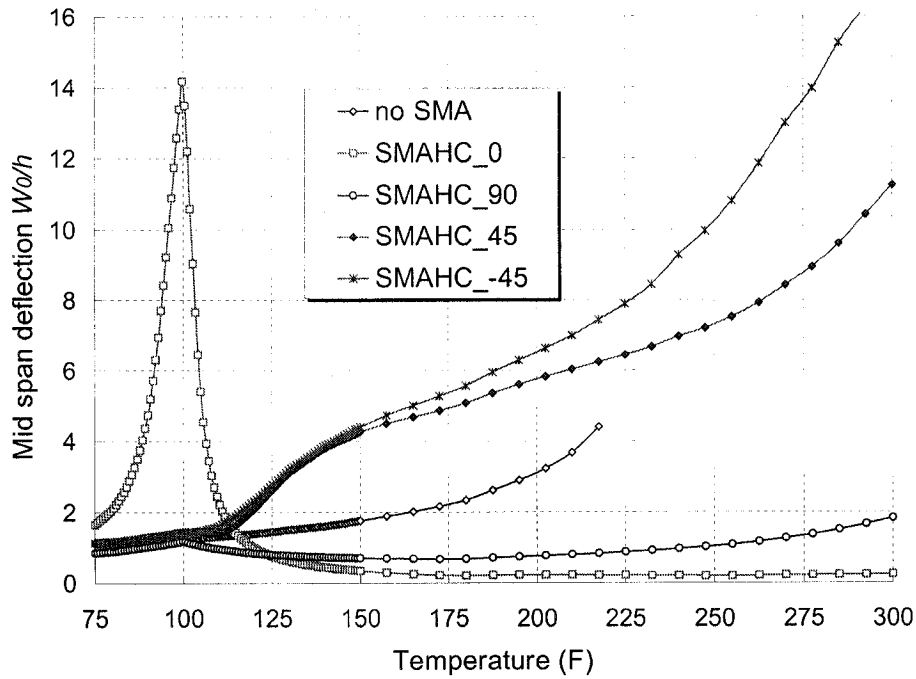

(b) Post-activation stage

Figure 7-20: Buckling and postbuckling of the SSFF SMAHC plate with an initial imperfection of 0.1h, subject to pre-compression and subsequent elevated temperature load

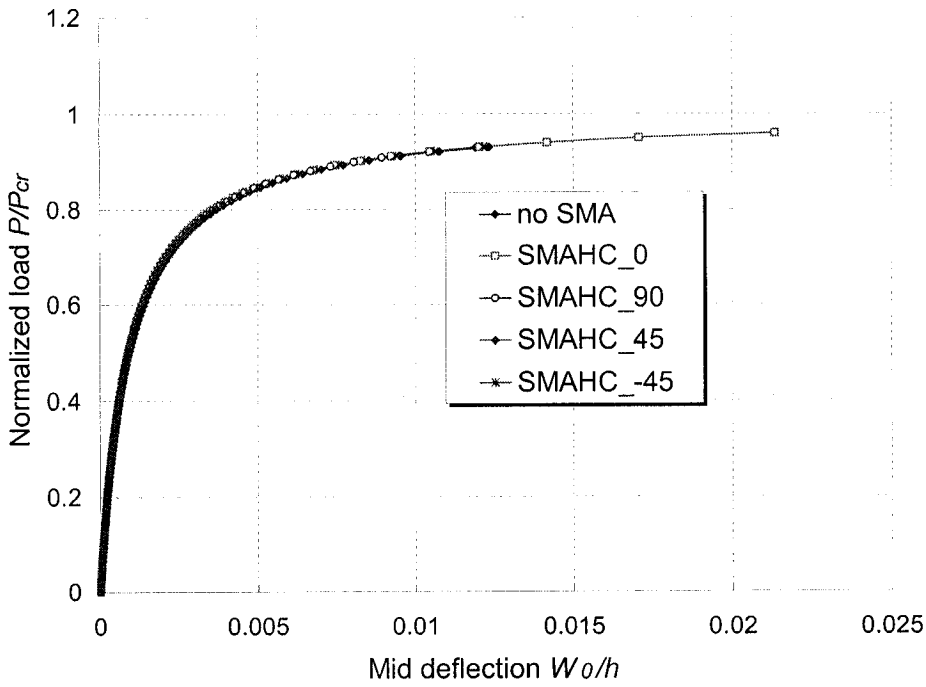

(a) Pre-actuation stage

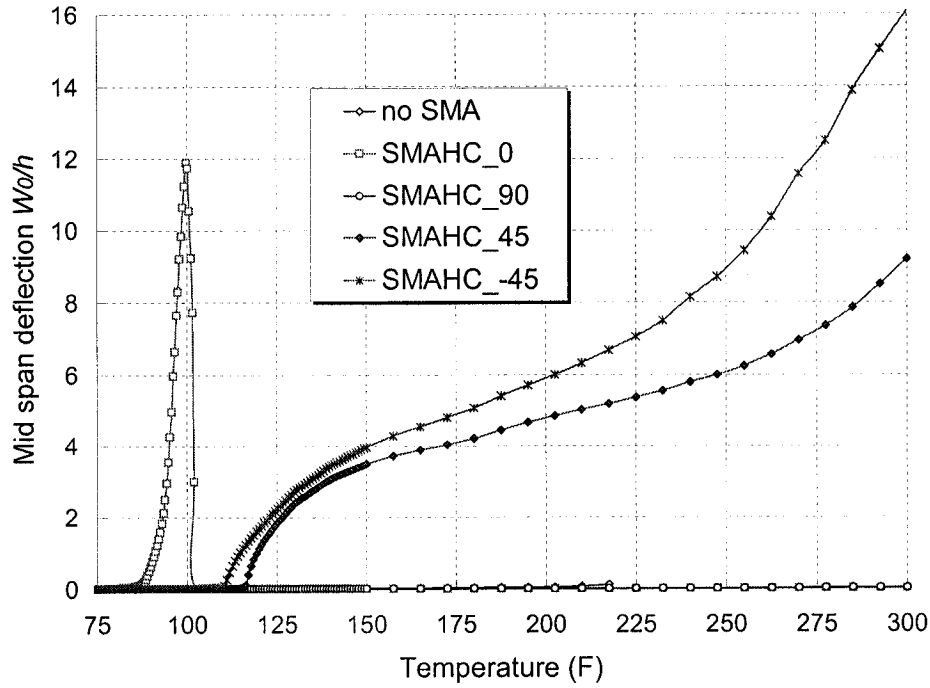

(b) Post-activation stage

Figure 7-21: Buckling and postbuckling of the SSFF SMAHC plate with an initial imperfection of 0.001h, subject to pre-compression and subsequent elevated temperature load

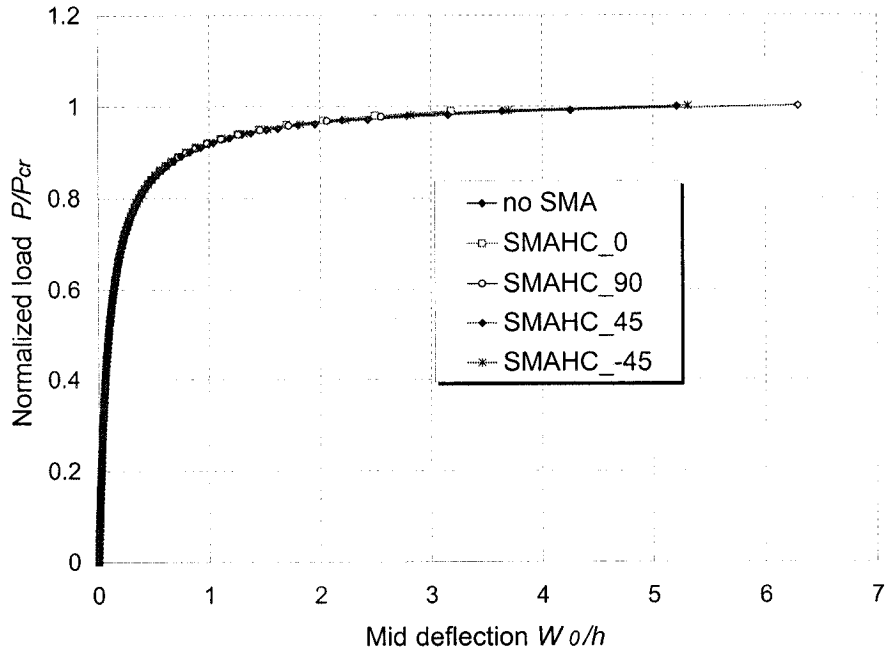

(a) Pre-actuation stage

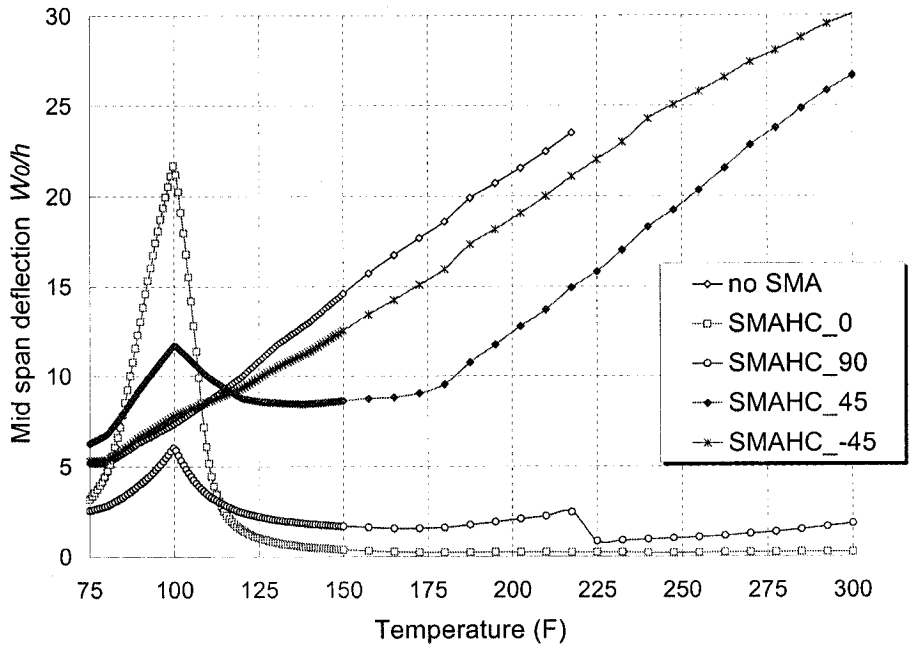

(b) Post-activation stage

Figure 7-22: Buckling and postbuckling of the SSFF SMAHC plate with a central cutout and an initial imperfection of 0.1h, subject to pre-compression and subsequent elevated temperature load

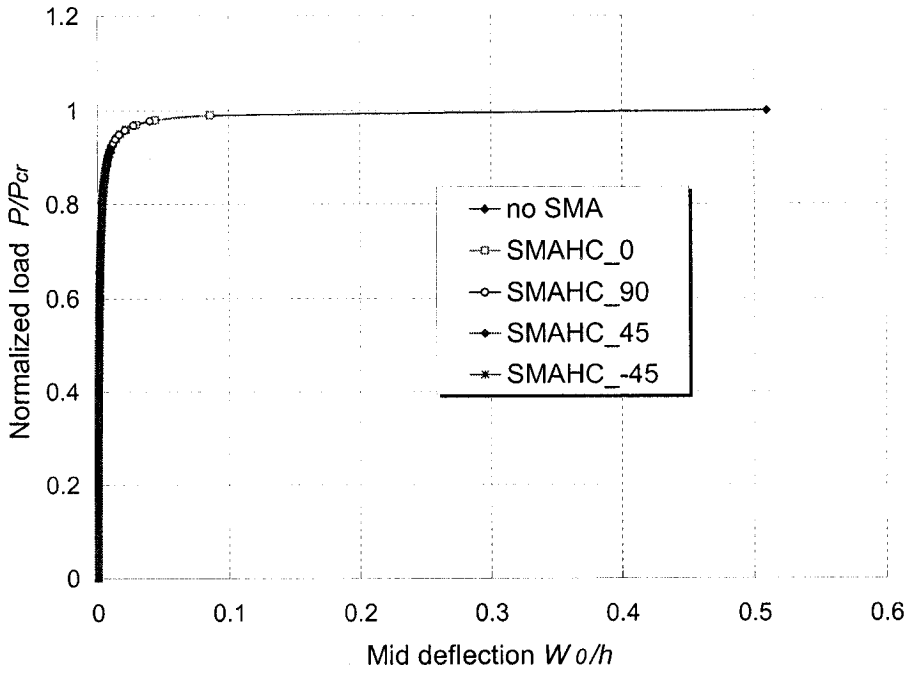

(a) Pre-actuation stage

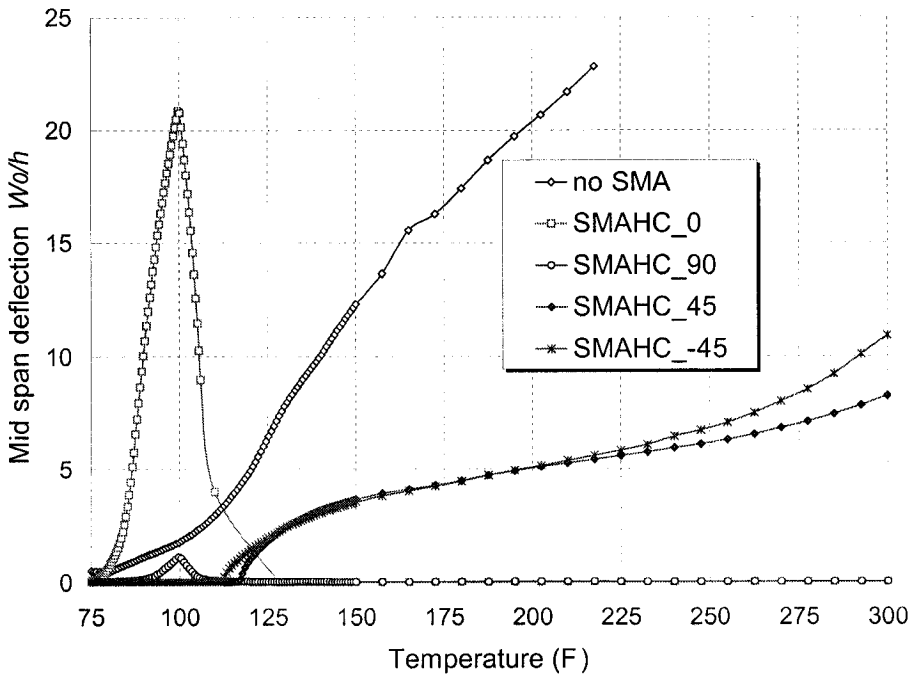

(b) Post-activation stage

Figure 7-23: Buckling and postbuckling of the SSFF SMAHC plate with a central cutout and an initial imperfection of 0.001h, subject to pre-compression and subsequent elevated temperature load

7.11 Appendix B-Typical experimental setup

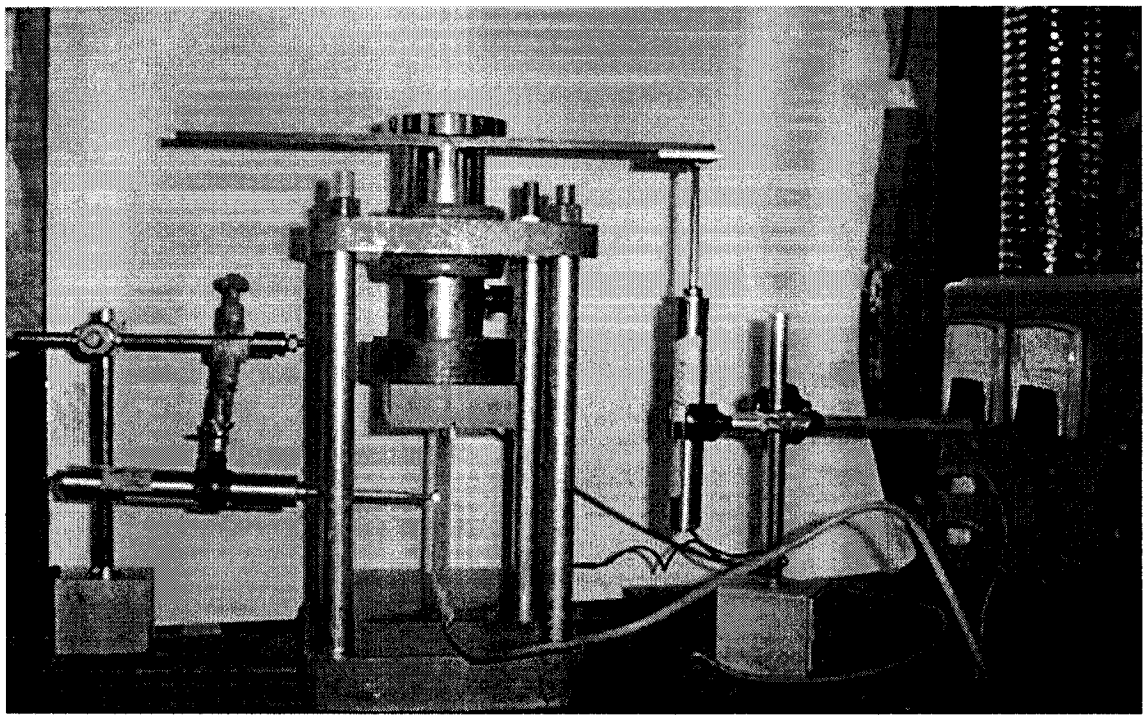

Figure 7-24: Typical experimental setup for the SSFF SMAHC plate

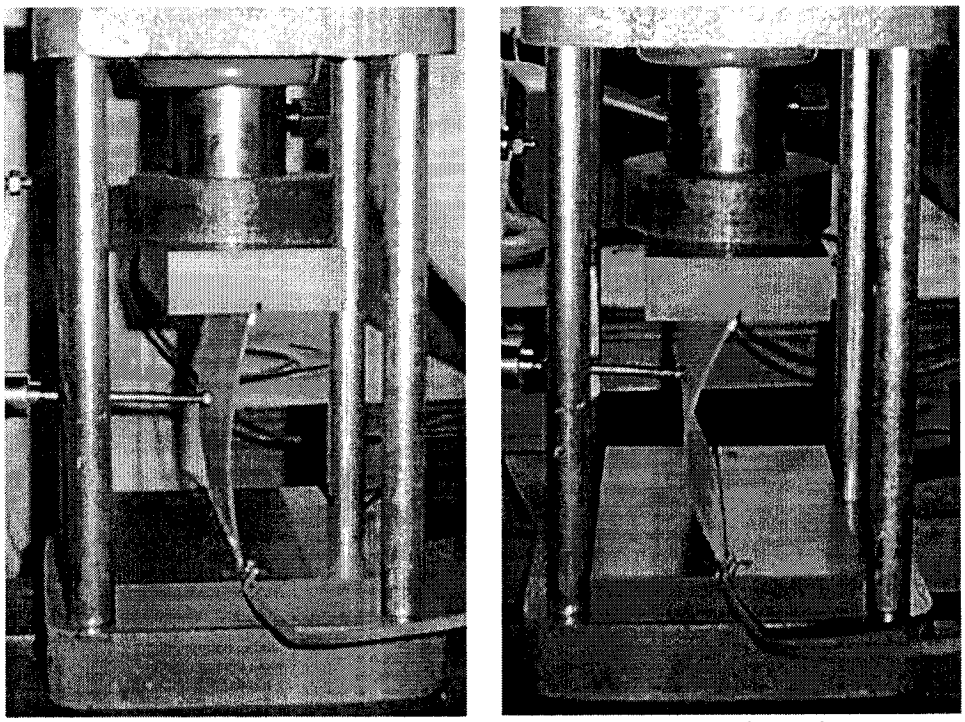

Before Heating wires After Heating wires

Figure 7-25: Change of lateral deflection in the SSFF SMAHC plate with SMA wire along 0° direction, i.e. parallel to the direction of compression load

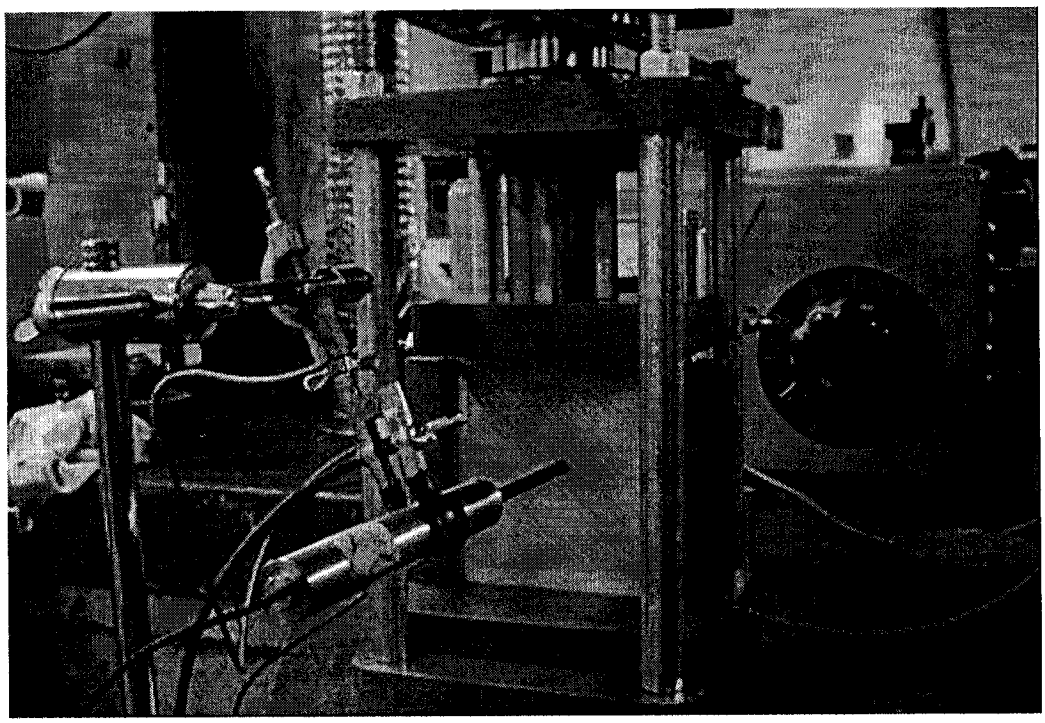

Figure 7-26: Typical experimental setup for the SSSS SMAHC plate

Chapter 8 Conclusions and recommendations

In this dissertation, the influence of a cutout on the structural response of cylindrical shells and tubes subject to axial loading was systematically investigated. The main objective of this work was to characterize the stability and crushing behaviors of metallic and FRP tubular structures having a cutout, subject to static, quasi-static and dynamic compression loadings. In thin-walled cylindrical shells under axial loading conditions, buckling and postbuckling behaviors are more pronounced than material failure, such as yielding and fracture. In moderately thick-walled shells, failure is associated with the global structural behavior, either loss of stability or being crushed, depending on the rate of the applied compression load. In this investigation, the crushing behavior and energy absorption capacity of both unidirectional pultruded tubes and hybrid pultruded/braided tubes were considered. The proposed hybrid pultruded/ braided tube was demonstrated to be an economical and effective energy absorption structural component.

This thesis also investigated the feasibility of mitigating the local instability of cylindrical shell structures having a cutout, with the use of shape memory alloy materials.

Considerable amount of useful numerical and experimental results were generated through these investigations. This chapter provides a summary of the works carried out, followed by conclusions and recommendations for future work in this field.

8.1 Conclusions

8.1.1 Buckling and postbuckling of thin-walled and moderately thick walled cylindrical shells with a cutout

In general, the presence of a cutout significantly reduces the buckling capacity of the tubular shells, with the results being affected by the location and size of the cutout.

It was demonstrated that the presence of a cutout in the moderately thick-walled tubular shells induced global bending, leading to the collapse of the tubes when the cutout was located near the mid-height of the shell, whereas when the cutout was located

near the loaded end, local buckling would dominate. A cutout located near the loaded end could effectively absorb energy, and redistribute the stress more efficiently. Another important finding was that the effective length of the shell could be reduced when the cutout was located near the loaded end, because of the stress redistribution near the cutout, thereby enhancing the buckling capacity of the tubes.

For thin-shell tubes with a cutout, the linear buckling analyses produced results well below those obtained from the nonlinear analyses. It is worth noting that a transition from lower local buckling modes to higher modes could occur when the cutout is located at mid-height of the short cylindrical shells, and near the loaded end in the long cylindrical shells. Therefore, the performance of such cylindrical shells could be optimized by properly situating the cutout along the length of the shells.

Very good correlation was also observed between the results of the experimental investigation and the numerical simulations with nonlinear buckling analyses. The result obtained from the systematic parametric numerical studies provided valuable insights into the behavior of the shells, and enabled us to produce empirical equations that could be effectively used to assess the buckling capacity of the shells with a square cutout.

8.1.2 Quasi-static and dynamic crushing behaviors of tubes having a cutout

As mentioned earlier, the presence of a cutout could significantly influence the crushing behaviors and energy absorption capacity of the cylindrical tubes.

In quasi-static crushing, the energy absorption efficiency of both aluminum and steel tubes was improved when the cutout location was moved from mid-height to near the tube's top end. In general, when the cutout was located at the mid-height, the tubes were crushed in a global buckling mode; conversely, when the cutout was located near the top end, the tubes crushed in a progressive crushing mode.

Under the dynamic impact conditions, as the velocity of the impacting mass increased, the negative influence of the cutout was decreased. However, this trend was not observed for the specific case of 5D aluminum tubes with the cutout located at $L_0 = 0.70L$, when subject to dynamic crushing, and also in the 2D steel tubes with a cutout at their mid-height, subject to quasi-static crushing.

Empirical equations for predicting the mean and peak crushing forces of aluminum and steel tubes with and without a cutout were developed. These equations were based on linear and nonlinear curve fitting to the results obtained from the parametric numerical study conducted in this research.

8.1.3 Energy absorption capacity and crushing behavior of hybrid pultruded and braided composite tubes

The hybrid tubes made of pultruded tube overwrapped by braiding were also considered as a component with great potential in energy absorbing applications. From the results obtained through the numerical simulations and experimental investigations, it was found that such hybrid tubes were more effective in absorbing energy than the pultruded tubes.

In the preliminary study, the $[0]_4$ pultruded tube was found to be able to absorb the highest magnitude of energy among all the tubes having the same thickness but different stacking sequences. However, the pultruded tubes often crushed in undesirable modes (such as asymmetric crushing and splitting modes).

The crushing behavior of the hybrid tubes was sensitive to tube length, braid thickness and loading conditions. While the carbon fiber braid could increase the energy absorption capacity very effectively, it did not produce the desirable local buckling failure mode. Moreover, the thinner braid (0.3 mm) was found to produce a more local buckling failure mode in comparison to the thicker braid (1.0 mm). Furthermore, braids were found to be most useful under dynamic axial impact, because the higher the impact velocity, the more contribution the braid would offer.

8.1.4 Mitigation of local instability of composite plates with and without a cutout

The effective coefficient of thermal expansion (ECTE) model of the shape memory alloy material was found to be very suitable and efficient for advanced structural analysis of shape memory alloy hybrid composite (SMAHC) components. It is also easy to implement the model into commercial finite element codes. As a preliminary work and feasibility study, the buckling and postbuckling behavior of SMAHC plate with and

without a cutout subject to in-plane pre-compression and a subsequent thermal loading was investigated numerically and experimentally.

By orienting the SMA wires along specific direction in the laminate structure, the actuation property of the shape memory alloy materials could be used to suppress the instability of FRP plates. For the four-side simply supported SMAHC plate, with the exception of the plate hosting SMA wires oriented at 45° direction, the shape memory alloy material was able to effectively mitigate the local instability of the SMAHC plate, subject to both in-plane compression and thermal load of elevated temperature.. The beneficial effect of SMA wires was maximized when the wires were oriented along -45°. It was also observed that such beneficial effect was not noteworthy in the SMAHC plates with two sides simply supported and two sides free boundary conditions. In fact, the presence of SMA wires oriented at 0°, 45° and -45° angles in these plates increased the lateral deflection when activated.

The stress concentration factor (SCF) at the edge of the cutout in the plates remained constant, at about 2.65, during pre-buckling stage. However, it then suddenly changed after the onset of buckling and during the postbuckling stage. The SCF was significantly influenced by the orientation of the SMA wires.

The observations from the numerical study were verified by an experimental investigation. Good qualitative agreements were observed.

8.2 Recommendations for future research

It is recommended that the following issues be investigated in future works:

(i) In the research conducted within this thesis, the quasi-static and dynamic crushing behaviors of aluminum and steel tubes having a cutout were studied. The developed empirical equations account for the effect of size of the cutout, in term of the net circumference ratio. However, as only one size of cutout was studied, future study should consider a range of practical cutout sizes, so that the developed empirical equations could accommodate the variation of cutout size.

(ii) The range of speed of the dynamic impact loading is between 0~20 m/s. Future work should consider higher speeds, thus expanding the study for considering real life crashes in automotive and aerospace structures.

(iii) Owing to the limitation of the impact testing facility in this work, only quasi-static crushing tests could be conducted in assessing energy absorption capacity and crushing behavior of hybrid pultruded and braided composite tubes. Dynamic crushing tests should be conducted in future to ascertain the integrity of the numerical results obtained within this thesis work.

(iv) The future work should also consider different combinations of pultrution and braid tubes, such as high strength carbon fiber pultrution tubes with glass or carbon fiber braids.

(v) The preliminary feasibility study on mitigation of local instability of FRP plates with and without a cutout with shape memory alloy wires indicated promising results. Both numerical and experimental works attested that SMA wires could be effectively used in mitigating the local instabilities in shells having a cutout. In order to calibrate the finite element model using ECTE material model of SMA, actual material testing should be carried out to characterize the effective engineering properties required as input into the model. These engineering properties include: the full relationship between the effective thermal expansion factor, the Young's modulus and its variation as a function of temperature.

(vi) In this work, the SMA wires were activated using a DC power supply. It was later realized that the effective length of each wire connected in the parallel mode was not exactly the same for each SMA wire. Therefore all SMA wires could not be uniformly activated. In future tests, the plates should be subject to a uniform temperature, so the issue of non-uniform SMA wire resistance would be eliminated. The higher temperature actuation would in turn limit the use of the conventional sensors (such as the LVDT used in our investigation). Therefore, the application of a laser

vibrometer can be considered and investigated for facilitating the measurement of lateral deflection of the plates/tubes.

(vii) Moreover, in order to increase the actuation force of the SMA, it is recommended that higher diameter wires or ribbons be used.

General References

Abosbaia A.A.S., Mahdi E, Hamouda A.M.S. and Sahari B.B. (2003), Quasi-static axial crushing of segmented and non-segmented composite tubes, *Composite Structures* 60: 327–343.

Alexander J.M. (1960), An approximate analysis of the collapse of thin cylindrical shells under axial loading, *Quarterly Journal of Mechanics and applied Mathematics* 13: 10-15.

Alghamdi A.A.A. (2001), Collapsible impact energy absorbers: an overview, *Thin-Walled Structures* 39: 189–213.

ANSYS User's manual, ANSYS Inc., Canonsburg, PA, USA, 2003.

Arbocz J. and Hol J.M.A.M., (1991), Collapse of axially compressed cylindrical shells with random imperfections, *AIAA Journal,* 29: 2247-2256.

Babbage J.M., Mallick P.K. (2002), Axial crush resistance of aluminum-composite hybrid tubes, Proceeding of *17th Annual Technical Conference of the American Society of Composite*, Paper No. 070.

Baker E.H., Kovalevsky L. and Rish F.L., *Structural analysis of shells*, McGraw-Hill Book Company, 1972.

Bathe K.J., Walczak J, Guillermin O, Bouzinov PA and Chen HY (1999), Advances in crush analysis, *Computers and Structures* 72: 31-47.

Baz A. and Tampe L. (1989), Active control of buckling of flexible beams, in *Proceeding of ASME: Design Technical Conference*, Montreal, Canada, 211-218.

Birman V. (1997), Stability of functionally graded shape memory alloy sandwich panels, *Smart Materials and Structures* 6: 278–286.

Birman V. (1999), Analysis of an infinite shape memory alloy plate with a circular hole subjected to biaxial tension, *International Journal of Solids and Structures* 36: 167-178.

Bleich F., *Buckling Strength of Metal Structures*, McGraw-Hill Book Company, Inc., New York, NY. 1952.

Bo Z. and Lagoudas D.C. (1994), Comparison of different thermomechanical models for shape memory alloys, *Adaptive Structures and Composite Materials: Analysis and Application*, AD-45/MD-54: 9-19 ASME.

Bouchet J., Jacquelin E. and Hamelin P. (2000), Static and dynamic behavior of combined composite aluminum tube for automotive applications, *Composites Science and Technology* 60: 1891-1900.

Bouchet J., Jacquelin E. and Hamelin P. (2002), Dynamic axial crushing of combined composite aluminum tube: the role of both reinforcement and surface treatments, *Composite Structures* 56: 87–96.

Boyd J.G. and Lagoudas D.C. (1994), A constitutive model for simultaneous transformation and reorientation in memory materials, *Mechanics of Phase Transformations and Shape Memory Alloys*, AMD-89/PVP-292: 159-172 ASME.

Brinson L.C. (1993), One-dimensional constitutive behavior of shape memory alloys: thermomechanical derivation with non-constant material functions and redefined martensite internal variable, *Journal of Intelligent Material Systems and Structures* 4: 229-242.

Buehler W.J. and Wiley R.C. (1962), TiNi-Ductile Intermetallic Compound, *Transactions of the American Society of Metals* 55: 269-276.

Buehler W.J. and Wiley R.C. (1965), Nickle-based alloys, *US Patent* 3,174,851.

Chiu C.H. and Lu C.K. (1997), Crushing characteristics of 3-D braided composite square tubes, *Journal of Composite Materials* 31 (22): 2309-2327.

Chryssanthopoulos M.K., Elghazouli A.Y. and Esong I.E., (2000), Validation of FE models for buckling analysis of woven GFRP shells, *Composite structures*, 49:355-367

Chiu C.H., Tsai K.H. and Huang W.J. (1999), Crush-failure modes of 2D triaxially braided hybrid composite tubes, *Composites Science and Technology* 59: 1713-1723.

Choi S., Lee J.J., Seo D.C. and Choi S.W. (1999), The active buckling control of laminated composite beams with embedded shape memory alloy wires, *Composite Structures* 47: 679-686.

Cook R.D., Malkus D.S., Plesha M.E. and Witt R., *Concepts and Applications of Finite Element Analysis*, John Wiley & Sons Inc, 2001.

Crisfield M.A. (1981), A fast incremental/iterative solution procedure that handle "snap through", *Computer Structures* 13: 55-62.

Dipaolo B.P., Monteiro P.J.M. and Gronsky R. (2004), Quasi-static axial crush response of a thin-wall, stainless steel box component, *International Journal of Solids and Structures* 41: 3707-3733.

El-Hage H.H. (2004), A numerical study on the quasi-static axial crush characteristics of square aluminum and aluminum-composite hybrid tubes, *PhD thesis*, Department of Mechanical Engineering, University of Windsor.

Farley G.L. and Jones R.M. (1992), Crushing characteristics of continuous fiber reinforced composite tubes, *Journal of Composite Materials* 26 (1): 37-50.

Florence A.L. and Goodier J.N. (1968), Dynamic plastic buckling of cylindrical shells in sustained axial compressive flow, *Transactions of the ASME, Journal of Applied Mechanics* 35 (1): 80-86.

Forde B.W.R. and Stiemer S.F. (1987), Improved arc length orthogonality methods for nonlinear finite element analysis, *Computer & Structures* 27: 625-630.

Guillowa S.R., Lu G. and Grzebietab R.H. (2001), Quasi-static axial compression of thin-walled circular aluminum tubes, *International Journal of Mechanical Sciences* 43: 2103-2123.

Gupta N.K., Velmurucan R. and Gupta S.K. (1997), An analysis of axial crushing of composite tubes, *Journal of Composite Materials* 31(13): 1262-1286.

Gupta N.K., Prasad E.G.L. (1999), Quasi-static and dynamic axial compression of glass/polyester composite hemi-spherical shells, *International Journal of Impact Engineering* 22: 757-774.

Hamada H., Ramakrishna S. and Sato H. (1996), Effect of fiber orientation on the energy absorption capability of carbon fiber/PEEK composite tubes, *Journal of Composite Materials* 30 (8): 947-963.

Han H.P., Ang K.K., Wang Q. and Taheri F. (2006a), Buckling enhancement of epoxy columns using embedded shape memory alloy spring actuators. *Journal of Composite Structures* 72 (2): 200-211.

Han H.P., Taheri F., Cheng J.Q. and Pegg N. (2006b), Numerical and experimental investigations of the response of aluminum cylinders with a cutout subject to axial compression, *Thin Wall Structures* 44: 254–270.

Han H.P., Taheri F., Pegg N., Lu Y. (2006c), A numerical study on the axial crushing response of hybrid pultruded and braided tubes, Accepted for publication in *Composite Structures.*

Hilburger M.W., Vicki O.B. and Michael P.N., (2001), Buckling behaviour of compression-loaded quasi-isotropic curved panels with a circular cutout, *International Journal of Solids and Structures* 38: 1495-1522.

Jia H. (1998), Impact damage resistance of shape memory alloy hybrid composite structures, *PhD thesis*, Virginia Polytechnic Institute and State University.

Jones N., *Structural Impact*, Cambridge University Press, 1997.

Jullien J.F. and Limam A. (1998), Effect of openings on the buckling of cylindrical shells subjected to axial compression, *Thin-Walled Structures*, 31: 187-202.

Kormi K., Webb D.C. and Montague P. (1993), Crash behaviour of circular tubes with large side openings, *International Journal of Mechanical Science* 35 (3/4): 193-208.

Lekhnistskii's G., Tsai W.S. and Cheron T., *Anisotropic plates*, Gordon and Breach Science Publishers, New York, 1968.

Liang C. and Rogers C.A. (1990), One-dimensional thermomechanical constitutive relations for shape memory materials, *Journal of Intelligent Material Systems and Structures* 1: 207-234.
Lindberg H.E. and Florence A.L., *Dynamic pulse buckling: Theory and Experiment*, Martinus Nijhoff Publishers, 1987.

Litle W.A., *Reliability of shell buckling predictions*, The MIT Press, Cambridge, Massachusetts, 1964.

Loughlan J., Thompson S.P. and Smith H. (2002), Buckling control using embedded shape memory actuators and the utilization of smart technology in future aerospace platforms, *Composite Structures* 58:319–347.

LS-DYNA V.970 Keyword User's Manual, LSTC, Livermore, CA, USA, 1997.

Magee C.L. and Thornton P.H. (1978), Design consideration in energy absorption by structural collapse, *SAE Technical Paper No.* 780434.

Mahdi E., Sahari B.B., Hamouda A.M.S. and Khalid Y.A. (2001), An experimental investigation into crushing behavior of filament-wound laminated cone-cone intersection composite shell, *Composite Structures* 51: 211-219.

Mahdi E., Hamouda A.M.S. and Sahari B.B. (2002), Axial and lateral crushing of the laminate wound laminated composite curved compound system, *Advanced Composite Materials* 11 (2): 171-192.

Mahdi E., Hamouda A.M.S., Sahari B.B. and Khalid Y.A. (2003), Effect of hybridization on crushing behavior of carbon/glass fiber/epoxy circular–cylindrical shells, *Journal of Materials Processing Technology* 132: 49–57.

Mahdi E., Hamouda A.S.M. and Sen A.C. (2004), Quasi-static crushing behavior of hybrid and non-hybrid natural fiber composite solid cones, *Composite Structures* 66: 647–663.
Mahdi E., Hamouda A.S.M., Mokhtar A.S. and Majid D.L. (2005), Many aspects to improve damage tolerance of collapsible composite energy absorber devices, *Composite Structures* 67: 175–187.

Mamalis A.G., Yuan Y.B. and Viegelahn G.L. (1992), Collapse of thin wall composite sections subjected to high speed axial loading, *International Journal of vehicle Design* 13(5/6): 564-579.

Mamalis A.G., Manolakos D.E. and Demosthenous G.A., Ioannidis M.B. (1996), The static and dynamic axial collapse of fiberglass composite automotive frame rails, *Composite Structures* 34: 77-90.

Mamalis A.G., Manolakos D.E., Ioannidis M.B. and Kostazos P.K. (2003), Crushing of hybrid square sandwich composite vehicle hollow bodyshells with reinforced core subjected to axial loading: numerical simulation, *Composite Structures* 61: 175–186.

Mamalis A.G., Manolakos D.E., Ioannidis M.B. and Papapostolou D.P. (2005a), On the response of thin-walled CFRP composite tubular components subjected to static and dynamic axial compressive loading: experimental, *Composite Structures* 69: 407–420.

Mamalis A.G., Manolakos D.E., Ioannidis M.B. and Papapostolou D.P. (2005b), On the experimental investigation of crash energy absorption in laminate splaying collapse mode of FRP tubular components, *Composite Structures* 70: 413–429.

Mamalis A.G., Manolakos D.E., Ioannidis M.B. and Papapostolou D.P. (2005c), On the crushing response of composite sandwich panels subjected to edgewise compression: experimental, *Composite Structures* 71: 246–257.

Mantena P.R. and Mann R. (2003), Impact and dynamic response of high-density structural foams used as filler inside circular steel tube, *Composite Structures* 61: 291–302.

Marsoleka J. and Reimerdes H.G. (2004), Energy absorption of metallic cylindrical shells with induced non-axisymmetric folding patterns, *International Journal of Impact Engineering* 30: 1209–1223.

Murasea K. and Wada H. (2004), Numerical study on the transition of plastic buckling modes for circular tubes subjected to an axial impact load, *International Journal of Impact Engineering* 30: 1131-1146.

Okano M., Sugimoto K., Saito H., Nakai A. and Hamada H. (2005), Effect of the braiding angle on the energy absorption properties of a hybrid braided FRP tube, *Journal of Materials-Design and Applications* 219 (L1): 59-66.

Olovsson L., Simonsson K. and Unosson M. (2005), Selective mass scaling for explicit finite element analyses, *International Journal for Numerical Methods in Engineering* 63:1436-1445.

Otsuka K. and Shimizu K. (1986), Pseudo-elasticity and Shape Memory Effects in Alloys, *International Metals Reviews* 31 (3): 93-114.

Ramm E., Strategies for tracing the nonlinear response near limit points, in *Nonlinear Finite Element Analysis in Structural Mechanics*, Springer-Verlag, Berlin Germany 63-69, 1981.

Rogers C.A. and Robertshaw H.H. (1988), Shape Memory Alloy Reinforced Composites, Engineering Science Preprints 25, *Society of Engineering Science*, Inc., ESP25.8027.

Roh J.H., Oh I.K., Yang S.M., Han J.H. and Lee I. (2004), Thermal post-buckling analysis of shape memory alloy hybrid composite shell panels, *Smart Materials and Structures* 13: 1337–1344.

Sahu S.K. and Datta P.K. (2002), Dynamic stability of curved panels with cutouts, *Journal of Sound and Vibration* 251(4): 683-696.

Sahu S.K. and Datta P.K. (2003), Dynamic Stability of Laminated Composite Curved Panels with Cutouts, *Journal of Engineering Mechanics ASCE* Nov 2003 1245-1253.

Saito H., Chirwa E.C., Inai R. and Hamada H. (2002), Energy absorption of braiding pultrusion process composite rods, *Composite Structures* 55: 407–417.

Schneider F. and Jones N. (2004), Impact of thin-wall high strength steel structural section, Proceedings of the Institution of Mechanical Engineers 218 (D): *Journal of Automobile Engineering*, 131-158.

Schultz M.R. and Hyer M.W. (2001), Static and Dynamic Energy-Absorption Capacity of Graphite-Epoxy Tubular Specimens, *Mechanics of Composite Materials and Structures* 8: 231-247.

Shimamoto A., Azakami T. and Oguchi T. (2003), Reduction of KI and KII by the Shape-memory Effect in a TiNi Shape-memory Fiber-reinforced Epoxy Matrix Composite, *Experimental Mechanics* 43 (1): 77-82.

Shimamoto A., Ohkawara H. and Nogata F. (2004), Enhancement of mechanical strength by shape memory effect in TiNi fiber-reinforced composites, *Engineering Fracture Mechanics* 71: 737-746.

Shin K.C., Lee J.J., Kim K.H., Song M.C. and Huh J.S. (2002), Axial crush and bending collapse of an aluminum/GFRP hybrid square tube and its energy absorption capability, *Composite Structures* 57: 279-287.

Song H.W., Wan Z.M., Xie Z.M. and Du X.W. (2000), Axial impact behavior and energy absorption efficiency of composite wrapped metal tubes, *International Journal of Impact Engineering* 24:385-401.

Tafreshi A., (2002), Buckling and postbuckling analysis of composite cylindrical shells with cutout subjected to internal pressure and axial compression load, *International Journal of Pressure Vessels and Piping*, 79: 351-359

Taheri F., Shahin K. and Widiarsa I. (2002), On the parameters influencing the performance of reinforced concrete beams strengthened with FRP plates, Composite Structures 58 (2): 217-227.

Tanaka K. (1986), A thermomechanical sketch of shape memory effect: one-dimensional tensile behavior, *Res. Mechanica* 18: 251-263.

Tawfik M., Ro J.J. and Mei C. (2002), Thermal post-buckling and aeroelastic behavior of shape memory alloy reinforced plates, *Smart Materials and Structures* 11: 297–307.

Thompson S.P. and Loughlan J. (1995), The active buckling control of some composite column strips using piezoceramic actuators, *Composite Structures* 32 (1-4): 59-67.

Timoshenko S.P. and Gere J.M., *Theory of elastic stability* (2nd Edition), McGraw-Hill, New York, 1961.

Tsai X.Y. and Chen L.W. (2002), Dynamic stability of a shape memory alloy wire reinforced composite beam, *Composite Structures* 56: 235–241.

Turner T.L. (2000a), "A New Thermoelastic Model for Analysis of Shape Memory Alloy Hybrid Composites", *Journal of Intelligent Material Systems and Structures* 11: 382-394.

Turner T.L. (2000b), SMA hybrid composites for dynamic response abatement applications, Proceedings of the *7th International Conference on Recent Advances in Structural Dynamics*, 1, 453-465, The Institute of Sound and Vibration Research, University of Southampton, England.

Turner T.L., Lach C.L. and Cano R.J. (2001), Fabrication and characterization of SMA hybrid composites, *SPIE 8th Annual International Symposium on Smart Structures and Materials; Active Materials: Behavior and Mechanics*, SPIE Vol. 4333, Paper No. 4333-60, Newport Beach, CA.

Turner T.L. and Patel H.D. (2004), Analysis of SMA hybrid composite structures using commercial codes, Smart Structures and Materials: Modeling, Signal Processing, and Control, *Proceedings of SPIE* Vol. 5383, Paper No. 12, San Diego, CA.

Tylikowski A. (1998), Dynamic stability of rotating composite shells with thermoactive shape memory alloy fibers, *Journal of Thermal Stresses* 21: 327-339.

Ugural A.C., *Stresses in plate and shells*, McGraw-Hill Book Company, 1981.

Velmurugan R., Gupta N.K., Solaimurugan S. and Elayaperumal A. (2004), The effect of stitching on FRP cylindrical shells under axial compression, *International Journal of Impact Engineering* 30: 923-938.

Wang B. and Lu G. (2002), Mushrooming of circular tubes under dynamic axial loading, *Thin-Walled Structures* 40: 167-182.

Wayman C.M. and Shimizu K. (1972), The Shape Memory ("Marmem") Effect in Alloys, *Metal Science Journal* 6: 175-183.

Wayman C.M. (1980), Some Applications of Shape-Memory Alloys, *Journal of Metals* June: 129-137.

Xu Z.J. (2002), Shape control of beam structures using shape memory alloy wire actuators, *M.Eng. thesis*, National University of Singapore.

Yamashita M., Gotoh M. and Sawairi Y. (2003), Axial crush of hollow cylindrical structures with various polygonal cross-sections Numerical simulation and experiment, *Journal of Materials Processing Technology* 140: 59-64.

Yeh M.K., Lin M.C. and Wu W.T., (1999), Bending buckling of an elastoplastic cylindrical shell with a cutout, *Engineering Structures*, 21: 996–1005.

Zhang Z., Investigation on dynamic pulse buckling and damage behavior of composite laminated beam subjected to axial impulse, *PhD thesis*, Faculty of Engineering, Dalhousie University, 2004

Zhang Z. and Taheri F. (2004), Dynamic pulse-buckling behavior of quasi-ductile' carbon/epoxy and E-glass/epoxy laminated composite beams, *Composite Structures* 64 (3-4): 269-274.

Zhao H. and Abdennadher S. (2004), On the strength enhancement under impact loading of square tubes made from rate insensitive metals, *International Journal of Solids and Structures* 41: 6677-6697.

Zienkiewicz O.C., *The Finite Element Method*, third edition, McGraw-Hill, London, 1977.